

# **Synthesis of Ternary Layered Double Hydroxides And Their Composites For Environmental Applications**

**Thesis Submitted  
in Partial Fulfillment of the Requirements for the  
Degree of**

**DOCTOR OF PHILOSOPHY  
by**

**JIGYASA PATHAK  
(2K19/PHDAC/05)**

**Under the Supervision of  
DR. POONAM SINGH  
Assistant Professor, Department of Applied Chemistry  
Delhi Technological University**



**To the  
Department of Applied Chemistry**

**DELHI TECHNOLOGICAL UNIVERSITY  
(Formerly Delhi College of Engineering)  
Shahbad Daulatpur, Main Bawana Road, Delhi-110042, India**

**December, 2025**

**© DELHI TECHNOLOGICAL UNIVERSITY-2025**

**All rights reserved**

## ACKNOWLEDGEMENTS

This thesis marks the end of a long and enriching journey, one that would not have been possible without the support, encouragement, and guidance of many individuals.

First and foremost, I express my deepest gratitude to my supervisor, **Dr. Poonam Singh**, for her insightful feedback, and constant encouragement throughout this research. Your mentorship not only shaped the direction of this thesis but also significantly influenced my growth as a researcher. I am sincerely thankful to **Prof. Prateek Sharma**, Vice Chancellor of Delhi Technological University, for providing me the opportunity to pursue my research at this esteemed institution. My heartfelt appreciation goes to my lab mates and fellow researchers, especially **Dr. Bhamini Pandey, Dr. Pooja Singh, Priyanka Yadav, Ashwani Kr. Tiwari, Ritu Sharma, and Versha Joshi**, for the stimulating discussions, brainstorming sessions, and shared experiences—both challenging and joyful—that made this journey memorable. Special thanks to **Dr. Iftkhar Ahmad** and **Dr. Iqra Ashraf** for their valuable input, resources, and for enriching my research with interdisciplinary perspectives. I gratefully acknowledge the technical and administrative staff of the Department of Applied Chemistry, DTU, especially **Mr. Dheeraj Kumar** and **Mr. Deepak**, for their assistance with logistics, equipment, and day-to-day support. I am also thankful for the financial support provided by Delhi Technological University which enabled the successful completion of this research. I am immensely grateful to all my friends for always being there with a listening ear, words of encouragement, and moments of laughter that kept me grounded. To my friends beyond the academic world: thank you for reminding me that life exists outside the lab and for being my source of joy, laughter, and balance. Most importantly, I thank the almighty God, and my family—my parents **Mrs. Nisha Pathak** and **Mr. Anand Ballabh**, my sister **Ms. Chayanika Bhatt**, and my husband **Mr. Rohan Chawla**, for their endless patience, unconditional love, and belief in me. Your emotional support was my greatest strength.

To all those who have been a part of this journey in ways big or small—thank you. This thesis stands as much on your support as on my effort.

(Jigyasa Pathak)



## DELHI TECHNOLOGICAL UNIVERSITY

(Formerly Delhi College of Engineering)  
Shahbad Daulatpur, Main Bawana Road,  
Delhi-110042, India

### CANDIDATE'S DECLARATION

I **Jigyasa Pathak** hereby certify that the work which is being presented in the thesis entitled "**Synthesis of Ternary Layered Double Hydroxides and their Composites for Environmental Applications**" in partial fulfilment for the award of the Degree of Doctor of Philosophy, submitted in the Department of **Applied Chemistry**, Delhi Technological University is an authentic record of my own work carried out during the period from 19/07/2019 to 31/11/2025 under the supervision of **Dr. Poonam Singh**. The matter presented in the thesis has not been submitted by me for the award of any other degree of this or any other Institute.

**Jigyasa Pathak**

**2K19/PHDAC/05**



## DELHI TECHNOLOGICAL UNIVERSITY

(Formerly Delhi College of Engineering)  
Shahbad Daulatpur, Main Bawana Road,  
Delhi-110042, India

### CERTIFICATE BY THE SUPERVISOR(S)

Certified that **Jigyasa Pathak (2K19/PHDAC/05)** has carried out their research work presented in this thesis entitled "**Synthesis of Ternary Layered Double Hydroxides and their Composites for Environmental Applications**" for the award of **Doctor of Philosophy** from Department of Applied Chemistry, Delhi Technological University, Delhi, under my supervision. The thesis embodies results of original work, and studies are carried out by the student herself and the contents of the thesis do not form the basis for the award of any other degree to the candidate or to anybody else from this or any other University/Institution.

**Dr. Poonam Singh**

(Supervisor)

Assistant Professor

Department of Applied Chemistry

Delhi Technological University

Date:

## ABSTRACT

The thesis focuses on the synthesis of layered double hydroxides (LDH) and their composite materials under ambient conditions, with emphasis on environmental applications. The structure, morphology, thermal stability, optical and catalytic behaviour of the synthesized LDHs were studied using various instrumentation techniques. Further, the synthesized lattice was utilized for the elimination of toxic effluents i.e. nitroarene compounds (NACs) and anionic azo dyes from wastewater. In addition, ZnCuNi-LDO and ZnCuCe-LDO were used as photocatalysts for the degradation of Ciprofloxacin (CIF) drug and cationic/anionic azo dyes. Afterwards, a smartphone-based approach was opted for the determination of dye concentration. The results obtained were in agreement with those obtained from UV-Vis spectrophotometer. Upon the successful formation of layered structure, the structure regaining capability i.e. memory effect and anion exchange properties were investigated. The PXRD and FTIR results confirmed the structure regaining ability of the lattice i.e. memory effect as well as the exchange of anion in the interlayer region. Moreover, the synthesis of carbon nitride-based composite materials was also carried out with synthesized LDHs, and were later used for the degradation of *p*-NP and Congo Red (CR). Subsequently, the magnetically separable Fe<sub>3</sub>O<sub>4</sub>/SiO<sub>2</sub>/ZnCuNi-LDH composite was synthesized using electrostatic self-assembly method. The composite was utilized for the catalytic hydrogenation of *p*-NP and reduction of cationic dye Rhodamine B (RhB).

*To my family and friends,  
who believed in me even when  
I doubted myself.*

## LIST OF PUBLICATIONS

### Journal Articles

1. **Jigyasa Pathak**, Sarla Yadav, Bhamini Pandey, Poonam Singh. Comprehensive Insights into Anionic Layered Materials: Assembly, Synthesis, Reactivity, and Application Paradigms, *Advances in Colloid and Interface Science*, Elsevier.  
<https://doi.org/10.1016/j.cis.2025.103696> (I.F. = 19.3) (**SCIE**)
2. Sarla Yadav, **Jigyasa Pathak**, Purusottam Majhi, Sandeep Kaushik, A.K. Shukla, Raminder Kaur, Ravinder Kumar, Poonam Singh. Lac-based-biosynthesis of zinc–copper mixed metal oxide nanoparticles and evaluation of their antifungal activity against *A. alternata* and *F. oxysporum*. *Materials Chemistry and Physics* 2025;330:130152.  
<https://doi.org/10.1016/j.matchemphys.2024.130152> (I.F. = 4.7) (**SCIE**)
3. **Jigyasa Pathak** and Poonam Singh. Zinc-Copper-Nickel Mixed Metal Oxide as Heterogeneous Catalytic Material for the Reductive Degradation of Nitroarene and Azo Dye. *Catalysis Letters* 2024;154:5280-5293. <https://doi.org/10.1007/s10562-024-04754-3> (I.F. = 2.4) (**SCIE**)
4. **Jigyasa Pathak** and Poonam Singh. Ultrafast catalytic reduction of organic pollutants using ternary zinc–copper–nickel layered double hydroxide. *Applied Organometallic Chemistry* 2024;38:e7507. <https://doi.org/10.1002/aoc.7507> (I.F. = 3.5) (**SCIE**)

5. **Jigyasa Pathak** and Poonam Singh. Layered double hydroxides–polymer matrix composites: nexus materials for energy storage applications. *Chemical Papers* 2024;78:7375-7393. <https://doi.org/10.1007/s11696-024-03624-x> (I.F. = 2.5) (**SCIE**)

6. **Jigyasa Pathak**, Bhamini Pandey, Poonam Singh, Ravinder Kumar, Sandeep Kaushik, Ishwar Prasad Sahu, Tarun Kumar Thakur. Exploring the Paradigm of Phyto-Nanofabricated Metal Oxide Nanoparticles: Recent Advancements, Applications, and Challenges. *Molecular Biotechnology* 2023. <https://doi.org/10.1007/s12033-023-00799-8> (I.F. = 2.86) (**SCIE**)

7. Bhamini Pandey, **Jigyasa Pathak**, Poonam Singh, Ravinder Kumar, Amit Kumar, Sandeep Kaushik and Tarun Kumar Thakur. Microplastics in the Ecosystem: An Overview on Detection, Removal, Toxicity Assessment, and Control Release 2023;15:51. <https://doi.org/https://doi.org/10.3390/w15010051> (I.F. = 3.0) (**SCIE**)

8. **Jigyasa Pathak** and Poonam Singh. Synthesis and characterization of ternary layered double hydroxide containing zinc/copper/nickel and its PANI composite. *Polymer Composites* 2022;43:7836-7844. <https://doi.org/10.1002/pc.26895> (I.F. = 4.7) (**SCI/SCIE**)

9. **Jigyasa Pathak** and Poonam Singh. Adsorptive Removal of Congo Red Using Organically Modified Zinc–Copper–Nickel Ternary Metal Hydroxide: Kinetics, Isotherms and Adsorption Studies. *Journal of Polymers and the Environment* 2022;31:327-344. <https://doi.org/10.1007/s10924-022-02612-0> (I.F. = 5.0) (**SCIE**)

10. **Jigyasa Pathak** and Poonam Singh. Evaluating the photocatalytic activity of ZnCuCe-MMO for the degradation of Basic Red 2 and Methyl Orange dyes: Spectrophotometric and Smartphone-based detection. *Journal of Molecular Structure* **(1st Revision received)**

11. **Jigyasa Pathak**, Bhamini Pandey, Poonam Singh et al. Structure–Activity Correlation in ZnCu-Layered Materials: Influence of Ni Doping and Thermal Conversion. **(Communicated)**

12. Sarla Yadav, **Jigyasa Pathak**, Poonam Singh et al. Microplastics as Emerging Contaminants: An Overview of their Properties, Distribution, Analysis, Remediation and Challenges. **(Communicated)**

13. **Jigyasa Pathak** and Poonam Singh. Catalytic decoloration of water-soluble nitro compound and azo dye using LDH/CN composites. **(Under preparation)**

14. **Jigyasa Pathak** and Poonam Singh. Synergistic Catalytic Activity of Fe<sub>3</sub>O<sub>4</sub>/SiO<sub>2</sub>/ZnCuNi-LDH-based Magnetic Composite for NAC and Azo Dye Detoxification in Aqueous Medium. **(Under preparation)**

### **Book Chapters**

1. **Jigyasa Pathak**, Ravinder Kumar, Poonam Singh, Municipal Solid Waste and Climate Change BT - Integrated Waste Management: A Sustainable Approach from Waste to Wealth, in: A. Gupta, R. Kumar, V. Kumar (Eds.), Springer Nature Singapore, Singapore, 2024;207–221. [https://doi.org/10.1007/978-981-97-0823-9\\_10](https://doi.org/10.1007/978-981-97-0823-9_10).

### **Conference/Workshop Proceedings:**

1. **Jigyasa Pathak**, Poonam Singh (2019), **participated** in the International Conference on Atomic Molecular, Optical and Nano Physics with Applications, organized by Delhi Technological University Delhi, 18<sup>th</sup> -20<sup>th</sup> December, 2019.
2. **Jigyasa Pathak**, Poonam Singh (2021), **oral presentation** on title: “Ternary Layered double hydroxide: Synthesis, Characterization and Optical Properties”, International Conference on Innovation and Application in Science and Technology, organized by Department of Applied Sciences, Galgotias College of Engineering and Technology Greater Noida (UP), 21<sup>st</sup> - 23<sup>rd</sup> December, 2021.
3. **Jigyasa Pathak**, Poonam Singh (2022), **oral presentation** on title: “Synthesis and Characterization of ZnCuNi-LDH loaded GG/PAM Hydrogel”, International Conference on Advances in Chemical Sciences and Nanocomposites-ACSN 2022, organized by Zakir Husain Delhi College (Delhi) & ISAS, 1<sup>st</sup> - 2<sup>nd</sup> April, 2022.
4. **Jigyasa Pathak**, Poonam Singh (2022), **participated** in the International Conference on 9<sup>th</sup> Asian Network for Natural and Unnatural Materials organized by Department of Chemistry, University of Delhi (Delhi), 8<sup>th</sup> April, 2022.
5. **Jigyasa Pathak**, Poonam Singh (2022), **oral presentation** on title: “Green Chemistry and Sustainable Practices in Industry: Needs and Challenges”, 2nd International Conference on Green and Sustainable Chemistry Conference-2022 organized by Department of Chemistry, Manav Rachna University Faridabad (Haryana), 17th - 19th November, 2022.

6. **Jigyasa Pathak**, Poonam Singh (2022), **poster presentation** on title: “Synthesis, Characterization and Techno-Economic Challenges Associated With Nanomaterials”, International Conference on Nanotechnology; Opportunities & Challenges (ICNOC-2022) by Department of Applied Sciences & Humanities, Jamia Millia Islamia (Central University), New Delhi, 28th - 30th November, 2022.

7. **Jigyasa Pathak**, Poonam Singh (2024), **oral presentation** on title: “Facile Synthesis of Organo-Modified Layered Ternary Metal Hydroxide for Wastewater Treatment”, International Conference on Emerging Techno-Economic Development for Sustainable Environment, organized by Department of Chemical Engineering, IPS Academy Indore (MP), 12<sup>th</sup> – 13<sup>th</sup> January, 2024.

### **Workshops and Seminars**

1. Participated in INUP-i2i 6<sup>th</sup> User Awareness Workshop on ‘Fabrication & Characterization Facility for Nanotechnology’ held at IIT Delhi – 4<sup>th</sup> - 5<sup>th</sup> March, 2023.
2. Participated in STUTI advanced instrumentation workshop on ‘Advanced Characterization Techniques in Condensed Matter’ conducted by Birla Institute of Science and Technology, Pilani and Amity University under auspices of DST, GoI – 17<sup>th</sup> – 23<sup>rd</sup> January, 2023.
3. Attended workshop on “Intellectual Property (IP) Awareness Programme” organized by IPR cell, Delhi Technological University, Delhi, held from 12-14th December 2022.
4. Participated in online Workshop on ‘Accelerators/Incubation-Opportunities for Students & Faculties Early-Stage Entrepreneurs’ organized by Department of Applied Chemistry, Delhi Technological University, Delhi - 19<sup>th</sup> June, 2021.

# TABLE OF CONTENTS

<b>ACKNOWLEDGEMENTS</b>	<b>iii</b>
<b>CANDIDATE'S DECLARATION</b>	<b>iv</b>
<b>CERTIFICATE BY THE SUPERVISOR(S)</b>	<b>v</b>
<b>ABSTRACT</b>	<b>vi</b>
<b>DEDICATION</b>	<b>viii</b>
<b>LIST OF PUBLICATIONS</b>	<b>ix</b>
<b>LIST OF TABLES</b>	<b>xx</b>
<b>LIST OF FIGURES</b>	<b>xxii</b>
<b>LIST OF SYMBOLS, ABBREVIATIONS AND NOMENCLATURE</b>	<b>xxix</b>
<b>CHAPTER 1 INTRODUCTION AND LITERATURE REVIEW</b>	<b>1-48</b>
1.1 Introduction	2
1.1.1 Layered Materials	2
1.1.2 Anionic Layered Materials	3
1.1.2.1 Hydroxy Double Salts (HDS)	4
1.1.2.2 Layered Hydroxy Salts (LHSs)	4
1.1.2.3 Layered Rare Earth Hydroxides (LREs)	5
1.1.2.4 Layered Double Hydroxides (LDHs)	5
1.2 Assembly Chemistry of LDHs	8
1.2.1 Compositional Flexibility	10
1.2.1.1 Metal Types and Ratios	10
1.2.1.2 Interlayer Anions	11
1.3 Synthesis Methods	12
1.3.1 Coprecipitation	13
1.3.2 Urea Hydrolysis	14
1.3.3 Sol-Gel Method	14
1.3.4 Anion Exchange Method	15

1.3.5 Hydrothermal Method	16
1.3.6 Reconstruction	16
1.3.7 Miscellaneous methods	17
1.4 Properties of LDH	20
1.4.1 Anion Exchange	20
1.4.2 Surface Basicity	21
1.4.3 Adsorption Capacity	22
1.4.4 Redox Behaviour	22
1.4.5 Post-Synthesis Modification	23
1.4.6 Memory Effect	24
1.5 Applications	24
1.5.1 Water Remediation	25
1.5.1.1 Adsorption	26
1.5.1.2 Catalytic Reduction	28
1.5.1.3 Photocatalysis	29
1.5.2 Composite Fabrication	30
1.5.3 Miscellaneous	32
1.6 Significant Findings and Research Gap	34
1.7 Research Objectives	35
1.8 References	36

**CHAPTER 2 SYNTHESIS, CHARACTERIZATION AND CATALYTIC APPLICATIONS OF NOVEL ZnCuNi- TERNARY LAYERED DOUBLE HYDROXIDE FOR ORGANIC POLLUTANT REDUCTION 49-88**

2.1 Introduction	50
2.2 Materials and Methods	56
2.2.1 Materials	56
2.2.2 Instrumentation	57
2.2.3 Synthesis of ZnCuNi-LDH	57
2.2.4 Evaluation of Catalytic Activity	58

2.3 Results and Discussion	61
2.3.1 Characterisation Results	61
2.3.2 Catalytic Activity	66
2.4 Conclusion	82
2.5 References	83

**CHAPTER 3 SYNTHESIS, CHARACTERIZATION AND CATALYTIC APPLICATIONS OF ZnCuNi-TERNARY LAYERED DOUBLE OXIDE FOR REDUCTION AND DEGRADATION OF ORGANIC POLLUTANTS      89-118**

3.1 Introduction	90
3.2 Experimental	95
3.2.1 Materials	95
3.2.2 Synthesis of ZnCuNi-LDO	96
3.2.3 Catalytic activity of ZnCuNi-LDO	97
3.3 Results and Discussion	98
3.3.1 Characterisation Details	98
3.3.2 Catalytic Activity	102
3.4 Conclusion	113
3.5 References	114

**CHAPTER 4 SYNTHESIS AND CHARACTERIZATION OF ZnCuCe-LAYERED DOUBLE HYDROXIDE AND LAYERED DOUBLE OXIDE FOR PHOTOCATALYTIC APPLICATIONS      119-144**

4.1 Introduction	120
4.2 Experimental Section	123
4.2.1 Materials	123
4.2.2 Synthesis of ZnCuCe-LDH	124
4.2.3 Synthesis of ZnCuCe-LDO	124
4.2.4 Characterization	125
4.2.5 Evaluation of Photocatalytic Activity	125

4.2.6 Smartphone-based Colourimetric Analysis for Estimation of Photocatalytic Degradation of Azo Dyes	126
4.3 Results and Discussion	127
4.3.1 Microstructural, Morphological, and Optical Characterisation Results	127
4.3.2 Photocatalytic Activity	132
4.3.3 Smartphone-based analysis of photocatalytic degradation of azo dyes	138
4.4 Conclusion	140
4.5 References	141

**CHAPTER 5 INSIGHTS INTO THE LOW SOLVENT SYNTHESIS, STRUCTURAL MEMORY EFFECT PROPERTY AND ANION EXCHANGE ABILITY OF ZnCuNi-LAYERED DOUBLE HYDROXIDE** **145-164**

5.1 Introduction	146
5.2 Experimental Section	150
5.2.1 Low Solvent Synthesis	150
5.2.2 Calcination and Regeneration of ZnCuNi-LDH	150
5.2.3 Fabrication of PANI/ZnCuNi-LDH composite	151
5.2.4 Instrumentation	152
5.3 Results and Discussion	152
5.3.1 Low-Solvent Synthesis	152
5.3.2 Demonstration of Memory Effect Property	153
5.3.3 Characterization of PANI intercalated ZnCuNi-LDH	155
5.4 Conclusions	161
5.5 References	161

**CHAPTER 6 SYNTHESIS, CHARACTERIZATION AND CATALYTIC APPLICATIONS OF CARBON NITRIDE/LDH-BASED COMPOSITE MATERIALS** **157-190**

6.1 Introduction	156
------------------	-----

6.2 Materials and Methods	169
6.2.1 Materials	169
6.2.2 Synthesis of Carbon Nitride (CN)	170
6.2.3 Synthesis of ZnCuNi-LDH and ZnCuCe-LDH	170
6.2.4 Synthesis of ZnCuNi-LDH/CN and ZnCuCe-LDH/CN composites	
	171
6.2.5 Instrumentation	172
6.2.6 Evaluation of Catalytic Activity	172
6.3 Results and Discussion	173
6.3.1 Structural and Morphological Properties	173
6.3.2 Catalytic Activity	176
6.4 Conclusion	185
6.5 References	186

**CHAPTER 7 SYNTHESIS, CHARACTERIZATION AND CATALYTIC APPLICATIONS OF MAGNETICALLY SEPARABLE  $\text{Fe}_3\text{O}_4/\text{SiO}_2/\text{ZnCuNi-LDH}$  BASED COMPOSITE MATERIALS 191-218**

7.1 Introduction	192
7.2 Materials and Methods	197
7.2.1 Materials	197
7.2.2 Preparation of <i>Cleome viscosa</i> seed extract	197
7.2.3 Synthesis of Iron Oxide nanoparticles	198
7.2.4 Synthesis of $\text{SiO}_2$ coated IONPS	198
7.2.5 Synthesis of magnetically separable $\text{Fe}_3\text{O}_4/\text{SiO}_2/\text{ZnCuNi-LDH}$ composite	
	199
7.2.6 Instrumentation	200
7.2.7 Evaluation of Catalytic Activity	200
7.2.8 Reusability and Catalyst Recovery	201
7.3 Results and Discussion	201
7.3.1 Structural and Morphological Analysis	201

7.3.2 Catalytic Activity	206
7.3.3 Recyclability and Catalyst Recovery	209
7.3.4 Comparison with Reported Catalysts	211
7.3.5 Postulated Mechanism	212
7.4 Conclusion	214
7.5 References	215

## **CHAPTER 8 CONCLUSIONS, FUTURE PROSPECTS AND SOCIAL IMPACT**

**219-224**

8.1 Conclusion	220
8.2 Future Scope	222
8.3 Social Impact	223

## LIST OF TABLES

Table 1.1 Anionic layered materials reported in literature.	6
Table 1.2 Synthesis methods employed for LDH synthesis.	18
Table 1.3 Adsorption application of LDHs.	27
Table 1.4 Catalytic reduction application of LDHs.	29
Table 1.5 Photocatalytic application of LDHs.	30
Table 1.6 LDH-based composites and their applications.	32
Table 2.1 Structure and formula of model pollutants employed in the study.	56
Table 2.2 Molar ratios of constituents in various compositions of ZnCuNi-LDH.	58
Table 2.3 Experimental values for catalytic reduction of various pollutants.	73
Table 2.4 Comparison of rate constants of ZnCuNi-LDH with previously reported catalysts.	82
Table 3.1 Structure and formula of model pollutants employed in the study.	95
Table 3.2 Structures of potential products formed on the catalytic treatment of <i>p</i> -NA and MO with NaBH <sub>4</sub> and ZnCuNi-LDO.	106
Table 3.3 Comparison of catalytic performance of ZnCuNi-LDO with previously reported catalysts.	113
Table 4.1 Structure and formula of model pollutants employed in the study.	123

Table 4.2 Colour parameters of BR2 and MO dye solutions with different concentrations. 139

Table 5.1 Functional group analysis of PANI-intercalated LDH. 157

Table 6.1 Structure and formula of model pollutants employed in the study. 170

Table 6.2 The rate constants for the catalytic degradation of *p*-NP and CR using NaBH<sub>4</sub> and LDH/CN composites. 181

Table 6.3 Comparison of catalytic performance of ZnCuNi-LDH/CN and ZnCuCe-LDH/CN composites with previously reported catalysts. 184

Table 7.1 Structure and formula of model pollutants employed in the study. 197

Table 7.2 Comparison of catalytic activity of Fe<sub>3</sub>O<sub>4</sub>/SiO<sub>2</sub>/ZnCuNi-LDH composite for reduction of *p*-NP and RhB with previously reported catalysts. 211

## LIST OF FIGURES

Figure 1.1 Classification of layered materials.	6
Figure 1.2 Structural features of LDHs.	9
Figure 1.3 Conventional methods of synthesis of LDHs.	12
Figure 1.4 Properties of LDHs.	20
Figure 1.5 Various applications of LDHs.	25
Figure 2.1 Detrimental impacts of water pollution on aquatic, human, and plant health.	54
Figure 2.2 Synthesis of ternary ZnCuNi-LDH via acid hydrolysis method.	58
Figure 2.3 PXRD patterns of LDHs formed using various Zn/Cu/Ni molar ratios (a) 5:0.25:0.25 mmoles and (b) 4.25:0.375:0.375 mmoles.	62
Figure 2.4 PXRD diffractogram of ternary ZnCuNi-LDH.	63
Figure 2.5 FTIR spectrum of ternary ZnCuNi-LDH.	63
Figure 2.6 TGA thermogram of ternary ZnCuNi-LDH (under N <sub>2</sub> atmosphere).	64
Figure 2.7 (a) SEM micrograph and (b) EDX spectrum of ternary ZnCuNi-LDH with inset SEM image.	65
Figure 2.8 (a) N <sub>2</sub> adsorption-desorption isotherm and (b) corresponding pore size distribution plots with inset of enlarged view of pore size distribution between 0-20 nm of ternary ZnCuNi-LDH.	66

Figure 2.9 (a) UV-Vis absorption spectrum and (b) linear fitting of pseudo-first kinetics model for the  $\text{NaBH}_4$  - assisted catalytic hydrogenation of *p*-NP using ZnCuNi-LDH. 68

Figure 2.10 (a) UV-Vis absorption spectrum and (b) linear fitting of pseudo-first kinetics model for the  $\text{NaBH}_4$  – assisted catalytic hydrogenation of *p*-NA using ZnCuNi-LDH. 69

Figure 2.11 (a) UV-Vis absorption spectrum and (b) linear fitting of pseudo-first kinetics model for the  $\text{NaBH}_4$  - assisted catalytic reduction of MO using ZnCuNi-LDH. 70

Figure 2.12 (a) UV-Vis absorption spectrum and (b) linear fitting of pseudo-first kinetics model for the  $\text{NaBH}_4$  - assisted catalytic reduction of Amaranth using ZnCuNi-LDH. 72

Figure 2.13 (a) UV-Vis absorption spectrum and (b) linear fitting of pseudo-first kinetics model for the  $\text{NaBH}_4$  - assisted catalytic reduction of Brilliant Black BN using ZnCuNi-LDH. 73

Figure 2.14 UV-Vis absorption spectra for the catalytic reduction of *p*-NP by varying dosage (a, b, c) of ZnCuNi-LDH. 74

Figure 2.15 UV-Vis absorption spectra for the catalytic reduction of MO by varying dosage (a, b, c) of ZnCuNi-LDH. 75

Figure 2.16 UV-Vis absorption spectra for the catalytic reduction of various concentrations of *p*-NP (a, b, c) by ZnCuNi-LDH. 77

Figure 2.17 UV-Vis absorption spectra for the catalytic reduction of various concentrations of MO (a, b, c) by ZnCuNi-LDH. 78

Figure 2.18 UV-Vis absorption spectrum for  $\text{NaBH}_4$  - assisted simultaneous reduction and degradation of *p*-NP and MO by ZnCuNi-LDH. 79

Figure 2.19 Recyclability of ZnCuNi-LDH for catalytic reduction of (a) *p*-NP, MO and (b) mixture of dyes. 80

Figure 2.20 Potential mechanism for the NaBH <sub>4</sub> -assisted catalytic degradation of <i>p</i> -NP and MO by ZnCuNi-LDH.	81
Figure 3.1 Schematic representation of synthesis of ZnCuNi-LDO.	96
Figure 3.2 TGA thermogram of ZnCuNi-LDH.	99
Figure 3.3 Comparative plot of PXRD patterns of ZnCuNi-LDH and ZnCuNi-LDO.	100
Figure 3.4 (a) SEM micrograph and (b) EDX spectrum of ZnCuNi-LDO.	100
Figure 3.5 (a) N <sub>2</sub> adsorption-desorption isotherm and (b) corresponding pore size distribution plots of ZnCuNi-LDO.	101
Figure 3.6 Time-dependent UV-Vis absorption spectrum of hydrogenation of <i>p</i> -NA using (a) only NaBH <sub>4</sub> (b) using NaBH <sub>4</sub> and ZnCuNi-LDO, and (c) linear regression of pseudo-first kinetics model for the NaBH <sub>4</sub> -assisted hydrogenation of <i>p</i> -NA using ZnCuNi-LDO.	103
Figure 3.7 Time-dependent UV-Vis absorption spectrum of reduction of MO using (a) only NaBH <sub>4</sub> , (b) using NaBH <sub>4</sub> and ZnCuNi-LDO, and (c) linear regression of pseudo-first-order kinetics model for the NaBH <sub>4</sub> -assisted reduction of MO using ZnCuNi-LDO.	105
Figure 3.8 Postulated mechanism for the NaBH <sub>4</sub> - assisted catalytic degradation of <i>p</i> -NA and MO using ZnCuNi-LDO.	107
Figure 3.9 LC-MS chromatograms of (a) untreated MO (0 min) and (b) by-products obtained on NaBH <sub>4</sub> -assisted catalytic reduction of MO using ZnCuNi-LDO and (c) potential degradation pathway of MO.	110

Figure 3.10 (a) UV-Vis absorbance spectrum and (b) kinetics plot for photocatalytic degradation of ciprofloxacin by ZnCuNi-LDO.	111
Figure 4.1 Synthesis of ternary ZnCuCe-LDH and ZnCuCe-LDO.	125
Figure 4.2 Custom setup designed for smartphone-based colourimetric determination of dye concentration.	127
Figure 4.3 PXRD diffractogram of ternary ZnCuCe-LDH and ZnCuCe-LDO.	128
Figure 4.4 FTIR spectrum of ternary ZnCuCe-LDH and ZnCuCe-LDO.	129
Figure 4.5 SEM micrograph and EDX spectrum of ternary (a) ZnCuCe-LDH and (b) ZnCuCe-LDO.	130
Figure 4.6 (a) $N_2$ adsorption-desorption isotherm and (b) corresponding pore size distribution plots with inset of enlarged view of pore size distribution between 0-20 nm of ternary ZnCuCe-LDO.	131
Figure 4.7 (a) UV-DRS spectrum and (b) Tauc plot of ternary ZnCuCe-LDO.	132
Figure 4.8 (a) Time-dependent UV-Vis absorbance spectrum and (b) kinetics plot for photocatalytic degradation of BR2 by ZnCuCe-LDO.	134
Figure 4.9 (a) Time-dependent UV-Vis absorbance spectrum and (b) kinetics plot for photocatalytic degradation of MO by ZnCuCe-LDO.	136
Figure 4.10 (a) Time-dependent UV-Vis absorbance spectrum with inset plot of $C_t/C_0$ and time $t$ , and (b) kinetics plot for photocatalytic degradation of CIF by ZnCuCe-LDO.	138
Figure 4.11 Calibration plots for (a,b) BR2 and (c,d) MO dye concentrations based on $RGB_{parameter}$ and UV-Vis spectrophotometry respectively.	139
Figure 5.1 Structures of different forms of polyaniline.	149

Figure 5.2 Schematic representation of the calcination-regeneration process for demonstrating memory effect property of LDHs.	151
Figure 5.3 Schematic representation of the synthesis of PANI/ZnCuNi-LDH composite using anion exchange property.	151
Figure 5.4 PXRD pattern of ZnCuNi-LDH synthesized using low-solvent synthesis approach.	152
Figure 5.5 Comparative plots of PXRD patterns of pristine, calcined, and regenerated ZnCuNi-LDH.	153
Figure 5.6 Comparative FTIR spectra comparison of parent ZnCuNi-LDH, its calcined product and regenerated ZnCuNi-LDH.	154
Figure 5.7 Comparative plots of PXRD patterns of ZnCuNi-LDH and PANI/ZnCuNi-LDH composite.	155
Figure 5.8 Comparative plots of FTIR spectra of ZnCuNi-LDH and PANI/ZnCuNi-LDH composite.	157
Figure 5.9 Thermogravimetric traces of (a) ZnCuNi-LDH with interlayer acetate anion and (b) PANI intercalated ZnCuNi-LDH.	159
Figure 5.10 (a) SEM-EDX image of ZnCuNi-LDH, and (b,c) SEM-EDX image and elemental mapping in PANI intercalated ZnCuNi-LDH.	160
Figure 6.1 Various types of nanocatalysts used for wastewater remediation.	168
Figure 6.2 Preparation of (a) carbon nitride (CN) and (b) LDH/CN composites.	171
Figure 6.3 Structures of melamine and postulated tristriazine structure of CN.	173

Figure 6.4 Comparative PXRD patterns of (a) CN, ZnCuNi-LDH, ZnCuNi-LDH/CN, and (b) CN, ZnCuCe-LDH, ZnCuCe-LDH/CN. 174

Figure 6.5 (a) SEM micrograph, (b) EDX spectrum and (c) elemental mapping of ZnCuNi-LDH/CN composite. 175

Figure 6.6 UV-Vis absorption spectrum and linear fitting of pseudo-first kinetics model respectively for the NaBH<sub>4</sub>-assisted catalytic reduction of (a,b) *p*-NP and (c,d) CR dye using ZnCuNi-LDH/CN composite. 179

Figure 6.7 UV-Vis absorption spectrum and linear fitting of pseudo-first kinetics model for the NaBH<sub>4</sub> - assisted catalytic reduction of (a,b) *p*-NP and (c,d) CR dye using ZnCuCe-LDH/CN composite. 181

Figure 7.1 Schematic representation of synthesis of seed extract and Fe<sub>3</sub>O<sub>4</sub> NPs. 198

Figure 7.2 Schematic representation of synthesis of Fe<sub>3</sub>O<sub>4</sub> NPs using seed extract. 198

Figure 7.3 Schematic representation of synthesis of seed extract and Fe<sub>3</sub>O<sub>4</sub> NPs. 199

Figure 7.4 Schematic representation of synthesis of Fe<sub>3</sub>O<sub>4</sub>/SiO<sub>2</sub>/ZnCuNi-LDH composite. 199

Figure 7.5 Comparative plot of PXRD patterns of ZnCuNi-LDH, Fe<sub>3</sub>O<sub>4</sub>, SiO<sub>2</sub> coated Fe<sub>3</sub>O<sub>4</sub>, and Fe<sub>3</sub>O<sub>4</sub>/SiO<sub>2</sub>/ZnCuNi-LDH. 202

Figure 7.6 FTIR spectrum of Fe<sub>3</sub>O<sub>4</sub>/SiO<sub>2</sub>/ZnCuNi-LDH. 203

Figure 7.7 (a) SEM micrograph, (b) EDX spectrum and (c) elemental mapping of Fe<sub>3</sub>O<sub>4</sub>/SiO<sub>2</sub>/ZnCuNi-LDH. 205

Figure 7.8 (a) UV-Vis absorption spectrum and (b) linear fitting of pseudo-first kinetics model for the NaBH<sub>4</sub> - assisted catalytic reduction of *p*-NP using Fe<sub>3</sub>O<sub>4</sub>/SiO<sub>2</sub>/ZnCuNi-LDH composite. 207

Figure 7.9 (a) UV-Vis absorption spectrum and (b) linear fitting of pseudo-first kinetics model for the NaBH<sub>4</sub> - assisted catalytic reduction of *p*-NP using Fe<sub>3</sub>O<sub>4</sub>/SiO<sub>2</sub>/ZnCuNi-LDH composite. 208

Figure 7.10 (a) Recyclability studies of Fe<sub>3</sub>O<sub>4</sub>/SiO<sub>2</sub>/ZnCuNi-LDH composite for catalytic reduction of *p*-NP and RhB (b) Magnetic separation of Fe<sub>3</sub>O<sub>4</sub>/SiO<sub>2</sub>/ZnCuNi-LDH composite after reduction of *p*-NP and RhB. 210

Figure 7.11 Postulated mechanism for the NaBH<sub>4</sub> - assisted catalytic degradation of *p*-NP and RhB using Fe<sub>3</sub>O<sub>4</sub>/SiO<sub>2</sub>/ZnCuNi-LDH composite. 213

## LIST OF SYMBOLS, ABBREVIATIONS AND NOMENCLATURE

LDH	Layered Double Hydroxides
HDS	Hydroxy Double Salts
LHS	Layered Hydroxy Salts
LRH	Layered Rare Earth Hydroxides
2D	Two Dimensional
LDO	Layered Double Oxide
SNAS	Separate Nucleation and Aging Steps
DNA	Deoxyribo Nucleic Acid
SDG	Sustainable Development Goals
POP	Persistent Organic Pollutants
MOF	Metal-Organic Framework
AOP	Advanced Oxidation Process
CB	Conduction Band
VB	Valence Band
ROS	Reactive Oxygen Species
TM	Transitional Metal
UN	United Nations
PANI	Polyaniline
NACs	Nitroarene Compounds
<i>p</i> -NP	<i>p</i> -Nitrophenol
<i>p</i> -AP	<i>p</i> -Aminophenol
<i>p</i> -NA	<i>p</i> -Nitroaniline

<i>p</i> -PD	<i>p</i> -Phenylenediamine
CR	Congo Red
MO	Methyl Orange
Ama	Amaranth
BB	Brilliant Black
BR2	Basic Red 2
RhB	Rhodamine B
CIF	Ciprofloxacin
PXRD	Powder X-Ray Diffraction
FTIR	Fourier Transform Infrared
TGA	Thermogravimetric Analysis
SEM	Scanning Electron Microscopy
EDX	Energy Dispersive X-ray Spectroscopy
UV	Ultra Violet
Vis	Visible
DRS	Diffuse Reflectance spectrum
BET	Brunauer-Emmett Teller
BJH	Barrett-Joyner-Halenda
$S_{BET}$	Specific Surface Area
$\lambda_{max}$	Absorbance Maxima
$k$	Rate constant
REC	Rare Earth Cation
RGB	Red-Green-Blue

IONP

Iron Oxide Nanoparticles

TEOS

Tetraethyl Ortho Silicate

***CHAPTER - 1***

***INTRODUCTION AND LITERATURE  
REVIEW***

---

# **CHAPTER - 1**

## **INTRODUCTION AND LITERATURE REVIEW**

---

### **1.1 Introduction**

#### **1.1.1 Layered Materials**

The last few decades have witnessed monumental growth in the field of materials science and engineering, thereby serving as a strong pillar that forms the backbone of modern technology development. In this regard, layered materials have emerged as exceptional materials that have catapulted nanoscience to astonishing new heights in a rather short time since the discovery of graphene, the first discovered layered material in 2004[1,2]. Layered materials are prominent network solids with anisotropic bonding that are characterized by their distinctive two-dimensional architecture wherein the intralayer components are strongly bonded internally by means of covalent bonds. The adjacent layers are only weakly bonded to each other via weak interlayer forces - electrostatic bonds, Van der Waal interactions and hydrogen bonding[3,4]. Consequently, layered materials possess readily tailorabile structures and exhibit remarkable physicochemical properties as well as surface modification, intercalation, and functionalisation abilities that are not observed in their bulk counterparts. As a result of their structural versatility and tunable properties, layered materials have emerged as a cornerstone in the advancement of several industrial and medical applications, including energy storage, biomedicine, and sensing. But their utility remains severely underexplored in various environmental issues, such as the elimination of pollutants for wastewater remediation. Some of the more common layered materials that have demonstrated significant potential across diverse applications include naturally occurring clay minerals (eg. montmorillonite, smectite), graphite, and engineered compounds such as chalcogenides and layered double hydroxides (LDHs)[5–8]. The individual layers of all these materials often possess fixed charges, and on basis of the charges, these layered materials can be classified as (a) cationic having negative charges on layers and exchangeable cations, (b) neutral having no charge on layers and (c) anionic having positive charge on layers and

exchangeable anions (Figure 1.1). For instance, aluminosilicates are some the most widely known and researched cationic layered materials consisting of a skeleton made of tetrahedral silicon and octahedral aluminium cations connected together by oxygen atoms[9]. The layers are stacked together via hydrogen bonding, Van der Waals force or electrostatic forces. Graphite is classified as a neutral layered solid because it consists of sheets of carbon atoms bound together in a hexagonal fashion, where the carbon atoms are covalently bonded, and the layers are held together by van der Waals forces [10]. Anionic layered materials, such as LDHs, hydroxy double salts (HDSs), layered hydroxy salts (LHSs), layered rare earth hydroxides (LREs) contain 2D network structures. Their positively charged layers are composed of divalent, trivalent, or a mixture of multivalent metal cations, while replaceable anionic moieties are present in the interlayer region[11]. The innate ability of layered materials to accommodate a wide range of chemical modifications and intercalations profoundly expands their utility, and therefore has positioned them at the forefront of research aimed at addressing pressing technological and environmental challenges[12].

The most prevalent layered minerals found in nature are cationic and neutral, while the synthesis of anionic layered materials remains predominantly confined to laboratory settings. Although cationic and neutral layered materials find utility in a wide range of applications, they often lack anion exchange properties, that limits their tailorability to a high degree. Conversely, anionic layered materials exhibit exceptional anion exchange capabilities, that have established them as key candidates for innovative solutions in fields ranging from catalysis and energy storage to environmental remediation. Their facile and low-cost synthesis, coupled with unique physicochemical properties, render them as highly adaptable materials that have captivated the attention of researcher groups and industries.

### **1.1.2 Anionic Layered Materials**

Anionic layered materials are a broad class of 2D network solids that are primarily formed by stacking of positively charged layers composed of cations and inorganic/organic/polymeric anion molecules that are present in the interlayer domains to maintain charge neutrality. These layered materials are generally hydrated, and

interest has been growing towards the usage of anionic layered materials for their potential utility in various scientific and industrial avenues due to their physicochemical properties. On basis of the number and types of cations that make up the layers, anionic layered materials can be classified into four subcategories as given below (Table 1.1).

### 1.1.2.1 Hydroxy Double Salts (HDS)

HDS are 2D materials that bear striking similarities to the mineral brucite ( $\text{Mg(OH)}_2$ ) in terms of structural characteristics, wherein the layers contain edge-sharing  $\text{M(OH)}_6$  octahedra with one-third vacant sites[13]. Their composition can be described using the formula  $[\text{M}^{2+}_{1-a}\text{M}^{2+}_a(\text{OH})_{2-b}](\text{A}^{m-})_{b/m}\cdot\text{nH}_2\text{O}$  where  $\text{M}^{2+}$  and  $\text{M}^{2+}$  are different divalent cations such as Mg, Zn, Co, etc. The isomorphic substitution of the intralayer metal cations by another divalent cation results in the formation of hydroxy double salts, and the substituting cations are present in tetrahedral sites lying above and below the layers. The intrinsic hydroxyl vacancies render the layers as positively charged and are filled by the direct bonding of anions known as grafting. HDS structures may exist in triclinic, hexagonal, monoclinic or orthorhombic symmetries, depending on the specific composition of cations and anions. Essentially, cations occupy the octahedral sites and they are surrounded by -OH groups while anions and water molecules exist in the interlamellar region. For instance, Pandey et al. synthesized ethylene glycol intercalated Zn/Cu-HDS using a facile one-pot synthesis route and utilised the lattice for the adsorptive uptake of CR dye[14].

### 1.1.2.2 Layered Hydroxy Salts (LHSs)

LHSs possess all the features of HDS, but their layers are composed only one type of cations. They are generally represented by the formula  $\text{M}^{II}(\text{OH})_{2-a}(\text{A}^{-x})_{a/x}\cdot\text{nH}_2\text{O}$ , wherein  $\text{M}^{II}$  and  $\text{A}^{x-}$  denote the divalent/trivalent cation making up the layer and the anionic species present in the interlayer region respectively[15]. Their crystal symmetry depends on the type and arrangement of cations as well as the type, orientation, and symmetry of interlayer anions and stacking sequence of hydroxide layers. They usually exist in hexagonal or orthorhombic symmetries, while triclinic symmetries have also been observed in some studies that may occur due to stacking

faults, polytypism and prominent cation/anion features. Common examples of these materials include layered salts of zinc, yttrium, nickel and copper. For instance, copper hydroxy nitrate and coppery hydroxy acetate can be represented using the formula  $\text{Cu}(\text{OH})_3\text{NO}_3$ .

#### 1.1.2.3 Layered Rare Earth Hydroxides (LREs)

LREs are another class of inorganic materials under the category of anionic lamellar solids whose layers are composed of trivalent rare earth cations and hydroxide groups, rendering them positively charged, and leading to intercalation of anionic species in the hydrated interlayer region. Their crystal structure is engineered from the  $\text{Ln}(\text{OH})_3$  framework, and can be described using the general formula  $\text{Ln}_2(\text{OH})_5\text{A} \cdot x\text{H}_2\text{O}$  wherein the rare earth cations are represented by  $\text{Ln}$  (eg. La, Eu, Ce, etc.), and interlayer anions are represented by  $\text{A}$  (eg.  $\text{Cl}^-$ ,  $\text{NO}_3^-$ , etc. )[16]. Due to the variable oxidation states and high coordination number of rare earth cations, LREs may either possess dodecahedral or monocapped square antiprism-type environments in the lattice. They exhibit distinctive photoluminescence behaviour due to the optical properties of rare-earth cations and have found applications in optical devices, fluorescence sensing, and bioimaging. For instance, a recent study by Wang et al. described the synthesis of yttrium-containing LRE and exchange the pre-existing  $\text{Cl}^-$  anions with  $\text{SO}_4^{2-}$  and  $\text{H}_2\text{PO}_4^-$  molecules, for the purpose of utilising the lattice as proton conductors.

#### 1.1.2.4 Layered Double Hydroxides (LDH)

LDHs are a *sui generis* class of anion-exchangeable host-guest materials that have piqued the curiosity of researchers due to their unique structures and multifunctional behaviour. Since the discovery of hydrotalcite, a naturally occurring anionic layered material in the 19<sup>th</sup> century, LDHs have attained the status of technologically important materials and have become a cornerstone in nanomaterial sciences and associated fields. Their distinctive layered architecture, capacity for interlayer and intralayer modification, high chemical and thermal stability and specific surface areas have established LDHs as a platform for innovation across scientific disciplines. Their structural attributes can be outlined by the general formula  $[\text{M}^{2+}_{1-y}\text{M}^{3+}_y(\text{OH})_2](\text{A}^{x-})_{y/x} \cdot m\text{H}_2\text{O}$ , ( $\text{M}^{2+}$  = divalent cations (e.g.,  $\text{Zn}^{2+}$ ,  $\text{Co}^{2+}$ ,  $\text{Mg}^{2+}$ ,  $\text{Ca}^{2+}$ , etc.),  $\text{M}^{3+}$  = trivalent

cations (e.g.,  $\text{Al}^{3+}$ ,  $\text{Fe}^{3+}$ ,  $\text{La}^{3+}$ ,  $\text{Cr}^{3+}$ , etc.),  $\text{A}^{x-}$  = charge compensating interlayer exchangeable anions). 'y' describes the ratio of  $(\text{M}^{3+})/(\text{M}^{2+} + \text{M}^{3+})$ [17]. The wide palette of LDH compositions enables incorporation of various main group, transition, and rare earth metals, granting access to properties ranging from redox activity and magnetism to luminescence. The ability to intercalate and exchange a broad spectrum of inorganic and organic anions renders LDHs highly adaptable hosts for molecules, ions, and nanoparticles. As a result, LDHs are being increasingly regarded as superior substitutes to conventional materials for catalytic, adsorptive, and ion exchange applications from the perspective of green chemistry. Advantages such as recyclability, biocompatibility, low toxicity, recoverability, and large surface area open up several new avenues for their use in various fields.

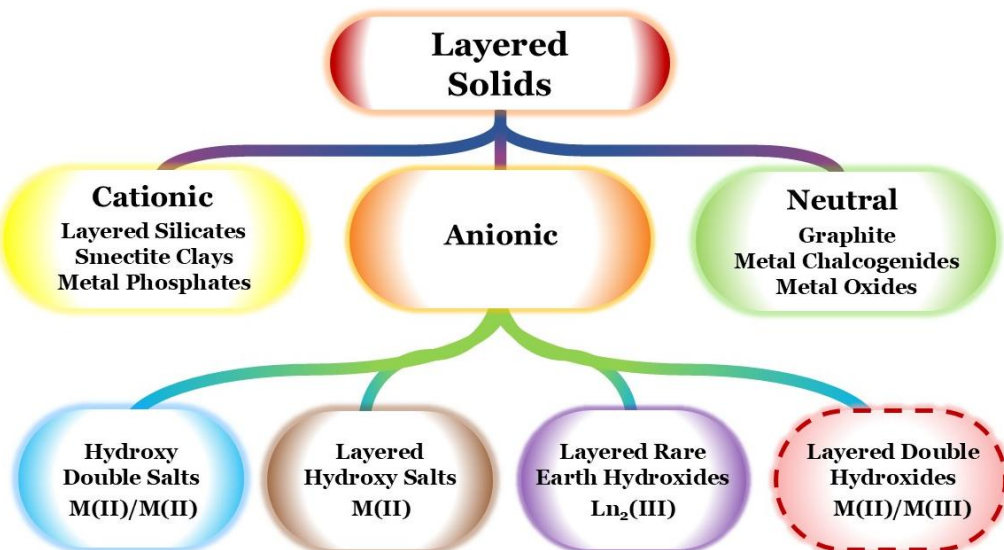


**Figure 1.1** Classification of layered materials.

**Table 1.1** Anionic layered materials reported in literature.

Anionic layered material	Interlayer anion	Synthesis method	Application	Reference
MgZn-HDS	Chloride ( $\text{Cl}^-$ )	-	Intercalation and release of naproxen, diclofenac	[18]
FeZn-HDS				

			sodium and valproic acid	
Zn/Cu HDS	Ethylene Glycol	One-pot synthesis	Adsorption of CR dye	[14]
CuZn-HDS	Acetate (CH <sub>3</sub> COO <sup>-</sup> )	One-pot synthesis	Anion exchange reaction using Cl <sup>-</sup> , NO <sub>3</sub> <sup>-</sup> , C <sub>6</sub> H <sub>5</sub> COO <sup>-</sup> , CH <sub>3</sub> (CH <sub>2</sub> ) <sub>11</sub> OSO <sup>3-</sup>	[19]
Zn- LHS	Heptanoate (CH <sub>3</sub> (CH <sub>2</sub> ) <sub>5</sub> CO O <sup>-</sup> )	--	Anticorrosion barrier for Zinc protection	[20]
Zn-LHS	Tannic Acid	Precipitatio n	Antimicrobial and antioxidant activity, antibiofilm formation and toxicity evaluation	[21]
Ni-LHS	Nitrate (NO <sub>3</sub> <sup>-</sup> )	Anion	Electrocatalyst	[22]
Co-LHS		grafting	for oxygen evolution reaction	
Zn-LHS	Carbonate (CO <sub>3</sub> <sup>2-</sup> )	Hydrother mal	Methylene blue degradation	[23]
Eu-LRE	Chloride (Cl <sup>-</sup> )	Homogene ous precipitatio n	Anion Exchange properties	[16]
Y <sub>2</sub> (OH) <sub>5</sub> Cl·1.5H <sub>2</sub> O	8- Hydroxypyren e-1,3,6- trisulfonic acid	Hydrother mal	Fluorescent test paper sensor	[24]

RE <sub>2</sub> (OH) <sub>5</sub> NO <sub>3</sub> · <i>n</i> H <sub>2</sub> O (RE = La, Pr, Nd, Sm, Eu, Gd, Tb, Dy, Ho, and Y)	Molybdate (MoO <sub>4</sub> <sup>2-</sup> )	Electrodeposition	Photoluminescent films for solid-state lighting	[25]
RE-LRH (RE= Gd, Eu)	2,2'-bipyridine-4,4'-dicarboxylic acid (4,4'-BDA), 2,2'-bipyridine-5,5'-dicarboxylic acid (5,5'-BDA)	Coprecipitation-Hydrothermal	Phosphorescence properties	[26]
ZnCuAl-LDH	Sulphate (SO <sub>4</sub> <sup>2-</sup> )	Coprecipitation	Antibacterial ceramics	[27]
NiCoFe-LDH	sodium dodecyl sulfate (SDS)	Coprecipitation	Supercapacitor	[28]
MgAlCe-LDH	benzotriazole-5 carboxylic acid	Hydrothermal	Self-healing protective coating for Zn-Al-Mg coated steel	[29]
CaMgAl-LDH	Chloride (Cl <sup>-</sup> )	Coprecipitation	Immobilisation of Cd(II)	[30]
Ce-NiFe LDH	Carbonate (CO <sub>3</sub> <sup>2-</sup> )	Hydrothermal	Chlorine storage	[31]

## 1.2 Assembly Chemistry of LDHs

LDHs derive their layered framework from brucite mineral (Mg(OH)<sub>2</sub>), wherein layers are composed of central Mg<sup>2+</sup> cations surrounded by 6 hydroxyl groups at vertices,

thereby forming a neutral lattice with octahedral geometry. The assembly chemistry of layered double hydroxides (LDHs) is centered on the orchestrated formation of positively charged, brucite-like host layers composed of divalent and trivalent metal cations coordinated octahedrally by hydroxide ions. The partial substitution of some portion of divalent cations by trivalent cations gives rise to a net positive charge on the layers, necessitating the intercalation of charge-balancing anions and water molecules in the interlayer galleries (Figure 1.2). This region is highly adaptable, containing both inorganic and organic anions and variable amounts of water, that influence the hydration state and distance between two consecutive layers - termed as gallery height - thereby contributing to the dynamic ion-exchange properties of LDHs. The individual layers are held together by the action of weak forces of attraction - electrostatic interaction, Van der Waals forces, and hydrogen bonding, that results in the formation of a three-dimensional turbostratic structure having stacked layers. It is important to note that the type of intercalated anions strongly influences the gallery height and basal spacing. Hao et al. reported a study corroborating this observation, and reported the synthesis of ZnAl-LDH that was intercalated with four different anionic species[32]. They reported that an increase in the basal spacing of the LDH lattice was observed with the increase in size of anionic moiety.

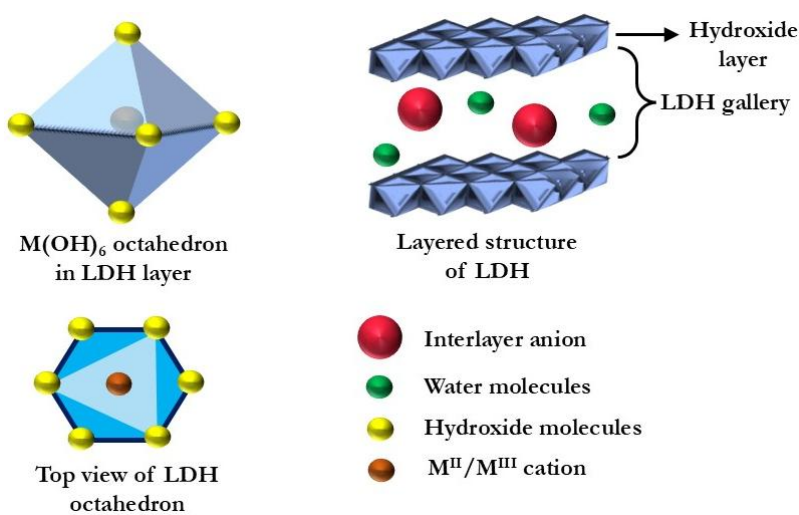


**Figure 1.2** Structural features of LDHs.

In LDH monolayers, arrangement of atoms can occur in the trigonal prismatic structure that is formed due to the presence of opposing hydroxyl groups on one another in a

vertical manner, or the octahedral arrangement that is the consequence of the arrangement of  $\text{OH}^-$  in an offset manner. These layers are held together by Van der Waals interactions between them, and the difference in stacking orientation can give rise to different polytypes in bulk LDHs. These include rhombohedral, denoted by 3R, and hexagonal, denoted by 2H, and are considered to be the best in respect of the hydroxide ions present in the layers[33]. As a consequence of the unique structural features of LDH, their assembly process is profoundly tunable. The types and ratios of metal cations, the choice of interlayer anions, and the degree of hydration impact the crystal parameters and can be easily modified to produce LDHs with desired physicochemical characteristics. Such assembly chemistry underpins the extraordinary versatility of LDHs, enabling their broad utility in catalysis, environmental remediation, biomedical delivery, and other applications.

### 1.2.1 Compositional Flexibility

The compositional flexibility of LDHs arises from presence of cations of two different valencies in the layers, as well as mobile and exchangeable anions in interlayer region. These cationic and anionic species can be replaced, and this adaptability is foundational to their structural diversity, thereby promoting their application in catalysis, environmental remediation, energy storage, and functional nanomaterials.

#### 1.2.1.1 Metal Types and Ratios

Due to the versatility of LDH structure, several different types of metal cations can be incorporated into the layers in various combinations. For the formation of stable LDHs, the cations must meet the prescribed ionic radius criteria. This enables their effective accommodation into the octahedral sites that are formed by the surrounding hydroxide groups without destabilizing or causing excessive lattice strain. Based on extensive literature survey, it was found that the ionic radii of cations typically fall within the range of 0.50 to 0.74 Å for stable layer formation. Examples of divalent cations used for LDH synthesis include  $\text{Zn}^{2+}$ ,  $\text{Co}^{2+}$ ,  $\text{Ni}^{2+}$ ,  $\text{Ca}^{2+}$ ,  $\text{Cu}^{2+}$ ,  $\text{Mg}^{2+}$ , etc, while to achieve isomorphic substitution, trivalent cations such as  $\text{Al}^{3+}$ , transition metals (eg.  $\text{Fe}^{3+}$ ,  $\text{Cr}^{3+}$ ,  $\text{Mn}^{3+}$ ,  $\text{Sc}^{3+}$ , etc.) as well as rare earth metal cations ( $\text{Ce}^{3+}$ ,  $\text{Y}^{3+}$ ,  $\text{Eu}^{3+}$ ,  $\text{La}^{3+}$ , etc) are used. In addition, some studies have also reported the use of monovalent (eg.  $\text{Li}^+$ ), and

tetravalent (eg.  $Ti^{4+}$ ) cations for producing LDH lattices. Furthermore, the ratio of divalent to trivalent cations ( $M^{2+}:M^{3+}$ ), typically lying between 0.2 and 0.33, determines positive charge density on the layers, and affects the crystallinity, anion exchange behaviour as well as adsorption and catalytic behaviour of lattice. The values above and below the prescribed limit may result in the formation of pure hydroxides or different compounds.

The most widely studied LDHs are binary LDH, that contain one divalent and one trivalent cation. But the availability of only two types of cations hinders their utility due to limited tunability. Therefore, several groups have synthesized ternary LDHs containing combinations of three cations, that offer the advantages of three cations in the lattice. Recently, some forays have also been made into synthesizing LDHs with more than three LDHs, including quaternary and high-entropy LDHs containing multiple different cations, enabling advanced property tuning. The substitution of variable cations helps in tailoring of the redox, magnetic, luminescent, and surface properties, thereby allowing the precise optimization to specific applications such as catalysis, energy storage, or drug delivery.

### 1.2.1.2 Interlayer Anions

LDHs feature a robust structure and their interlayer galleries can host a wide variety of exchangeable anions since there is virtually no restraint on the nature of anions that can be intercalated in the interlayer region. These interlayer anions help in balancing the charge deficit created on the LDH layers and contribute in maintaining the structural integrity of the lattice. The mobility of these anions aids their exchange and helps in the modulation of interlayer spacing, hydration state, and surface chemistry. Therefore, several types of inorganic ( $Cl^-$ ,  $NO_3^-$ ,  $CO_3^{2-}$ ,  $SO_4^{2-}$ ,  $CH_3COO^{2-}$ ,  $PO_4^{3-}$ , etc.), organic, polymeric, metallorganic complexes, silicates, biomolecules, enzymes, polyoxometalate, drugs, dyes, and iso and heteropoly anions have been reported to be intercalated in the LDH galleries.

The relative affinity of LDHs for different anions generally follows the order:  $CO_3^{2-} > SO_4^{2-} > OH^- > F^- > Cl^- > Br^- > NO_3^- > I^-$  [34]. The high affinity of LDHs for  $CO_3^{2-}$  anions may be attributed to several factors, including: high charge and size compatibility

leading to strong electrostatic interactions and effective charge neutralization, the planar geometry and polydentate (three oxygen atoms) nature. This leads to strong hydrogen bonding of  $\text{CO}_3^{2-}$  with the layers and the water molecules and stabilization of the lattice energy. Therefore, the complete exchange of carbonate anions from the LDH lattice is very difficult to achieve. Additionally, complex anions may exhibit three possible orientations, including monolayer, simple bilayers, and interpenetrating or perpendicular bilayers. The size of anion determines their orientation in the interlayer and is often aligned in order to maximise their interaction with the surroundings, thereby playing a key role in altering the interlayer spacing. Therefore, the type, arrangement, exchangeability, and interaction of anions with the layers directly dictates the versatility and application scope of LDHs.

### 1.3 Synthesis Methods

Since the number of LDHs found in nature is quite limited, their synthesis remains predominantly lab-based. A variety of methods have been developed for the fabrication of LDHs containing several different combinations of cations and anions (Figure 1.3). The most commonly used methods have been described below.

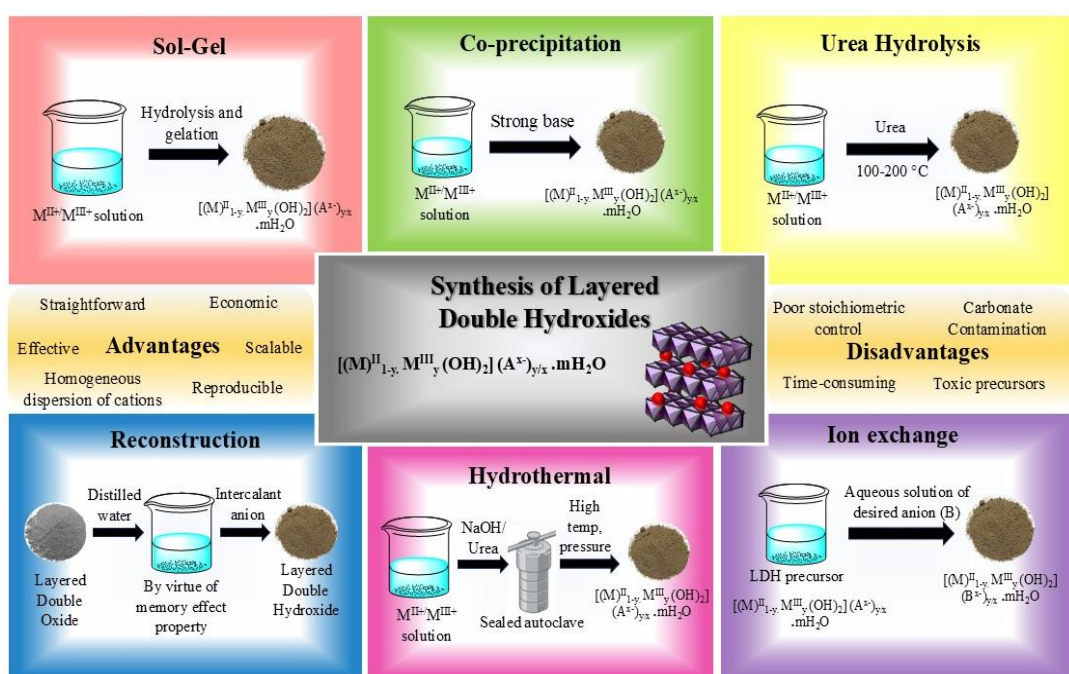


Figure 1.3 Conventional methods of synthesis of LDHs.

### 1.3.1 Coprecipitation

Coprecipitation is the oldest, easiest, and most commonly used “one-pot” method for LDH synthesis. This method involves the simultaneous precipitation of a divalent metal hydroxide and trivalent metal hydroxide from a supersaturated solution by the action of a strong base that can act as a precipitating agent (eg. sodium hydroxide, potassium hydroxide, ammonia, urea, etc.). The desired intercalant anion for the LDH lattice is usually present in the form of a soluble ionic species in the reaction mixture (eg. sodium carbonate for carbonate ( $\text{CO}_3^{2-}$ ) as the desired intercalant anion). The basic principle behind co-precipitation is the condensation of hexa-aqua metal complexes in aqueous medium, that results in the generation of layered structures analogous to brucite, having homogeneous distribution of constituent metallic cations in the layers and interlamellar anions along with water molecules. External parameters such as solution pH, precursor concentration, addition rate, ageing and reaction time, and temperature have a profound impact on the synthesized product.

This process can occur at either constant or variable pH, but a constant pH is mostly preferred, as it yields products with more size uniformity. Furthermore, depending on the type of product desired, conditions such as high or low supersaturation may also be employed. Coprecipitation under high supersaturation utilises highly concentrated metal cation solutions and is performed at high solution pH values, that results in high nucleation rates and numerous small particles. In the case of coprecipitation at low saturation, the usage of low concentration metal precursors coupled with their slow addition at pH values ranging between 7 and 10 results in materials with high crystallinity due to the rate of crystal growth being higher than the rate of nucleation. Inspite of these modifications in the synthesis method, products formed using coprecipitation often possess low quality, have large number of impurities, and generate particles with large sizes due to agglomeration during ageing time. To overcome these drawbacks, this process is often combined with various post-synthesis methods such as hydrothermal treatment, microwave irradiation and ultrasonication to maintain better control over particle morphology, size, and crystallinity. In a recent study, Luo et al. used the coprecipitation method for synthesis of NiFe-LDH, that was further utilised for the adsorptive removal of fluoride ions from aqueous medium[35].

### 1.3.2 Urea Hydrolysis

The urea hydrolysis method is similar to coprecipitation since it also involves the homogenous precipitation of metal hydroxides. However, this methodology is contingent on the slow thermal decomposition of urea, a weak Brønsted base, that leads to the generation of ammonia and carbon dioxide in the reaction mixture. Ammonia aids the controlled precipitation of the divalent and trivalent metal hydroxides to form LDH by slowing and homogeneously increasing the pH of reaction mixture, while carbon dioxide provides carbonate anions that are intercalated into the LDH galleries. The hydrolysis of urea occurs as follows:



The rate of this reaction can be altered by controlling the reaction temperature, since hydrolysis of urea is an extremely temperature-sensitive process. This is a highly scalable synthesis method since the slow, uniform increase in solution pH ensures homogeneous nucleation and growth, resulting in highly crystalline, well-ordered LDH particles. It is often utilised to synthesize products for applications where high crystallinity and size uniformity are the key requirements. The major drawback associated with this method is its limited interlayer anion diversity due to the almost exclusive intercalation of carbonate anions in lattices synthesized using this method. Furthermore, the extended reaction times and difficulty in precipitating most trivalent cation species other than  $\text{Al}^{3+}$  also hinder its wide-scale applicability. In a recent study, Samuel et al. fabricated flexible supercapacitors using CoCe-LDH that were synthesized via urea hydrolysis method[36].

### 1.3.3 Sol-Gel Method

The use of sol-gel method for LDH synthesis is relatively new, but has now become one of the most preferred methods due to its facile nature. In this method, metallic precursors (such as metal alkoxides, acetates, acetylacetones and other inorganic salts) form a colloidal dispersion termed a liquid sol. This sol undergoes hydrolysis and partial condensation reactions to form a solid gel phase, that is then aged and dried. The rates of hydrolysis and condensation reactions majorly control the properties of the synthesized product. Additionally, external parameters such as pH, nature and

concentration of the metallic precursors, choice of solvent, and the temperature of synthesis also have a huge impact on product properties. This method can be used effectively for the coating of substrates for the fabrication of LDH films and coatings. The sol-gel approach yields pure, high-quality products with high specific surface areas, and is especially useful in minutely controlling the particle size and pore size of the products. Still, poor sample crystallinity is a challenge that often arises in this method, but it can be effectively addressed by employing additional treatments, such as microwave irradiation, hydrothermal treatment, and ultrasonication. Klydziute et al. reported the synthesis of MgZnAl-LDH and MgAlLa-LDH using the sol-gel route[37].

### 1.3.4 Anion Exchange Method

Anion exchange is an indirect route for LDH synthesis, that is generally employed when the chosen metal cations are unstable at high pH as well as for the intercalation of several different types of anions in the LDH interlayer region. This is generally a two-step process where an LDH lattice is first synthesized using coprecipitation method with monovalent anions such as  $\text{Cl}^-$ ,  $\text{NO}_3^-$ , etc present in the interlayer region. To achieve the exchange of anions, the synthesized lattice is treated with a solution containing an excess of the anions to be intercalated, thereby resulting in the formation of desired LDH lattice. Since the reaction is based on the strength of electrostatic forces between the layers and the anions, monovalent anions that exhibit weaker electrostatic forces can be easily replaced by multivalent anions exhibiting stronger forces. Therefore, the choice of using monovalent anions in the initial LDH is based on the ease of exchanging the anion, that is often difficult with multivalent anions. Furthermore, choice of solvent, reaction temperature, and pH also play a huge role in determining the outcome of the reaction. Higher temperatures favour the anion exchange reactions, while solution pH should be above for 4.0 in order to maintain the integrity of the hydroxyl layers. This method is especially useful for obtaining several LDH lattices from a single precursor, and is generally opted over the conventional coprecipitation method for intercalation of large-sized anions. Recently, Yu et al. synthesized a series of MgAl-LDH containing nitrate, molybdate, stannate, and SDS by the anion-exchange method for protection of Mg alloy surfaces[38].

### 1.3.5 Hydrothermal Method

This method is typically employed to achieve precise control over particle size, phase purity, and morphology, while also refining the particle size distribution. In this method, divalent and trivalent metal precursors are treated with a base under elevated temperature and autogenous pressure in a sealed autoclave to form the products. This method yields LDHs with highly uniform nanostructures and is especially helpful in the fabrication of high-quality products having a large variation in LDH composition when combined with other methods such as coprecipitation, urea hydrolysis, etc. Changes in reaction conditions such as heating temperature, time, and precursor concentration are beneficial in governing the particle size, morphologies and aspect ratios of synthesized LDHs. Hydrothermal method can be modified to obtain materials for desired applications by tailoring the LDH via functionalisation, doping, and intercalation of wide variety of inorganic/organic/polymeric moieties. In a study by Choi et al., CoMgAl-LDH was synthesized on  $\gamma$ -Al<sub>2</sub>O<sub>3</sub> surface by the hydrothermal treatment using urea as a precipitating agent[39].

### 1.3.6 Reconstruction

This method, also known as rehydration, leverages the unique “memory effect” property of LDHs, that allows them to regain their original structure after calcination and subsequent rehydration. The procedure entails the initial calcination of the LDH lattice at temperatures of 350 °C - 550 °C, thereby leading to the removal of hydroxyl groups, interlayer anion and water molecules, and subsequent collapse of the layered arrangement to form layered double oxide (LDO). The LDO is then treated with an aqueous solution of desired anion, resulting in the regaining of layered structure and formation of parent LDH, but with the intercalated desired anion. This method involves the dissolution of the mixed oxides and reprecipitation as LDH, and has proved to be successful for intercalation of organic molecules and anions with bigger molecular sizes, that is often found to be difficult to achieve through other methods. It allows the fine-tuning of LDH properties, and can also be used to regenerate LDHs that have been deactivated in catalysis and adsorption applications. Although this method has several benefits, products obtained using reconstruction method may

suffer from variable morphology, poor size control and crystallinity, and partial/mixed intercalation of anions. In a study by Yasmina et al, MgAl-LDH was immobilised with Ni(II) Schiff base using the reconstruction method[40].

### 1.3.7 Miscellaneous methods

Apart from the traditional methods employed for the synthesis of LDHs, several alternative methods have been developed and utilised for their fabrication in recent times. These include separate nucleation and ageing steps (SNAS) method, template synthesis, polyol method, mechanochemical method, and the Chimie-Douce method. The SNAS method separates the nucleation and ageing processes during LDH synthesis, leading to the sudden nucleation of LDH seeds and a subsequent controlled and milder ageing step, resulting in products possessing small, nanosized LDH platelets with uniform and well-defined morphologies [41]. The mechanochemical method is based on the principle of solid-state mixing and entails the use of mechanical energy (in the form of ball milling, grinding, etc). for the induction of chemical reaction between the precursors to form LDHs[42]. They have the advantage of being waste-free and solvent-free/solvent-minimized processes, thereby being environmentally friendly and producing pure phase products with relative ease. Template synthesis utilises a template/scaffold to guide the assembly of LDHs, such that the final product possesses structural and morphological attributes similar to those of the template[43]. The choice of template, whether inorganic (SiO<sub>2</sub>, micelles, polymers, etc.) or biological (proteins, DNA, viruses, etc.), has a profound impact on the porosity, surface area, and other physical properties of the lattice. The polyol method utilises the principles of soft chemistry and involves the forced hydrolysis of metal precursors in polyol medium to form LDH platelets. The Chimie-Douce method utilises low temperatures and mild conditions to synthesize LDHs[44]. It combines the steps of the sol-gel and anion exchange method to obtain versatile LDHs with high crystallinity and the desired properties. However, these methods are currently in the nascent stages of development and application, and there is considerable scope for exploring these methods for synthesis of cost-effective LDHs with desirable properties. Table 1.2 describes the procedure and drawbacks of some methods used for synthesis of LDHs.

**Table 1.2** Synthesis methods employed for LDH synthesis.

Method	Procedure	Drawback
Co-precipitation	Simultaneous precipitation of metal hydroxides by strong precipitating agent in presence of desired interlayer anions.	Synthesized LDH may have poor crystallinity and presence of impurity.
Urea Hydrolysis	Addition of urea to metal salts solution followed by refluxing.	LDHs with low charge density cannot be synthesized via urea hydrolysis.
Sol-Gel Method	Hydrolysis of metal salts and partial condensation of a metal precursor result in sol formation, followed by gel formation due to a gelation reaction.	Method has low output and high cost.
Ion exchange	Pre-synthesized LDH having $\text{Cl}^-$ or $\text{NO}_3^-$ ions added to the solution containing anions to be intercalated.	Presence of carbonate ions makes the de-intercalation difficult.
Hydrothermal	Two solutions containing M(II) & M(III) metal salts added dropwise to a solution containing base while stirring. Suspension is then transferred to a Teflon lined autoclave and treated at high temperature and pressure.	Low output and high production cost.
Reconstruction	Calcination of LDHs at high temperatures to remove interlayer water, anions, and hydroxyl groups, forming LDO. Reformation of LDHs by dispersing LDO in an aqueous solution of desired anion.	Formation of products with poor crystallinity and partial intercalation.

Salt-Oxide Method	Aqueous solutions of metal oxides and metal chloride (in excess) are mixed, resulting in LDH formation.	Difficulty in controlling reaction kinetics.
Mechanochemical Method	Metal salt precursors are mixed or ground together in presence or absence of solvent.	Difficulty in controlling particle morphology and purity.
Template Synthesis	Inorganic precursors react at the interface of organic self-assembled aggregates (used as template) in solution to form organic-inorganic composites. Removal of organic template gives inorganic LDH.	Post-synthesis process required for the removal of template.
Chimie-Douce Method	$\gamma$ -oxyhydroxide precursor undergoes hydrolysis, polymerisation and condensation mechanisms to form a solid solution containing the LDH product.	Impure product formation and costly raw materials.
SNAS Method	Precursors undergo homogenization and nucleation process by application of vigorous forces in a colloidal mill. Afterwards, the nucleation mixture undergoes an ageing process separately, yielding the LDH product.	Complex reactor systems required for synthesis of LDHs.
Polyol Method	Metal acetate precursors get hydrolyzed in a polyol solvent medium (eg. Diethylene glycol) while under reflux to form desired LDHs.	High temperature conditions required.
Electrodeposition Method	Nitrate ions from metal nitrate precursors are electrically reduced, leading to evolution of hydroxide ions, which increases the pH of the solution and results in LDH film deposition.	Wastage of raw materials and high cost for reaction setup.

## 1.4 Properties of LDH

LDHs exhibit a host of exemplary properties that are intrinsic to their unique layered structure and composition (Figure 1.4). Some of these properties are explained below.



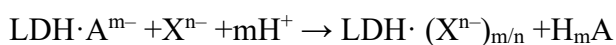
**Figure 1.4** Properties of LDHs.

### 1.4.1 Anion Exchange

The anion exchange property of LDHs is one of their most important and unique features. It refers to the ability of LDHs to reversibly exchange their loosely bound interlayer anions with other anionic species from the surrounding medium, without significantly disrupting their layered structure. The interlayer domain acts as a flexible "cavity" that can accommodate a wide range of anions, and its dimensions can adjust according to the size, shape, and charge of the incoming guest species. The anion exchange reaction takes place via two pathways, either



or



Anion exchange is typically a fast process and may be quantitative depending on the species of anion being exchanged. Since the composition, concentration, and conditions of the exchange solution can be adjusted, it allows precise external control

on the components of the resulting lattice. The anion exchange process is mainly driven by electrostatic forces, van der Waal and hydrogen bonding, due to which anions with higher charge, smaller size, and greater hydrogen bonding ability are generally held more tightly between the layers, thereby making their exchange more difficult. The metal cation composition (species, valence, ratio, and size) and the morphology of the LDH can be finely tuned to adjust the charge density, interlayer spacing, and ultimately, the anion-exchange performance. By altering these parameters, the affinity and capacity for guest anions can be selectively enhanced for applications such as selective adsorption, drug delivery, or pollutant capture.

#### 1.4.2 Surface Basicity

One of the key factors that influences the tailorability and utility of LDHs is their surface acidity and basicity. The tunability of their surface chemistry is a consequence of their unique and flexible layered structure as well as amphoteric nature, and can be altered using different synthesis methods and surface modifications. LDHs are inherently basic due to the presence of hydroxide ( $\text{OH}^-$ ) moieties on the layers and the interlayer anions present in the LDH galleries that can interact with acidic species, making them Brønsted bases. Basicity of LDHs can be further enhanced by the introduction of more oxygen atoms in the lattice, that can be achieved by their conversion into mixed hydroxides on thermal treatment at high temperatures. Meanwhile, acidity in LDHs appears by virtue of the compositional trivalent cations, that act as Lewis acid sites. Additionally, the surface hydroxyl groups and intercalated water molecules can also act as Brønsted acid sites. The acidic nature of LDHs can be enhanced by increasing the ratio of trivalent cations in the lattice, as well as by intercalating acidic species into the layered structure. Essentially, cation and anion composition and ratios play a pivotal role in determining the surface chemistry of LDHs and provide precise control over the nature of active sites. Furthermore, the introduction of transition and rare earth metals in the layers, and surface modification with specific functional groups also hold the potential to tune the acidity and basicity of LDHs, thereby monitoring their multifunctionality for various applications.

### 1.4.3 Adsorption Capacity

Surface adsorption describes the uptake of species onto the external faces and edge sites of LDH crystallites. The surface adsorption capacity of LDHs arises from a synergy of high external surface area, positive surface charge, chemisorptive functional groups, and tunable composition. The maximum adsorption at the surface is directly related to the available external area. Increasing LDH surface area by minimizing layer stacking or exfoliating into thinner platelets substantially enhances adsorption. Furthermore, LDHs synthesized to yield thinner, plate-like nanostructures or nanosheets expose more active surface sites for adsorption, thereby contributing to enhanced surface adsorption capacity. Additionally, the surface porosity of LDHs and distribution of micro/mesopores facilitate the access of guest molecules to the surface, thereby impacting the adsorption ability of LDHs. The metal cation composition, charge density on the layers, as well as vacancies and defects, influence the surface properties of LDHs. Advances in structural engineering, composite formation, and surface modification continue to push capacities higher, enabling selectivity across a wide variety of pollutants. Both the inherent host structure and opportunities for modification make LDHs among the most versatile and powerful sorbents for environmental, analytical, and industrial applications

### 1.4.4 Redox Behaviour

LDHs demonstrate rich and tunable redox properties due to their mixed-metal composition, the presence of variable oxidation states, and the structural flexibility of both the layers and the interlayer domain. Due to the partial substitution of divalent by trivalent cations and the subsequent generation of net positive charge on LDH surface, they gain the ability of electron transfer both within the lattice and at the external surface. The cations may get oxidised or reduced, and the presence of both reduced and oxidized metal ions near each other supports intervalence charge transfer. Furthermore, the interlayer anions can mediate the electron transfer process, and their selectivity affects electron transport pathways. Their redox activities can be enhanced by intercalation or adsorption of redox-active species in the lattice that engage in electron transfer reactions. In addition, redox chemistry in LDHs arises from the

dynamic environment within the layers and galleries, and the ability to mediate electron transfer both within the structure and with external substrates. LDHs support both chemical (direct or coupled) and electrochemical (Faradaic) redox transformations, thereby providing versatility for energy storage, catalysis, environmental remediation, and sensing applications.

#### 1.4.5 Post-Synthesis Modification

Post-synthesis modifications are often adopted to tune the chemical, structural and functional attributes of LDHs, thereby enhancing the existing properties of synthesized LDHs. A large spectrum of structural, textural, and compositional modifications is possible for layered materials such as (1) cation/anion exchange, (2) surface functionalisation, (3) composite/hybrid formation, (4) exfoliation of layers and colloidal solution formation and (5) topotactic transformation into LDOs. Constituent modifications in LDH may be achieved by exchanging the anions present in the interlayer region, and some reports have also described the partial substitution of the intralayer cations, thereby improving the compositional versatility of LDHs. Another effective way to modify LDH surface is by functionalising it with organic moieties such as surfactants, carboxylic acids, polymers, biomolecules, enzymes, etc[45]. This modification can help in introducing hydrophobicity and dispersibility in the lattice, and is also viable for providing higher number of reactive sites on the LDH surface for further reactions. The impregnation of LDH surface with metal and metal oxide nanoparticles such as Ag, Au, Pt, TiO<sub>2</sub>, Fe<sub>3</sub>O<sub>4</sub>, etc, contributes to the enhancement of catalytic, magnetic, and optical properties of the lattice[46–48]. Furthermore, the formation of inorganic/organic hybrids by combining LDHs with other materials such as polymers, carbonaceous materials, zeolites, and other 2D materials is highly beneficial. This approach helps in overcoming the drawbacks of both materials while giving rise to new or enhanced properties in the lattice[49–52]. In addition, the exfoliation ability, that is essentially the delamination of LDH layers into single or few-layer nanosheets, helps in augmenting the surface area and reactivity of LDHs, thereby making them more useful in various fields[53]. LDHs can also be topotactically transformed into mixed oxide structures called LDOs by calcination, that leads to the collapse of the layered structure[54]. These amorphous LDOs often

possess enhanced surface areas, high porosity, and high thermal stability, rendering them extremely useful in adsorption and catalytic applications. All these post-synthesis modifications help in tailoring LDHs and expanding their utility in new frontiers.

#### **1.4.6 Memory Effect**

One of the most unique and interesting features of LDHs is their structural memory effect property, that essentially involves the regaining of layered structure by LDH via hydration after being thermally treated. When LDHs are thermally treated at temperatures in the range  $300\text{ }^{\circ}\text{C}$ -  $500\text{ }^{\circ}\text{C}$ , they lose the interlayer anions and water molecules and their layered structure gets dismantled, leading to the formation of LDOs[55]. But on being dispersed in an aqueous solution containing desired anion, LDHs regain their parent layered structure, albeit with the new desired anion present in the interlayer region.

This property is the basis of the reconstruction method for LDH synthesis, and the regaining of layered structure and exchange of counter anions majorly influences the basicity of the sample. Furthermore, the memory effect only comes into play within a specific temperature range. If the calcination temperature is too high, the lattice does not reform to its original structure, and this may result in the irreversible formation of oxide or spinel-type structures. The memory effect property can serve as an effective methodology for the regeneration of catalysts, intercalation of large-sized anions, and for anion capture.

#### **1.5 Applications**

Layered double hydroxides (LDHs) are highly adaptable materials characterised by a unique layered structure and exceptional properties. Owing to this, they have carved out a niche for themselves in various scientific and technological fields. Some of their applications have been described below (Figure 1.5).



**Figure 1.5** Various applications of LDHs.

### 1.5.1 Water Remediation

In a world with limited potable water sources and burgeoning water pollution, water remediation has become a pressing requirement to fulfill the needs of an ever-growing population. As per the United Nations SDG-6, clean water and sanitation are a basic human right for all, but billions of people in the world do not have access to fresh and clean water[56]. Factors such as climate change, growing urbanization, and agricultural practices have contributed immensely to the issue of water scarcity. Due to the unimpeded release of untreated and polluted effluents from industries into water bodies, water pollution levels in existing water sources have also increased significantly, further exacerbating existing problems.

Specifically, the contamination of water bodies with dyes, nitroarene compounds (NACs), and drugs is especially problematic, as these toxins exhibit bioaccumulative and biomagnification tendencies. Moreover, their high chemical and thermal stabilities, along with their antimicrobial properties, prevent decomposition, thereby leading to exacerbated detrimental physiological effects in flora and fauna [57–59]. Even at low concentrations, these pollutants inhibit the photosynthesis rates in plants, thereby affecting germination rates and root/shoot growth, while in case of animals and animals, these pollutants can cause skin, eye, and respiratory issues, and can

potentially exert mutagenic, genotoxic, and carcinogenic effects. Due to the coloured nature of majority of these pollutants, they degrade the aesthetic value of water bodies and block sunlight, thereby negatively affecting photosynthesis in algae and aquatic plants. As a result, these grave issues underscore the urgent need for the development of effective solutions for wastewater purification.

To combat these issues, various physical, chemical, mechanical, and biological processes have been designed and employed to produce clean water. These include adsorption, chlorination, membrane filtration, disinfection, ozonation, sedimentation, coagulation-flocculation, activated sludge process, biodegradation, and reverse osmosis, among others[60–65]. However, the shortcomings of these treatment processes reduce their efficacy, resulting in these existing water treatment technologies being only partly successful in addressing this problem. Among these processes, heterogeneous catalysis using LDHs has gained recognition as a unique strategy for mitigation of water pollution due to its green chemistry-based approach, excellent performance and cost-effective nature[66].

### 1.5.1.1 Adsorption

The process of adsorption entails the adherence of atoms, ions, or molecules onto a solid surface by the action of physical and/or chemical forces. In terms of water treatment, this process typically involves the accumulation of contaminants called adsorbate on the surface of an adsorbent material. Adsorption mainly proceeds forward by the action of intermolecular forces of attraction, and can occur through a variety of mechanisms such as physisorption (e.g., van der Waals, hydrogen bonding,  $\pi$ - $\pi$  interactions, etc.) and chemisorption (e.g., ionic interaction). Adsorption is a straightforward and efficient process for the removal of both organic and inorganic pollutants from the environment. In literature, the sequestration of a variety of organic and inorganic contaminants such as dyes, biomolecules, heavy metals, surfactants, persistent organic pollutants (POPs), endocrine disruptors, etc. from aqueous medium has been reported. Due to the high specific surface area, abundance of active sites, good stability, and biocompatible nature, the use of LDHs as adsorbents for abatement of several pollutants has been widely studied. For instance, Das et al. synthesized

ternary LDH consisting of Mg, Al, and Fe, and utilised it for the uptake of malachite green (MG) dye[67]. A study by Rathee et al. reported the hydrothermal synthesis of NiFeTi-LDH for the uptake of anionic azo dyes - methyl orange, congo red, methyl blue, and orange G[68]. However, despite its merits, adsorption has certain disadvantages, including a limited adsorption capacity of the adsorbent, a lack of selectivity, and the difficulty in separating and regenerating the adsorbent due to the need for energy-intensive procedures or additional chemicals. These aspects must be carefully considered when implementing adsorption for wastewater remediation. Table 1.3 summarizes the performance of some LDH materials employed for the adsorptive elimination of various types of pollutants from aqueous medium.

**Table 1.3** Adsorption application of LDHs.

Adsorbent	Pollutants	pH	Adsorption	Removal	Reference
			capacity	efficiency	
			$q_{\max}$ (mg/g)	(%)	
Fe/Cr LDH	Hg <sup>2+</sup>	5	116	-	[69]
MgAl-LDH	Cr(VI)	-	47.62	~96	[70]
EDTA- MgAl-LDH	Cr(VI)	-	32.46	~79	
NiZn- LDH	Azorubine	6-7	223	96.02	[71]
Zn-Co-Ni LDH	Methyl Orange	2-10	1871.65	>90	[72]
CaMgFe-LDH	Arsenic	-	16	47	[73]
Polyoxometalate- ZnAlFe LDH	Methylene Blue	-	67.47	-	[74]
NiAlTi-LDH	Orange II	4-10	2000	100	[75]
	Methyl Orange	9	1250	96.7	
	Tetracycline		238.09	100	
FeMgZe-LDH	Fluoride	3	88.55	97.57	[76]
MgAlFe-LDH	U(VI)	6	263.16	-	[77]
CoMgAl-LDH	1-	5	258.5	-	[78]
FeMgAl-LDH	naphthoacetic acid	5	288.5	-	

BO <sub>3</sub> <sup>-</sup> intercalated CoMgAl-LDO	Congo Red Methyl Orange	-	1493.25 990.1	93.17 80.55	[79]
---	----------------------------	---	------------------	----------------	------

### 1.5.1.2 Catalytic Reduction

In the realm of wastewater remediation, the catalytic reduction process has emerged as a topic of considerable interest due to its economic viability, remarkable selectivity, cost-effectiveness, and reusability of the nanocatalyst. Among the catalytic processes, the catalytic reduction of organic pollutants using NaBH<sub>4</sub> is particularly attractive due to its convenient and rapid operating procedure, that eliminates the need for toxic chemicals or complex machinery. This process entails the use of a strong reducing agent such as sodium borohydride (NaBH<sub>4</sub>) for the reduction of pollutant molecules and their transformation into less toxic or harmless substances. NaBH<sub>4</sub>, on its own, is a strong reductant and is able to reduce some molecules, but often the process is kinetically hindered, resulting in sluggish reaction rates and an incredibly high time taken for the reaction to reach completion. To overcome this, the use of a catalyst is usually favoured since it can drive reaction rates forward and make the reaction kinetically favourable. In particular, the reduction of dyes and NACs is particularly advantageous since the by-products of the reaction are often commercially and industrially important materials. Therefore, in literature, a variety of materials such as noble metals, metal and metal oxide nanoparticles, MOFs, carbonaceous materials, etc., have been employed for the catalytic reduction process. Recently, the use of LDH-based materials has been explored for the catalytic reduction of these species since LDHs fulfil all the criteria for an ideal catalyst including large surface area, active sites, surface basicity, colloidal dispersion activity, and redox behaviour. Taking advantage of these properties, Kansal et al. utilised NiCo-LDH nanosheets for the catalytic hydrogenation of *p*-nitrophenol (*p*-NP) to *p*-aminophenol (*p*-AP)[80]. Wei et al. fabricated a CuNiAl-LDH-Reduced Graphene Oxide nanosheet array and applied it for the catalytic reduction of *p*-NP and methyl orange (MO) dye[81]. Table 1.4 summarizes the performance of some LDH materials employed for the catalytic reduction of various NACs and azo dyes in aqueous medium.

**Table 1.4** Catalytic reduction application of LDHs.

Catalyst	Pollutants	Removal efficiency (%)	Reference
CoAl-LDH	<i>p</i> -NA	69	[82]
	<i>p</i> -nitrobenzylalcohol	60	
	2,6-dinitrophenol	71	
	Rhodamine B	100	
	Rhodamine 6G	100	
NiCo-LDH	<i>p</i> -NP	-	[80]
NiMn-LDH	<i>p</i> -NP	-	[83]

### 1.5.1.3 Photocatalysis

Photocatalysis is a robust and highly advanced oxidation process (AOP) that is used to achieve the mineralisation of molecules on the catalyst surface under the influence of a light source such as ultraviolet, visible, or sunlight. In this method, the exposure of the catalyst surface to the light source results in the excitation of electrons from the valence band (VB) to the conduction band (CB) of the material, leaving behind holes in the VB. The interaction of these electrons and holes with oxygen and water molecules respectively leads to the generation of reactive oxygen species (ROS) that aid the reduction of the target molecules by degrading their structures and converting them into benign products before their complete mineralisation into CO<sub>2</sub> and H<sub>2</sub>O. This photochemical reaction involves two simultaneous reactions, where the first reaction is oxidation due to photo-induced positive holes, and the second reaction entails reduction due to photo-induced negative electrons. This method offers several advantages over traditional wastewater treatment processes, including no possibility of toxic secondary pollutant generation, ease of recyclability and separation, as well as high efficacy even at low concentrations. In literature, a variety of semiconductor-based materials, particularly metal oxides, have been employed for photocatalytic applications in wastewater treatment. As an emerging material of interest, LDHs have also found utility as photocatalysts due to their efficient charge separation, tunable

composition, excellent light absorption, and surface adsorption. A study by Huang et al. tested the MgZnIn-LDH and its calcined products for the degradation of the methylene blue (MB) dye [84]. In another example, Saliba et al. developed a CdAl-LDH photocatalyst and investigated its application for the degradation of methylene blue (MB) [85]. Table 1.5 summarizes the performance of some LDH materials employed for the photocatalytic degradation of various pollutants.

**Table 1.5** Photocatalytic application of LDHs.

Photocatalyst	Pollutant	Removal	Reference
		Efficiency (%)	
ZnCoAl-LDH	Orange II	90	[86]
MgCuFe-LDH	Rhodamine B	99.5	[87]
MnMgFe-LDH	Methylene blue	99	[88]
ZnAlFe-LDH	2,4-DNP	-	[89]
CoFeNi-LDH	Congo Red	100	[90]
	Rhodamine B	100	
Mg-Al-Ti LDO	Methylene Blue	71	[91]
EDTA intercalated-	Methylene Blue	98	[84]
MgZnIn LDO			
ZnAlTi-LDO	Methylene Blue	99	[92]
NiZnAl-LDO	Orange G	99	[93]
ZnNiAl-LDO	<i>p</i> -NP	93.0	[94]
ZnNiIn-LDO	Methylene Blue	88.5	[95]
ZnAlCe-LDO	Rhodamine B	97.8	[96]
	Paracetamol	98.9	
MgAlLa-LDO	Methylene Blue	99.89	[97]
ZnCuCo-LDO	Sulfamethazine	95	[98]
CuMgFe-LDO	Phenol	95.3	[99]

### 1.5.2 Composite Fabrication

The fabrication of composite materials represents a developing area of study and entails the formation of a new material by the synergistic combination of two materials, wherein one forms the matrix phase and the other acts as the filler. In composite

materials, the negative aspects of the constituents are essentially eliminated, while new or enhanced properties may be observed in the material. Composites exhibit several functional properties such as high surface area, stability and durability, reusability, enhanced mechanical strength, and enhanced separability. Due to these properties, composites find applications in almost every frontier, ranging from aeronautics to catalysis and energy storage, medicine and construction. Several research groups have combined LDHs with a variety of materials such as inorganic/organic polymers, carbonaceous materials, metal and metal oxide nanoparticles, clays, etc., for the development of various types of composites. In particular, metal oxide and carbon-based composites have become the focal point of research due to their tailorability and versatility.

While carbonaceous materials and metal oxides are attractive materials that possess a host of interesting properties such as high surface area, versatility and tunability, cost-effectiveness, eco-friendly nature as well as high chemical and thermal stability, both these materials suffer from certain drawbacks that hinder their usage. Carbon-based materials often possess limited intrinsic catalytic activity and agglomeration tendencies, making it challenging and expensive to achieve their uniform synthesis at scale. Furthermore, their surface functionalization is challenging, and there are some concerns related to the potential toxic behaviour of nanocarbons. While in case of metal oxide nanoparticles, agglomeration tendencies paired with poor dispersibility and risk of metal leaching, and their limited selectivity in catalytic reactions impair their practical use. The combination of carbonaceous materials and metal oxides with LDHs can bring forth a material that overcomes these drawbacks. Furthermore, advantageous properties such as high surface area, good conductivity, high catalytic activities, high selectivity, and versatility due to tunable structures can make the resulting composites highly beneficial materials for various applications. Consequentially, these LDH-based composites have gained immense attention in the past few years, and their stature as ideal catalytic materials has gained significant heights. This growing interdisciplinary field can greatly leverage the expertise and facilities built around LDH research over the past decade. Table 1.6 summarises the applications of LDH-based composite materials reported in the literature.

**Table 1.6** LDH-based composites and their applications.

Constituents of Composite	Application	Reference
MgCoAl-LDH, Graphene	Methyl orange removal	[100]
NiCoAl-LDH, CuCo <sub>2</sub> S <sub>4</sub> , Ni foam	Supercapacitor	[101]
NiCoFe-LDH, Polyaniline	Supercapacitor	[102]
ZnMgAl-LDH, Acrylonitrile-butadiene-styrene	Flame retardance	[41]
NiMgAl- LDH, g-C <sub>3</sub> N <sub>4</sub>	UO <sub>2</sub> <sup>2+</sup> removal	[103]
CoNiAl-LDH, Zeolitic imidazolate framework-67 (ZIF-67)	Electrocatalyst for oxygen evolution reaction	[104]
LaCoFe-LDH, Reduced graphene oxide	Electrochemical sensing of urea	[105]
NiCoAl-LDH, Sulfourea	Flexible supercapacitors	[106]
ZnAlLa-LDH, Amaranth carbonaceous material	Photodegradation of ibuprofen	[107]
ZnAlTi-LDO, Fullerene	Photodegradation of Bisphenol A	[108]
MgZnAl-LDO, g-C <sub>3</sub> N <sub>4</sub>	Adsorption and photodegradation of oxytetracycline, tetracycline, chlortetracycline, doxycycline	[109]
Azo-modified NiZnAl-LDH, Polypropylene	Fire retardance	[110]

### 1.5.3 Miscellaneous

In addition to their applications in water treatment and composite formation, LDHs find use in a variety of other fields. These include energy storage, sensing, catalysts for organic transformations, and as antimicrobial materials[111–114]. The highly

tailorable layered structures of LDHs along with their good electrical conductivities, redox activities and high surface area enables their use in energy storage applications since their structure allows for high capacity, fast and selective ion transport, outstanding cycling stability, and easy modification for target applications. Therefore, their use in batteries and supercapacitors is steadily gaining popularity, and advances in composite design and nanoscale engineering have established them as prime candidates for fabrication of energy storage devices in the next few years[17].

LDHs are excellent candidates for organic transformation applications such as oxidation, reduction, condensation, and other key chemical reactions catalysed by LDHs due to several distinctive properties. Their anion exchange behaviour and intercalation capacity allow them to readily intercalate catalytic species or active organic functionalities, promoting selective catalysis and enabling the design of novel inorganic-organic supramolecular catalysts. Furthermore, their activity as both Brønsted and Lewis acid or base makes them versatile catalysts for a broad range of organic transformations, including aldol condensation, Knoevenagel condensation, Michael addition, etc[115]. Therefore, these features enable LDHs to serve as versatile, efficient, and green catalysts for a wide variety of organic transformations.

For sensing applications, the use of LDHs is highly favoured due to their high surface area and hierarchical porous structure since they provide numerous active sites for analyte adsorption and interactions. This enhances sensitivity and facilitates rapid response in sensors. Furthermore, their intrinsic catalytic activity and redox behaviour enable the electrochemical detection of various compounds, such as glucose, dopamine, and hydrogen peroxide. Their ability to immobilize a variety of guest molecules, including enzymes, fluorophores, and quantum dots due to high ion exchange capacity also contributes to their use as sensors[116].

LDHs are excellent candidates for use as antimicrobial agents due to several unique physicochemical and biological properties that directly contribute to their effectiveness against a broad range of pathogens. They are known to exhibit prominent antimicrobial activity against various types of pathogens via multiple antimicrobial mechanisms. LDHs possess the ability to intercalate and protect antimicrobial agents

(e.g., antibiotics, natural compounds) within their structure, enabling sustained release and enhanced efficacy[117,118]. Therefore, they combine direct microbial killing (physical disruption, ion release, ROS generation), protective and tunable nanocarrier capabilities, inhibition of biofilms, and long-term, broad-spectrum efficacy with low cytotoxicity, biocompatibility, and structural stability for diverse applications.

## 1.6 Significant Findings and Research Gap

Since their discovery in the 19<sup>th</sup> century, layered double hydroxides (LDHs) have emerged as nanosubstrates of interest owing to their excellent properties such as high surface area, low anion selectivity, porosity, surface chemistry, and excellent anion exchangeability. Their synthesis and use have become the focal point of research due to their biocompatibility and eco-friendly nature, since they also align with the principles of green chemistry. LDHs composed of various combinations of cations and anions have been reported, with the majority of them being binary LDHs. But due to their restricted compositional tunability owing to the presence of only two cations, the scope of their applications becomes quite limited due to inferior performances, limited active site density, and reduced intrinsic activities. Although a few ternary LDHs have been reported in literature, but success has been achieved with only a few combinations of cations due to difficulty in governing oxidation states. Furthermore, LDHs reported in literature are generally synthesized using conventional methods such as coprecipitation, urea hydrolysis, sol-gel, anion exchange, and reconstruction. But these methods suffer from several disadvantages such as low crystallinity and purity of products, use of toxic precursors and reaction conditions, complex instrumentation, high temperatures and pressures as well as less control over product morphology and agglomeration tendency. Furthermore, issues such as high CO<sub>2</sub> contamination and difficulty in its removal, thereby requiring complex inert air set-ups make these processes less cost-effective.

During the extensive literature survey, it was also found that for the purpose of wastewater remediation, several methods such as adsorption, membrane filtration, coagulation-flocculation, disinfection, activated sludge process, etc., have been devised and are currently in use. But these methods are unable to achieve complete

decontamination of water, and also suffer from other drawbacks such as secondary pollutant generation, limited efficacy against pathogens, high cost and complexity in handling, membrane fouling, and the use of toxic chemicals. Conversely, catalytic methods for water treatment have aroused strong interest since they have the potential to overcome all the issues faced by conventional wastewater remediation methods while exhibiting excellent efficiency towards toxin removal. In this purview, cationic clays, noble metals, metal oxides, and carbonaceous nanomaterials such as fullerenes, carbon dots and nanotubes (CNT), graphene, carbon black, activated carbon, diamond, graphite, biochar, etc., are some materials that have captured the attention of researchers for catalytic applications. Although these materials exhibit excellent catalytic performances, their use remains quite limited due to high costs and complexities in synthesis, catalytic deactivation. Furthermore, the majority of these materials exhibit agglomeration tendencies, lack of recyclability, and difficulty in separation. On the contrary, the compositional flexibility of LDHs spans the periodic table, and a rich and exciting spectrum of structures and properties can be achieved through the various synthesized lattices. Furthermore, their few drawbacks can be overcome by opting for methods such as thermal treatment and composite formation. Keeping this in view, LDHs and LDH-based materials can be regarded as the ideal candidates for synthesis of catalytic materials for wastewater treatment.

Based on the literature review, an attempt has been made to synthesize novel transition metal-based ternary LDHs using a simple acid hydrolysis methodology that eliminates the need for the use of toxic chemicals, harsh bases and extreme reaction conditions. Furthermore, it was deduced that ternary LDHs containing combinations of Zn/Cu/Ni and Zn/Cu/Ce remain scarcely reported, and there is a dearth of studies exploring the utility of LDHs and LDH-based composites in wastewater remediation applications as catalytic materials.

### 1.7 Research Objectives

- I. Exploration of the optimal synthesis conditions for obtaining solids of technological importance.

- II. Synthesis of various combinations of LDH containing Zn (divalent metal ion) with trivalent metal ions, i.e., Cu, Ni, Ce, using methodologies such as acid hydrolysis, low solvent synthesis, etc.
- III. Optimization of phase composition followed by detailed study and analysis of catalytic properties of synthesized LDHs.
- IV. Investigation of structure regaining capability of LDHs due to memory effect property after calcination-regeneration experiments.
- V. Intercalation of simple/complex organic and inorganic anions within the LDH lattices using anion exchange method.
- VI. Incorporation of polymer into the LDH galleries via in situ polymerization or by direct intercalation of a high molecular weight macromolecule, and ion-exchange process to synthesize the host in the presence of the polymer.
- VII. Fabrication of LDH-based composite materials and evaluation of their catalytic activities.

## 1.8 References

- [1] A.G. Olabi, M.A. Abdelkareem, T. Wilberforce, E.T. Sayed, Application of graphene in energy storage device – A review, *Renew. Sustain. Energy Rev.* 135 (2021) 110026. <https://doi.org/10.1016/j.rser.2020.110026>.
- [2] S.D. Xie, Y. Liu, Z.Y. Wu, G.L. Shen, R.Q. Yu, Application of Inorganic Layered Materials in Electrochemical Sensors, *Chinese J. Anal. Chem.* 43 (2015) 1648–1655. [https://doi.org/10.1016/S1872-2040\(15\)60879-9](https://doi.org/10.1016/S1872-2040(15)60879-9).
- [3] A. Majid, A. Jabeen, Characteristics, Strategies and Applications of Layered Materials: An Introduction, in: A. Majid, A. Jabeen (Eds.), *Layeredness Mater. Charact. Strateg. Appl.*, Springer Nature Singapore, Singapore, 2023: pp. 1–16. [https://doi.org/10.1007/978-981-99-6299-0\\_1](https://doi.org/10.1007/978-981-99-6299-0_1).
- [4] D.L. Duong, S.J. Yun, Y.H. Lee, Van der Waals Layered Materials: Opportunities and Challenges, *ACS Nano* 11 (2017) 11803–11830. <https://doi.org/10.1021/acsnano.7b07436>.
- [5] S. Liu, H. Zhang, X. Peng, J. Chen, L. Kang, X. Yin, Y. Yusuke, B. Ding, Emerging Issues and Opportunities of 2D Layered Transition Metal Dichalcogenide Architectures for Supercapacitors, *ACS Nano* 19 (2025) 13591–13636. <https://doi.org/10.1021/acsnano.5c01512>.
- [6] X. Fu, Y. Liu, X. Wang, L. Kang, T. Qiu, Graphene-based advanced materials for energy storage and conversion systems: Progress, challenges, and commercial future, *Appl. Energy* 386 (2025) 125566. <https://doi.org/10.1016/j.apenergy.2025.125566>.

[7] R. Umapathi, C.V. Raju, M. Safarkhani, J. Haribabu, H.U. Lee, G.M. Rani, Y.S. Huh, Versatility of MXene based materials for the electrochemical detection of phenolic contaminants, *Coord. Chem. Rev.* 525 (2025) 216305. <https://doi.org/10.1016/j.ccr.2024.216305>.

[8] C. Van Le, M. Ju, T.T.T. Nguyen, H. Lee, H. Yoon, Hetero-layered 2D materials: Scalable preparation and energy applications, *Mater. Sci. Eng. R Reports* 163 (2025) 100937. <https://doi.org/10.1016/j.mser.2025.100937>.

[9] M. El Alouani, H. Saufi, B. Aouan, R. Bassam, S. Alehyen, Y. Rachdi, H. El Hadki, A. El Hadki, J. Mabrouki, S. Belaaouad, H. Ez-Zaki, N. Barka, A comprehensive review of synthesis, characterization, and applications of aluminosilicate materials-based geopolymers, *Environ. Adv.* 16 (2024) 100524. [https://doi.org/https://doi.org/10.1016/j.envadv.2024.100524](https://doi.org/10.1016/j.envadv.2024.100524).

[10] R. Yadav, A.K. Sharma, S. Sharma, Advance Development in Natural Graphite Material and Its Applications: A Review, *Mining, Metall. Explor.* 42 (2025) 361–385. <https://doi.org/10.1007/s42461-024-01167-z>.

[11] Z. Chen, Q. Fan, M. Huang, H. Cölfen, The Structure, Preparation, Characterization, and Intercalation Mechanism of Layered Hydroxides Intercalated with Guest Anions, *Small* 19 (2023) 1–22. <https://doi.org/10.1002/smll.202300509>.

[12] J.-M. Oh, T.T. Biswick, J.-H. Choy, Layered nanomaterials for green materials, *J. Mater. Chem.* 19 (2009) 2553–2563. <https://doi.org/10.1039/B819094A>.

[13] E. Kandare, J.M. Hossenlopp, Hydroxy double salt anion exchange kinetics: Effects of precursor structure and anion size, *J. Phys. Chem. B* 109 (2005) 8469–8475. <https://doi.org/10.1021/jp0465433>.

[14] B. Pandey, P. Singh, V. Kumar, Adsorption of anionic dye from aqueous environment using surface-engineered Zn/Cu hydroxy double salt-based material: mechanistic, equilibrium and kinetic studies, *J. Environ. Sci. Heal. - Part A Toxic/Hazardous Subst. Environ. Eng.* 58 (2023) 869–884. <https://doi.org/10.1080/10934529.2023.2243193>.

[15] D.C. Pereira, D.L.A. De Faria, V.R.L. Constantino, CuII hydroxy salts: Characterization of layered compounds by vibrational spectroscopy, *J. Braz. Chem. Soc.* 17 (2006) 1651–1657. <https://doi.org/10.1590/S0103-50532006000800024>.

[16] F. Geng, H. Xin, Y. Matsushita, R. Ma, M. Tanaka, F. Izumi, N. Iyi, T. Sasaki, New layered rare-earth hydroxides with anion-exchange properties, *Chem. - A Eur. J.* 14 (2008) 9255–9260. <https://doi.org/10.1002/chem.200800127>.

[17] M. Zhao, Q. Zhao, B. Li, H. Xue, H. Pang, C. Chen, Recent progress in layered double hydroxide based materials for electrochemical capacitors: Design, synthesis and performance, *Nanoscale* 9 (2017) 15206–15225. <https://doi.org/10.1039/c7nr04752e>.

[18] A.Y.A. Kaassis, S.M. Xu, S. Guan, D.G. Evans, M. Wei, G.R. Williams, Hydroxy double salts loaded with bioactive ions: Synthesis, intercalation mechanisms, and functional performance, *J. Solid State Chem.* 238 (2016) 129–138. <https://doi.org/10.1016/j.jssc.2016.03.019>.

[19] J.T. Rajamathi, S. Britto, M. Rajamathi, Synthesis and anion exchange reactions of a layered copper-zinc hydroxy double salt, Cu<sub>1.6</sub>Zn<sub>0.4</sub>(OH)<sub>3</sub>(OAc)<sub>2</sub>·H<sub>2</sub>O, *J. Chem. Sci.* 117 (2005) 629–633. <https://doi.org/10.1007/BF02708291>.

[20] E. Rocca, C. Caillet, A. Mesbah, M. Francois, J. Steinmetz, Intercalation in zinc-layered hydroxide: Zinc hydroxyheptanoate used as protective material on zinc, *Chem. Mater.* 18 (2006) 6186–6193. <https://doi.org/10.1021/cm0616026>.

[21] D.M. Romero-García, C.A. Velázquez-Carriiles, C. Gomez, G. Velázquez-Juárez, J.M. Silva-Jara, Tannic acid-layered hydroxide salt hybrid: assessment of antibiofilm formation and foodborne pathogen growth inhibition, *J. Food Sci. Technol.* 60 (2023) 2659–2669. <https://doi.org/10.1007/s13197-023-05790-4>.

[22] A. V. Radha, S. Weiß, I. Sanjuán, M. Ertl, C. Andronescu, J. Breu, The Effect of Interlayer Anion Grafting on Water Oxidation Electrocatalysis: A Comparative Study of Ni- and Co-Based Brucite-Type Layered Hydroxides, Layered Double Hydroxides and Hydroxynitrate Salts, *Chem. - A Eur. J.* 27 (2021) 16930–16937. <https://doi.org/10.1002/chem.202100452>.

[23] S. Megala, S. Prabhu, S. Harish, M. Navaneethan, S. Sohila, R. Ramesh, Enhanced photocatalytic dye degradation activity of carbonate intercalated layered Zn, ZnNi and ZnCu hydroxides, *Appl. Surf. Sci.* 481 (2019) 385–393. <https://doi.org/10.1016/j.apsusc.2019.03.091>.

[24] Y. Shen, R. Hong, X. He, C. Wang, X. Wang, S. Li, X. Zhu, D. Gui, Utilizing excited-state proton transfer fluorescence quenching mechanism, layered rare earth hydroxides enable ultra-sensitive detection of nitroaromatic, *J. Colloid Interface Sci.* 673 (2024) 564–573. <https://doi.org/10.1016/j.jcis.2024.06.075>.

[25] X. Wu, S. Qin, R. Zhang, Y. Guo, J. Huang, Photoluminescent Films of MoO<sub>4</sub>-2 Exchanged Layered Rare-Earth Hydroxides for Solid-State Lighting, *ACS Appl. Nano Mater.* 7 (2024) 19593–19601. <https://doi.org/10.1021/acsanm.4c03550>.

[26] Z. Zhao, H. Lin, T. Yang, L. Zhang, Q. Liu, C. Zhang, F. Qian, Coordination-induced and tunable layered rare-earth hydroxide-complex intercalated nanohybrid phosphorescent photosensitizer and therapy, *RSC Adv.* 14 (2024) 7430–7439. <https://doi.org/10.1039/d3ra07310f>.

[27] G. Mishra, B. Dash, S. Pandey, D. Sethi, Ternary layered double hydroxides (LDH) based on Cu- substituted Zn-Al for the design of efficient antibacterial ceramics, *Appl. Clay Sci.* 165 (2018) 214–222. <https://doi.org/10.1016/j.clay.2018.08.021>.

[28] X. Li, J. Yang, J. Chen, J. Sun, J. Liu, X. Cui, L. Zou, High-performance ternary NiFeCo-LDH nanosheets for supercapacitors by cation modulation and sodium dodecyl sulfonate intercalation, *J. Mater. Chem. A* 12 (2024) 2887–2901. <https://doi.org/10.1039/D3TA06505G>.

[29] M. Mahmood, M. Mubeen, W. Wang, M. Tabish, H. Murtaza, M. Jawad, J. Wang, Y. Lv, J. Zhao, B. Fan, Mechanically robust and self-healing protective coating for Zn-Al-Mg coated steel enhanced by benzotriazole-5 carboxylic acid intercalated MgAlCe ternary LDH, *Prog. Org. Coatings* 201 (2025) 109107. <https://doi.org/https://doi.org/10.1016/j.porgcoat.2025.109107>.

[30] X. Zhang, J. Rui, S. Yang, R. Fu, Y. Qiu, Enhanced immobilization of Cd(II) by successive isomorphic substitution with Ca(II) and Mg(II) from ternary layered double hydroxides, *J. Hazard. Mater.* 490 (2025). <https://doi.org/10.1016/j.jhazmat.2025.137771>.

[31] Z. Song, Q. Yin, Z. Zhao, X. Li, Z. Li, J. Yu, Q. Yuan, D. Zhao, Y. zhi Li, Y. Sui, J. Qi, J. Han, Fluoride-Ion-Mediated Fabrication of Cerium-Incorporated Ternary Layered Double Hydroxide Microflowers for Enhanced Chlorine Storage, *Adv. Funct. Mater.* (2025). <https://doi.org/10.1002/adfm.202500494>.

[32] Z. Hao, Z. Tian, X. Tian, L. Ma, Y. Gao, M. Shao, R. Zhang, Interlayer anions modulated ZnAl-layered double hydroxides for enhanced photocatalytic CO<sub>2</sub> reduction, *J. Alloys Compd.* 995 (2024) 174828. <https://doi.org/https://doi.org/10.1016/j.jallcom.2024.174828>.

[33] S.J. Mills, A.G. Christy, J.-M.R. Génin, T. Kameda, F. Colombo, Nomenclature of the hydrotalcite supergroup: natural layered double hydroxides, *Mineral. Mag.* 76 (2012) 1289–1336. <https://doi.org/10.1180/minmag.2012.076.5.10>.

[34] S.J. Xia, Z.M. Ni, Q. Xu, B.X. Hu, J. Hu, Layered double hydroxides as supports for intercalation and sustained release of antihypertensive drugs, *J. Solid State Chem.* 181 (2008) 2610–2619. <https://doi.org/10.1016/j.jssc.2008.06.009>.

[35] Y. Luo, Y. Wu, D. Wu, C. Huang, D. Xiao, H. Chen, S. Zheng, P.K. Chu, NiFe-Layered Double Hydroxide Synchronously Activated by Heterojunctions and Vacancies for the Oxygen Evolution Reaction, *ACS Appl. Mater. Interfaces* 12 (2020) 42850–42858. <https://doi.org/10.1021/acsami.0c11847>.

[36] J.M. Samuel, P. Navaneeth, T.G. Satheesh Babu, P.V. Suneesh, Fabrication of flexible printed supercapacitor with high cycling stability using Cobalt-Cerium layered double hydroxide, *J. Ind. Eng. Chem.* (2025) 1–12. <https://doi.org/10.1016/j.jiec.2025.03.026>.

[37] G. Klydziute, L. Gliaudyte, D. Sokol, D. Vasiliauskiene, T.C.K. Yang, A. Kareiva, Sol-gel synthesis, characterization and application of metal-substituted Mg<sub>2-x</sub>Zn<sub>x</sub>Al<sub>1</sub> and Mg<sub>2</sub>Al<sub>1-x</sub>L<sub>x</sub> layered double hydroxides, *J. Sol-Gel Sci. Technol.* (2025). <https://doi.org/10.1007/s10971-025-06778-6>.

[38] A. Yu, Y. Song, N. Wang, Y. Tian, H. Chen, Study on the corrosion and self-healing behavior of different anion-intercalated layered double hydroxides coatings on Mg alloy surfaces, *Surfaces and Interfaces* 56 (2025) 105680. <https://doi.org/10.1016/j.surfin.2024.105680>.

[39] Y. Choi, S. Mun, K.B. Lee, Direct synthesis of vertically oriented Co-Mg-Al layered double hydroxide on spherical  $\gamma$ -Al<sub>2</sub>O<sub>3</sub> for passive NO<sub>x</sub> adsorber, *Appl. Surf. Sci.* 687 (2025) 162248. <https://doi.org/10.1016/j.apsusc.2024.162248>.

[40] B. Yasmina, B.C. Eddine, F. Manel, S. Dounia, B. Hamza, O. Ali, B. Riadh, B. Mokhtar, Reconstructed MgAl hydrotalcite, LDH-immobilized Ni(II)Schiff base complex composite for the electrooxidation of methanol, *J. Mol. Struct.* 1320 (2025) 139581. <https://doi.org/10.1016/j.molstruc.2024.139581>.

[41] S. Xu, L. Zhang, Y. Lin, R. Li, F. Zhang, Layered double hydroxides used as flame retardant for engineering plastic acrylonitrile-butadiene-styrene (ABS), *J. Phys. Chem. Solids* 73 (2012) 1514–1517. <https://doi.org/10.1016/j.jpcs.2012.04.011>.

[42] E. Conterosito, W. Van Beek, L. Palin, G. Croce, L. Perioli, D. Viterbo, G. Gatti, M. Milanesio, Development of a fast and clean intercalation method for organic molecules into layered double hydroxides, *Cryst. Growth Des.* 13 (2013) 1162–1169. <https://doi.org/10.1021/cg301505e>.

[43] F. Li, Z. Sun, H. Jiang, Z. Ma, Q. Wang, F. Qu, Ion-Exchange Synthesis of Ternary FeCoNi-Layered Double Hydroxide Nanocage Toward Enhanced Oxygen Evolution Reaction and Supercapacitor, *Energy and Fuels* 34 (2020) 11628–11636. <https://doi.org/10.1021/acs.energyfuels.0c02533>.

[44] C. Vaysse, L. Guerlou-Demourgues, E. Duguet, C. Delmas, Acrylate intercalation and in situ polymerization in iron-, cobalt-, or manganese-substituted nickel hydroxides, *Inorg. Chem.* 42 (2003) 4559–4567. <https://doi.org/10.1021/ic026229s>.

[45] A. Grover, I. Mohiuddin, A.K. Malik, J.S. Aulakh, Adsorption studies of organic dyes on surfactant modified Zn-Al layered double hydroxide, in: 2020. <https://doi.org/10.13140/RG.2.2.10003.71202>.

[46] E. Dvininov, M. Ignat, P. Barvinschi, M.A. Smithers, E. Popovici, New SnO<sub>2</sub>/MgAl-layered double hydroxide composites as photocatalysts for cationic dyes bleaching, *J. Hazard. Mater.* 177 (2010) 150–158. <https://doi.org/10.1016/j.jhazmat.2009.12.011>.

[47] T.T.T. Le Hoang, N. Insin, N. Sukpirom, Catalytic activity of silver nanoparticles anchored on layered double hydroxides and hydroxyapatite, *Inorg. Chem. Commun.* 121 (2020) 108199. <https://doi.org/10.1016/j.inoche.2020.108199>.

[48] C. Li, G. Zhao, T. Zhang, T. Yan, C. Zhang, L. Wang, L. Liu, S. Zhou, F. Jiao, A novel Ag@TiON/CoAl-layered double hydroxide photocatalyst with

enhanced catalytic memory activity for removal of organic pollutants and Cr(VI), *Appl. Surf. Sci.* 504 (2020) 144352. <https://doi.org/10.1016/j.apsusc.2019.144352>.

[49] W. Hu, L. Chen, M. Du, Y. Song, Z. Wu, Q. Zheng, Hierarchical NiCo-layered double hydroxide nanoscroll@PANI nanocomposite for high performance battery-type supercapacitor, *Electrochim. Acta* 338 (2020) 1–9. <https://doi.org/10.1016/j.electacta.2020.135869>.

[50] S. Saghir, Z. Xiao, Hierarchical mesoporous ZIF-67@LDH for efficient adsorption of aqueous Methyl Orange and Alizarine Red S., *Powder Technol.* 377 (2021) 453–463. <https://doi.org/10.1016/j.powtec.2020.09.006>.

[51] S.K. Dash, S. Nayak, S. Das, K. Parida, Smart 2D-2D Nano-Composite Adsorbents of LDH-Carbonaceous Materials for the Removal of Aqueous Toxic Heavy Metal Ions: A Review, *Curr. Environ. Eng.* 5 (2018) 20–34. <https://doi.org/10.2174/2212717805666180111162743>.

[52] G. Sriram, A. Bendre, T. Altalhi, H.Y. Jung, G. Hegde, M. Kurkuri, Surface engineering of silica based materials with Ni–Fe layered double hydroxide for the efficient removal of methyl orange: Isotherms, kinetics, mechanism and high selectivity studies, *Chemosphere* 287 (2022) 131976. <https://doi.org/10.1016/j.chemosphere.2021.131976>.

[53] L. Wu, Z. Hu, G. Chen, Z. Li, A convenient green preparation of layered double hydroxide/polyacrylamide nanocomposite hydrogels with ultrahigh deformability, *Soft Matter* 11 (2015) 9038–9044. <https://doi.org/10.1039/c5sm02232k>.

[54] Q. Yan, X. Hou, G. Liu, Y. Li, T. Zhu, Y. Xin, Q. Wang, Recent advances in layered double hydroxides (LDHs) derived catalysts for selective catalytic reduction of NO<sub>x</sub> with NH<sub>3</sub>, *J. Hazard. Mater.* 400 (2020) 123260. <https://doi.org/10.1016/j.jhazmat.2020.123260>.

[55] K. Takehira, Recent development of layered double hydroxide-derived catalysts – Rehydration, reconstitution, and supporting, aiming at commercial application –, *Appl. Clay Sci.* 136 (2017) 112–141. <https://doi.org/10.1016/j.clay.2016.11.012>.

[56] UN-Water, UN Water, 2021 : Summary Progress Update 2021 - SDG 6 — Water and Sanitation for All, Geneva, 2021. <https://www.unwater.org/news-data-on-global-progress-towards-ensuring-water-and-sanitation-for-all-by-2030/>.

[57] T. Islam, M.R. Repon, T. Islam, Z. Sarwar, M.M. Rahman, Impact of textile dyes on health and ecosystem: a review of structure, causes, and potential solutions, *Environ. Sci. Pollut. Res.* 30 (2023) 9207–9242. <https://doi.org/10.1007/s11356-022-24398-3>.

[58] J. Tiwari, P. Tarale, S. Sivanesan, A. Bafana, Environmental persistence, hazard, and mitigation challenges of nitroaromatic compounds, *Environ. Sci.*

Pollut. Res. 26 (2019) 28650–28667. <https://doi.org/10.1007/s11356-019-06043-8>.

[59] J.O. Tijani, O.O. Fatoba, L.F. Petrik, A Review of Pharmaceuticals and Endocrine-Disrupting Compounds: Sources, Effects, Removal, and Detections, *Water, Air, Soil Pollut.* 224 (2013) 1770. <https://doi.org/10.1007/s11270-013-1770-3>.

[60] B. Pandey, P. Singh, V. Kumar, Photocatalytic-sorption processes for the removal of pollutants from wastewater using polymer metal oxide nanocomposites and associated environmental risks, *Environ. Nanotechnology, Monit. Manag.* 16 (2021) 100596. <https://doi.org/10.1016/j.enmm.2021.100596>.

[61] V.R. Moreira, Y.A.R. Lebron, L.V. de S. Santos, M.C.S. Amaral, Low-cost recycled end-of-life reverse osmosis membranes for water treatment at the point-of-use, *J. Clean. Prod.* 362 (2022). <https://doi.org/10.1016/j.jclepro.2022.132495>.

[62] S. Al-Asheh, M. Bagheri, A. Aidan, Membrane bioreactor for wastewater treatment: A review, *Case Stud. Chem. Environ. Eng.* 4 (2021). <https://doi.org/10.1016/j.cscee.2021.100109>.

[63] Y.N. Kanafin, D. Kanafina, S. Malamis, E. Katsou, V.J. Inglezakis, S.G. Poulopoulos, E. Arkhangelsky, Anaerobic membrane bioreactors for municipal wastewater treatment: A literature review, *Membranes (Basel)*. 11 (2021). <https://doi.org/10.3390/membranes11120967>.

[64] M. Malakootian, Y.D. Shahamat, H. Mahdizadeh, Optimization and modeling of p-nitroaniline removal from aqueous solutions in heterogeneous catalytic ozonation process using mgal-layered double hydroxides (Mgal-ldh cop), *Desalin. Water Treat.* 223 (2021) 114–127. <https://doi.org/10.5004/dwt.2021.27094>.

[65] M. Kimura, Y. Matsui, K. Kondo, T.B. Ishikawa, T. Matsushita, N. Shirasaki, Minimizing residual aluminum concentration in treated water by tailoring properties of polyaluminum coagulants, *Water Res.* 47 (2013) 2075–2084. <https://doi.org/10.1016/j.watres.2013.01.037>.

[66] V. Vaiano, D. Sannino, O. Sacco, The use of nanocatalysts (and nanoparticles) for water and wastewater treatment by means of advanced oxidation processes, Elsevier Inc., 2020. <https://doi.org/10.1016/B978-0-12-819941-1.00009-2>.

[67] S. Das, S.K. Dash, K.M. Parida, Kinetics, Isotherm, and Thermodynamic Study for Ultrafast Adsorption of Azo Dye by an Efficient Sorbent: Ternary Mg/(Al + Fe) Layered Double Hydroxides, *ACS Omega* 3 (2018) 2532–2545. <https://doi.org/10.1021/acsomega.7b01807>.

[68] G. Rathee, A. Awasthi, D. Sood, R. Tomar, V. Tomar, R. Chandra, A new biocompatible ternary Layered Double Hydroxide Adsorbent for ultrafast

removal of anionic organic dyes, *Sci. Rep.* 9 (2019) 1–14. <https://doi.org/10.1038/s41598-019-52849-4>.

[69] H. Bahrami, M. Mejmarian, H. Jafari, F. Rasekh, Synthesis of new Fe/Cr LDH for removal of  $Hg^{2+}$  ion from aqueous solutions and adsorption study using smartphone-based colorimetry, *Environ. Nanotechnology, Monit. Manag.* 18 (2022) 100702. <https://doi.org/10.1016/j.enmm.2022.100702>.

[70] J. Li, L. Yan, Y. Yang, X. Zhang, R. Zhu, H. Yu, Insight into the adsorption mechanisms of aqueous hexavalent chromium by EDTA intercalated layered double hydroxides: XRD, FTIR, XPS, and zeta potential studies, *New J. Chem.* 43 (2019) 15915–15923. <https://doi.org/10.1039/c9nj03479j>.

[71] A. Nait-Merzoug, O. Guellati, S. Djaber, N. Habib, A. Harat, J. El-Haskouri, D. Begin, M. Guerioune, Ni/Zn Layered Double Hydroxide (LDH) Micro/Nanosystems and Their Azorubine Adsorption Performance, *Appl. Sci.* 11 (2021) 8899. <https://doi.org/10.3390/app11198899>.

[72] Z. Jie, J. Yichen, L. Ping, L. Yang, T. Huiyuan, D. Xiuhong, W. Zehua, D. Xianying, L. Chunguang, C. Jiehu, Rational construction and understanding the effect of metal cation substitution of three novel ternary Zn-Co–Ni-LDHs from 2D to 3D and its enhanced adsorption properties for MO, *Environ. Sci. Pollut. Res.* 30 (2023) 3383–3401. <https://doi.org/10.1007/s11356-022-22303-6>.

[73] J. Zhou, W. Shu, Y. Gao, Z. Cao, J. Zhang, H. Hou, J. Zhao, X. Chen, Y. Pan, G. Qian, Enhanced arsenite immobilization via ternary layered double hydroxides and application to paddy soil remediation, *RSC Adv.* 7 (2017) 20320–20326. <https://doi.org/10.1039/c6ra28116h>.

[74] M. Xu, B. Bi, B. Xu, Z. Sun, L. Xu, Polyoxometalate-intercalated ZnAlFe-layered double hydroxides for adsorbing removal and photocatalytic degradation of cationic dye, *Appl. Clay Sci.* 157 (2018) 86–91. <https://doi.org/10.1016/j.clay.2018.02.023>.

[75] G. Rathee, N. Singh, R. Chandra, Simultaneous Elimination of Dyes and Antibiotic with a Hydrothermally Generated NiAlTi Layered Double Hydroxide Adsorbent, *ACS Omega* (2020). <https://doi.org/10.1021/acsomega.9b03785>.

[76] Y. Zhang, K. Huang, Defluoridation behavior of layered Fe-Mg-Zr hydroxides and its continuous purification of groundwater, *Colloids Surfaces A Physicochem. Eng. Asp.* 578 (2019). <https://doi.org/10.1016/j.colsurfa.2019.123640>.

[77] J. Tu, X. Peng, S. Wang, C. Tian, H. Deng, Z. Dang, G. Lu, Z. Shi, Z. Lin, Effective capture of aqueous uranium from saline lake with magnesium-based binary and ternary layered double hydroxides, *Sci. Total Environ.* 677 (2019) 556–563. <https://doi.org/10.1016/j.scitotenv.2019.04.429>.

[78] T.-B. Fang, H. Xiao, L.-X. Zhao, N. Li, L.-Y. Luan, Z.-X. Yan, J.-M. Lin, R.-

S. Zhao, Magnetic ternary layered double hydroxides for efficient removal of 1-naphthalene acetic acid from waters: Adsorption behavior and mechanism, *J. Environ. Chem. Eng.* 11 (2023) 109490.  
<https://doi.org/https://doi.org/10.1016/j.jece.2023.109490>.

[79] J. Miao, X. Zhao, Y.X. Zhang, Z.L. Lei, Z.H. Liu, Preparation of hollow hierarchical porous CoMgAl-borate LDH ball-flower and its calcinated product with extraordinary adsorption capacity for Congo red and methyl orange, *Appl. Clay Sci.* 207 (2021) 106093.  
<https://doi.org/10.1016/j.clay.2021.106093>.

[80] S. Kansal, P. Singh, S. Biswas, A. Chowdhury, D. Mandal, S. Priya, T. Singh, A. Chandra, Superior-catalytic performance of Ni–Co layered double hydroxide nanosheets for the reduction of p-nitrophenol, *Int. J. Hydrogen Energy* 48 (2023) 21372–21382.  
<https://doi.org/10.1016/j.ijhydene.2022.04.213>.

[81] Z. Wei, Y. Li, L. Dou, M. Ahmad, H. Zhang, Cu<sub>3</sub>- xNi<sub>x</sub>Al-Layered Double Hydroxide-Reduced Graphene Oxide Nanosheet Array for the Reduction of 4-Nitrophenol, *ACS Appl. Nano Mater.* 2 (2019) 2383–2396.  
<https://doi.org/10.1021/acsanm.9b00273>.

[82] S.R. Leandro, I.J. Marques, R.S. Torres, T.A. Fernandes, P.D. Vaz, C.D. Nunes, Nitroarene and dye reduction with 2:1 Co/Al layered double hydroxide catalysts – Is gold still necessary?, *Inorganica Chim. Acta* 521 (2021) 120336.  
<https://doi.org/10.1016/j.ica.2021.120336>.

[83] V. Sharma, M. Aman, S. Omar, NiMn-Layered Double Hydroxide Porous Nanoarchitectures as a Bifunctional Material for Accelerated p-Nitrophenol Reduction and Freestanding Supercapacitor Electrodes, *ACS Appl. Nano Mater.* 5 (2022) 15651–15664. <https://doi.org/10.1021/acsanm.2c03719>.

[84] L. Huang, S. Chu, J. Wang, F. Kong, L. Luo, Y. Wang, Z. Zou, Novel visible light driven Mg–Zn–In ternary layered materials for photocatalytic degradation of methylene blue, *Catal. Today* 212 (2013) 81–88.  
<https://doi.org/https://doi.org/10.1016/j.cattod.2012.08.026>.

[85] D. Saliba, S.E. El Jamal, A. Jonderian, M. Ammar, M. Hmadeh, M. Al-Ghoul, Tuning the structural properties of cadmium-Aluminum layered double hydroxide for enhanced photocatalytic dye degradation, *RSC Adv.* 10 (2020) 43066–43074. <https://doi.org/10.1039/d0ra08006c>.

[86] S. Kim, J. Fahel, P. Durand, E. André, C. Carteret, Ternary Layered Double Hydroxides (LDHs) Based on Co-, Cu-Substituted ZnAl for the Design of Efficient Photocatalysts, *Eur. J. Inorg. Chem.* 2017 (2017) 669–678.  
<https://doi.org/10.1002/ejic.201601213>.

[87] J. Zhu, Z. Zhu, H. Zhang, H. Lu, Y. Qiu, Efficient degradation of organic pollutants by peroxyomonosulfate activated with MgCuFe-layered double hydroxide, *RSC Adv.* 9 (2019) 2284–2291.  
<https://doi.org/10.1039/C8RA09841G>.

[88] R.G.L. Gonçalves, H.M. Mendes, S.L. Bastos, L.C. D'Agostino, J. Tronto, S.H. Pulcinelli, C.V. Santilli, J.L. Neto, Fenton-like degradation of methylene blue using Mg/Fe and MnMg/Fe layered double hydroxides as reusable catalysts, *Appl. Clay Sci.* 187 (2020) 105477. <https://doi.org/10.1016/j.clay.2020.105477>.

[89] A. Mantilla, F. Tzompantzi, J.L. Fernández, J.A.I. Díaz Góngora, G. Mendoza, R. Gómez, Photodegradation of 2,4-dichlorophenoxyacetic acid using ZnAlFe layered double hydroxides as photocatalysts, *Catal. Today* 148 (2010) 119–123. <https://doi.org/10.1016/j.cattod.2009.02.036>.

[90] H. Zeng, W. Zhang, L. Deng, J. Luo, S. Zhou, X. Liu, Y. Pei, Z. Shi, J. Crittenden, Degradation of dyes by peroxyomonosulfate activated by ternary CoFeNi-layered double hydroxide: Catalytic performance, mechanism and kinetic modeling, *J. Colloid Interface Sci.* 515 (2018) 92–100. <https://doi.org/10.1016/j.jcis.2018.01.016>.

[91] K. Hosni, O. Abdelkarim, N. Frini-Srasra, E. Srasra, Synthesis, structure and photocatalytic activity of calcined Mg-Al-Ti-layered double hydroxides, *Korean J. Chem. Eng.* 32 (2015) 104–112. <https://doi.org/10.1007/s11814-014-0199-8>.

[92] X. Wang, P. Wu, Z. Huang, N. Zhu, J. Wu, P. Li, Z. Dang, Solar photocatalytic degradation of methylene blue by mixed metal oxide catalysts derived from ZnAlTi layered double hydroxides, *Appl. Clay Sci.* 95 (2014) 95–103. <https://doi.org/10.1016/j.clay.2014.03.016>.

[93] X. Wang, P. Wu, Y. Lu, Z. Huang, N. Zhu, C. Lin, Z. Dang, NiZnAl layered double hydroxides as photocatalyst under solar radiation for photocatalytic degradation of orange G, *Sep. Purif. Technol.* 132 (2014) 195–205. <https://doi.org/10.1016/j.seppur.2014.05.026>.

[94] G. Zhang, L. Hu, R. Zhao, R. Su, Q. Wang, P. Wang, Microwave-assisted synthesis of ZnNiAl-layered double hydroxides with calcination treatment for enhanced PNP photo-degradation under visible-light irradiation, *J. Photochem. Photobiol. A Chem.* 356 (2018) 633–641. <https://doi.org/10.1016/j.jphotochem.2018.02.010>.

[95] D. Pan, S. Ge, J. Zhao, J. Tian, Q. Shao, L. Guo, X. Mai, T. Wu, V. Murugadoss, H. Liu, T. Ding, S. Angaiah, Z. Guo, Synthesis and Characterization of ZnNiIn Layered Double Hydroxides Derived Mixed Metal Oxides with Highly Efficient Photoelectrocatalytic Activities, *Ind. Eng. Chem. Res.* 58 (2019) 836–848. <https://doi.org/10.1021/acs.iecr.8b04829>.

[96] J. Zhu, Z. Zhu, H. Zhang, H. Lu, Y. Qiu, L. Zhu, S. Küppers, Enhanced photocatalytic activity of Ce-doped Zn-Al multi-metal oxide composites derived from layered double hydroxide precursors, *J. Colloid Interface Sci.* 481 (2016) 144–157. <https://doi.org/10.1016/j.jcis.2016.07.051>.

[97] M. Xu, M. Qian, G. Pan, Y. Guo, T. Wu, Photocatalytic Activity of La-Containing Mixed- Metal Oxides Derived from Layered Double Hydroxides

to Degrade Methylene Blue in the Presence of H<sub>2</sub>O<sub>2</sub>, *Clays Clay Miner.* 67 (2019) 253–264. <https://doi.org/10.1007/s42860-019-00023-2>.

[98] P. Gholami, A. Khataee, M. Ritala, Template-free hierarchical trimetallic oxide photocatalyst derived from organically modified ZnCuCo layered double hydroxide, *J. Clean. Prod.* 366 (2022) 132761. <https://doi.org/10.1016/j.jclepro.2022.132761>.

[99] Y. Chen, J. Yan, D. Ouyang, L. Qian, L. Han, M. Chen, Heterogeneously catalyzed persulfate by CuMgFe layered double oxide for the degradation of phenol, *Appl. Catal. A Gen.* 538 (2017) 19–26. <https://doi.org/10.1016/j.apcata.2017.03.020>.

[100] T.S. Kazeem, M. Zubair, M. Daud, N.D. Mu’azu, M.A. Al-Harthi, Graphene/ternary layered double hydroxide composites: Efficient removal of anionic dye from aqueous phase, *Korean J. Chem. Eng.* 36 (2019) 1057–1068. <https://doi.org/10.1007/s11814-019-0284-0>.

[101] X.J. Cao, H.Y. Zeng, X. Cao, S. Xu, G.B.F.C. Alain, K.M. Zou, L. Liu, 3D-hierarchical mesoporous CuCo<sub>2</sub>S<sub>4</sub>@NiCoAl hydroxide/Ni foam material for high-performance supercapacitors, *Appl. Clay Sci.* 199 (2020) 105864. <https://doi.org/10.1016/j.clay.2020.105864>.

[102] L. Liu, X. Hu, H.Y. Zeng, M.Y. Yi, S.G. Shen, S. Xu, X. Cao, J.Z. Du, Preparation of NiCoFe-hydroxide/polyaniline composite for enhanced-performance supercapacitors, *J. Mater. Sci. Technol.* 35 (2019) 1691–1699. <https://doi.org/10.1016/j.jmst.2019.04.003>.

[103] Y. Zou, P. Wang, W. Yao, X. Wang, Y. Liu, D. Yang, L. Wang, J. Hou, A. Alsaedi, T. Hayat, X. Wang, Synergistic immobilization of UO<sub>2</sub><sup>2+</sup> by novel graphitic carbon nitride @ layered double hydroxide nanocomposites from wastewater, *Chem. Eng. J.* 330 (2017) 573–584. <https://doi.org/10.1016/j.cej.2017.07.135>.

[104] J. Xu, Y. Zhao, M. Li, G. Fan, L. Yang, F. Li, A strong coupled 2D metal-organic framework and ternary layered double hydroxide hierarchical nanocomposite as an excellent electrocatalyst for the oxygen evolution reaction, *Electrochim. Acta* 307 (2019) 275–284. <https://doi.org/10.1016/j.electacta.2019.03.210>.

[105] S. Khataee, G. Dehghan, Z. Shaghaghi, A. Khataee, An enzyme-free sensor based on La-doped CoFe-layered double hydroxide decorated on reduced graphene oxide for sensitive electrochemical detection of urea, *Microchim. Acta* 191 (2024). <https://doi.org/10.1007/s00604-024-06221-7>.

[106] J. Wang, Z. Wang, N. Liu, C. Liu, J. Yan, C.C. Li, J. Cui, J. Liu, X. Hu, Y. Wu, Al doped Ni-Co layered double hydroxides with surface-sulphuration for highly stable flexible supercapacitors, *J. Colloid Interface Sci.* 615 (2022) 173–183. <https://doi.org/10.1016/j.jcis.2022.01.172>.

[107] X. Shen, Z. Zhu, H. Zhang, G. Di, T. Chen, Y. Qiu, D. Yin, Carbonaceous

composite materials from calcination of azo dye-adsorbed layered double hydroxide with enhanced photocatalytic efficiency for removal of Ibuprofen in water, *Environ. Sci. Eur.* 32 (2020). <https://doi.org/10.1186/s12302-020-00351-4>.

[108] L. Ju, P. Wu, X. Lai, S. Yang, B. Gong, M. Chen, N. Zhu, Synthesis and characterization of Fullerene modified ZnAlTi-LDO in photo-degradation of Bisphenol A under simulated visible light irradiation, *Environ. Pollut.* 228 (2017) 234–244. <https://doi.org/10.1016/j.envpol.2017.05.038>.

[109] C. Madhusha, I. Munaweera, V. Karunaratne, N. Kotegoda, Synergistic adsorption-photocatalytic degradation of different antibiotics in seawater by a porous g-C<sub>3</sub>N<sub>4</sub> / calcined-LDH and its application in synthetic mariculture wastewater, *J. Agric. Food Chem.* 68 (2020) 8962–8975. <https://doi.org/10.1016/j.jhazmat.2021.126183>.

[110] P.J. Wang, X.P. Hu, D.J. Liao, Y. Wen, T.R. Hull, F. Miao, Q.T. Zhang, Dual fire retardant action: The combined gas and condensed phase effects of azo-modified NiZnAl layered double hydroxide on intumescence polypropylene, *Ind. Eng. Chem. Res.* 56 (2017) 920–932. <https://doi.org/10.1021/acs.iecr.6b03953>.

[111] D.S. Patil, S.A. Pawar, H.J. Kim, J.C. Shin, Hierarchical manganese-iron-layered double hydroxide nanosheets for asymmetric supercapacitors, *Energies* 13 (2020). <https://doi.org/10.3390/en13184616>.

[112] A.A. Wani, A.M. Khan, Y.K. Manea, M.A.S. Salem, M. Shahadat, Selective adsorption and ultrafast fluorescent detection of Cr(VI) in wastewater using neodymium doped polyaniline supported layered double hydroxide nanocomposite, *J. Hazard. Mater.* 416 (2021) 125754. <https://doi.org/10.1016/j.jhazmat.2021.125754>.

[113] J. Li, Y. Xu, Z. Ding, A.H. Mahadi, Y. Zhao, Y.F. Song, Photocatalytic selective oxidation of benzene to phenol in water over layered double hydroxide: A thermodynamic and kinetic perspective, *Chem. Eng. J.* 388 (2020) 124248. <https://doi.org/10.1016/j.cej.2020.124248>.

[114] S. Dutta, T.K. Jana, S.K. Halder, R. Maiti, A. Dutta, A. Kumar, K. Chatterjee, Zn<sub>2</sub>Al-CO<sub>3</sub> Layered Double Hydroxide: Adsorption, Cytotoxicity and Antibacterial Performances, *ChemistrySelect* 5 (2020) 6162–6171. <https://doi.org/10.1002/slct.202001264>.

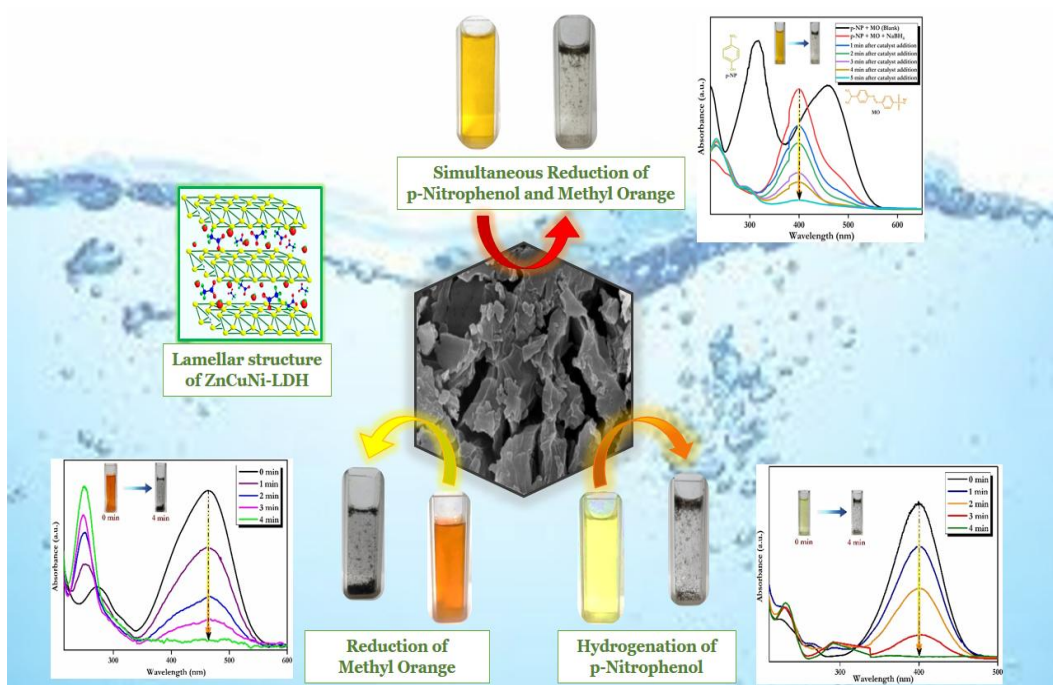
[115] Y. Yang, W. Zhu, D. Cui, C. Lü, Mussel-inspired preparation of temperature-responsive polymer brushes modified layered double hydroxides@Pd/carbon dots hybrid for catalytic applications, *Appl. Clay Sci.* 200 (2021) 105958. <https://doi.org/10.1016/j.clay.2020.105958>.

[116] X.Z. Li, S.R. Liu, Y. Guo, Polyaniline-intercalated layered double hydroxides: Synthesis and properties for humidity sensing, *RSC Adv.* 6 (2016) 63099–63106. <https://doi.org/10.1039/c6ra10093g>.

- [117] V. Bugatti, L. Vertuccio, S. Zara, F. Fancello, B. Scanu, G. Gorrasi, Green pesticides based on cinnamate anion incorporated in layered double hydroxides and dispersed in pectin matrix, *Carbohydr. Polym.* 209 (2019) 356–362. <https://doi.org/10.1016/j.carbpol.2019.01.033>.
- [118] B. Gayani, A. Dilhari, G.K. Wijesinghe, S. Kumarage, G. Abayaweera, S.R. Samarakoon, I.C. Perera, N. Kottekoda, M.M. Weerasekera, Effect of natural curcuminoids-intercalated layered double hydroxide nanohybrid against *Staphylococcus aureus*, *Pseudomonas aeruginosa*, and *Enterococcus faecalis*: A bactericidal, antibiofilm, and mechanistic study, *Microbiologyopen* 8 (2019) 1–12. <https://doi.org/10.1002/mbo3.723>.

**CHAPTER - 2**

**SYNTHESIS, CHARACTERIZATION AND CATALYTIC APPLICATIONS OF NOVEL *ZnCuNi*- TERNARY LAYERED DOUBLE HYDROXIDE FOR ORGANIC POLLUTANT REDUCTION**



## **CHAPTER - 2**

# **SYNTHESIS, CHARACTERIZATION AND CATALYTIC APPLICATIONS OF NOVEL ZnCuNi- TERNARY LAYERED DOUBLE HYDROXIDE FOR ORGANIC POLLUTANT REDUCTION**

---

### **2.1 Introduction**

Layered double hydroxides (LDHs) are a class of new-age two-dimensional anionic clays that are becoming increasingly popular due to the recent boom in research interest towards functional nanomaterials. They bear close resemblance to hydrotalcite in terms of structure, possessing a layered arrangement, with water molecules and anions sandwiched in between the layers. The layers have an unconventional layout similar to that observed in brucite with divalent cations octahedrally coordinated with six hydroxyl moieties. The isomorphic substitution of some proportion of divalent cations with trivalent cations creates a charge deficit on the layers, rendering them positively charged and leading to the entrapment of anionic moieties within the interlayer region along with water molecules that hold the layers together via hydrogen bonding[1].

By virtue of these structural characteristics, LDHs are endowed with excellent physicochemical features such as high specific surface area, abundance of active sites, chemical and thermal stability, biocompatibility, and low toxicity[2]. Moreover, the versatility of these materials arises from the modulation potential of the internal architecture (geometric structure, particle size, morphology, surface defects), intralayer cation replacement, and exchangeability of the interlayer mobile anions. The anion exchange property can be used to incorporate inorganic/organic non-framework molecules of various sizes in the interlayer region to achieve enlarged basal spacing, and convert hydrophilic LDH lattice to hydrophobic for enhanced surface properties[3]. The metal hydroxide layers possess colloidal stability and can also be exfoliated easily on dispersion in a suitable medium, further enhancing their utility.

Along with these properties, LDHs also possess the rare “Memory Effect” property, courtesy of which they are able to regain their original structure on being exposed to anions and water molecules after calcination in the temperature range of 350 °C to 550 °C. Therefore, the unique combination of intriguing structural features with prospects of topological transformation have rendered LDHs as highly advantageous materials.

For the past few decades, commercially important LDHs were generally a combination of Ca, Mg, Al cations but recent studies have explored the use of transition metals (TMs) such as Cu, Ni, Co, Fe, etc in order to exploit their unique electronic, magnetic and optical properties while also profitably utilizing the layered structure of LDH. TMs can attain variable oxidation states due to which they can participate in redox reactions and facilitate electron transfer to other molecules. Furthermore, TMs possess partially filled d-orbitals that can overlap with the orbitals of other molecular species and enables them to have strong interactions, thereby stabilizing intermediates and lowering activation energies for reactions that occur on the LDH surface[4]. Additionally, the incorporation of transition metals in LDH lattice alters the electron clouds near the active sites, thereby enhancing the ability of LDH to bind to the molecules, due to which they can be combined with several anionic, cationic, and neutral ligands to obtain various types of homogenous and heterogeneous catalysts. TM incorporation can also create lattice defects and distortions that can serve as high-energy adsorption sites for the target molecules. Moreover, TMs can alter the morphological features of the particles, that provides more exposure to the active sites and enhances the affinity of LDHs to hold and transform other molecules. Thus, their special electronic structures, high surfaces area and large number of active sites result in surface adsorption and activation abilities of the LDH lattice. Taking advantage of these features, binary LDHs, that are the combination of two metal cations, have been extensively studied in literature[5–7]. For instance, Kansal et al. studied the reported the synthesis of NiCo-LDH nanosheets and applied them as catalysts for the hydrogenation of 4-nitrophenol[8]. In particular, binary LDHs based on zinc are quite popular among researchers due to their well-defined morphologies, excellent chemical stability, and widely reported adsorptive and catalytic behaviour as well as the biocompatible nature and low toxicity of Zn element. LDH lattices combining divalent

$Zn^{2+}$  with both transition metal and rare earth trivalent cations such as  $Al^{3+}$ ,  $Ni^{3+}$ ,  $Cr^{3+}$ ,  $La^{3+}$ ,  $Eu^{3+}$ , etc have been widely described in literature due to their incredible electrochemical performance and versatility in applications[9–11]. Pandey et al. utilized a novel  $ZnCu$ -LDH for the adsorptive removal of anionic Congo Red (CR), Erichrome Black T (EBT), and Methyl Orange (MO) dyes, and statistically optimized the process to attain the maximum adsorptive performance of the lattice[12]. In another example, Wang et al. incorporated two rare earth metal cations – La and Ce in a  $Zn$ -based LDH lattice, and carried out F-doping of the same. They evaluated the effect of rare earth metal cation incorporation and F-doping on the  $CO_2$  electrocatalytic performance of the LDH lattice[13]. But due to the availability of only two metals, the possibilities of metal combinations in binary LDHs remains limited, thereby hindering their capabilities and use in modern technology[14]. In order to enhance the properties of LDHs, one of the most preferred methodologies is the introduction of third transition metal in the lattice. The augmentation of unique geometrical and synergistic interactions in LDHs with the incorporation of another transition metals results in improved properties. Furthermore, the availability of increased number of active sites having diverse nature due to the three cations is useful in increasing the scope of applications of ternary LDHs to a much broader range. As a result, transition metal based-ternary LDHs have emerged as ground-breaking materials that find application in various fields such as water treatment, energy storage, catalysis, biomedics and composite synthesis. Nivangune et al. reported the synthesis of  $MgFeCe$ -LDH sing the combination of coprecipitation and hydrothermal method. The synthesized product was utilized as a heterogeneous catalyst for the transesterification of ethylene carbonate with methanol to form dimethyl carbonate selectively[15]. A ternary LDH consisting of Mg, Al and Fe was synthesized by Das et al. that was further utilized for the adsorption of Malachite Green (MG) dye. The adsorbent exhibited ultrafast adsorption of the dye under various conditions, making it an efficient material for adsorption applications[16].

Specifically, the inherent merits of ternary LDHs make them promising candidates for use as catalytic materials that can be utilized to tackle the widespread problem of water pollution, that is an issue requiring immediate attention[17]. Water contamination caused by growing industrialization and agriculture is causing an alarming decline in

the amount of readily available clean and safe water. As mentioned in a recent UN report published in 2021, billions of people are facing the problem of potable water scarcity[18]. To meet the needs of growing population, there has been an explosive increase in the unimpeded discharge of toxin-laden water in water bodies that leads to the release of recalcitrant pollutants such as organic azo dyes, heavy metals, nitroarene compounds (NACs), volatile organic compounds (VOCs), etc, ultimately leading to the deterioration of water quality due to their toxic nature. Specifically, NACs such as *p*-NP and *p*-NA, and azo dyes including methyl orange, amaranth and brilliant are some of the most prevalent and vicious pollutants that possess severe carcinogenic and mutagenic properties. NACs such as *p*-NP and *p*-NA pose tremendous risk to human health and aquatic life even at trace levels due to their high toxicity and high stability. On the other hand, Methyl orange, having the molecular formula  $C_{14}H_{14}N_3NaO_3S$  is an anionic azo dye commonly used as a pH indicator in laboratories as well as widely used in various industries, including textile, pulp and paper, and printing, among others. In azo dyes such as MO, the appearance of color is due to the existence of main azo (-N=N-) chromophore group. But MO is classified as an acutely toxic compound and has been reported to be mutagenic. Excessive exposure to MO may even cause skin and eye irritation, dermal corrosion, respiratory and gastrointestinal irritation, as well as nausea, vomiting, and diarrhea. Hence, the removal of MO from water sources has received major interest. Similarly, Amaranth, or Acid Red 27, is an anionic mono azo dye having molecular formula  $C_{20}H_{11}N_2Na_3O_{10}S_3$ . This reddish-brown dye is widely used as a colorant in the food and cosmetics industry. But its use has now been prohibited in several countries due to suspected carcinogenicity. In vivo combination of Amaranth with benzoate and salicylate, etc can cause several severe health issues, such as impaired liver functioning. Hence, the elimination of Amaranth from water sources needs to be seriously addressed. Additionally, Brilliant Black BN, having molecular formula  $C_{28}H_{17}N_6Na_4O_{14}S_4$  is a black-colored azo dye that finds prevalent use in the food industry. This dye is suspected to be genotoxic, mutagenic, and has been linked to worsening of asthma and DNA damage.

Therefore, the removal of such anthropogenic pollutants is imperative to maintain sufficient levels of potable water. Among these pollutants, nitroarene compounds (NACs) and azo dyes pose incredibly high risks to flora and fauna due to their

carcinogenic and mutagenic characteristics, as well as their bioaccumulative tendencies and high stabilities (Figure 2.1)[19,20]. Therefore, the development of new-age, low-cost, and effective hybrid water remediation technologies is of utmost importance to fulfill global water needs.



**Figure 2.1** Detrimental impacts of water pollution on aquatic, human, and plant health.

In this regard, the use of catalytic processes for pollutant elimination has gained prominence in present times due to their versatility, low cost, and high efficiency[21]. Specifically, NaBH<sub>4</sub>-assisted degradation of pollutants is a potent and eco-friendly strategy to achieve the decomposition of organic azo dyes and nitroarene molecules. This method is highly beneficial and the easy detectability of these degradation products using simple and easily available techniques such as absorption spectroscopy further lends highly profitable characteristics to this technique.

However, a major drawback associated with the reduction reaction facilitated by NaBH<sub>4</sub> is its kinetically unfeasibility that can be addressed by using NaBH<sub>4</sub> in the presence of a co-catalyst. Previously various classes of catalytic materials such as carbonaceous materials (eg. activated carbon, graphene oxide), metal-organic frameworks (MOFs), metal & metal hydroxide and oxide nanoparticles (eg. Ag, Au, ZnO, CuO, etc.) polymeric materials, and composites etc. as co-catalysts have been widely used for the hydrogenation of NACs and degradation of dye molecules[22–24]. For instance, Ahmad et al. synthesized a composite consisting of iron oxide functionalised with Cu nanoparticles and applied it for NaBH<sub>4</sub>-assisted reduction of several organic pollutants[25]. Shahzaib et al. reported the synthesis of Fe<sub>3</sub>O<sub>4</sub>/ZIF-67@ZnO composite using a green synthesis method and employed it for the catalytic

reduction of rhodamine B and methylene blue dyes[26]. But drawbacks such as agglomeration tendency, complex and expensive synthesis methods, and low catalytic efficiency reduce the utility of these conventional materials in catalytic applications. Further, efficient catalytic materials should possess attributes such as high specific surface area and large number of active sites.

Keeping this in purview, transition metal-based LDHs are emerging contenders for use in catalytic transformations since they satisfy all the criteria required for these applications and also bring along the added advantages of layered structure and anion exchange abilities. In the recent past, a few groups have ventured into the use of transition metal based- ternary LDHs as co-catalysts for the  $\text{NaBH}_4$ -assisted reduction of NACs and azo dyes, but still the number of available studies remain limited since it is especially difficult to govern the oxidation states of transition metal ions. Additionally, the studies based on LDHs that do investigate the catalytic reduction process generally describe the functionalization of LDH with noble metal nanoparticles such as palladium, gold etc. This process is often complex and requires precise control over the precursors and the reaction condition, and utilizes toxic chemicals for their synthesis. Hence, the synthesis of novel transition metal-based ternary LDHs that can act as efficient catalysts using a simple fabrication method is still quite challenging and needs to be explored.

Therefore, this study aims to obtain a novel ternary  $\text{ZnCuNi-LDH}$  using a facile acid hydrolysis method and characterize the synthesized lattice using a variety of techniques. The feasibility of using synthesized  $\text{ZnCuNi-LDH}$  as a catalyst for the reduction of various toxic organic pollutants was studied, and the hydrogenation of 2 NACs (*p*-Nitrophenol (*p*-NP) and *p*-Nitroaniline (*p*-NA)), and reductive degradation of different azo dyes (Amaranth, Brilliant Black, and Methyl Orange) were systematically investigated. To achieve this objective, the impact of influencing parameters, including catalyst dosage and pollutant concentration, was studied while the universality and the recyclability of  $\text{ZnCuNi-LDH}$  in the catalysis process were also assessed. The results revealed that the NACs and organic azo dyes underwent rapid and efficacious reduction when  $\text{NaBH}_4$  was employed as a reductant and  $\text{ZnCuNi-LDH}$  was used as the catalyst, warranting the use of  $\text{ZnCuNi-LDH}$  in future wastewater remediation applications.

## 2.2 Materials and Methods

### 2.2.1 Materials

Zinc acetate dihydrate  $\text{Zn}(\text{CH}_3\text{COO})_2 \cdot 2\text{H}_2\text{O}$  (Merck, 98.0% purity), copper acetate monohydrate  $\text{Cu}(\text{CH}_3\text{COO})_2 \cdot \text{H}_2\text{O}$  (Merck, 98.0% purity), hydrogen peroxide  $\text{H}_2\text{O}_2$  (Merck, 30%), acetic acid glacial 100%  $\text{CH}_3\text{COOH}$  (Merck), and nickel acetate tetrahydrate  $\text{Ni}(\text{CH}_3\text{COO})_2 \cdot 4\text{H}_2\text{O}$  (CDH, 98.00% purity),  $\text{NaBH}_4$  (Sigma Aldrich,  $\geq 98.00\%$ ), *p*-Nitrophenol (GLR chemicals, 98.00%), *p*-Nitroaniline (GLR chemicals, 99.00%), Amaranth (CDH Chemicals), Brilliant Black (CDH Chemicals), and Methyl Orange (Merck) were of analytical grade unless otherwise stated, and were used as received without purification. Table 2.1 gives information about the structure, formulas, and  $\lambda_{max}$  of model pollutant molecules employed in this study.

**Table 2.1** Structure and formula of model pollutants employed in the study.

Model Pollutant	Structure	$\lambda_{max}$ (nm)	Molecular Formula
<i>p</i> -Nitrophenol		400	$\text{C}_6\text{H}_5\text{NO}_3$
<i>p</i> -Nitroaniline		380	$\text{C}_6\text{H}_6\text{N}_2\text{O}_2$
Amaranth		520	$\text{C}_{20}\text{H}_{11}\text{N}_2\text{Na}_3\text{O}_{10}$ S <sub>3</sub>
Brilliant Black		490	$\text{C}_{28}\text{H}_{17}\text{N}_6\text{Na}_4\text{O}_{14}$ S <sub>4</sub>
Methyl Orange		463	$\text{C}_{14}\text{H}_{14}\text{N}_3\text{NaO}_3\text{S}$

### 2.2.2 Instrumentation

Crystallographic properties of the sample were studied by the use of Powder X-ray diffraction (PXRD) diffractograms collected using a high-resolution Bruker diffractometer (D8 Discover) using Cu K $\alpha$  radiation. Data was recorded at 298 K over the range of  $2\theta = 5\text{--}70^\circ$  at scan rate of 1.0 s/step and step size 0.02. The various functional group present in synthesized material were analyzed using Fourier transform infrared (FTIR) spectrum collected with the help of a Perkin Elmer 2000 Fourier-transform infrared spectrometer by the KBr disk technique. Thermal degradation behaviour was evaluated by Thermo gravimetric analysis (TGA) data that was recorded using the Pyris 1® Thermo gravimetric Analyzer in the range 50–900°C at heating rate of 5°C min $^{-1}$  under flowing nitrogen. SEM imaging and EDX analysis of the synthesized samples was done using a Zeiss Gemini SEM microscope. The specific surface area ( $S_{BET}$ ) and average pore size distribution were obtained by BET-BJH (Barrett-Joyner-Halenda) N<sub>2</sub> adsorption-desorption technique on a Quanta chrome Nova-1000 instrument at liquid nitrogen temperature 77k.

### 2.2.3 Synthesis of ZnCuNi-LDH

The synthesis of ZnCuNi-LDH with different Zn/Cu/Ni molar ratios was carried out using a facile acid hydrolysis method that first entails the preparation of aqueous solutions of zinc acetate dihydrate, copper acetate monohydrate and nickel acetate tetrahydrate in 10 mL distilled water separately. Following this, solutions of copper acetate monohydrate and nickel acetate tetrahydrate were combined with zinc acetate dihydrate solution with constant stirring until complete homogeneity was achieved. The acid hydrolysis process was initiated by adding 5 mL of 30% H<sub>2</sub>O<sub>2</sub> solution along with 30 mL distilled water to the reaction solution. A shift in the solution color from greenish-blue to brown indicated the formation of ZnCuNi-LDH. Subsequently, the reaction mixture was subjected to ultrasonication for 30 minutes to prevent aggregate formation and to attain uniformly-sized LDH particles. The reaction mixture was then stirred continuously for one day at room temperature and finally, the solution was placed in oven at 60°C for complete drying to obtain LDH precursors. The synthesis procedure of the samples is schematically represented in Figure 2.2. and the compositions of various combinations of synthesized LDHs are presented in Table 2.2.



**Figure 2.2** Synthesis of ternary ZnCuNi-LDH via acid hydrolysis method.

**Table 2.2** Molar ratios of constituents in various compositions of ZnCuNi-LDH.

Combination	Zn (mmol)	Cu (mmol)	Ni (mmol)
1	5.00	0.25	0.25
2	4.25	0.375	0.375

## 2.2.4 Evaluation of Catalytic Activity

### 2.2.4.1 Catalytic Hydrogenation of NACs

Solutions of NaBH<sub>4</sub> (50 mM) and NACs (10 mM) were prepared using distilled water, and further solutions were prepared by diluting the stock solutions. The hydrogenation reactions of *p*-NP and *p*-NA using NaBH<sub>4</sub> were studied in order to probe the catalytic efficacy of ZnCuNi-LDH. The reaction progress was monitored both visually and spectrophotometrically by observing old absorption bands at  $\lambda_{max} = 400$  nm for *p*-NP and 380 nm for *p*-NA, and new absorption bands of the byproducts formed in the time-dependent UV spectrum.

#### 2.2.4.1.1 *p*-Nitrophenol

NaBH<sub>4</sub>-assisted hydrogenation of *p*-nitrophenol (*p*-NP) using ZnCuNi-LDH was accomplished using the reducing agent NaBH<sub>4</sub> in presence of ZnCuNi-LDH as the catalyst. Initiation of the reaction was done by adding freshly prepared NaBH<sub>4</sub> solution (50 mM, 10 mL) and distilled water (10 mL) to aqueous solution of *p*-NP (1 mM, 10 mL) and the reaction mixture was stirred well to ensure homogeneity. This was followed by the addition of ZnCuNi-LDH catalyst (5 mg) to reaction mixture at room temperature and recording the absorbance at fixed time intervals using Shimadzu UV-

Vis spectrophotometer. The kinetics of the reaction were assessed by determining the change in absorbance of reaction mixture at  $\lambda_{max} = 400$  nm at a time interval of one minute till the peak completely disappeared and solution became colourless.

#### 2.2.4.1.2 *p*-Nitroaniline

Similarly, the reduction experiment for *p*-nitroaniline (*p*-NA) was carried out by first stirring *p*-NA aqueous solution (1mM, 10 mL) with freshly prepared NaBH<sub>4</sub> solution (50mM, 10 mL) and distilled water (10 mL), and then followed by addition of ZnCuNi-LDH (5 mg) at room temperature. The progression of catalytic reduction was evaluated by measuring the absorbance of reduction mixture at  $\lambda_{max} = 380$  nm at 1-minute intervals till the solution was completely decolourised.

#### 2.2.4.2 Catalytic Degradation of Azo Dyes

To evaluate the decolourisation ability of LDHs towards azo dyes, catalytic reduction was carried out using Ama, BB and MO as model molecules. First, 100 mg L<sup>-1</sup> stock solutions of Ama, BB, and MO dyes, and 50 mM stock solution of NaBH<sub>4</sub> were prepared.

##### 2.2.4.2.1 Methyl Orange

For the catalytic degradation of MO dye, MO solution (100 mg L<sup>-1</sup>, 10 mL) was stirred with freshly prepared NaBH<sub>4</sub> solution (50 mM, 10 mL) and distilled water (10 mL) to ensure complete mixing. Following this, ZnCuNi-LDH catalyst (5 mg) was added to the reaction mixture. The reduction progress was assessed by measurement of the absorbance at  $\lambda_{max} = 463$  nm for MO at one-minute intervals till peak disappeared and solution was completely decolourised.

##### 2.2.4.2.2 Amaranth

The catalytic reduction of Amaranth dye was studied in a similar manner as MO, wherein Ama dye solution (100 mg L<sup>-1</sup>, 10 mL) was mixed with freshly prepared NaBH<sub>4</sub> solution (50 mM, 10 mL) and distilled water (10 mL) till homogenous solution was obtained. Subsequently, ZnCuNi-LDH catalyst (5 mg) was introduced into the reaction mixture, and the reduction progress was assessed by observing the time-dependent UV absorbance spectrum at  $\lambda_{max} = 520$  nm at one-minute intervals till the reaction mixture became colourless and the absorption peak disappeared completely.

### 2.2.4.2.3 Brilliant Black

The catalytic reduction of Brilliant Black dye was also studied in a similar manner, and it involved the mixing of BB dye solution ( $100 \text{ mg L}^{-1}$ , 10 mL) with freshly prepared  $\text{NaBH}_4$  solution (50 mM, 10 mL) and distilled water (10 mL) till uniformity of colour was achieved in the solution. Then,  $\text{ZnCuNi-LDH}$  catalyst (5 mg) was added to the reaction mixture and the reaction progress was examined from the time-dependent UV-Vis absorption spectra at  $\lambda_{max} = 490 \text{ nm}$ . The changes in absorption spectrum were noted at one-minute intervals till the dye was completely decolourised and the peak at 490 nm was not visible anymore.

The percentage degradation of chosen toxic moieties was calculated using Equation 2.1:

$$\text{Percentage degradation} = \frac{(C_o - C_f)}{C_o} \times 100 \quad (2.1)$$

where  $C_o$  and  $C_f$  denote the initial and terminal concentrations of NAC and azo dyes.

### 2.2.4.3 Effect of Influencing Parameters

The influence of various parameters such as catalyst dosage, and pollutant concentration on the catalytic activity of  $\text{ZnCuNi-LDH}$  were also assessed.

#### 2.2.4.3.1 Effect of Catalyst Dosage

The impact of dose of catalyst on the *p*-NP and MO degradation was investigated using three different amounts. Briefly, pollutant solution (*p*-NP = 50 mM, 10 mL; MO = 100  $\text{mg L}^{-1}$ , 10 mL) was stirred with freshly prepared  $\text{NaBH}_4$  solution (50 mM, 10 mL) and distilled water (10 mL) to ensure complete mixing. At later stage, various dosages of  $\text{ZnCuNi-LDH}$  catalyst (2.5 mg, 5 mg and 10 mg) were added to the reaction mixture one by one to study the effect of dosage on the catalytic activity of  $\text{ZnCuNi-LDH}$ . The progress of reaction was assessed by measurement of the absorbance at  $\lambda_{max} = 400 \text{ nm}$  for *p*-NP and 463 nm for MO at one-minute intervals till peak disappeared and solutions were completely decolourised.

#### 2.2.4.3.2 Effect of Pollutant Concentration

The impact of pollutant concentration on the degradation of *p*-NP and MO was investigated using 3 different concentrations. The concentrations chosen for the investigation were as follows: i.e. 0.25 mM, 0.50 mM and 1.00 mM for *p*-NP, and 25 ppm, 50 ppm and 100 ppm for MO. For the catalytic reaction, solutions of various

concentrations of the pollutants *p*-NP and MO were stirred one by one with freshly prepared NaBH<sub>4</sub> solution (50 mM, 10 mL) and distilled water (10 mL) till they were well-mixed. Afterwards, ZnCuNi-LDH catalyst (5 mg) was added to the reaction mixture to study the effect of pollutant concentration on the catalytic efficiency of ZnCuNi-LDH on pollutant solutions of various concentrations. The progress of the reduction reactions was assessed by measurement of the time dependent UV-Vis absorption spectrum at  $\lambda_{max} = 400$  nm for *p*-NP and 463 nm for MO at one-minute intervals till absorption peak disappeared and solutions became completely colourless.

#### 2.2.4.4 Universality of Catalyst

The universality of ZnCuNi-LDH as a catalyst for the simultaneous degradation of *p*-NP and MO was assessed. For this study, 5 mL of *p*-NP solution (1 mM) was combined with 5 mL MO solution (100 mg L<sup>-1</sup>), following which 10 mL freshly prepared NaBH<sub>4</sub> solution and 10 mL distilled water were mixed into pollutant solution mixture. After the addition of ZnCuNi-LDH catalyst, the reaction mixture was stirred and the absorbance was recorded at stipulated time intervals.

#### 2.2.4.5 Reusability and Recyclability

The reusability of ZnCuNi-LDH for reduction of *p*-NP, MO, and mixture of dyes was investigated for five cycles. After each reduction reaction, catalyst was recovered and washed with distilled water, dried at 60°C, and then used for subsequent catalytic cycles.

### 2.3 Results and Discussion

#### 2.3.1 Characterisation Results

The PXRD pattern of LDHs typically consists of a high-intensity reflection at lower  $2\theta$  value and low-intensity reflections at higher  $2\theta$  values, and this pattern is specific to anionic clays. The PXRD diffractograms of LDHs synthesized using different Zn/Cu/Ni molar ratios, shown in Figure 2.3, presented similar patterns. It is important to note that the synthesized samples exhibited the characteristic pattern of LDH, with the appearance of a single, sharp, and intense reflection around  $2\theta = 11^\circ$ , thereby suggesting the successful formation of well-defined LDH phase in both combinations. In order to exploit the complete benefits of the LDH lattice, ZnCuNi-LDH having

higher substitution of Cu and Ni (combination 2) was selected and utilized for further studies.

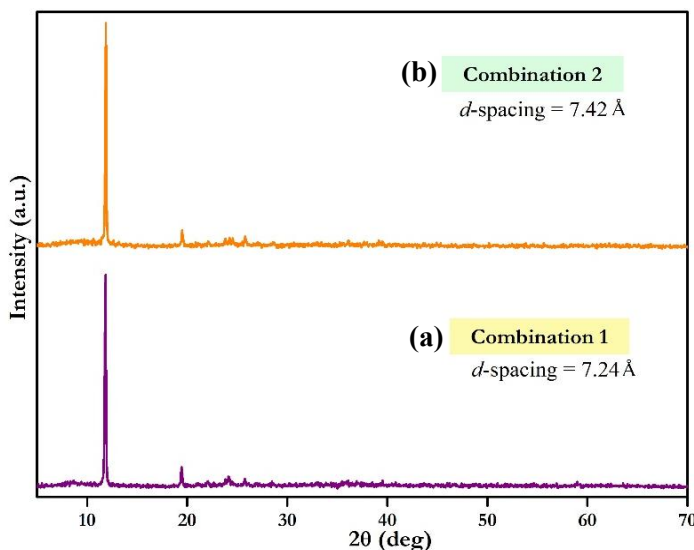


**Figure 2.3** PXRD patterns of LDHs formed using various Zn/Cu/Ni molar ratios (a) 5:0.25:0.25 mmoles and (b) 4.25:0.375:0.375 mmoles.

The PXRD diffractogram of ZnCuNi-LDH, presented in Figure 2.4, showed the characteristic diffraction peaks of crystalline layered materials, consisting of high-intensity reflections at lower  $2\theta$  and low-intensity reflections at higher  $2\theta$  angles. The high-intensity reflection was indexed to the (002) crystal plane and diffraction peaks were indexed under hexagonal symmetry with lattice parameters being  $a = 3.19 \text{ \AA}$  and  $c = 14.9 \text{ \AA}$ [27]. The sharp and symmetric nature of peaks suggested the formation of highly crystalline LDH with coherently stacked 2D layers. The  $d$ -spacing for the (002) basal plane, found to be  $7.42 \text{ \AA}$ , and the gallery height, calculated to be  $2.62 \text{ \AA}$ , were indicative of the monolayer alignment of acetate anions in the interlamellar region, keeping in view the thickness of brucite sheet ( $4.8 \text{ \AA}$ ) and edge to edge length of acetate anion ( $3.6 \text{ \AA}$ )[28]. Furthermore,  $d$ -spacing value of synthesized ZnCuNi-LDH was found to be completely different from those of zinc hydroxy acetate, copper hydroxy acetate, or nickel hydroxy acetate, thereby confirming the formation of lattice in pure phase with isomorphically substituted Cu and Ni cations in the LDH layers[29–31]. Furthermore, it was concluded that the acid hydrolysis method is a simple yet effective method for the synthesis of LDHs.

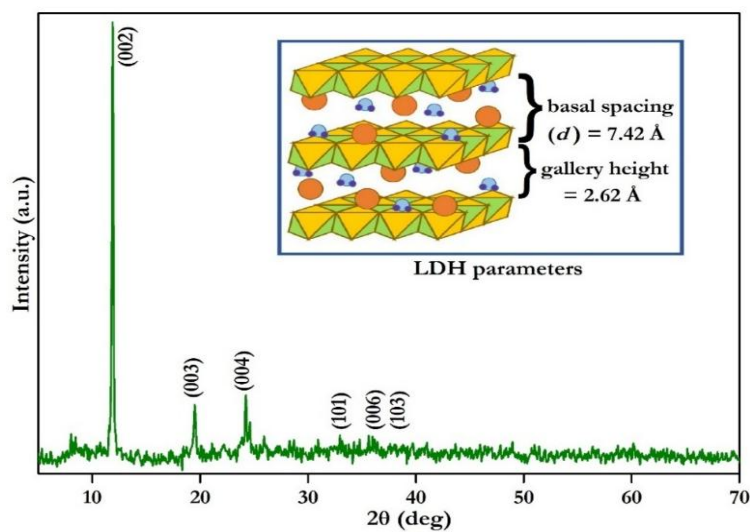


**Figure 2.4** PXRD diffractogram of ternary ZnCuNi-LDH.

The FTIR spectrum of LDH (Figure 2.5) displayed a band at  $3371\text{ cm}^{-1}$  with significant broadness, and was assigned to vO-H stretching and interlayer water molecules while the shoulder appearing at  $3013\text{ cm}^{-1}$  indicated hydrogen bonded vO-H---O. The bands at  $2995\text{ cm}^{-1}$ ,  $1540\text{ cm}^{-1}$  and  $1411\text{ cm}^{-1}$  were attributed to stretching vibrations of C-H bond and antisymmetric & symmetric vibration modes of COO- group respectively. Fingerprint vibration modes of acetate anions were observed at  $1340$ ,  $1030$ ,  $955$ ,  $692$  and  $611\text{ cm}^{-1}$  that were ascribed to bending/rocking modes of  $-\text{CH}_3$  group, C-C stretching, and bending and rocking modes of  $-\text{CO}_2$  moiety respectively. The bands observed below  $700\text{ cm}^{-1}$  were representative of vM-O linkage and indicated the links of metal ions of with the  $-\text{OH}$  groups (O-M-O, M-O and M-O-M) present in the LDH layers[29].

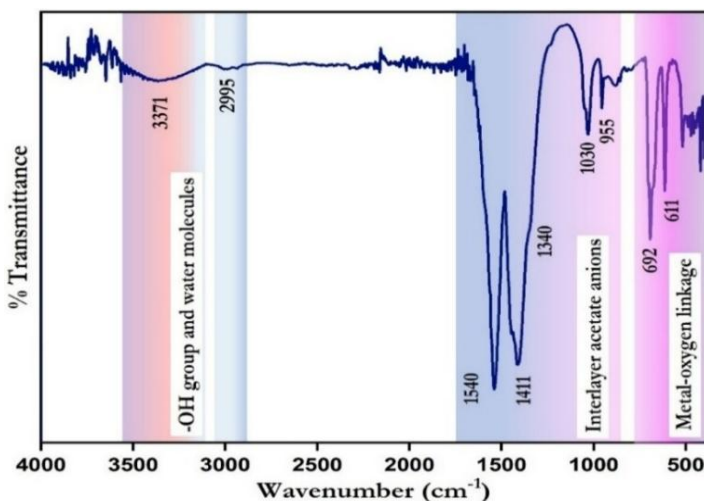


**Figure 2.5** FTIR spectrum of ternary ZnCuNi-LDH.

The thermal stability and weight loss of prepared ZnCuNi-LDH was determined from the TGA thermogram presented in Figure 2.6. The thermal decomposition of ZnCuNi-LDH was found to be a three-tier process, wherein the first stage of weight loss from room temperature to 220°C was attributed to the elimination of physiosorbed and interlayer water molecules, with a mass loss of 6.82%. The second stage, from 220°C to 385°C, involved decarboxylation, dehydroxylation, and removal of interlayer acetate ions from the LDH lattice and showed the maximum mass loss of 41.73%. The final stage occurred above 385°C wherein further dehydroxylation and decarboxylation resulted in collapse of layered arrangement and formation of pure phase mixed metal oxide[32]. The aggregate mass loss during the thermal degradation of ZnCuNi-LDH was found to be 49.9%.

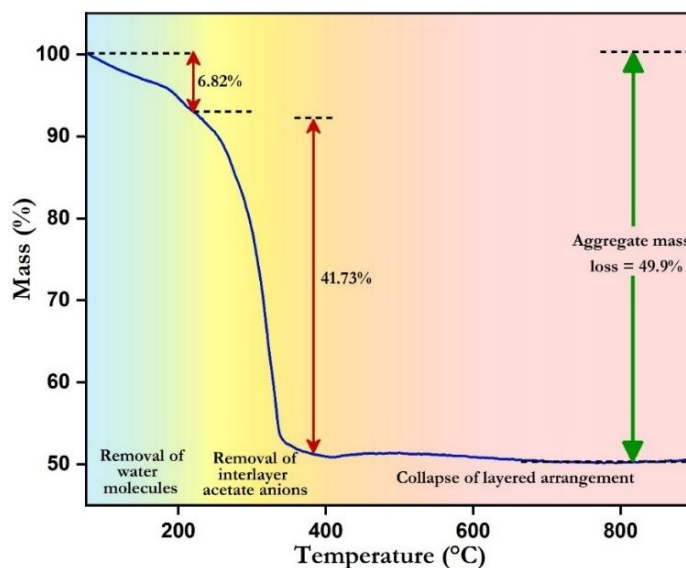


**Figure 2.6** TGA thermogram of ternary ZnCuNi-LDH (under N<sub>2</sub> atmosphere).

SEM imaging was conducted to identify the morphological and surface textural features of ZnCuNi-LDH. SEM micrograph (Figure 2.7a) clearly showed the presence of coherent lamellar orientation of LDH, corroborating the formation of layered structure of LDH. In addition, the EDX analysis was carried out to ascertain the elemental composition. The presence of Zn, Cu, Ni, C and O elements in the EDX profile (Figure 2.7b) confirmed the homogenous distribution of compositional elements in the synthesized heterogeneous ZnCuNi-LDH.

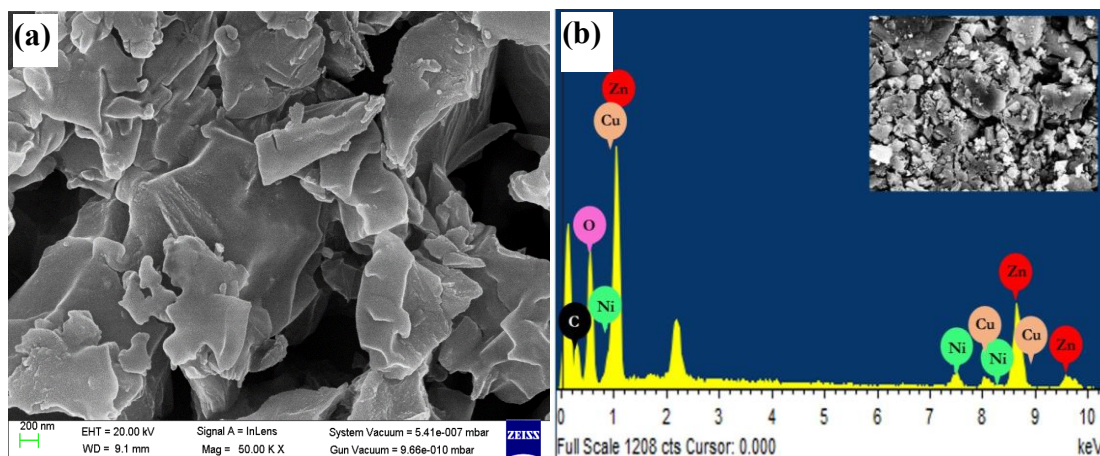


**Figure 2.7** (a) SEM micrograph and (b) EDX spectrum of ternary ZnCuNi-LDH with inset SEM image.

The specific surface area and porosity of ZnCuNi-LDH were determined using  $N_2$  adsorption-desorption study by BET analysis. The specific surface area ( $S_{BET}$ ) was found to be  $10.267\text{ m}^2\text{g}^{-1}$ , and the pore volume was  $0.004\text{ cc g}^{-1}$ . The average pore diameter, calculated from the  $N_2$  desorption data using the BJH method, was found to be  $1.716\text{ nm}$ . The shape of the isotherm in the range  $0.2 < P/P_0 < 0.8$  (Figure 2.8a) resembled the Type-IV isotherm according to IUPAC classification, and indicated the presence of non-cylindrical mesopores in the synthesized LDH. Furthermore, a small amount of  $N_2$  adsorption was observed below  $P/P_0 = 0.2$  and above  $P/P_0 = 0.8$ , indicating the appearance of micropores and macropores respectively[33]. The few macropores could be attributed to the existence of inter-particle spaces in the layered structure, usually observed in topotactic materials. The H4-type hysteresis loop also pointed to the existence of micropores and narrow slit-shaped mesopores in the synthesized ZnCuNi-LDH that may have appeared due to the lamellar arrangement[34]. Additionally, the pore diameter data presented in Figure 2.8b demonstrated the extensive scattering of micropores and mesopores, as well as macropores throughout the synthesized product, indicating prominent non-uniformity in ZnCuNi-LDH. The presence of large number of mesopores may be a contributing factor for the high catalytic activity of ZnCuNi-LDH.

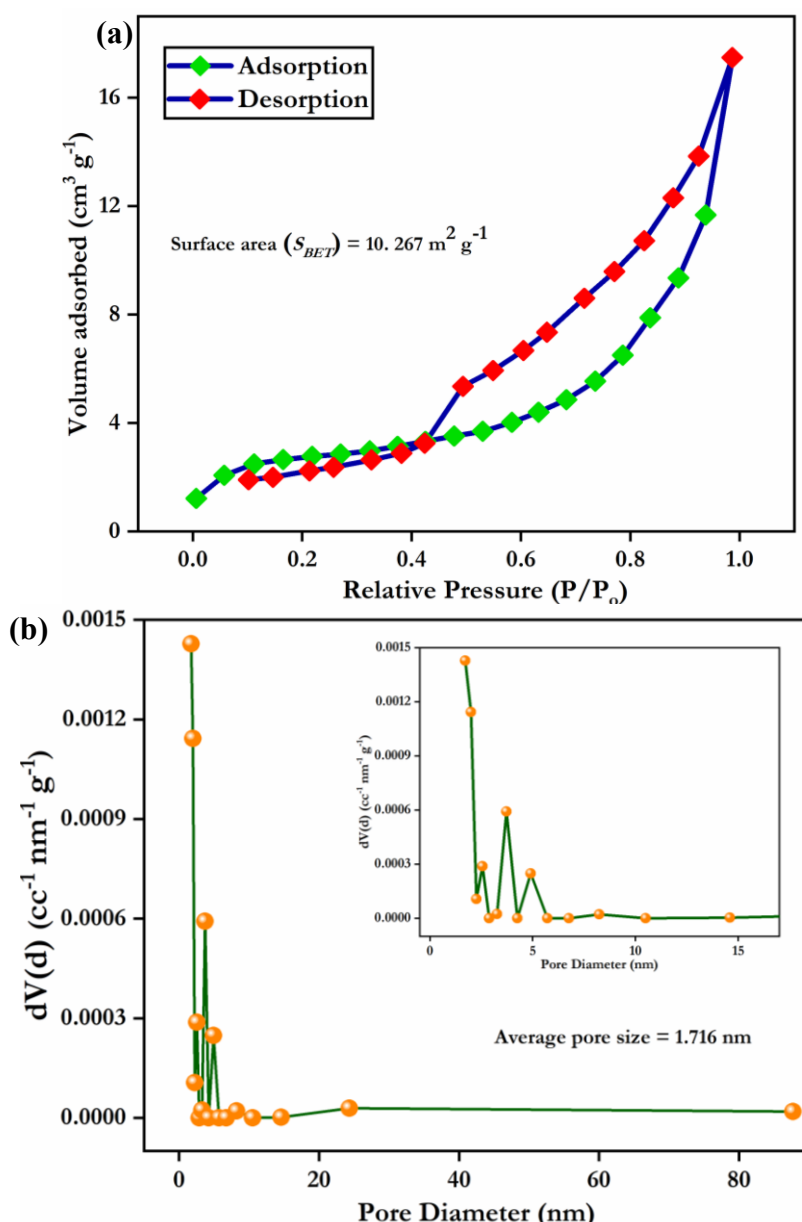


**Figure 2.8** (a) N<sub>2</sub> adsorption-desorption isotherm and (b) corresponding pore size distribution plots with inset of enlarged view of pore size distribution between 0-20 nm of ternary ZnCuNi-LDH.

### 2.3.2 Catalytic Activity

The efficacy of synthesized ZnCuNi-LDH as a co-catalyst with NaBH<sub>4</sub> reductant for the hydrogenation/reduction of nitroarenes and azo dyes was examined using UV-Visible spectrophotometer. The progress of catalytic reduction was evaluated by observing the change in absorbance values of solution of selected model molecules. Further, since the concentration of NaBH<sub>4</sub> (50 mM) was much greater than that of

NACs (1 mM) and azo dyes (100 mg L<sup>-1</sup>), the reaction rate was considered to be free of the influence of BH<sub>4</sub><sup>-</sup> concentration. Hence, the hydrogenation of NACs and reduction of azo dyes was considered to follow pseudo-first order kinetics, as presented in Equation 2.2[35].

$$\ln\left(\frac{C_t}{C_0}\right) = K \quad (2.2)$$

Where K denotes rate constant, and C<sub>0</sub> and C<sub>t</sub> are the initial and final concentrations of NACs and azo dyes.

Since the evaluated molecules possessed distinct colours and yielded absorption peaks in the visible region, reaction rate was evaluated in terms of comparative absorptive intensity. Therefore, using Beer-Lambert's law (Equation 2.3)

$$A = \varepsilon Cl \quad (2.3)$$

Kinetics of reaction were expressed in terms of absorption by the Equation 2.4 [36]:

$$\ln\left(\frac{C_t}{C_0}\right) = \ln\left(\frac{A_t}{A_0}\right) = kt \quad (2.4)$$

Where A<sub>0</sub> and A<sub>t</sub> are the initial and final absorbance of NACs and azo dyes.

### 2.3.2.1 Catalytic hydrogenation of NACs

In the current study, the catalytic hydrogenation of two NACs - *p*-NP and *p*-NA - was studied as model reactions.

#### 2.3.2.1.1 *p*-NP

In case of *p*-NP (Figure 2.9a), mixing of solution of NaBH<sub>4</sub> and *p*-NP produced an absorbance peak at  $\lambda_{max} = 400$  nm as a consequence of the generation of nitrophenolate ion. Then on addition of synthesized LDH, the intensity of peak at 400 nm began to decrease along with a new peak at 302 nm. The appearance of the new peak confirmed the production of *p*-aminophenol (*p*-AP) on *p*-NP reduction, and was confirmed by decrease in intensity of peak at 400 nm. The peak disappeared completely after 4 minutes, indicating the ultrafast hydrogenation of *p*-NP. The percentage reduction of *p*-NP was evaluated using Eqn 2.1 and was found to be 98.8%. The rate of reaction (k) was evaluated to be 1.058 min<sup>-1</sup> ( $R^2 = 0.79$ ) in accordance with the pseudo-first order model (Figure 2.9b). The action of NaBH<sub>4</sub> and LDH catalyst supports the addition of hydrogen to the nitro group of *p*-NP, resulting in the formation of *p*-AP that exhibits an absorbance peak at 302 nm.

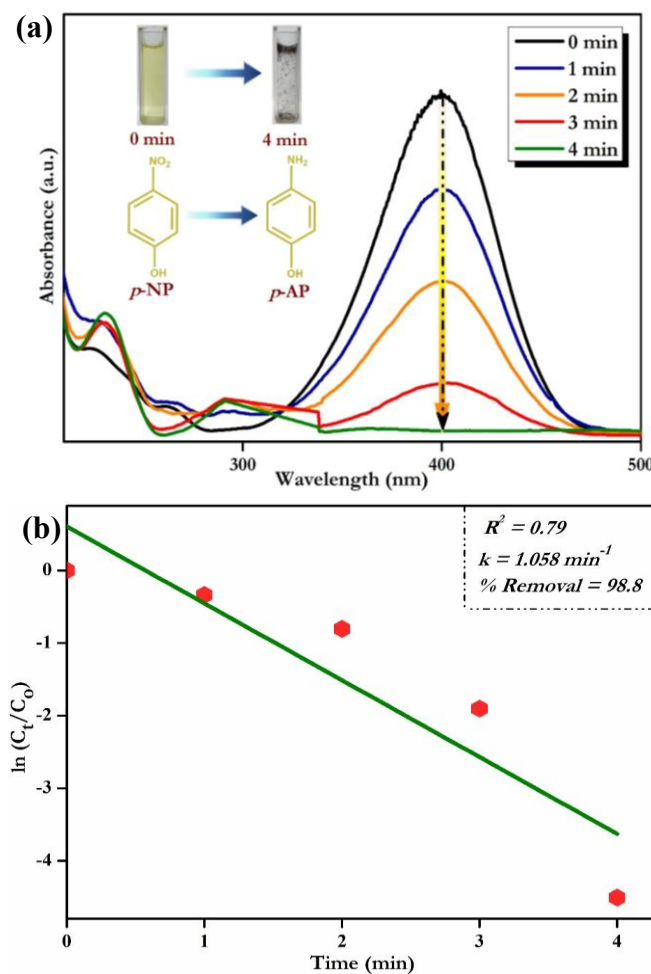


**Figure 2.9** (a) UV-Vis absorption spectrum and (b) linear fitting of pseudo-first kinetics model for the  $\text{NaBH}_4$  - assisted catalytic hydrogenation of *p*-NP using ZnCuNi-LDH.

### 2.3.2.1.2 *p*-NA

The catalyst-assisted hydrogenation of *p*-NA was evaluated in a similar manner as *p*-NP. The UV-Visible spectrum presented in Figure 2.10a showed a prominent peak at  $\lambda_{max} = 380 \text{ nm}$  on mixing of  $\text{NaBH}_4$  solution and *p*-NA solution. On introduction of ZnCuNi-LDH to the reaction mixture, the peak intensity at 380 nm decreased rapidly before ultimately disappearing after 3 minutes. Meanwhile, the appearance of a new peak at 304 nm on addition of LDH was attributed to the formation of *p*-phenylenediamine (*p*-PD) as byproduct. The percentage reduction of *p*-NA, calculated using Eqn 2.1, was found to be 95.3%. Using pseudo first order kinetics, rate constant of reduction ( $k$ ) was calculated to be  $0.98 \text{ min}^{-1}$  ( $R^2 = 0.94$ ) ((Figure 2.10b)). Due to the reductive action of  $\text{NaBH}_4$  and catalytic activity of LDH, hydrogen moiety is added to

the nitro group of *p*-NA, resulting in the formation of *p*-PD that exhibited an absorbance peak at 302 nm.

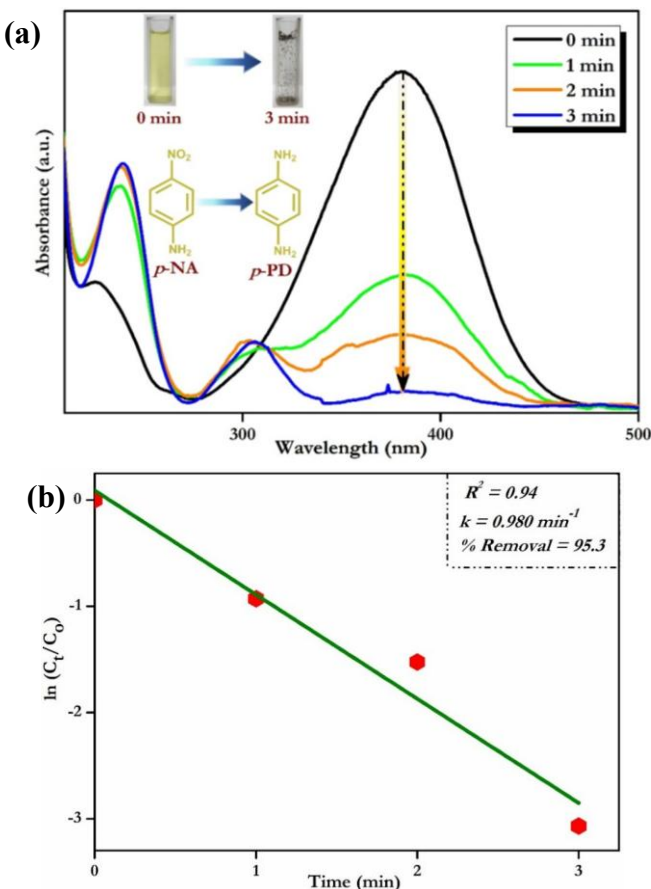


**Figure 2.10** (a) UV-Vis absorption spectrum and (b) linear fitting of pseudo-first kinetics model for the  $\text{NaBH}_4$  – assisted catalytic hydrogenation of *p*-NA using ZnCuNi-LDH.

### 2.3.2.2 Catalytic reduction of Azo dyes

Azo dyes find prevalent use in several industries, but their detrimental effects far outweigh their benefits. Therefore, their elimination from water sources is of utmost importance in order to safeguard public health. Therefore, in the current study, catalytic reduction of three commonly used dyes – MO, Ama, and BB was attempted using  $\text{NaBH}_4$  in presence of ZnCuNi-LDH catalyst.

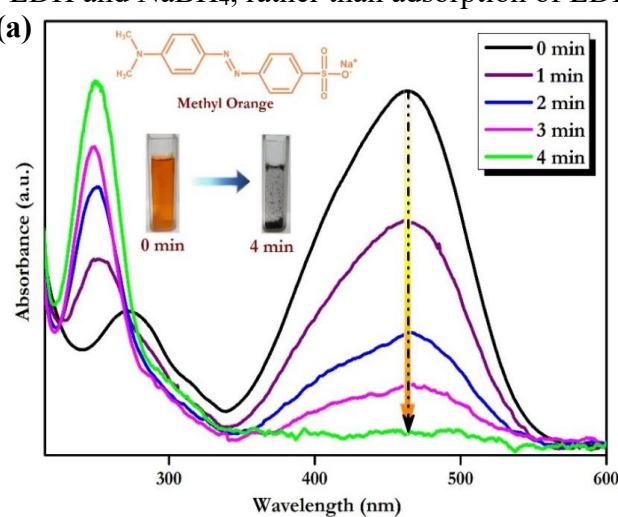
#### 2.3.2.2.1 Methyl Orange

Reduction of MO using  $\text{NaBH}_4$  is an effective and thermodynamically favorable approach to achieve its degradation but it is rendered kinetically unfavorable due to the electrostatic repulsion between  $\text{BH}_4^-$  moiety and anions of the dye molecules. Hence,  $\text{NaBH}_4$  is able to only partially reduce the azo group but is unable to break the

N-N bonding. The addition of ZnCuNi-LDH aids the degradation by adsorbing the active species on its surface and facilitating electron transfer between them. Thus, LDH can act as an excellent catalytic material for  $\text{NaBH}_4$  assisted- degradation of MO.

The UV-Vis absorbance vs wavelength plot for the catalytic reduction of MO is presented in Figure 2.11a. Absorbance change was noted at  $\lambda_{max} = 463$  nm for MO. No change in the peak intensity and position was observed on addition of  $\text{NaBH}_4$  alone. However, on addition of ZnCuNi-LDH catalyst, the intensity of peak centered at 463 nm began to decrease rapidly while a new peak emerged at 250 nm, along with a visible decrease in the intensity of color of the reaction mixture. As the reaction progressed, the peak at 463 nm kept decreasing rapidly until eventually it disappeared completely and intensity of peak at 250 nm kept increasing. The solution was completely decolourised within the short time span of 4 minutes. Percentage degradation of dye, calculated using Eqn 2.1, was found to be 96.4%.

The rate constant  $k$ , obtained by linearly regressing experimental data to the pseudo first order model, was evaluated to be  $0.797 \text{ min}^{-1}$  ( $R^2 = 0.91$ ) (Figure 2.11b). The action of  $\text{NaBH}_4$  and LDH catalyst caused the cleavage of the chromophoric azo (-N=N-) group of MO, leading to the formation of new degradation products possibly including sulfanilic acid and *N,N*- Dimethyl-*p*-phenyleneamine, that exhibited absorbance peaks around 248 nm and 242 nm respectively[37,38]. The emergence of new peak at 250 nm in the recorded absorbance spectra may be attributed to these species and along with the disappearance of peak at 463 nm, it gives evidence for the rapid degradation of MO by LDH and  $\text{NaBH}_4$ , rather than adsorption of LDH.



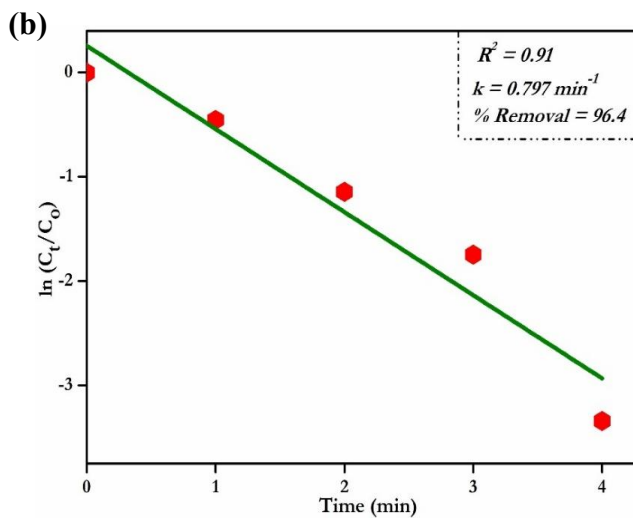


**Figure 2.11** (a) UV-Vis absorption spectrum and (b) linear fitting of pseudo-first kinetics model for the  $\text{NaBH}_4$  - assisted catalytic reduction of MO using  $\text{ZnCuNi-LDH}$ .

### 2.3.2.2.2 Amaranth

The absorbance plot of Amaranth dye solution consisted of a prominent peak at  $\lambda_{max} = 520$  nm (Figure 2.12a). Therefore, the catalytic reduction of Ama was investigated by monitoring the absorbance change at  $\lambda_{max} = 520$  nm. On addition of only  $\text{NaBH}_4$  to the dye solution, no change in the visual appearance of the solution and the peak at lambda max remained unchanged; rather the emergence of a new peak was observed at 377 nm. This new peak was attributed to the reduction of chromophoric azo (-N=N-) group to -NH-NH- by  $\text{NaBH}_4$ . But the appearance of peaks at both 520 nm and 377 nm indicated that only partial reduction of azo group occurred at this stage. Therefore, an efficient catalyst was needed for the complete reduction of the -N=N- bond.

To achieve this,  $\text{ZnCuNi-LDH}$  catalyst was added to the reaction mixture, and it was observed that reaction mixture was decolourised rapidly and a steady reduction in the intensity of peak centered at  $\lambda_{max} = 520$  nm along with the simultaneous appearance of a new peak at 328 nm was observed. The disappearance of the peak at 520 nm was attributed to the breakdown of chromophore present in Ama dye molecules, while the formation of naphthionic acid as a degradation by-product may have been responsible for the emergence of new peak at 328 nm[39]. The reaction mixture was completely decolourised within 2 minutes, suggesting ultrafast reduction of Amaranth dye by  $\text{ZnCuNi-LDH}$  catalyst. Absorbance of solution was recorded at 520 nm at one-minute

intervals and percentage degradation was calculated to be 97.3%. Since the reduction of Ama was assumed to be independent of NaBH<sub>4</sub>, the pseudo-first order model was applied to determine the kinetics of the reaction. The rate constant (*k*), calculated by performing linear regression analysis on the experimental data, was found to be 1.807 min<sup>-1</sup> (*R*<sup>2</sup> = 0.91) (Figure 2.12b).

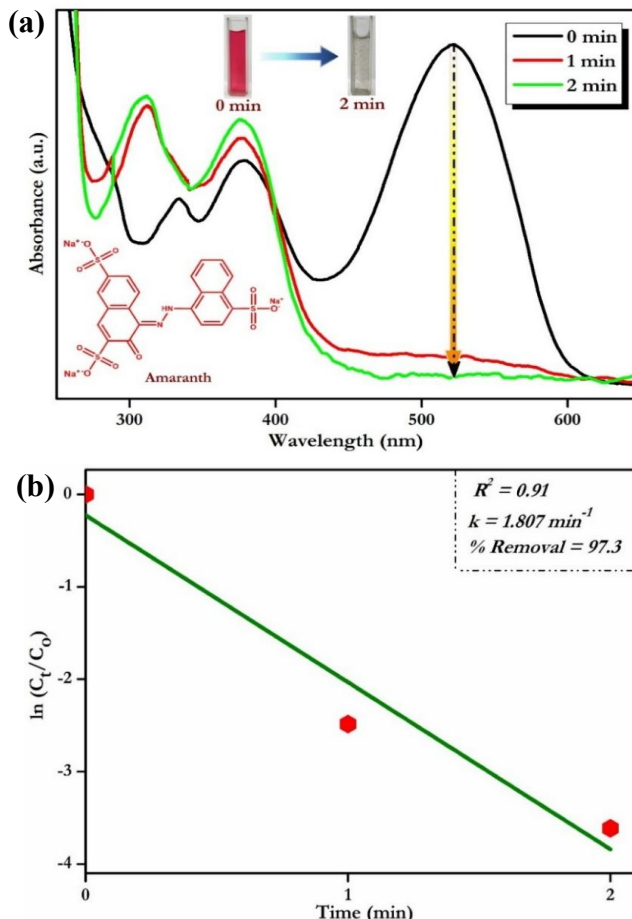


**Figure 2.12** (a) UV-Vis absorption spectrum and (b) linear fitting of pseudo-first kinetics model for the NaBH<sub>4</sub> - assisted catalytic reduction of Amaranth using ZnCuNi-LDH.

### 2.3.2.2.3 Brilliant Black

Although NaBH<sub>4</sub>-assisted catalytic reduction of several toxic azo dyes has been widely reported, virtually no reports are available about the catalytic reduction of BB. The absorption maxima for BB dye typically appears at  $\lambda_{max} = 571$  nm (Figure 2.13a) but addition of NaBH<sub>4</sub> to BB solution caused the peak to shift from 571 nm to 490 nm. This shift was attributed to the partial cleavage of  $-\text{N}=\text{N}-$  azo bond and its reduction

to  $-\text{NH}-\text{NH}-$  bond[40]. Further, on addition of ZnCuNi-LDH, the peak at 490 nm reduced in intensity, along with the appearance of a new peak at 251 nm. Complete decolourisation of BB was attained within 4 minutes of reaction initiation, and at this stage, the peak at  $\lambda_{max} = 490$  nm vanished completely. The percentage degradation efficiency of BB was calculated to be 95.2% and linear regression of experimental data to pseudo 1<sup>st</sup> order model yielded  $k$  value of 0.707 min<sup>-1</sup> ( $R^2 = 0.95$ ) (Figure 2.13b).

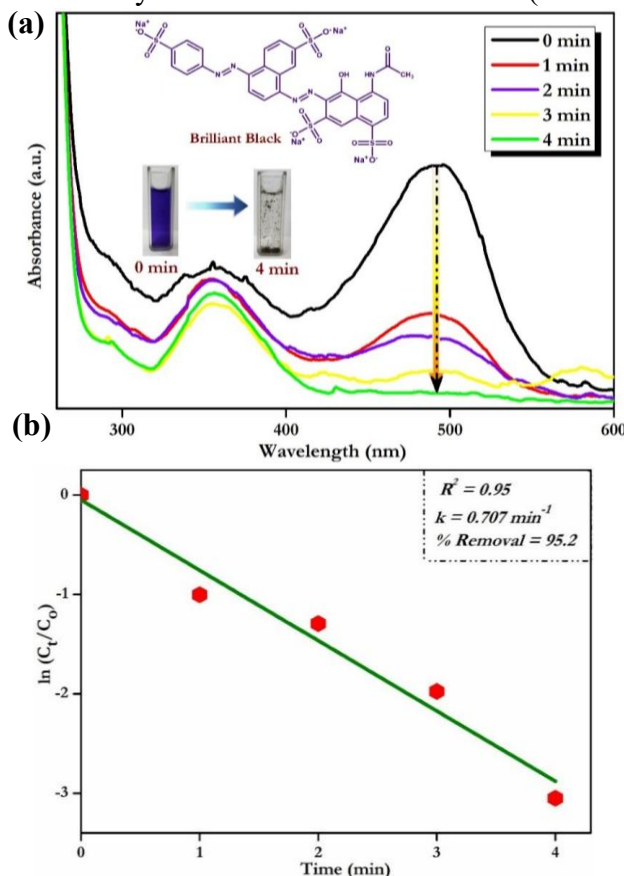


**Figure 2.13** (a) UV-Vis absorption spectrum and (b) linear fitting of pseudo-first kinetics model for the  $\text{NaBH}_4$  - assisted catalytic reduction of Brilliant Black BN using ZnCuNi-LDH.

Table 2.3 presents the values of percentage degradation, time expended and rate of reaction for the catalytic reduction experiments.

**Table 2.3** Experimental values for catalytic reduction of various pollutants.

Pollutant	Percentage	Time	Rate of reaction ( $k$ )
	Degradation (%)		(min $^{-1}$ )
<i>p</i> -NP	98.8	4	1.058
<i>p</i> -NA	95.3	3	0.980

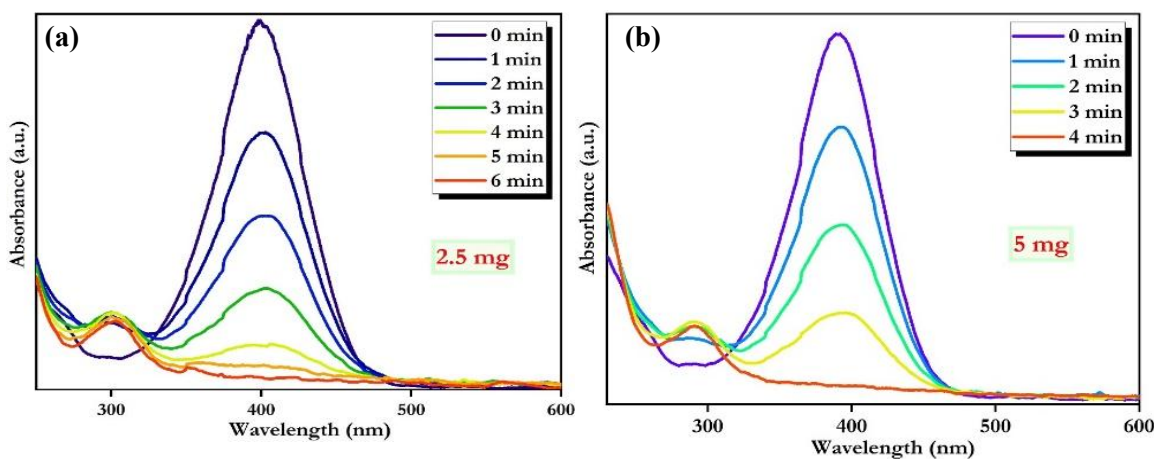
MO	96.4	4	0.797
Ama	97.3	2	1.807
BB	95.2	4	0.707

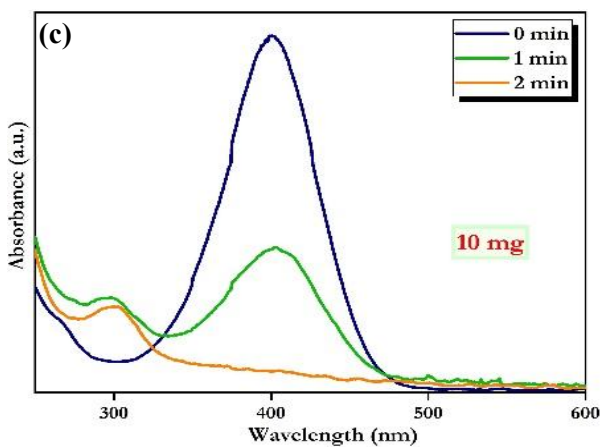
### 2.3.2.3 Effect of influencing parameters

The performance of a catalyst is influenced by various parameters. Therefore, the effect of catalyst dosage and pollutant concentration on catalytic activity of ZnCuNi-LDH were studied by choosing *p*-NP and MO as model pollutants.

#### 2.3.2.3.1 Effect of catalyst dosage

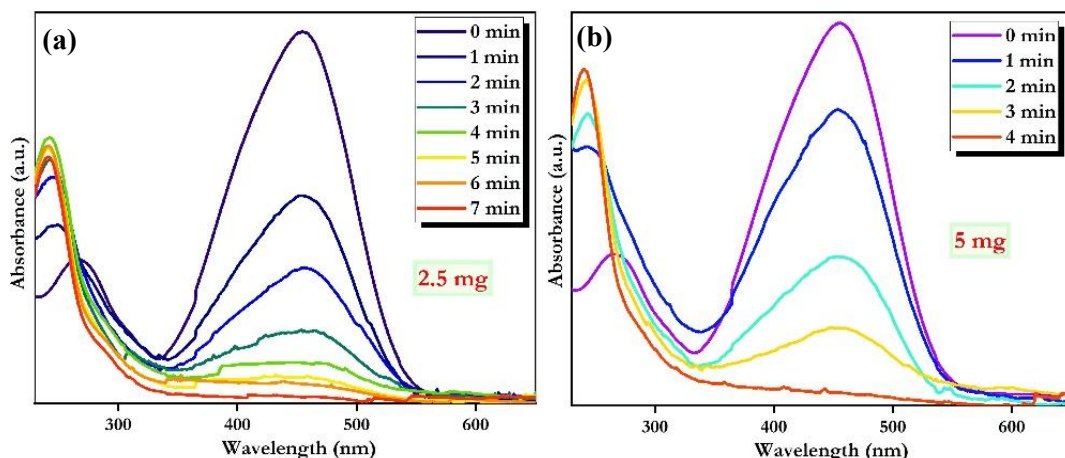
The plots presented in Figure 2.14a-c provide an insight into the influence of ZnCuNi-LDH dosage on reduction of *p*-NP and MO. The absorption spectrum of *p*-NP presents a prominent peak at  $\lambda_{max} = 400$  nm that shows pronounced decrease in intensity on addition of various dosages of catalyst to 1 mM *p*-NP solution. The addition of 2.5 mg catalyst led to the complete hydrogenation of *p*-NP within 6 minutes. Increase in dosage of ZnCuNi-LDH to 5 mg and 10 mg led to decrease in time required for the complete *p*-NP hydrogenation, and the reactions were completed in even shorter durations of 4 minutes and 2 minutes respectively. Therefore, the time expended for reduction of 1 mM *p*-NP solution using various dosages of ZnCuNi-LDH catalyst followed the trend: 2.5 mg > 5.0 mg > 10 mg.





**Figure 2.14** UV-Vis absorption spectra for the catalytic reduction of *p*-NP by varying dosage (a, b, c) of ZnCuNi-LDH.

The NaBH<sub>4</sub>-assisted reduction of MO dye using various dosages of ZnCuN-LDH catalyst is presented in Figure 2.15a-c. Similar to *p*-NP, in case of MO dye also, in all the dosage scenarios, the absorption spectrum presented an intense peak at  $\lambda_{max} = 463$  nm that decreased with the addition of catalyst to 100 ppm MO solution. It was observed that on addition of 2.5 mg catalyst, the dye solution was completely decolorized within just 7 minutes. On increasing ZnCuNi-LDH dosage to 5 mg and 10 mg, dye decolorization was completed within 4 minutes and 2 minutes respectively, and it may be attributed to faster reduction of model molecules. Therefore, the time expended for reduction of 100 ppm MO solution using various dosages of ZnCuNi-LDH catalyst followed the trend: 2.5 mg > 5.0 mg > 10 mg.



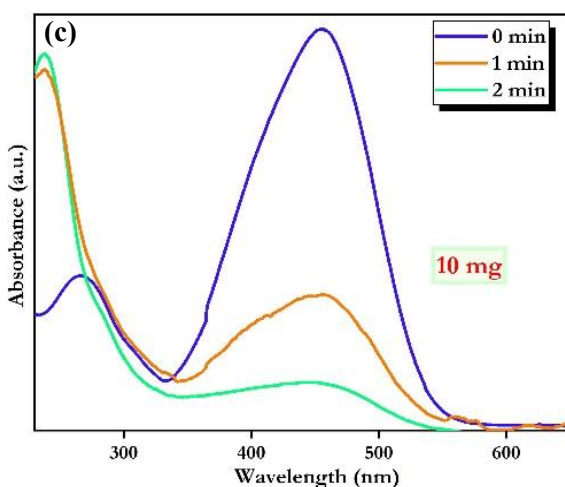


**Figure 2.15** UV-Vis absorption spectra for the catalytic reduction of MO by varying dosage (a, b, c) of ZnCuNi-LDH.

The observed trend of decreased reaction times with increased catalyst dosages is potentially the consequence of lower dosage, that results in availability of fewer active sites to catalyse the reduction reaction, leading to more time being expended for the reaction to be completed. Increase in dosage of ZnCuNi-LDH resulted in the availability of more active sites being available for reaction, thereby resulting in accelerated reduction process and faster culmination of reaction [26].

### 2.3.2.3.2 Effect of pollutant concentration

The impact of pollutant concentration on catalytic activity of ZnCuNi-LDH was studied using three concentrations for *p*-NP and MO. The plots presented below provide insights into the catalytic reduction process at various concentrations of the chosen model molecules. In case of *p*-NP, the absorption spectrum presented in Figure 2.16a-c exhibits a peak at 400 nm that shows a pronounced decrease on addition of 5 mg catalyst. Here, in case of 0.25 mM *p*-NP concentration, complete decolourisation of reaction mixture was observed within just 1 minute of catalyst addition. On increasing *p*-NP concentration to 0.50 mM and 1.00 mM, reduction time increased to 2 minutes and 4 minutes respectively. Therefore, on using 5 mg ZnCuNi-LDH as catalyst, the time expended for reduction of various concentration of *p*-NP solution followed the trend: 0.25 mM > 0.50 mM > 1.00 mM.

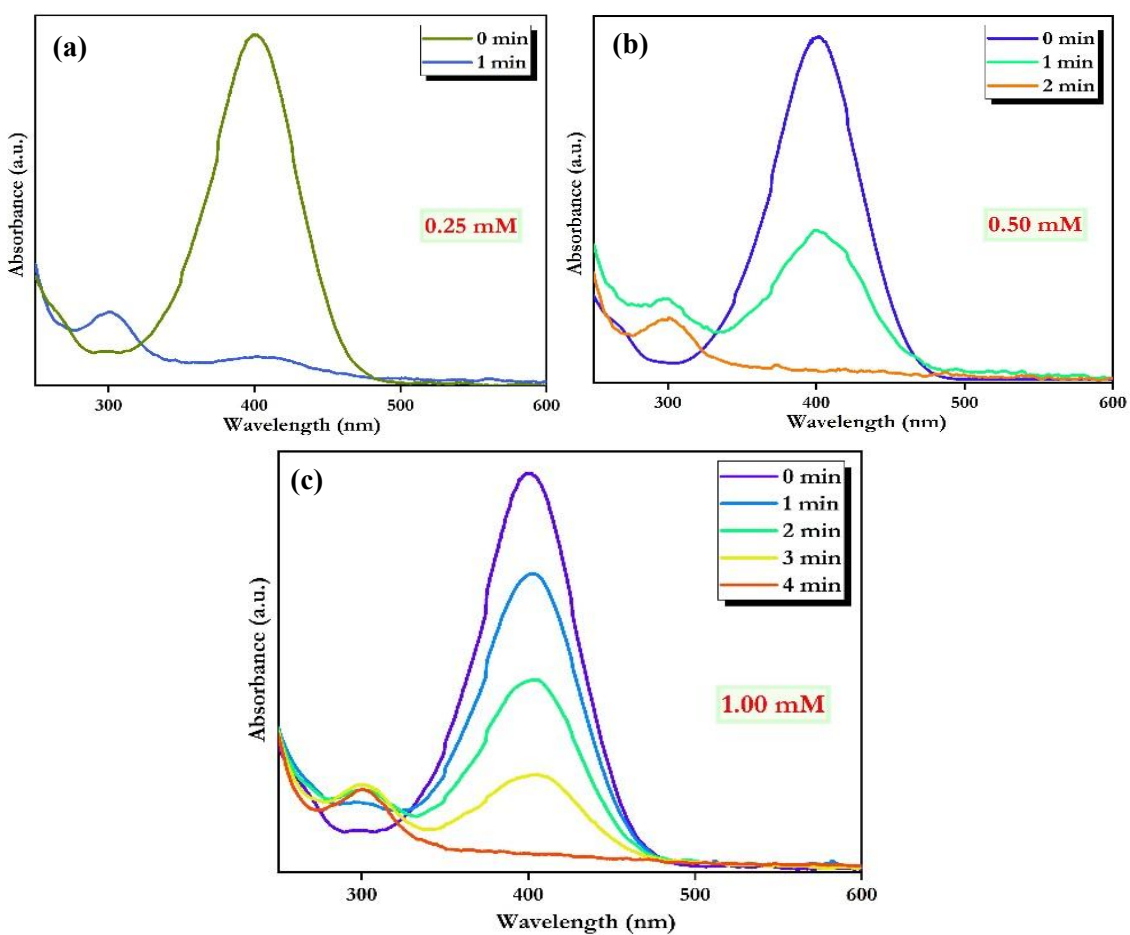


**Figure 2.16** UV-Vis absorption spectra for the catalytic reduction of various concentrations of *p*-NP (a, b, c) by ZnCuNi-LDH.

A similar trend was observed for the reduction of MO dye, as presented in Figure 2.17a-c. Addition of 5 mg catalyst to 25 ppm MO solution led to complete reduction of dye within just 2 minutes. Increase in dye concentration resulted in the increase of catalytic reduction time to 3 minutes and 4 minutes respectively. Therefore, on using 5 mg ZnCuNi-LDH as catalyst, the time expended for reduction of various concentration of MO solution followed the trend: 25 ppm > 50 ppm > 100 ppm.

The increase in reaction time may be attributed to the fact that at lower concentration, fewer number of pollutant molecules need to be catalyzed, thereby leading to faster reduction of all pollutant molecules in less time. Conversely, at higher concentrations, more number of molecules are required to be reduced, and thus more time is expended for the complete reduction of the pollutants, thereby leading to increased reaction time for complete decolourisation[41].

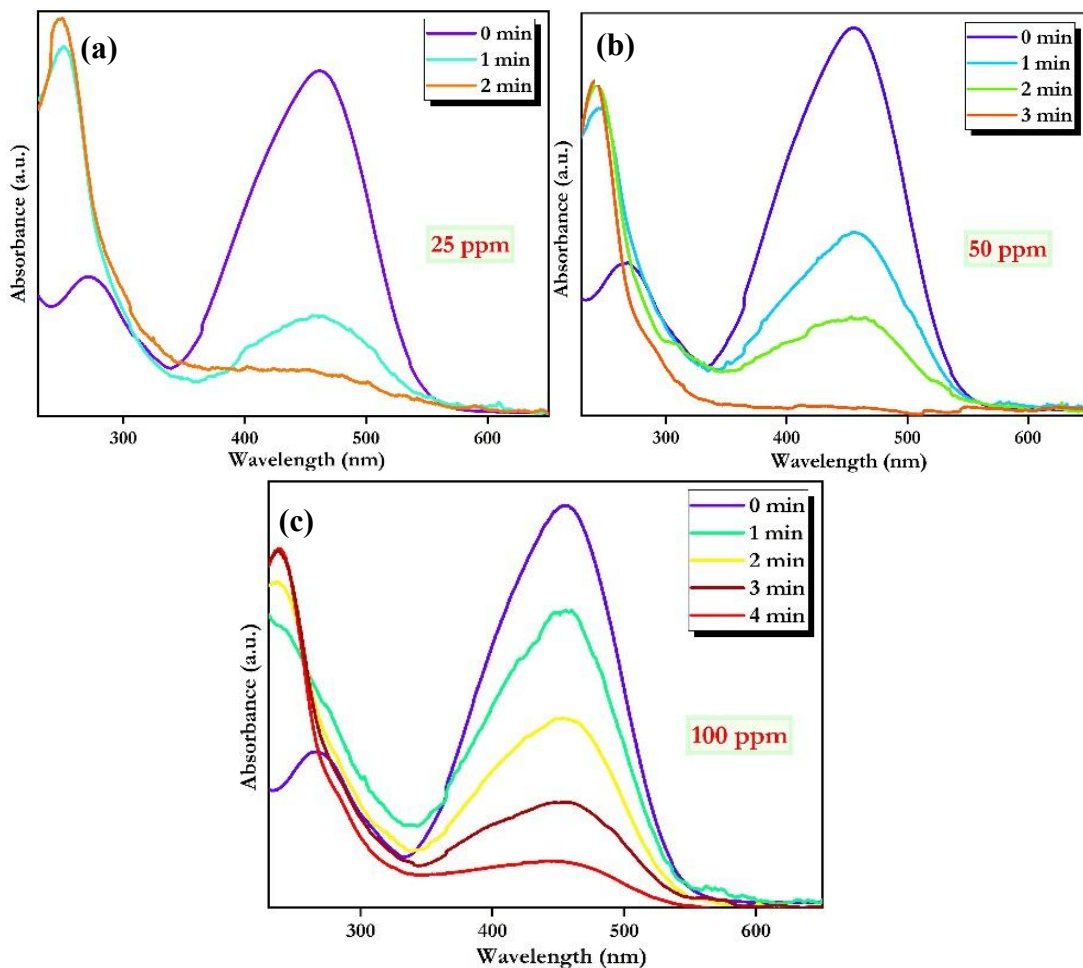


**Figure 2.17** UV-Vis absorption spectra for the catalytic reduction of various concentrations of MO (a, b, c) by ZnCuNi-LDH.

#### 2.3.2.4 Universality of ZnCuNi-LDH as catalyst

The universality of a catalyst is a fundamental parameter in determining the practical and profitable usability of the material in large-scale industrial applications. An efficient catalyst must possess the ability to simultaneously reduce/degrade various types of molecules into simple and benign by-products. Therefore, in order to ascertain the universal catalytic behaviour of synthesized ZnCuNi-LDH, simultaneous reduction of *p*-NP and MO was carried out. It was observed that the absorbance spectrum of the blank mixture of *p*-NP and MO exhibited a peak at 318 nm that can be attributed to *p*-NP molecules while the peak at 463 nm appears due to MO molecules. On addition of NaBH<sub>4</sub>, the peak at 318 nm disappeared and a new peak appeared at 400 nm due to the conversion of *p*-NP molecules to phenolate anions (Figure 2.18). The peak at 463

nm does not shift in position but only decreased in intensity and appeared as a neck in the hybrid spectrum due to the closeness of the  $\lambda_{max}$  values of *p*-NP and MO.

Further, on addition of ZnCuNi-LDH, the intensity of the hybrid spectrum decreased rapidly and eventually disappeared within a short span of 5 minutes, along with the decolourization of the reaction mixture. The rapid decolourization of the reaction mixture elucidated the fact that ZnCuNi-LDH can be successfully used as a universal catalytic material for the simultaneous reduction of NACs and anionic azo dyes.

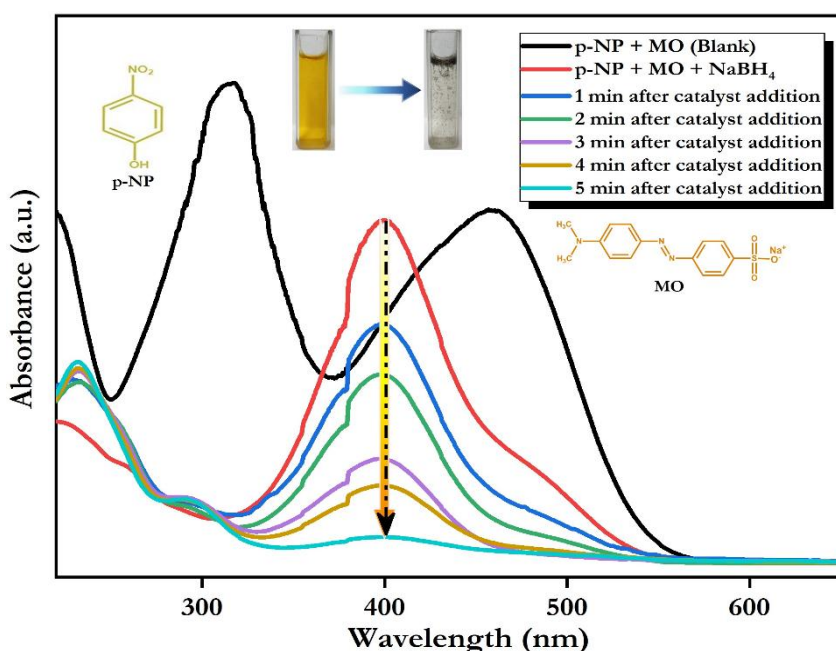


**Figure 2.18** UV-Vis absorption spectrum for  $\text{NaBH}_4$  - assisted simultaneous reduction and degradation of *p*-NP and MO by ZnCuNi-LDH.

### 2.3.2.5 Reusability and Recyclability

The recyclability of heterogeneous catalysts is a significant factor that impacts their profitable commercial use. Therefore, studies were carried out to determine the reusability of the synthesized catalysts for the hydrogenation of *p*-NP and reduction of MO as well as mixture of dyes. The results presented in Figure 2.19a indicate that ZnCuNi-LDH sustained up to 90% removal efficacy in just 4 minutes for the reduction of *p*-NP and MO even after 5 cycles. Moreover, ZnCuNi-LDH also exhibited excellent catalytic reduction ability of upto 88% within 5 minutes towards mixture of MO, Ama and BB dyes even after 5 cycles, as shown in Figure 2.19b. These results suggest that ZnCuNi-LDH is a robust catalyst that can be easily recovered and utilized for

consecutive catalytic cycles without any significant decrease in catalytic performance. The slight decrease in removal efficacy may be attributed to the loss and agglomeration of catalytic material during the recovery and reuse stages.

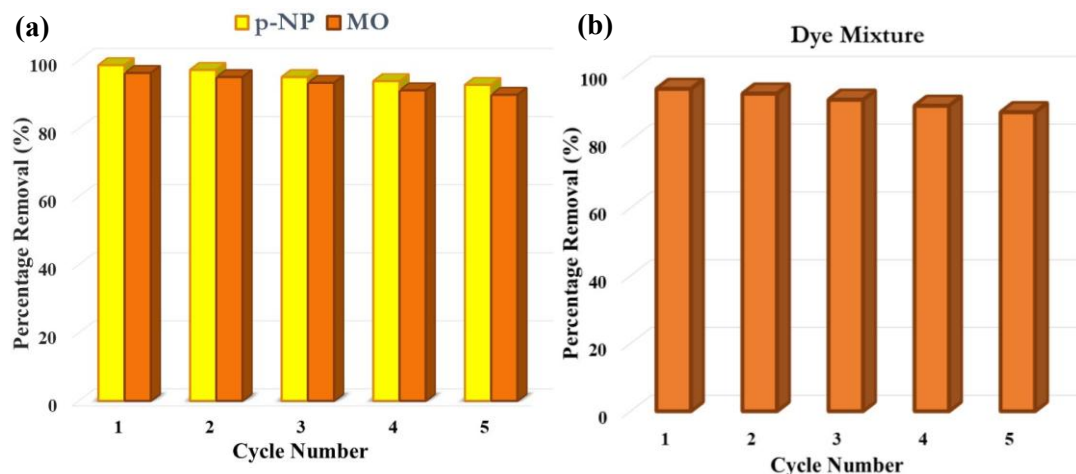


**Figure 2.19** Recyclability of ZnCuNi-LDH for catalytic reduction of (a) *p*-NP, MO and (b) mixture of dyes.

### 2.3.2.6 Plausible mechanism for catalytic activity of ZnCuNi-LDH

The surface catalytic reduction of nitro compounds and organic dyes by ZnCuNi-LDH potentially proceeds through the Langmuir-Hinshelwood mechanism, involving three steps: (1) dissociative adsorption of reactants onto LDH surface, (2) interaction between adsorbed moieties, and (3) desorption of reduction products from LDH surface. In aqueous medium,  $\text{NaBH}_4$  breaks down into  $\text{Na}^+$  and  $\text{BH}_4^-$  ions.  $\text{BH}_4^-$  anions further hydrolyses into  $\text{BO}_2^-$  and  $\text{H}_2$  and these moieties are adsorbed onto LDH since they possess high surface area (Figure 2.20).

For the degradation of *p*-NP and *p*-NA,  $\text{H}_2$  is adsorbed on ZnCuNi-LDH surface, resulting in metal-hydride complex formation. The action of this complex as a hydrogen-mediator facilitates  $\text{H}_2$  transfer to the  $-\text{NO}_2$  group along with electrons. This aids in the hydrogenation of  $-\text{NO}_2$  group, converting it to  $-\text{NH}_2$  and resulting in the formation of *p*-aminophenol and *p*-phenylenediamine as reduction products following the hydrogenation of *p*-NP and *p*-NA respectively.

While in case of organic dyes, ZnCuNi-LDH acts as a redox catalyst and facilitates the transfer of electrons to the dye molecules. In the reaction mixture, initially the anionic dye molecules get adsorbed onto the positively charged LDH surface via electrostatic

forces of attraction. Then, due to the electron relay behaviour of LDH, electrons are transferred from the electron-donating  $\text{BO}_2^-$  moiety to the electron-accepting dye molecules, leading to their reduction. Lastly, the reduction products present on LDH surface get desorbed and diffused into the solution. The synergistic interactions between the copper and nickel atoms present in the lattice may also contribute and augment the electron relay ability of the  $\text{ZnCuNi-LDH}$ , and result in the ultrafast reduction of NACs and organic dyes (Figure 2.20).

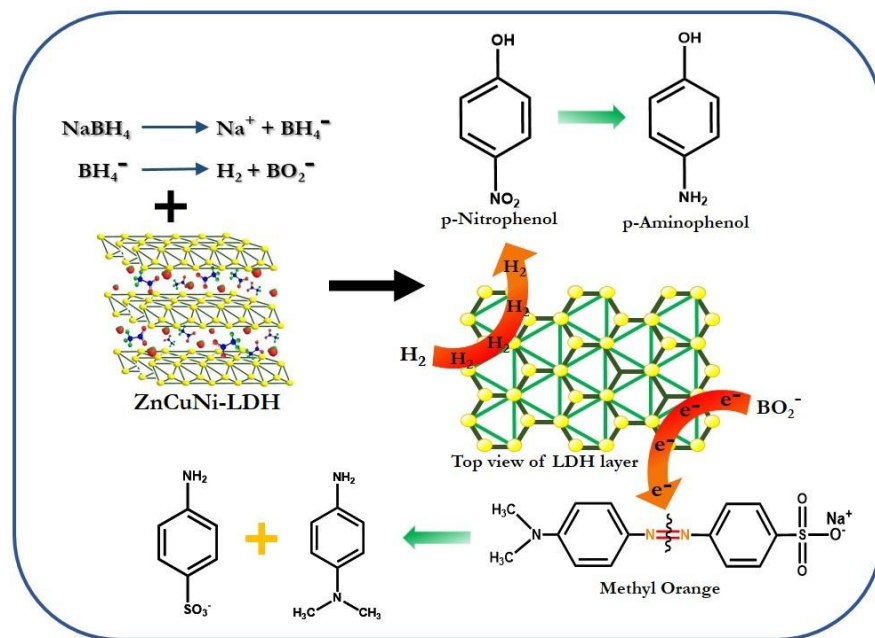


**Figure 2.20** Potential mechanism for the  $\text{NaBH}_4$ -assisted catalytic degradation of *p*-NP and MO by  $\text{ZnCuNi-LDH}$ .

### 2.3.2.7 Comparison with reported catalysts

The comparison of the catalytic activity of  $\text{ZnCuNi-LDH}$  with previously reported catalysts towards the reduction of *p*-NP, *p*-NA, MO, and Ama is presented in Table 2.4. Virtually no reports were available for the catalytic reduction of BB dye. The rate constants for reactions catalyzed by  $\text{ZnCuNi-LDH}$  were found to be comparable or even better than the rate constants of most reported catalysts. Therefore, it may be concluded that  $\text{ZnCuNi-LDH}$  can act as exemplary catalyst for the catalytic reduction of both nitroarene compounds and azo dyes. The superior catalytic activity may be attributed to the small size, high surface area and homogeneous distribution of Zn, Cu and Ni cations in the  $\text{ZnCuNi-LDH}$  matrix.

**Table 2.4** Comparison of rate constants of ZnCuNi-LDH with previously reported catalysts

Pollutant	Catalyst	Rate constant ( $k_{app}$ )	Reference
<i>p</i> -NP	Au NPs-LMW chitosan	0.2537 min <sup>-1</sup>	[42]
	Magnetite-Ag/LDH/Starch	0.30 s <sup>-1</sup>	[43]
	Fe <sub>3</sub> O <sub>4</sub> @PPy-MAA/Ag	0.08 min <sup>-1</sup>	[44]
	Pd/NiFe-LDH	0.37 min <sup>-1</sup>	[45]
	ZnCuNi-LDH	1.058 min <sup>-1</sup>	This work
<i>p</i> -NA	CoAl-LDH	0.40 min <sup>-1</sup>	[14]
	Ag-PNiM microgel	0.0852 min <sup>-1</sup>	[46]
	Au Nanorods	0.0564 s <sup>-1</sup>	[47]
	CMC/ZnAl-LDH/Au-beads	0.7486 min <sup>-1</sup>	[48]
MO	ZnCuNi-LDH	0.98 min <sup>-1</sup>	This work
	Ag-Cu Rhizome Powder	0.0029 s <sup>-1</sup>	[23]
	Asp-Au NPs	0.314 min <sup>-1</sup>	[24]
	Au NPs-LMW chitosan	0.2701 min <sup>-1</sup>	[42]
	Nitrogen doped-C <sub>3</sub> N <sub>4</sub> /Sodium Alginat	0.0649 min <sup>-1</sup>	[49]
Ama	ZnCuNi-LDH	0.797 min <sup>-1</sup>	This work
	Ag-Cu Rhizome Powder	0.0009 s <sup>-1</sup>	[23]
	Asp-Au NPs	0.228 min <sup>-1</sup>	[24]
	AuNPs/CNC	0.025 s <sup>-1</sup>	[50]
	ZnCuNi-LDH	1.807 min <sup>-1</sup>	This work

## 2.4 Conclusion

In summary, ternary ZnCuNi-LDH was successfully synthesized through a facile acid hydrolysis route and was later used as an efficient catalyst for the rapid hydrogenation of *p*-NP, *p*-NA, as well as for the reductive degradation of MO, Ama, and BB dyes. ZnCuNi-LDH exhibited more than 95% degradation efficiency for all the chosen model pollutants within 4 minutes and followed the order: 98.8% (*p*-NP) > 95.3% (*p*-NA) for the NACs, while for organic azo dyes the trend - Ama (97.0%) > MO (96.4%) > BB dyes (95.2%) - was followed. The kinetics of the reduction reactions best aligned with the pseudo 1<sup>st</sup> order model, and rate constant values (*k*) for the catalytic

hydrogenation of *p*-NP and *p*-NA were calculated to be  $1.058 \text{ min}^{-1}$  and  $0.98 \text{ min}^{-1}$  respectively, whereas rate constant values (*k*) for reductive degradation of MO, Ama and BB were calculated to be  $0.797 \text{ min}^{-1}$ ,  $1.807 \text{ min}^{-1}$  and  $0.707 \text{ min}^{-1}$  respectively. In addition, catalyst dosage and pollutant concentration extensively influenced the catalytic performance of the synthesized lattice, as the time required for completion of the catalytic reduction process shared a directly proportional relationship with the dosage of the catalyst, but it was inversely related to the concentrations of the model pollutants. Furthermore, ZnCuNi-LDH rapidly decolourised a binary solution consisting of *p*-NP and MO, thereby exhibiting its universality as a catalyst. The synthesized catalytic material also exhibited more than 90% reduction efficiency even after 5 regeneration cycles. Thus, the present work reports the facile synthesis, excellent catalytic activity, and recyclability of ternary ZnCuNi-LDH that can be used as an effective catalytic material for the degradation of NACs and azo dyes.

## 2.5 References

- [1] L.P.F. Benício, R.A. Silva, J.A. Lopes, D. Eulálio, R.M.M. dos Santos, L.A. De Aquino, L. Vergütz, R.F. Novais, L.M. Da Costa, F.G. Pinto, J. Tronto, Layered double hydroxides: Nanomaterials for applications in agriculture | Hidróxidos duplos lamelares: Nanomateriais para aplicações na agricultura, Rev. Bras. Cienc. Do Solo 39 (2015). <https://doi.org/10.1590/01000683rbcs20150817>.
- [2] C. Li, M. Wei, D.G. Evans, X. Duan, Layered double hydroxide-based nanomaterials as highly efficient catalysts and adsorbents, Small 10 (2014) 4469–4486. <https://doi.org/10.1002/smll.201401464>.
- [3] X. Duan, J. Lu, D.G. Evans, Assembly chemistry of anion-intercalated layered materials, Elsevier B.V., 2011. <https://doi.org/10.1016/B978-0-444-53599-3.10017-4>.
- [4] A. Tsyganok, A. Sayari, Incorporation of transition metals into Mg-Al layered double hydroxides: Coprecipitation of cations vs. their pre-complexation with an anionic chelator, J. Solid State Chem. 179 (2006) 1830–1841. <https://doi.org/10.1016/j.jssc.2006.03.029>.
- [5] X. Guo, Y. Ruan, Z. Diao, K. Shih, M. Su, G. Song, D. Chen, S. Wang, L. Kong, Environmental-friendly preparation of Ni–Co layered double hydroxide (LDH) hierarchical nanoarrays for efficient removing uranium (VI), J. Clean. Prod. 308 (2021) 127384. <https://doi.org/10.1016/j.jclepro.2021.127384>.
- [6] Z. Wu, H. Zhang, L. Luo, W. Tu, ZnCo binary hydroxide nanostructures for the efficient removal of cationic dyes, J. Alloys Compd. 806 (2019) 823–832. <https://doi.org/10.1016/j.jallcom.2019.07.295>.

[7] L.L. Zhou, W.X. Li, H.B. Zhao, J.S. Wang, B. Zhao, NiTi-layered double hydroxide nanosheets toward high-efficiency flame retardancy and smoke suppression for silicone foam, *Polym. Degrad. Stab.* 204 (2022) 110104. <https://doi.org/10.1016/j.polymdegradstab.2022.110104>.

[8] S. Kansal, P. Singh, S. Biswas, A. Chowdhury, D. Mandal, S. Priya, T. Singh, A. Chandra, Superior-catalytic performance of Ni–Co layered double hydroxide nanosheets for the reduction of p-nitrophenol, *Int. J. Hydrogen Energy* 48 (2023) 21372–21382. <https://doi.org/10.1016/j.ijhydene.2022.04.213>.

[9] M. Bini, V. Ambrogi, A. Donnadio, A. Di Michele, P. Ricci, M. Nocchetti, Layered double hydroxides intercalated with fluoride and methacrylate anions as multifunctional filler of acrylic resins for dental composites, *Appl. Clay Sci.* 197 (2020) 105796. <https://doi.org/10.1016/j.clay.2020.105796>.

[10] Y. Meng, S. Xia, G. Pan, J. Xue, J. Jiang, Z. Ni, Preparation and photocatalytic activity of composite metal oxides derived from Salen-Cu(II) intercalated layered double hydroxides, *Korean J. Chem. Eng.* 34 (2017) 2331–2341. <https://doi.org/10.1007/s11814-017-0135-9>.

[11] S. Megala, S. Prabhu, S. Harish, M. Navaneethan, S. Sohila, R. Ramesh, Enhanced photocatalytic dye degradation activity of carbonate intercalated layered Zn, ZnNi and ZnCu hydroxides, *Appl. Surf. Sci.* 481 (2019) 385–393. <https://doi.org/10.1016/j.apsusc.2019.03.091>.

[12] B. Pandey, P. Singh, Statistical optimization of process parameters for ultrafast uptake of anionic azo dyes by efficient sorbent: Zn/Cu layered double hydroxide, *Appl. Organomet. Chem.* 37 (2023) 7072. <https://doi.org/https://doi.org/10.1002/aoc.7072>.

[13] J. Wang, T. Liu, R. Xu, Y. Zhang, Effect of F Doping on CO<sub>2</sub> Electrocatalytic Performance of Zinc-Based Rare Earth Layered Double Hydroxides, *Catal. Letters* (2024). <https://doi.org/10.1007/s10562-023-04526-5>.

[14] S.R. Leandro, I.J. Marques, R.S. Torres, T.A. Fernandes, P.D. Vaz, C.D. Nunes, Nitroarene and dye reduction with 2:1 Co/Al layered double hydroxide catalysts – Is gold still necessary?, *Inorganica Chim. Acta* 521 (2021) 120336. <https://doi.org/10.1016/j.ica.2021.120336>.

[15] N.T. Nivangune, V. V. Ranade, A.A. Kelkar, MgFeCe Ternary Layered Double Hydroxide as Highly Efficient and Recyclable Heterogeneous Base Catalyst for Synthesis of Dimethyl Carbonate by Transesterification, *Catal. Letters* 147 (2017) 2558–2569. <https://doi.org/10.1007/s10562-017-2146-x>.

[16] S. Das, S.K. Dash, K.M. Parida, Kinetics, Isotherm, and Thermodynamic Study for Ultrafast Adsorption of Azo Dye by an Efficient Sorbent: Ternary Mg/(Al + Fe) Layered Double Hydroxides, *ACS Omega* 3 (2018) 2532–2545. <https://doi.org/10.1021/acsomega.7b01807>.

[17] S. Mallakpour, H. Tabebordbar, Layered double hydroxide polymer

nanocomposites for catalysis, Elsevier Ltd, 2020.  
<https://doi.org/10.1016/b978-0-08-101903-0.00020-9>.

[18] UN-Water, UN Water, 2021 : Summary Progress Update 2021 - SDG 6 — Water and Sanitation for All, Geneva, 2021. <https://www.unwater.org/new-data-on-global-progress-towards-ensuring-water-and-sanitation-for-all-by-2030/>.

[19] U.N.E. Programme, Marine Plastic Debris and Microplastics: Global Lessons and Research to Inspire Action and Guide Policy Change, (n.d.).  
<https://wedocs.unep.org/20.500.11822/7720>.

[20] X. Qu, J. Brame, Q. Li, P.J.J. Alvarez, Nanotechnology for a safe and sustainable water supply: Enabling integrated water treatment and reuse, *Acc. Chem. Res.* 46 (2013) 834–843. <https://doi.org/10.1021/ar300029v>.

[21] Y. Deng, R. Zhao, Advanced Oxidation Processes (AOPs) in Wastewater Treatment, *Curr. Pollut. Reports* 1 (2015) 167–176.  
<https://doi.org/10.1007/s40726-015-0015-z>.

[22] A. Ucar, M. Findik, I.H. Gubbuk, N. Kocak, H. Bingol, Catalytic degradation of organic dye using reduced graphene oxide–polyoxometalate nanocomposite, *Mater. Chem. Phys.* 196 (2017) 21–28.  
<https://doi.org/10.1016/j.matchemphys.2017.04.047>.

[23] E.M. Bakhsh, M. Ismail, U. Sharafat, K. Akhtar, T.M. Fagieh, E.Y. Danish, S.B. Khan, M.I. Khan, M.A. Khan, A.M. Asiri, Highly efficient and recoverable Ag–Cu bimetallic catalyst supported on taro-rhizome powder applied for nitroarenes and dyes reduction, *J. Mater. Res. Technol.* 18 (2022) 769–787. <https://doi.org/10.1016/j.jmrt.2022.02.062>.

[24] N. Garg, S. Bera, L. Rastogi, A. Ballal, M. V. Balaramakrishna, Synthesis and characterization of L-asparagine stabilised gold nanoparticles: Catalyst for degradation of organic dyes, *Spectrochim. Acta - Part A Mol. Biomol. Spectrosc.* 232 (2020) 118126. <https://doi.org/10.1016/j.saa.2020.118126>.

[25] I. Ahmad, G. Aalam, M. Amir, A. Chakravarty, S.W. Ali, S. Ikram, Development of highly efficient magnetically recyclable Cu<sup>2+</sup>/Cu<sup>0</sup> nano-photocatalyst and its enhanced catalytic performance for the degradation of organic contaminations, *Sci. Total Environ.* 846 (2022) 157154.  
<https://doi.org/10.1016/j.scitotenv.2022.157154>.

[26] A. Shahzaib, S. Khan, I. Ahmad, S.M. Alshehri, T. Ahamad, N. Nishat, Green synthesis of ZIF-67 composite embedded with magnetic nanoparticles and ZnO decoration for efficient catalytic reduction of rhodamine B and methylene blue, *Chem. Inorg. Mater.* 2 (2024) 100037.  
<https://doi.org/10.1016/j.cinorg.2024.100037>.

[27] J. Pathak, P. Singh, Synthesis and Characterization of Ternary Layered Double Hydroxide containing Zinc/Copper/Nickel and its PANI Composite, *Polym. Compos.* 43 (2022) 7836.

https://doi.org/https://doi.org/10.1002/pc.26895.

[28] H.C. Greenwell, W. Jones, D.N. Stamires, P. O'Connor, M.F. Brady, A one-pot synthesis of hybrid organo-layered double hydroxide catalyst precursors, *Green Chem.* 8 (2006) 1067–1072. <https://doi.org/10.1039/b605851e>.

[29] L. Poul, N. Jouini, F. Fievet, Layered hydroxide metal acetates (metal = zinc, cobalt, and nickel): Elaboration via hydrolysis in polyol medium and comparative study, *Chem. Mater.* 12 (2000) 3123–3132. <https://doi.org/10.1021/cm991179j>.

[30] S.P. Newman, W. Jones, Comparative Study of Some Layered Hydroxide Salts Containing Exchangeable Interlayer Anions, *J. Solid State Chem.* 148 (1999) 26–40. <https://doi.org/10.1006/jssc.1999.8330>.

[31] A. Kasai, S. Fujihara, Layered single-metal hydroxide/ethylene glycol as a new class of hybrid material, *Inorg. Chem.* 45 (2006) 415–418. <https://doi.org/10.1021/ic051528d>.

[32] T.S. Kazeem, M. Zubair, M. Daud, N.D. Mu'azu, M.A. Al-Harthi, Graphene/ternary layered double hydroxide composites: Efficient removal of anionic dye from aqueous phase, *Korean J. Chem. Eng.* 36 (2019) 1057–1068. <https://doi.org/10.1007/s11814-019-0284-0>.

[33] R. Valéro, B. Durand, J.L. Guth, T. Chopin, Hydrothermal synthesis of porous zircon in basic fluorinated medium, *Microporous Mesoporous Mater.* 29 (1999) 311–318. [https://doi.org/10.1016/S1387-1811\(98\)00344-8](https://doi.org/10.1016/S1387-1811(98)00344-8).

[34] G. Carja, R. Nakamura, T. Aida, H. Niiyama, Textural properties of layered double hydroxides: Effect of magnesium substitution by copper or iron, *Microporous Mesoporous Mater.* 47 (2001) 275–284. [https://doi.org/10.1016/S1387-1811\(01\)00387-0](https://doi.org/10.1016/S1387-1811(01)00387-0).

[35] M. Thomas, G.A. Naikoo, M.U.D. Sheikh, M. Bano, F. Khan, Fabrication of hierarchically organized nanocomposites of Ba/alginate/carboxymethylcellulose/graphene oxide/Au nanoparticles and their catalytic efficiency in o-nitroaniline reduction, *New J. Chem.* 39 (2015) 9761–9771. <https://doi.org/10.1039/c5nj01765c>.

[36] S. Wunder, F. Polzer, Y. Lu, Y. Mei, M. Ballauff, Kinetic analysis of catalytic reduction of 4-nitrophenol by metallic nanoparticles immobilized in spherical polyelectrolyte brushes, *J. Phys. Chem. C* 114 (2010) 8814–8820. <https://doi.org/10.1021/jp101125j>.

[37] J. Gu, S. Kan, Q. Shen, J. Kan, Effects of sulfanilic acid and anthranilic acid on electrochemical stability of polyaniline, *Int. J. Electrochem. Sci.* 9 (2014) 6858–6869. [https://doi.org/10.1016/s1452-3981\(23\)10936-9](https://doi.org/10.1016/s1452-3981(23)10936-9).

[38] Y. Sha, I. Mathew, Q. Cui, M. Clay, F. Gao, X.J. Zhang, Z. Gu, Rapid degradation of azo dye methyl orange using hollow cobalt nanoparticles, *Chemosphere* 144 (2016) 1530–1535. <https://doi.org/10.1016/j.chemosphere.2015.10.040>.

[39] M.H. Mohamed, L.D. Wilson, J. V. Headley, K.M. Peru, Screening of oil sands naphthenic acids by UV-Vis absorption and fluorescence emission spectrophotometry, *J. Environ. Sci. Heal. - Part A Toxic/Hazardous Subst. Environ. Eng.* 43 (2008) 1700–1705.  
<https://doi.org/10.1080/10934520802330255>.

[40] Y. Zhang, F. Gao, B. Wanjala, Z. Li, G. Cernigliaro, Z. Gu, High efficiency reductive degradation of a wide range of azo dyes by SiO<sub>2</sub>-Co core-shell nanoparticles, *Appl. Catal. B Environ.* 199 (2016) 504–513.  
<https://doi.org/10.1016/j.apcatb.2016.06.030>.

[41] H. Dan, Y. Song, Y. Xu, Y. Gao, W. Kong, Y. Huang, Q. Yue, B. Gao, Green synthesis of Cu nanoparticles supported on straw-graphene composite for catalytic reduction of p-nitrophenol, *J. Clean. Prod.* 283 (2021) 124578.  
<https://doi.org/10.1016/j.jclepro.2020.124578>.

[42] H.I. Salaheldin, Chitosan Molecular Weight Effects on The Synthesis of Gold Nanoparticles and Catalytic Degradation of Environmental Pollutants, *J. Adv. Phys.* 14 (2018) 5388–5405.

[43] M. Dinari, F. Dadkhah, Swift reduction of 4-nitrophenol by easy recoverable magnetite-Ag/layered double hydroxide/starch bionanocomposite, *Carbohydr. Polym.* 228 (2020) 115392. <https://doi.org/10.1016/j.carbpol.2019.115392>.

[44] R. Das, V.S. Sypu, H.K. Paumo, M. Bhaumik, V. Maharaj, A. Maity, Silver decorated magnetic nanocomposite (Fe<sub>3</sub>O<sub>4</sub>@PPy-MAA/Ag) as highly active catalyst towards reduction of 4-nitrophenol and toxic organic dyes, *Appl. Catal. B Environ.* 244 (2019) 546–558.  
<https://doi.org/10.1016/j.apcatb.2018.11.073>.

[45] X. Zhou, J. Shi, X. Bai, Ultrasonic assisted preparation of ultrafine Pd supported on NiFe-layered double hydroxides for p-nitrophenol degradation, *Environ. Sci. Pollut. Res.* 29 (2022) 56178–56199.  
<https://doi.org/10.1007/s11356-022-19641-w>.

[46] Z.H. Farooqi, R. Khalid, R. Begum, U. Farooq, Q. Wu, W. Wu, M. Ajmal, A. Irfan, K. Naseem, Facile synthesis of silver nanoparticles in a crosslinked polymeric system by in situ reduction method for catalytic reduction of 4-nitroaniline, *Environ. Technol. (United Kingdom)* 40 (2019) 2027–2036.  
<https://doi.org/10.1080/09593330.2018.1435737>.

[47] S.G. Jiji, K.G. Gopchandran, Shape dependent catalytic activity of unsupported gold nanostructures for the fast reduction of 4-nitroaniline, *Colloids Interface Sci. Commun.* 29 (2019) 9–16.  
<https://doi.org/10.1016/j.colcom.2018.12.003>.

[48] A. Khalil, A. Khan, T. Kamal, A.A.P. Khan, S.B. Khan, M.T.S. Chani, K.A. Alzahrani, N. Ali, Zn/Al layered double hydroxide and carboxymethyl cellulose composite beads as support for the catalytic gold nanoparticles and their applications in the reduction of nitroarenes, *Int. J. Biol. Macromol.* 262

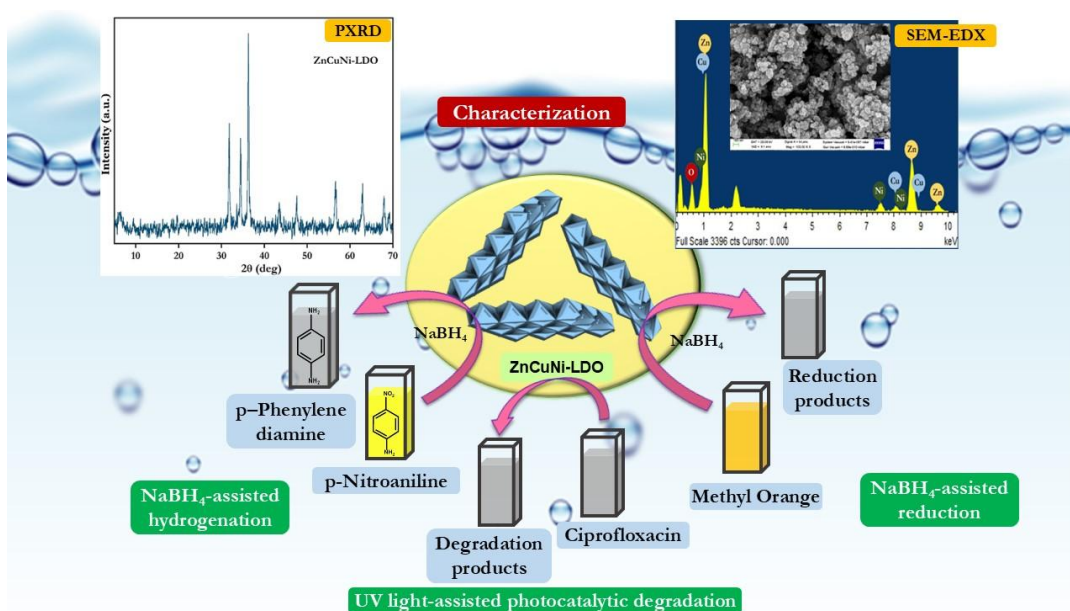
(2024) 129986. <https://doi.org/10.1016/j.ijbiomac.2024.129986>.

[49] M.J. Latif, S. Ali, S. Jamil, S. Bibi, T. Jafar, A. Rasheed, S. Noreen, A. Bashir, S. Rauf Khan, Comparative catalytic reduction and degradation with biodegradable sodium alginate based nanocomposite: Zinc oxide/N-doped carbon nitride/sodium alginate, *Int. J. Biol. Macromol.* 254 (2024) 127954. <https://doi.org/10.1016/j.ijbiomac.2023.127954>.

[50] M. Alle, S.H. Lee, J.C. Kim, Ultrafast synthesis of gold nanoparticles on cellulose nanocrystals via microwave irradiation and their dyes-degradation catalytic activity, *J. Mater. Sci. Technol.* 41 (2020) 168–177. <https://doi.org/10.1016/j.jmst.2019.11.003>.

**CHAPTER - 3**

**SYNTHESIS, CHARACTERIZATION AND CATALYTIC APPLICATIONS OF ZnCuNi-TERNARY LAYERED DOUBLE OXIDE FOR REDUCTION AND DEGRADATION OF ORGANIC POLLUTANTS**



# **CHAPTER - 3**

## **SYNTHESIS, CHARACTERIZATION AND CATALYTIC APPLICATIONS OF ZnCuNi-TERNARY LAYERED DOUBLE OXIDE FOR REDUCTION AND DEGRADATION OF ORGANIC POLLUTANTS**

---

### **3.1 Introduction**

Layered double hydroxides (LDHs) are a class of network solids that can act as multifarious catalytic materials by virtue of their lamellar structures, high specific surface area, basicity, and porosity. The components of a typical LDH lattice include divalent ( $M^{II}$ ) and trivalent ( $M^{III}$ ) cations in the layers, along with exchangeable anions and water molecules present in the interlamellar region due to which they can be easily tailored to serve various applications. One important aspect related to LDHs is that they can be heat-treated at moderate temperatures to lose the interlayer water molecules and anions, thereby leading to their topotactic transformation into layered double oxides (LDOs) that possess high porosity and surface areas[1]. This methodology can provide a simple pathway to obtain new-age materials with enhanced physicochemical and catalytic properties. These properties are an outcome of the homogenous distribution of the metal cations throughout their matrix, that is often difficult to achieve through conventional laboratory techniques. Moreover, these LDOs possess high thermal stability, and their outer surface is covered with an abundance of Lewis acidic and basic sites that are immensely beneficial for carrying out reduction and hydrogenation reactions[2]. In order to enhance these features, the incorporation of transition metals can be a suitable plan to improve the functionality and performance of LDOs since it helps in augmentation of the optical, electronic, and magnetic properties of these materials that give rise to synergistic interactions in the lattice. Several beneficial factors such as: (1) ability to attain variable oxidation states, (2) ability to strongly interact with various types of anionic, cationic, and neutral ligands, and (3) lattice defects and distortions make them the perfect addition to

enhance the features of LDOs. Additionally, since LDOs possess large surface areas with an abundance of easily accessible active sites, a large number of pores having optimum pore size and volume, as well as high chemical and thermal stability, they are ideal materials for various applications[3–5]. These factors contribute immensely towards the viability of LDOs as efficient materials for several applications. Till now, LDOs containing two metals, called binary LDOs, have garnered the majority of attention, but now the incorporation of third metal cation in the LDO lattice is being actively explored. The developments in this area aim to exploit the features of all three metal cations, since incorporation of a third cation holds the potential to enhance as well as alter the properties and performances of pre-existing lattices. The third cation can help in increasing the tailorability as well as fine-tuning the properties of ternary LDOs, due to the stronger synergistic interactions between the three cations, leading to an increase in the number and diversity of active sites and demonstration of enhanced activities in a broader range of applications. For instance, Xiang et al. synthesized ternary  $\text{MgO}/\text{ZnO}/\text{In}_2\text{O}_3$  heterostructured photocatalyst by calcination of  $\text{MgZnIn-LDH}$  at 300 °C, 500 °C and 800 °C, and evaluated its photocatalytic performance for the degradation of cationic methylene blue (MB) dye[1]. In another study, flower-like LDO composed of Zn, Al and In cations was synthesized by Yuan et al. using a hydrothermal method, and it was utilized for the fabrication of a microsphere electrode for zinc-nickel secondary batteries[2]. The addition of indium increases the specific surface area and porosity of the lattice, that contributes to inhibition of self-corrosion in the electrode, thereby improving electrochemical performance. Therefore, the possibility of using LDO in the field of catalysis and wastewater remediation may be combined effectively to curb the problem of potable water availability due to increasing water pollution.

In recent decades, wastewater treatment has become the need of the hour due to the dwindling availability of freshwater resources. The presence of toxins such as dyes and pigments, drugs, cosmetics, surfactants, pesticides, heavy metals, etc., affects the quality and aesthetic appearance of water sources while also exerting detrimental impacts on flora and fauna due to their carcinogenic and mutagenic properties. Specifically, nitroarene compounds (NACs), azo dyes, and pharmaceutical drugs are a

few of the most pernicious refractory pollutants that currently threaten our ecosystem. For instance, methyl orange (MO), an anionic azo dye, is a common pH indicator and textile dyeing agent wherein the presence of highly stable azo (-N=N-) chromophore group is responsible for the bright orange color of MO dye. According to several reports, MO has been found to be toxic and excessive exposure to MO may cause skin and eye irritation, nausea, and diarrhea[6,7]. The consumption of these toxic compounds, even in low quantities, can have major detrimental impacts on human, plant, and animal health, and their ability to bioaccumulate in marine flora and fauna further drives their toxicity on consumption throughout the various trophic levels. NACs such as *p*-Nitroaniline (*p*-NA) possess mutagenic traits and can cause severe issues such as methemoglobinemia, rashes, and toxicity on skin contact, and inhalation and ingestion have the potential to cause anaemia, liver damage, and even death. In addition, ciprofloxacin is a third-generation fluoroquinolone antibiotic used for the treatment of bacterial infections, and approximately 20-60% is excreted in active form into water bodies, leading to contamination. Ciprofloxacin (CIF) is a recalcitrant substance and gets accumulated in aquatic systems, resulting in the promotion of antimicrobial resistance (AMR) in environmental bacteria as well as the disruption of key ecosystem services performed by microbes, such as decomposition. By virtue of their high chemical and thermal stability, the sequestration of these pollutants from water bodies holds utmost importance in order to fulfill the exponentially increasing water needs across the globe. Although the removal of these pollutants has been attempted using several separation methods but these existing methodologies are not quite effective at removing such pollutants, and they also result in secondary pollutant production, thereby reducing their efficiency towards water treatment[8–11]. Furthermore, these methods are also plagued by several inherent issues like membrane fouling, adsorbent aggregation, toxic sludge formation, etc., that become a cause of concern and increase treatment costs, thereby limiting their real-time profitable usage. Thus, the development of alternative novel methodologies for the elimination of pollutants from water bodies has become an area of concern[12].

Among the various methodologies employed for water remediation, a great amount of success has been achieved with catalytic methods. Catalytic treatment of wastewater

for its purification includes the utilization of methodologies such as catalyst-assisted reduction, photocatalysis, transfer hydrogenation, Fenton process, etc. Specifically, NaBH<sub>4</sub>-assisted reduction and photocatalysis are two of the most highly advantageous methods used for contaminant degradation in aqueous medium. Photocatalysis involves the light-stimulated breakdown of pollutant molecules using a photocatalytic material that drives the chemical reaction by absorbing photons and generating electron-hole pairs, thereby helping in the formation of the reactive species[13]. The most commonly used photocatalysts include TiO<sub>2</sub> and ZnO, but there is immense scope for exploring materials that overcome the disadvantages of these materials such as wide bandgaps and catalyst deactivation. Meanwhile, NaBH<sub>4</sub>-assisted reduction involves the use of NaBH<sub>4</sub> as a reducing agent along with a catalyst for toxin elimination and production of water and carbon dioxide as benign by-products. NaBH<sub>4</sub> provides BH<sub>4</sub><sup>-</sup> anions that become the source of H<sub>2</sub> and electrons for molecule breakdown, while the catalyst aids the reaction's progress by making it kinetically feasible. The alignment of these catalyst-based methods with the principles of green chemistry combined with their advantages such as lower energy requirement and easy usability, universality and selectivity, possible synthesis of commercially viable by-products, high efficiency at low concentrations as well as the ease of separation of catalyst render them as highly suitable treatment processes for elimination of NACs, azo dye, and drugs from aqueous medium. The principal focus of catalytic processes lies on the breakdown, degradation, and mineralization of contaminant species, rather than their physical separation from the medium, that is often the mechanism of other treatment methods. This, in turn, warrants highly efficacious toxin removal while eliminating any possibilities of secondary pollutant formation and water wastage.

In this avenue, LDH-derived LDOs have carved a niche for themselves due to their unique physicochemical features such as synergistic effects between constituent metal cations, diverse active sites, and redox properties. However, the use of LDOs as photocatalytic materials for the degradation of drugs is extremely limited, and their utility in reductant-assisted reduction of toxins remains severely unexplored[14,15]. In this respect, transition metal-based LDOs can prove to be an excellent choice since they exhibit a myriad of exemplary catalytic properties due to the synergistic

interactions between the transition metals in the lattice. The use of zinc, copper, and nickel in LDOs is especially beneficial since these metals are abundantly available in nature and their extraction and processing are simple and economical. Their unique electronic structures give rise to electron transport and relay abilities, broad bandgaps (3.3 – 4.0 eV), high mechanical and thermal stabilities, as well as electron defects[16–18]. Due to their high surface areas and large number of active sites, these cations are able to adsorb and activate various molecules on their surface. The tailorability of their oxidation states often results in their use for the fabrication of superior homogenous (eg, organometallic complexes) and heterogeneous catalysts (eg, LDHs, Metal-organic frameworks (MOF)) by combining them with a variety of anionic, cationic, and neutral ligands. Additionally, their morphologies can be easily tailored, giving rise to special microstructures, and they often possess pyro- and piezo-electric properties along with special electronic, optical, and magnetic properties that can prove to be beneficial for a wide array of catalytic applications[9,19]. For instance, Murugahandham et al. reported the synthesis of ZnO nanobundles and employed them for the catalytic ozonation of 2-ethyl ethoxy acetate[18]. Belay et al. synthesized zero-valent copper and copper oxides using different precursors and studied their catalytic ability for the reduction of  $\text{NO}_3^-$  to  $\text{NO}_2^-$ [20]. In another study, Bhosale et al. reported the use of NiO nanorods for the catalytic synthesis of substituted benzimidazole, benzoxazole and benzothiazole[21]. But inspite of their several favourable characteristics, the combined use of Zn, Cu and Ni in LDHs and LDH derivatives remains scarcely reported. Furthermore, although few reports describing the use of LDHs for catalytic reduction of azo dyes and *p*-nitroaniline are available in literature, but virtually no reports describe the use of LDH-derived ZnCuNi-LDOs for catalytic reduction of organic pollutants[22–24].

Therefore, this work aims to explore the synthesis of ZnCuNi-LDO by the calcination of ZnCuNi-LDH[25]. The synthesized LDO was applied as a heterogeneous catalyst for the hydrogenation of *p*-NA and reduction of MO pollutants as well as the photocatalytic degradation of CIF, and kinetics analysis for the catalysis reactions were carried out. It was observed that ZnCuNi-LDO exhibited excellent catalytic

efficiencies and fast reaction rates for the hydrogenation of *p*-nitroaniline, reduction of methyl orange and degradation of CIF in short intervals of time.

### 3.2 Experimental

#### 3.2.1 Materials

Zinc acetate dihydrate  $\text{Zn}(\text{CH}_3\text{COO})_2 \cdot 2\text{H}_2\text{O}$  (Merck, 98.0% purity), copper acetate monohydrate  $\text{Cu}(\text{CH}_3\text{COO})_2 \cdot \text{H}_2\text{O}$  (Merck, 98.0% purity), hydrogen peroxide  $\text{H}_2\text{O}_2$  (Merck, 30%), acetic acid glacial 100%  $\text{CH}_3\text{COOH}$  (Merck), and nickel acetate tetrahydrate  $\text{Ni}(\text{CH}_3\text{COO})_2 \cdot 4\text{H}_2\text{O}$  (CDH, 98.00% purity),  $\text{NaBH}_4$  (Sigma Aldrich,  $\geq 98.00\%$ ), *p*-Nitroaniline (GLR chemicals, 99.00%), Methyl Orange (Merck) and Ciprofloxacin (CDH Chemicals) were of analytical grade unless otherwise stated, and were used as received without purification. Table 3.1 gives information about the structure,  $\lambda_{\text{max}}$  and molecular formulas of model pollutant molecules employed in this study.

**Table 3.1** Structure and formula of model pollutants employed in the study.

Model Pollutant	Structure	$\lambda_{\text{max}}$ (nm)	Molecular Formula
<i>p</i> -Nitroaniline		380	$\text{C}_6\text{H}_6\text{N}_2\text{O}_2$
Methyl Orange		466	$\text{C}_{14}\text{H}_{14}\text{N}_3\text{NaO}_3\text{S}$
Ciprofloxacin		276	$\text{C}_{17}\text{H}_{18}\text{FN}_3\text{O}_3$

### 3.2.2 Synthesis of ZnCuNi-LDO

ZnCuNi-LDO was prepared by the thermal treatment of ZnCuNi-LDH precursor as per the methodology described by Pathak et al.[26]. Briefly, 10 mL aqueous solutions of 4.249 mmol zinc acetate dehydrate, 0.37 mmol copper acetate monohydrate, and 0.37 mmol nickel acetate tetrahydrate were prepared by stirring, following which they were mixed. Then, 5 mL  $H_2O_2$  and 30 mL distilled water were added to the metal salts solution, and the resulting solution was sonicated for 30 minutes. Subsequently, the reaction mixture was stirred for 24 hours and then placed in oven at 60°C till complete removal of solvent was achieved. The obtained ZnCuNi-LDH precursor was then placed in silica crucible and calcined in muffle furnace at 350 °C for 6 hours to obtain black-greyish colored ZnCuNi-LDO. The schematic representation of ZnCuNi-LDO synthesis is shown in Figure 3.1.

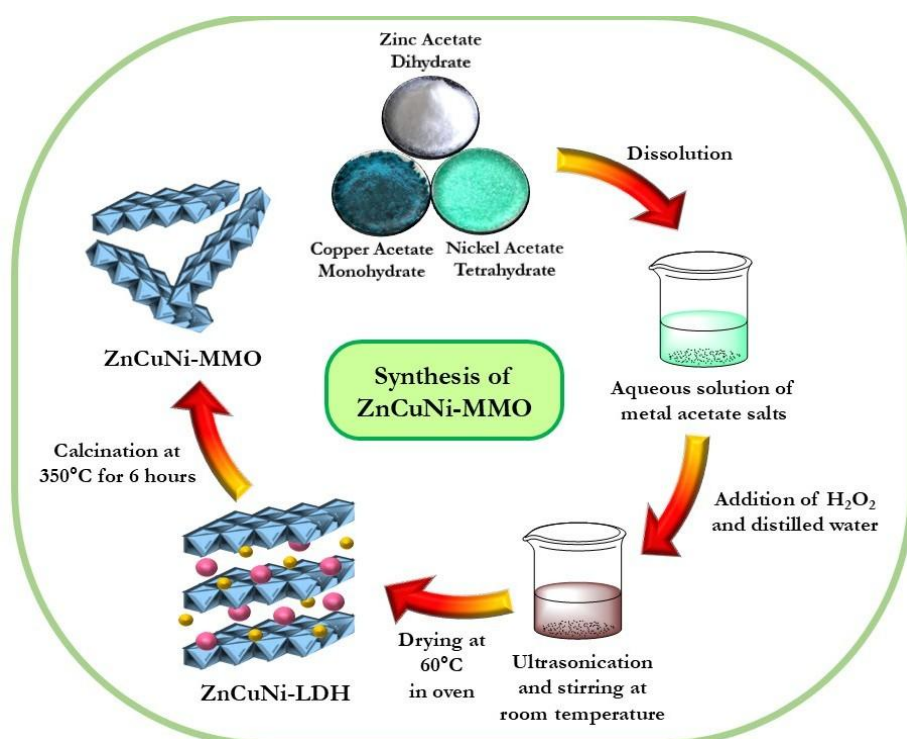


**Figure 3.1** Schematic representation of synthesis of ZnCuNi-LDO.

### 3.2.3 Catalytic activity of ZnCuNi-LDO

#### 3.2.3.1 NaBH<sub>4</sub>-assisted catalytic reduction

The catalytic ability of ZnCuNi-LDO for hydrogenation of *p*-nitroaniline (*p*-NA) and reduction of azo dye methyl orange (MO) were studied in presence of sodium borohydride (NaBH<sub>4</sub>) that acted as reducing agent. For this purpose, UV-Vis spectrophotometry was employed due to the distinct colouration of the chosen model contaminants.

For the hydrogenation of *p*-nitroaniline, *p*-NA solution (1mL, 1 mM) was mixed well with 1 mL of distilled water, followed by the addition of freshly prepared NaBH<sub>4</sub> solution (1 mL, 100 mM). After this, the catalytic reaction was initiated by addition of 0.001 g ZnCuNi-LDO to the reaction mixture. The progress of the hydrogenation reaction was determined by recording the absorption spectrum of p-NA at  $\lambda_{max} = 380$  nm using a UV-visible spectrophotometer at one-minute intervals till the solution was completely decolorized.

The catalytic reduction of MO dye using ZnCuNi-LDO was evaluated in a similar manner. MO solution (1 mL, 100 ppm) was mixed well with 1 mL distilled water and 1 mL of freshly prepared 100 mM NaBH<sub>4</sub> solution. Then 0.001 g LDO was added to the reaction mixture, and the reaction progress was determined by recording the absorption spectrum at  $\lambda_{max} = 466$  nm at one-minute intervals till complete decolorization of the solution.

The percentage degradation of *p*-NA and MO was calculated using Equation 3.1:

$$\text{Percentage degradation} = \frac{(C_0 - C_t)}{C_0} \times 100 \quad (3.1)$$

where C<sub>0</sub> and C<sub>t</sub> denote the concentrations of *p*-NA and MO solutions at zero time and time *t* respectively.

### 2.2.2 Photocatalytic Activity

Light-stimulated catalytic activity of the as-synthesized catalyst was investigated by degrading CIF drug under UV light illumination at room temperature using a custom-made photocatalytic reactor. The reactor set-up consisted of a dual-walled quartz tube that encased a high-pressure mercury vapour lamp (OSRAM India, 125 W) used for

providing UV light. The tube was immersed in a double-walled pyrex glass vessel and water circulation was maintained around the tube and vessel to avoid thermal effects. The entire set-up was housed in a dark wooden box to avoid any interaction with external light sources. To evaluate the photocatalytic activity, 0.05 g ZnCuNi-LDO was suspended in 100 mL of 20 ppm CIF aqueous solution in the photoreactor. The suspension of catalyst and drug solution was first stirred for 30 minutes in the absence of illumination in order to establish adsorption-desorption equilibrium. After removal of 3 mL aliquot from the suspension, the UV illumination was initiated and then aliquots were sampled at pre-fixed interval of 30 minutes. The retrieved solutions were centrifuged to remove solid component and their concentrations were determined by measuring absorbance at  $\lambda_{max} = 276$  nm for CIF using Shimadzu UV-Vis spectrophotometer. Percentage drug degradation of CIF was calculated using previously mentioned Eqn 3.1.

### 3.3 Results and Discussion

#### 3.3.1 Characterisation Details

The conversion of LDH to LDO can be achieved by simply thermally treating the LDH precursor at optimal temperature in order to maintain the advantageous features of LDHs while converting the hydroxide lattice to oxide. Therefore, to ascertain the temperature at which LDH should be calcined for its conversion to LDO, TGA technique was adopted and the obtained thermogram is presented in Figure 3.2. Thermal degradation of ZnCuNi-LDH due to calcination was found to be a three-step process involving the initial elimination of physisorbed and intercalated water molecules upto 215°C, followed by the subsequent decarboxylation, dehydroxylation and removal of interlayer acetate ions from the LDH lattice upto 350°C, resulting in the breakdown of lamellar structure of LDHs to form pure phase layered double oxide (LDO)[27]. Based on the above results, the optimal temperature for synthesis of ZnCuNi-LDO by calcination of ZnCuNi-LDH was found to be 350°C.

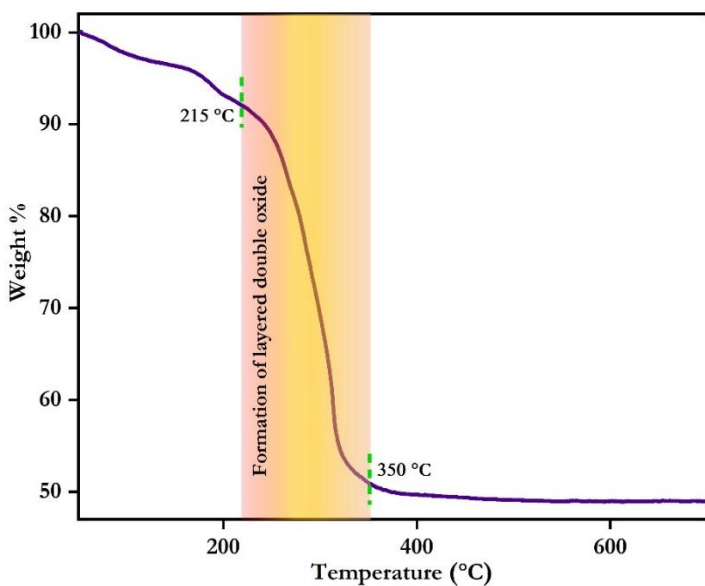


**Figure 3.2** TGA thermogram of ZnCuNi-LDH.

In order to evaluate the conversion of LDH to LDO and determine their crystallographic features, PXRD technique was utilised. The PXRD pattern of ZnCuNi-LDH, presented in Figure 3.3, was found to be consistent with the typical pattern of hydrotalcite-type materials, thereby corroborating the formation of highly crystalline LDH having pure phase with no impurities. The *d*-spacing for characteristic (002) plane was 7.41 Å and was in coherence with values previously reported in literature[28].

Upon calcination, collapse of the layered structure was expected, and it was corroborated by the disappearance of characteristic reflections of LDH in PXRD diffractogram. Furthermore, the emergence of new reflections at 31.8°, 34.56° and 36.39° was observed. These peaks were found to correspond to (100), (002), and (101) *hkl* planes of crystalline ZnO existing in the hexagonal wurtzite arrangement[29]. The lack of any reflections suggesting impurity, coupled with the above observations, suggested the formation of pure phase ZnCuNi-LDO. Additionally, it is crucial to highlight the absence of peaks corresponding to CuO and NiO, that may be attributed to the presence of Cu and Ni in very small ratios in the lattice. Therefore, on comparing the PXRD results of LDH and LDO, the hypothesis that thermal treatment of LDH at optimum temperature resulted in the successful formation of pure and homogenous LDO was supported[30]. Additionally, the average crystallite size, calculated using the Debye-Scherrer equation, was found to be 24.89 nm.

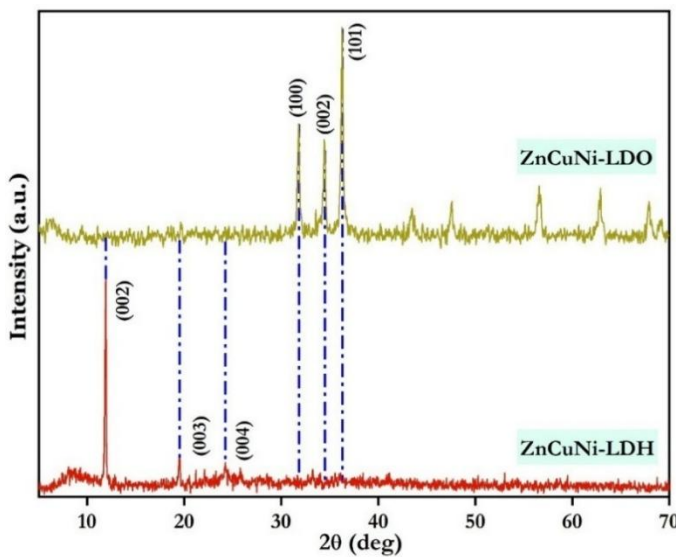


**Figure 3.3** Comparative plot of PXRD patterns of ZnCuNi-LDH and ZnCuNi-LDO.

The surface morphology and microstructure of ZnCuNi-LDO were analysed using SEM-EDX technique. The SEM micrograph presented in Figure 3.4a shows the absence of plate-like morphology due to layered structure of LDH and clearly indicated the presence of irregular spherical aggregates, thereby confirming the formation of LDO[31]. Further, presence of Zn, Cu and Ni was confirmed using EDX spectrum that clearly showed their homogeneous distribution in the lattice (Figure 3.4b).

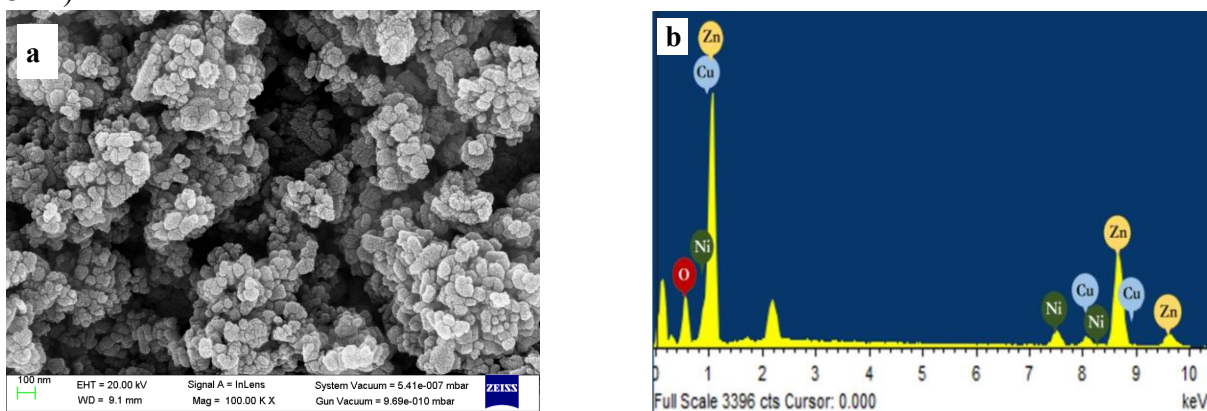


**Figure 3.4** (a) SEM micrograph and (b) EDX spectrum of ZnCuNi-LDO.

Surface area is a critical parameter that has a profound effect on the catalytic activity of a material. The specific surface area ( $S_{BET}$ ) and pore structure of ZnCuNi-LDO were investigated using  $N_2$  adsorption-desorption study by BET analysis (Figure 3.5a-b).  $S_{BET}$  was found to be  $25.617 \text{ m}^2 \text{ g}^{-1}$ , while the values of pore volume and average pore

diameter, calculated using the BJH method, were found to be  $0.174 \text{ cc g}^{-1}$  and  $25.206 \text{ nm}$  respectively. The shape of the isotherm was found to be similar to Type-IV, as described by IUPAC classification, and it was inferred that synthesized ZnCuNi-LDO possessed mesoporosity. The appearance of H3-type hysteresis loop indicated the existence of narrow slit-shaped pores in the mesoporous ZnCuNi-LDO aggregates[32]. The formation of pores may have been the consequence of the calcination of ZnCuNi-LDH. Therefore, the textural properties described above render ZnCuNi-LDO as suitable materials for catalytic applications.

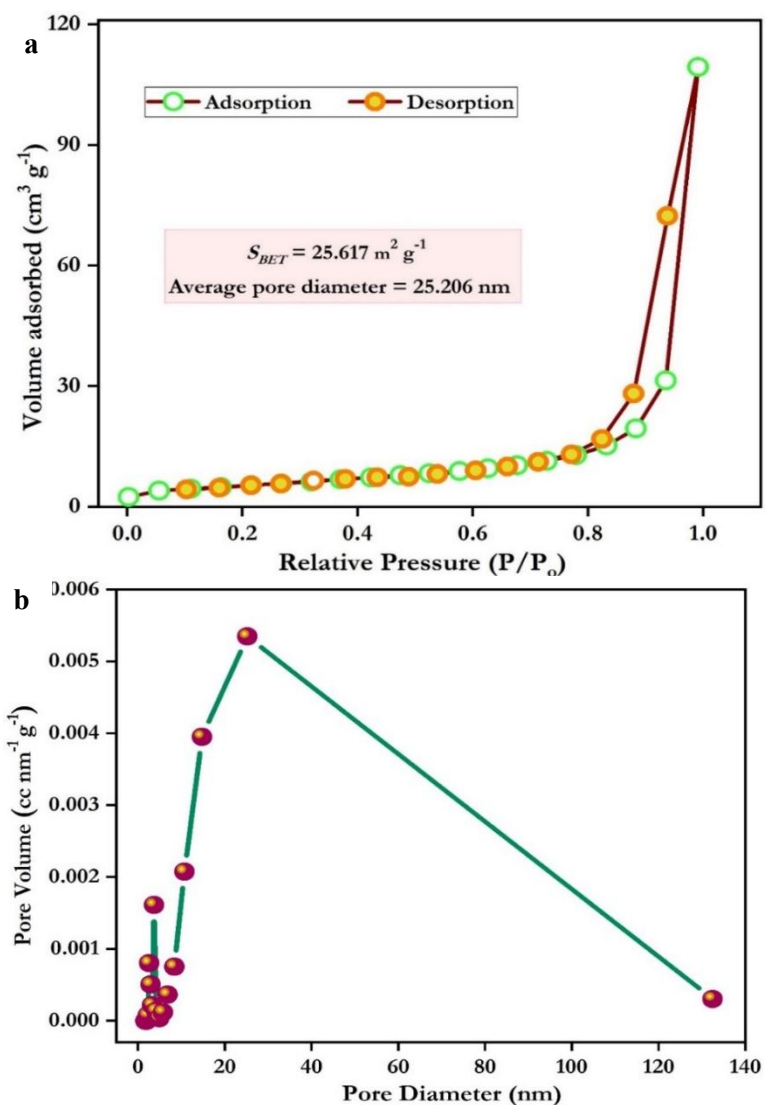


**Figure 3.5** (a)  $N_2$  adsorption-desorption isotherm and (b) corresponding pore size distribution plots of ZnCuNi-LDO.

### 3.3.2 Catalytic Activity

#### 3.3.2.1 NaBH<sub>4</sub>-assisted Catalytic reduction

The catalytic behaviour of ZnCuNi-LDO for the NaBH<sub>4</sub>-assisted hydrogenation of *p*-NA and reduction of MO was examined using time-dependent UV-Visible spectrophotometry. In the catalytic experiment, the rate of reaction was assumed to be independent of NaBH<sub>4</sub> concentration since NaBH<sub>4</sub> (100 mM) was in excess. Therefore, kinetics of the hydrogenation of *p*-NA and catalytic reduction of MO were evaluated in accordance with the pseudo-first order model presented in Equation 3.2 as follows:

$$\ln\left(\frac{C_t}{C_0}\right) = K \quad (3.2)$$

Where C<sub>0</sub> and C<sub>t</sub> are the initial and final concentrations of *p*-NA and MO.

The reaction rates were evaluated in terms of comparative absorptive intensity based on the Beer-Lambert's law (Equation 3.3) using Equation 3.4:

$$A = \varepsilon Cl \quad (3.3)$$

$$\ln\left(\frac{C_t}{C_0}\right) = \ln\left(\frac{A_t}{A_0}\right) = kt \quad (3.4)$$

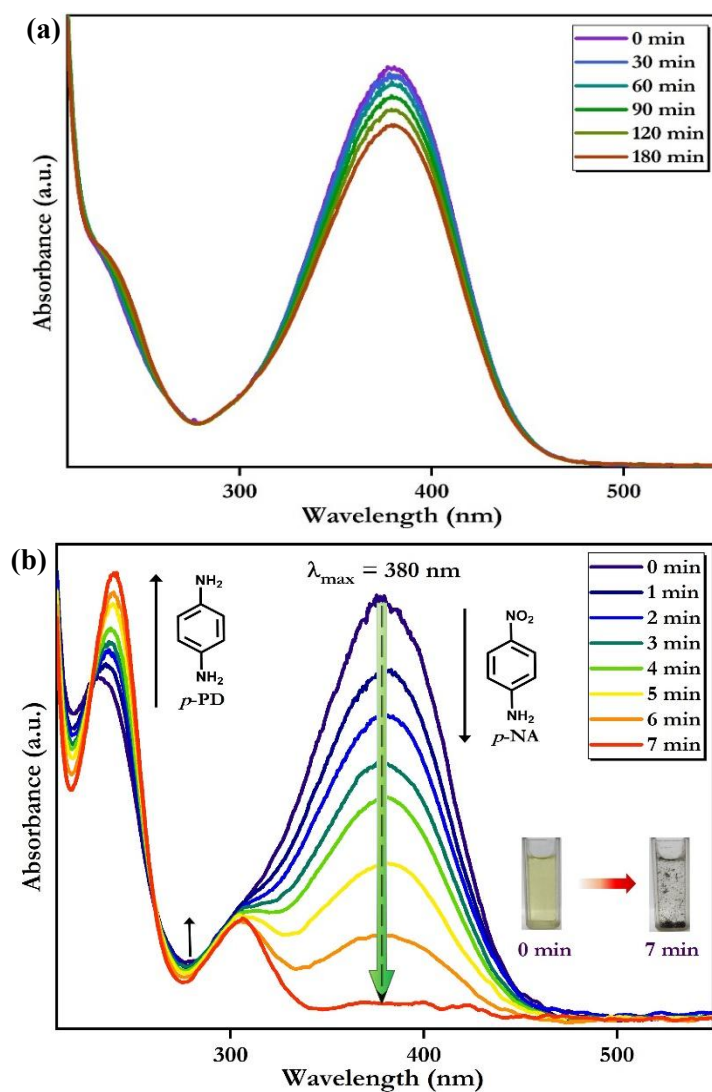
Where A<sub>0</sub> and A<sub>t</sub> are the initial and final absorbance of pollutant molecules while *k* denotes rate constant.

#### 3.3.2.1.1 Catalytic hydrogenation of *p*-NA

The hydrogenation product of *p*-NA, i.e. *p*-phenylenediamine (*p*-PD) is an important commercial product and thus the hydrogenation of *p*-NA by ZnCuNi-LDO was evaluated in the presence of excess NaBH<sub>4</sub>[33–35]. The time-dependent UV-Visible spectrum was recorded at  $\lambda_{max} = 380$  nm to monitor the hydrogenation of *p*-NA.

Initially, hydrogenation of *p*-NA was examined in the presence of only NaBH<sub>4</sub> in order to determine the role of the catalyst. The time-dependent UV-Visible spectra of *p*-NA hydrogenation using NaBH<sub>4</sub> are presented in Figure 3.6a. It was observed that when only NaBH<sub>4</sub> was added to the reaction mixture, there was a very slow decrease in the absorbance of *p*-NA, resulting in only 13.86% hydrogenation of *p*-NA even after 3 hours. However, upon addition of ZnCuNi-LDO to the reaction mixture, it was observed that the intensity of peak at  $\lambda_{max} = 380$  nm corresponding to *p*-NA began decreasing at a rapid rate and eventually disappeared after 7 minutes (Figure 3.6b).

The percentage removal efficiency, calculated using Eqn 3.1 was found to be 96.98%. The hydrogenation of *p*-NA due to conversion of the nitro group to amine group (-NH<sub>2</sub>) was further confirmed by visual examination of the reaction mixture that showed change in colour from bright yellow to colourless. Furthermore, the appearance of new peaks at 240 nm and 304 nm confirmed the formation of *p*-phenylenediamine (*p*-PD) as the hydrogenation product of *p*-NA (Table 3.2)[36]. Therefore, it was concluded that the addition of ZnCuNi-LDO to the reaction mixture was essential for the efficient hydrogenation of *p*-NA. The rate of reaction was evaluated by monitoring the decrease in absorbance of *p*-NA at  $\lambda_{max} = 380$  nm, and rate constant of reduction (*k*) was determined by linearly plotting  $\ln (C_f/C_0)$  versus reaction time *t* (min). Therefore, *k* was calculated from the kinetics data using Eqn 3.4 by employing the pseudo-first-order model and was found to be  $0.402\text{ min}^{-1}$  ( $R^2 = 0.74$ ) (Figure 3.6c).



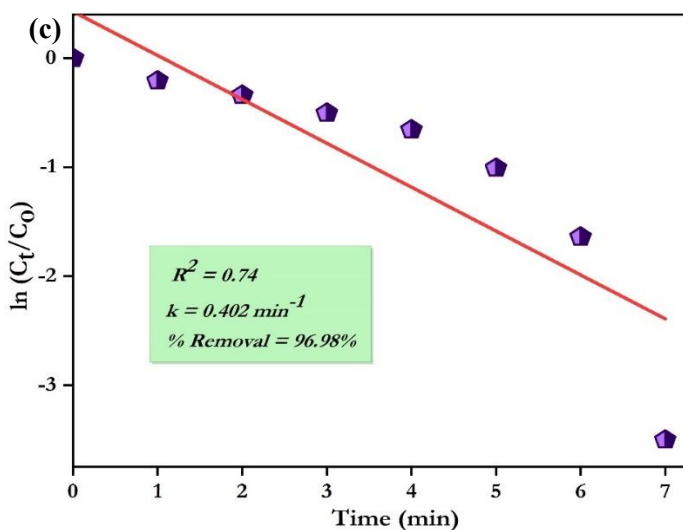


**Figure 3.6** Time-dependent UV-Vis absorption spectrum of hydrogenation of *p*-NA using (a) only  $\text{NaBH}_4$  (b) using  $\text{NaBH}_4$  and  $\text{ZnCuNi-LDO}$ , and (c) linear regression of pseudo-first kinetics model for the  $\text{NaBH}_4$ -assisted hydrogenation of *p*-NA using  $\text{ZnCuNi-LDO}$ .

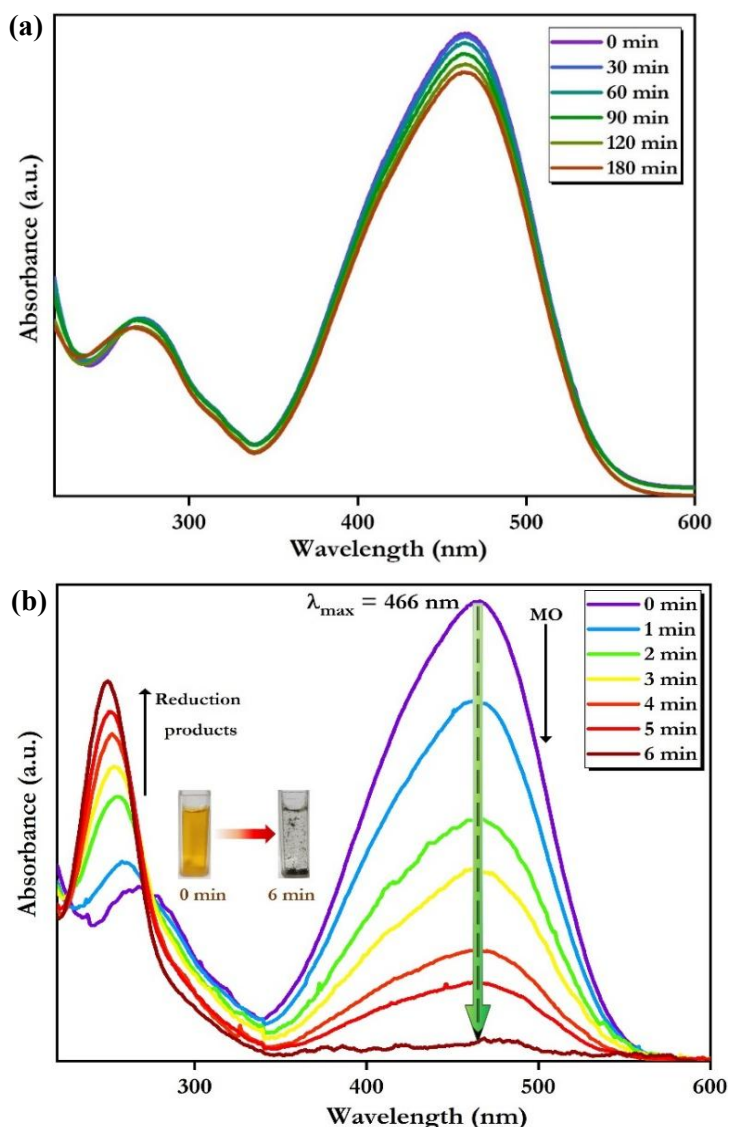
### 3.3.2.1.2 Methyl Orange reduction

An attempt was made to catalytically reduce MO using  $\text{NaBH}_4$  as the reducing agent and  $\text{ZnCuNi-LDO}$  as the catalyst. The process was monitored using a UV-Vis spectrophotometer.

Initially, catalytic reduction of MO was examined in the presence of  $\text{NaBH}_4$  and time-dependent UV-Visible spectrum was recorded at  $\lambda_{max} = 466$  nm to determine the extent of MO reduction (Figure 3.7a). It was observed that addition of only  $\text{NaBH}_4$  to the reaction mixture resulted in a very slow decrease in the absorbance of MO, leading to only 8.76% reduction of MO even after 3 hours. Subsequently, on addition of  $\text{ZnCuNi-LDO}$  to the reaction mixture, the intensity of absorbance maxima at  $\lambda_{max} = 466$  nm corresponding to MO dye began to decrease rapidly until its disappearance after 6 minutes along with the complete decolorisation of the reaction mixture, signifying complete reduction. Percentage reduction of MO, calculated using Eqn 3.1, was found to be 95.58%.

The formation of by-products was corroborated by the emergence of a new peak at 250 nm, and its intensity kept increasing with time (Figure 3.7b). Therefore, it was concluded that the addition of  $\text{ZnCuNi-LDO}$  to the reaction mixture was essential for the efficient reduction of MO. The rate constant  $k$ , calculated from Eqn 3.4 in

accordance with pseudo-first-order kinetics, was evaluated to be  $0.471 \text{ min}^{-1}$  ( $R^2 = 0.91$ ) (Figure 3.7c). It may be worth noting that the interaction of  $\text{NaBH}_4$  with MO molecules resulted in only partial reduction of the azo group, while the simultaneous action of  $\text{NaBH}_4$  and ZnCuNi-LDO catalyst was successful in breaking the chromophoric azo ( $-\text{N}=\text{N}-$ ) group of MO, leading to the formation of smaller amine moieties. The appearance of absorbance peaks around 250 nm may be attributed to the possible formation of hydrazine derivatives as reduction products, potentially including sulfanilic acid (Table 3.2) [37]. The disappearance of peak at 466 nm and the emergence of new peak at 250 nm corroborated the reduction of MO by the catalytic action of ZnCuNi-LDO.



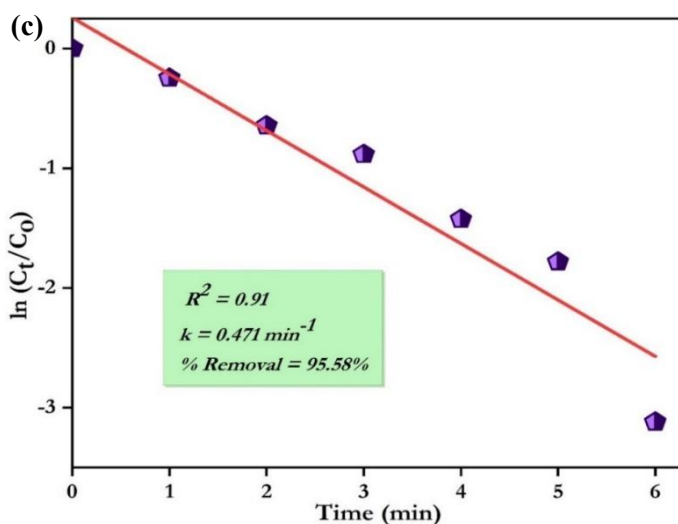


**Figure 3.7** Time-dependent UV-Vis absorption spectrum of reduction of MO using (a) only  $\text{NaBH}_4$ , (b) using  $\text{NaBH}_4$  and  $\text{ZnCuNi-LDO}$ , and (c) linear regression of pseudo-first-order kinetics model for the  $\text{NaBH}_4$ -assisted reduction of MO using  $\text{ZnCuNi-LDO}$ .

**Table 3.2** Structures of potential products formed on the catalytic treatment of *p*-NA and MO with  $\text{NaBH}_4$  and  $\text{ZnCuNi-LDO}$ .

Organic Pollutant	$\lambda_{max}$ of pollutant (nm)	By-product	$\lambda_{max}$ of by-product (nm)
<i>p</i> -NA	380	<i>p</i> -phenylenediamine 	240 and 304
MO	466	Sulfanilic Acid 	250

### 3.3.2.1.3 Postulated mechanism

The catalytic experiments showed that  $\text{ZnCuNi-LDO}$  can act as an excellent catalyst for the  $\text{NaBH}_4$ -assisted hydrogenation of *p*-NA and catalytic reduction of MO. The catalysis process is known to follow the Langmuir-Hinshelwood mechanism, which includes the adsorption of reactants on the catalyst surface followed by the interaction between the adsorbed reactants to form products. The potential mechanism for the

NaBH<sub>4</sub>-assisted hydrogenation of *p*-NA and catalytic reduction of MO is presented in Figure 3.8.

NaBH<sub>4</sub> is a good reducing agent and on addition to water, NaBH<sub>4</sub> produces nucleophilic borohydride (BH<sub>4</sub><sup>-</sup>) anions. These BH<sub>4</sub><sup>-</sup> anions break down into BO<sub>2</sub><sup>-</sup> that gets adsorbed onto the catalyst surface and delivers electrons and H<sub>2</sub> to the LDO surface. H<sub>2</sub> adsorbed on ZnCuNi-LDO surface forms a metal-hydride complex that aids in the transfer of H<sub>2</sub> and electrons to the -NO<sub>2</sub> group. This leads to the hydrogenation of -NO<sub>2</sub> group to -NH<sub>2</sub>, and results in the formation of *p*-phenylenediamine (*p*-PD).

While in case of MO, the dye molecules are adsorbed onto the ZnCuNi-LDO surface. ZnCuNi-LDO acts as an electron donor while the dye molecules act as an electron acceptor and get reduced to its hydrazine derivatives such as sulfanilic acid. Finally, the reduction products are desorbed from LDO surface, thereby regenerating it for further catalytic activity.

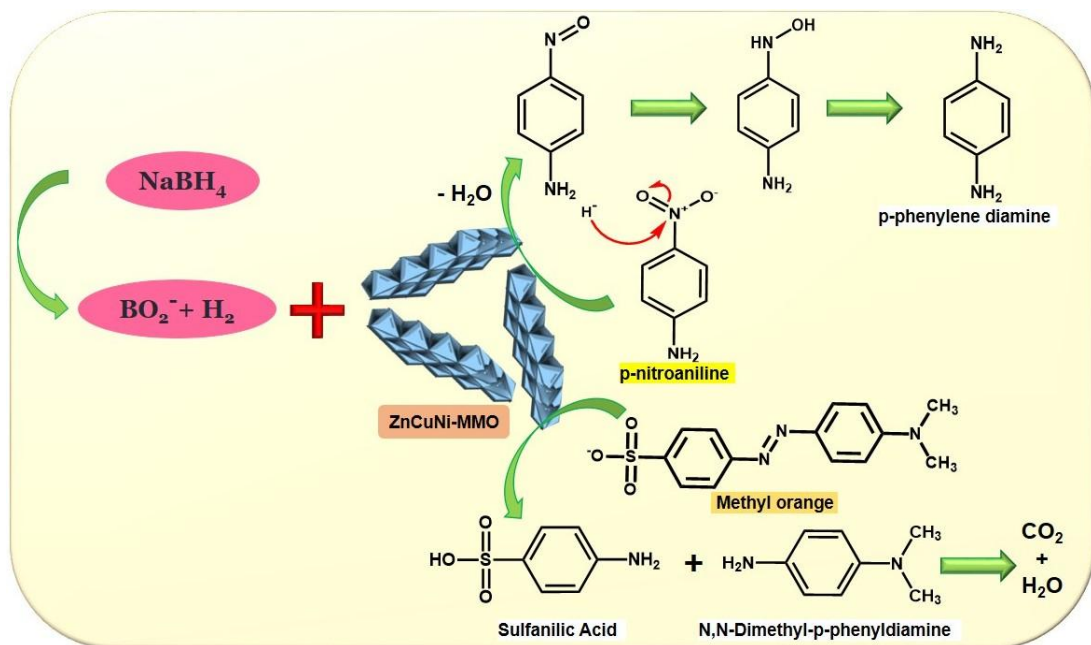


**Figure 3.8** Postulated mechanism for the NaBH<sub>4</sub>-assisted catalytic degradation of *p*-NA and MO using ZnCuNi-LDO.

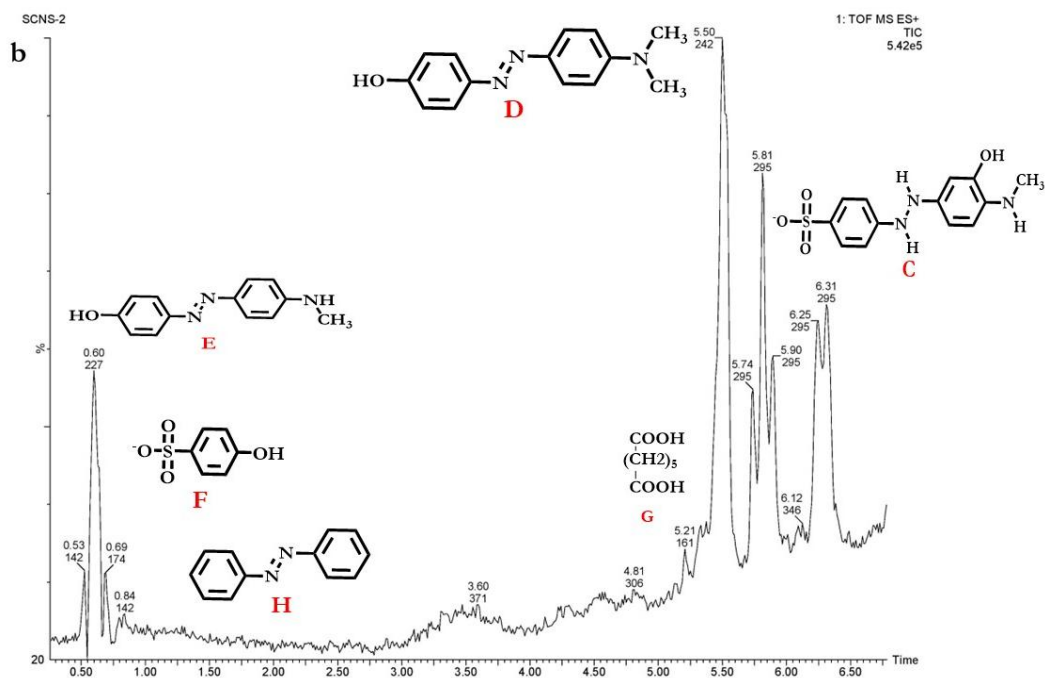
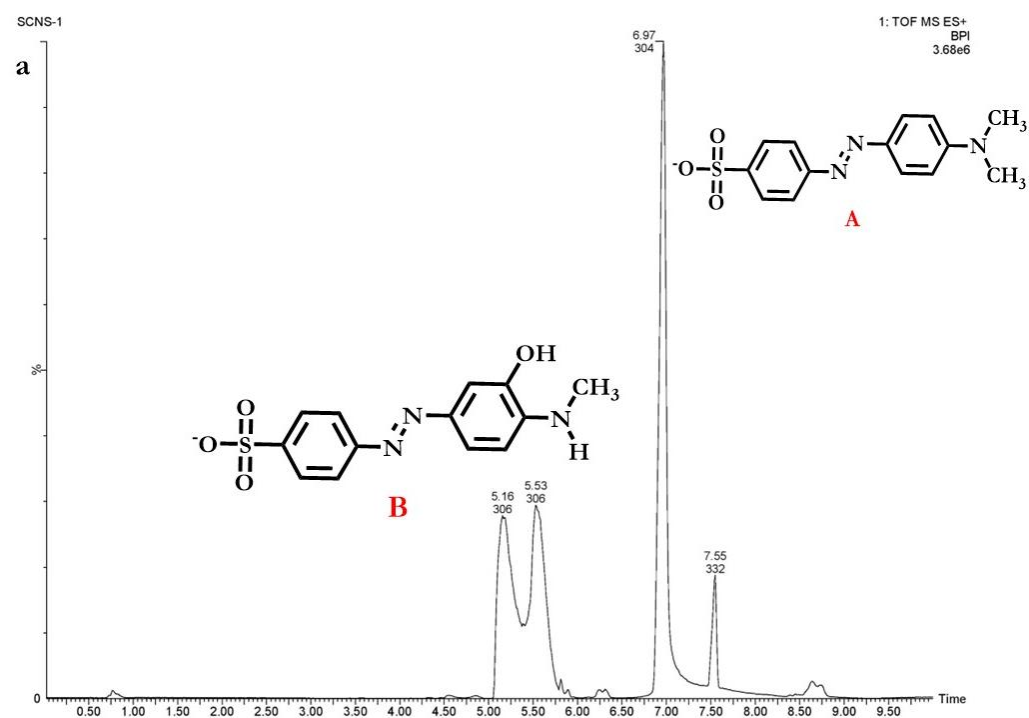
The products formed on the catalytic reduction of *p*-NA and MO are benign, can be easily degraded, less toxic, do not pollute, and hold commercial importance. Therefore,

catalytic reduction of *p*-NA and MO using ZnCuNi-LDO in the presence of NaBH<sub>4</sub> is a favourable methodology for eliminating these pollutants from aqueous medium.

### 3.3.2.1.4 Catalytic Degradation Products of Methyl Orange

The degradation products of MO dye were examined using LC-MS to gain a better understanding of the degradation process. The LC-MS chromatograms of untreated MO (0 min) and the reaction mixture after complete decolourisation of MO (6 min) in ESI<sup>+</sup> mode are presented in Figure 3.9. MO molecules (C<sub>14</sub>H<sub>14</sub>N<sub>3</sub>NaO<sub>3</sub>S) get converted to C<sub>14</sub>H<sub>14</sub>N<sub>3</sub>SO<sub>3</sub><sup>-</sup> due to the dissociation of Na<sup>+</sup> in water. In the LC-MS chromatogram presented in Figure 3.9a, the parent MO molecule exhibited a clear signal at *m/z* = 304 (A). Additionally, the signal at *m/z* = 306 (B) may correspond to the presence of monohydroxylated MO. Further, the LC-MS chromatogram presented in Figure 3.9b clearly shows the appearance of signals corresponding to by-products of MO degradation. The signals appearing at *m/z* = 295 (C), 242 (D), 227 (E), 174 (F), 161 (G) and 147 (H) correspond to the by-products (illustrated in Figure 3.9c) that were formed as a result of the degradation of MO in the presence of NaBH<sub>4</sub> and ZnCuNi-LDO[38–40].

Based on the potential degradation pathway of MO presented in Figure 3.9c, it may be assumed that the degradation of MO consisted of processes including bond cleavage, demethylation, hydroxyl group insertion, detachment of sulfonic group, benzene ring opening, and finally the mineralization of intermediates to potentially form CO<sub>2</sub>, H<sub>2</sub>O, NO<sub>3</sub><sup>-</sup>, SO<sub>4</sub><sup>2-</sup>, etc.



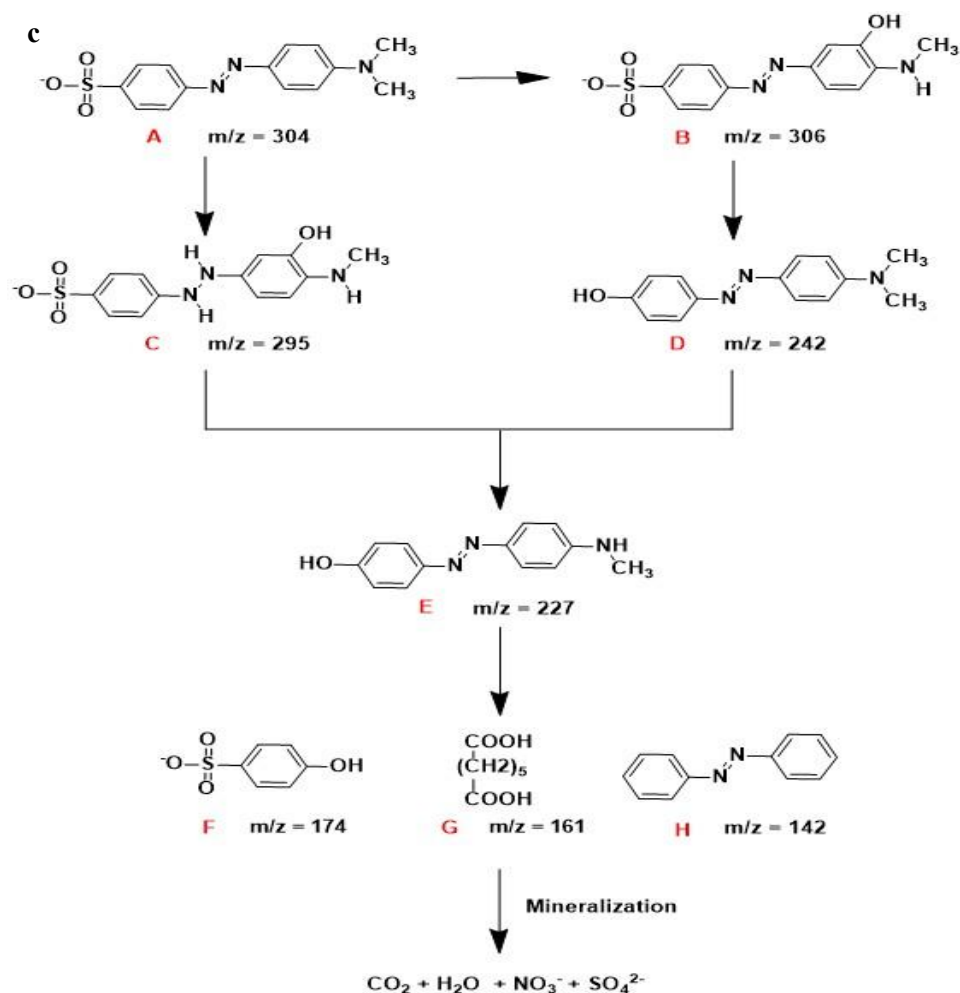
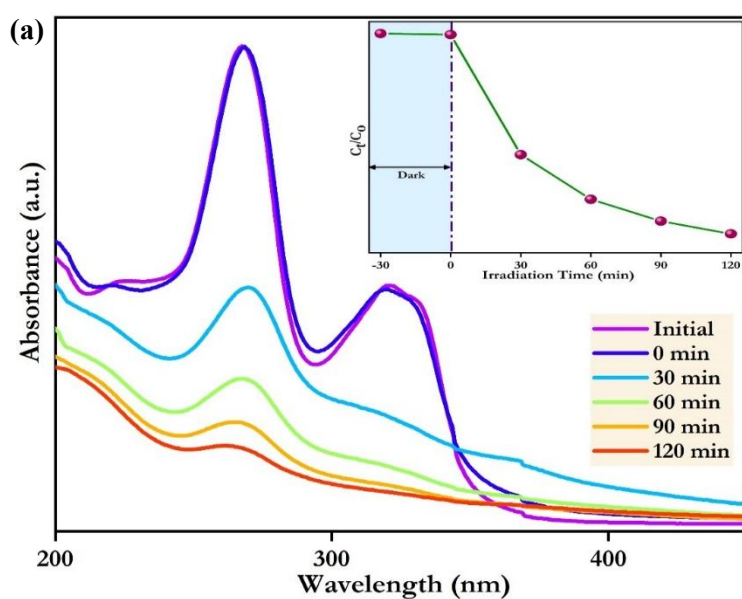


**Figure 3.9** LC-MS chromatograms of (a) untreated MO (0 min) and (b) by-products obtained on NaBH<sub>4</sub>-assisted catalytic reduction of MO using ZnCuNi-LDO and (c) potential degradation pathway of MO.

### 3.3.2.2 Photocatalytic Degradation of Ciprofloxacin

The light-stimulated catalytic performance of ZnCuNi-LDO was investigated by studying the degradation of CIF drug under UV light at room temperature and ambient pressure, and the observations are presented below. Figure 3.10 presents the time-dependent UV-Vis extinction spectra of CIF at various time intervals within a period of 120 minutes. In case of CIF, a principal extinction peak appears around  $\lambda_{max} = 270$  nm. From the absorption spectra, it may be deduced that virtually no amount of drug was adsorbed by ZnCuNi-LDO. Subsequently, on UV illumination, with the progress of photocatalytic reaction, the main peak of absorbance maxima for CIF appearing around  $\lambda_{max} = 270$  nm began decreasing steadily. The decrease in absorbance maxima

may be attributed to the oxidative decomposition of CIF under the influence of UV light and ZnCuNi-LDO. It may be noted that with the progress of the photocatalytic reaction, the peak demonstrated a slight blue shift that signified that CIF decomposition was a mineralization process. Based on the experimental data, it was determined that ZnCuNi-LDO demonstrated percentage degradation of 84.8% within 120 minutes towards CIF molecules. From the graph plotted between  $C/C_0$  and time  $t$  (Figure 3.10a inset)), it was deduced that under dark condition, there was no significant change in drug concentration with time while on UV illumination, concentration of CIF decreased with increase in reaction time. The plot between CIF concentration and time  $t$  presented in Figure 3.10b depicts that there was a good linear relationship between  $\ln(C_0/C_t)$  and  $t$ . Based on the value of  $R^2$  (0.96) obtained from the plot, it was concluded that the kinetics of the reaction could be successfully described using the pseudo-first-order model presented in Eqn 3.2. The value of the rate constant  $k$ , calculated from the slope of the graph plotted between  $\ln(C_0/C_t)$  and time  $t$ , was found to be  $0.0149 \text{ min}^{-1}$ . Thus, it was inferred that while adsorptive uptake of CIF by the synthesized material was found to be negligible, ZnCuNi-LDO acted as a highly efficacious photocatalyst and achieved the degradation of CIF under UV light efficiently within 120 minutes.



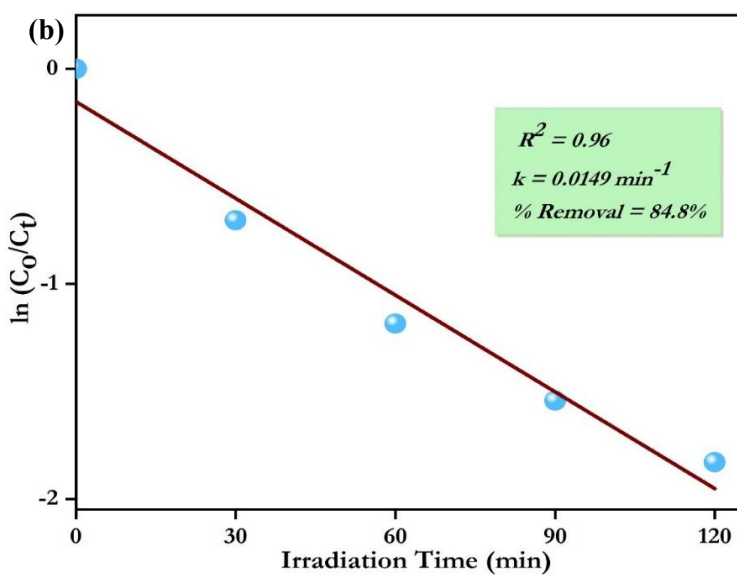


**Figure 3.10** (a) UV-Vis absorbance spectrum and (b) kinetics plot for photocatalytic degradation of ciprofloxacin by ZnCuNi-LDO.

### 3.3.2.3 Comparison with reported catalysts

The comparison of the catalytic activity of ZnCuNi-LDO with previously reported catalysts towards the hydrogenation of *p*-NA, catalytic reduction of MO and photocatalytic degradation of CIF is presented in Table 3.3. The degradation efficiencies of ZnCuNi-LDO for *p*-NA, MO, and CIF were found to be comparable or even better than those exhibited by the majority of reported catalysts in relatively shorter time intervals. Therefore, it may be concluded that ZnCuNi-LDO holds the potential to be an excellent candidate for the catalytic reduction of nitroarene compounds and azo dyes. The facile synthesis of this catalyst, coupled with its excellent catalytic performances, affirms the broad-spectrum potential of ZnCuNi-LDO for wastewater purification by tackling various anthropogenic contaminants, including azo dyes, NACs, and drugs. The superior catalytic activity may be attributed to the small size, high surface area and homogeneous distribution of Zn, Cu, and Ni in ZnCuNi-LDO catalyst, as well as the synergistic interactions between the transition metals Cu and Ni. It is important to note that ZnCuNi-LDO exhibits marginally slower catalytic reduction activity than its precursor ZnCuNi-LDH (reported in the previous chapter) for the reduction of *p*-NA and MO. However, ZnCuNi-LDO also possesses the potential to act as an effective photocatalyst for pollutant degradation, an ability

that was not exhibited by ZnCuNi-LDH. This may be attributed to the fact that thermal treatment of LDH causes structural reorganisation and defect reformation, resulting in the formation of new acidic and basic sites due to generation of coordinatively unsaturated metal cation and oxygen anions ( $O^{2-}$ ) respectively. These Lewis acid sites (metal cations) and Lewis basic sites (oxide ions) enables synergistic activation of reactants. Therefore, the conversion of ZnCuNi-LDH into ZnCuNi-LDO provides additional catalytic properties to the synthesized lattice, thereby establishing ZnCuNi-LDO as a multifunctional catalytic material.

**Table 3.3** Comparison of catalytic performance of ZnCuNi-LDO with previously reported catalysts.

<b>Pollutant</b>	<b>Catalyst</b>	<b>Time</b>	<b>Removal</b>	<b>Reference</b>
		(min)	Efficiency (%)	
<i>p</i> -NA	Bi <sub>2</sub> S <sub>3</sub>	10	96	[41]
	Au nanowire networks	17	100	[42]
	RGO-Ni Nanocomposite	190	93	[43]
	ZnCuNi-LDH	3	95.3	[44]
	ZnCuNi-LDO	7	96.98	This work
MO	Asp-Au NPs	10	>95	[37]
	NiFe <sub>2</sub> O <sub>4</sub> /γ-Fe <sub>2</sub> O <sub>3</sub>	36	100	[45]
	Ag-Cu Rhizome Powder	9	96	[46]
	ZnCuNi-LDH	4	96.4	[44]
	ZnCuNi-LDO	6	95.58	This work
CIF	Zn-doped Cu <sub>2</sub> O particles	240	94.7	[47]
	g-C <sub>3</sub> N <sub>4</sub> /TiO <sub>2</sub> /kaolinite	240	92	[48]
	Ag <sub>3</sub> PO <sub>4</sub> -NPs/Cu-NWs	150	85	[49]
	ZnCuNi-LDO	120	84.1	This work

### 3.4 Conclusion

In summary, an attempt was made to fabricate novel and homogenous ternary layered double oxide consisting of zinc, copper, and nickel by calcination of previously

prepared ZnCuNi-LDH. The specific surface area of  $25.617\text{ m}^2\text{g}^{-1}$ , estimated using BET, indicated their potential for catalytic applications. Keeping this in view, ZnCuNi-LDO was applied as a catalyst for the hydrogenation of *p*-NA and catalytic reduction of MO dye. ZnCuNi-LDO was able to successfully hydrogenate *p*-NA to *p*-phenylenediamine (*p*-PD), and reduce MO to its hydrazine derivatives, including sulfanilic acid, respectively, with efficiency of more than 95% within  $\sim 7$  minutes. The reaction rates, evaluated using the pseudo-first order model, were found to be comparatively higher than already existing catalysts, i.e.,  $0.402\text{ min}^{-1}$  (*p*-NA hydrogenation) and  $0.471\text{ min}^{-1}$  (MO dye reduction). The catalytic action of ZnCuNi-LDO with the intermediates  $\text{BO}_2^-$  and  $\text{H}_2$  that were produced on the hydrolysis of  $\text{NaBH}_4$  enables its action as an electron relay and facilitates the formation of metal-hydride complexes that catalyse the hydrogenation of *p*-NA and reduction of MO. Further, LC-MS technique was employed to identify potential products formed on the catalytic reduction of MO and the degradation pathway for MO was elucidated. Additionally, the use of ZnCuNi-LDO for photocatalytic applications was also investigated, and it demonstrated good efficiency for the degradation of ciprofloxacin drug within a time interval of 120 minutes. Photocatalytic degradation was found to follow pseudo-first-order kinetics and exhibited a reaction rate of  $0.0149\text{ min}^{-1}$ . Therefore, the obtained results provide several avenues for the use of ZnCuNi-LDO as a multivariate catalyst for use in  $\text{NaBH}_4$  – assisted catalysis and photocatalytic applications to accomplish the elimination of various types of pollutants in aqueous medium. The developed system has immense potential to contribute to the suppression of cancer-causing agents and antibiotic resistance in wastewater, while also offering prospects in other catalytic applications. This is an important advancement in addressing growing water pollution levels since residual dyes, NACs, and pharmaceutical products possess bioaccumulative tendencies and can prove to be cancer-causing and induce antibiotic resistance in bacteria, thereby posing significant risks to human health.

### 3.5 References

[1] X. Xiang, L. Xie, Z. Li, F. Li, Ternary  $\text{MgO}/\text{ZnO}/\text{In}_2\text{O}_3$  heterostructured photocatalysts derived from a layered precursor and visible-light-induced photocatalytic activity, *Chem. Eng. J.* 221 (2013) 7975.

https://doi.org/10.1016/j.cej.2013.02.030.

[2] L. Yuan, Z. Yang, F. Cui, Y. Rong, Q. Su, H. Chen, J. Wu, L. Deng, Flower-like Zn-Al-In layered double oxides synthesized by a facile hydrothermal method as ultra-high cycle stability anodic for zinc-nickel battery, *J. Alloys Compd.* 863 (2021). <https://doi.org/10.1016/j.jallcom.2020.158574>.

[3] A. Aljuaid, M. Almehmadi, A.A. Alsaiari, M. Allahyani, O. Abdulaziz, A. Alsharif, J.A. Alsaiari, M. Saih, R.T. Alotaibi, I. Khan, g-C<sub>3</sub>N<sub>4</sub> Based Photocatalyst for the Efficient Photodegradation of Toxic Methyl Orange Dye: Recent Modifications and Future Perspectives, *Molecules* 28 (2023) 3199. <https://doi.org/10.3390/molecules28073199>.

[4] M. Farhan Hanafi, N. Sapawe, A review on the water problem associate with organic pollutants derived from phenol, methyl orange, and remazol brilliant blue dyes, *Mater. Today Proc.* 31 (2020) A141–A150. <https://doi.org/10.1016/j.matpr.2021.01.258>.

[5] A. Ahmad, S.H. Mohd-Setapar, C.S. Chuong, A. Khatoon, W.A. Wani, R. Kumar, M. Rafatullah, Recent advances in new generation dye removal technologies: Novel search for approaches to reprocess wastewater, *RSC Adv.* 5 (2015) 30801–30818. <https://doi.org/10.1039/c4ra16959j>.

[6] J. Pathak, P. Singh, Adsorptive Removal of Congo Red Using Organically Modified Zinc–Copper–Nickel Ternary Metal Hydroxide: Kinetics, Isotherms and Adsorption Studies, *J. Polym. Environ.* 31 (2022) 327–344. <https://doi.org/10.1007/s10924-022-02612-0>.

[7] G.E. de S. dos Santos, P.V. dos S. Lins, L.M.T. de M. Oliveira, E.O. da Silva, I. Anastopoulos, A. Erto, D.A. Giannakoudakis, A.R.F. de Almeida, J.L. da S. Duarte, L. Meili, Layered double hydroxides/biochar composites as adsorbents for water remediation applications: recent trends and perspectives, *J. Clean. Prod.* 284 (2021) 124755. <https://doi.org/10.1016/j.jclepro.2020.124755>.

[8] S.A. Khan, L.A. Shah, Advanced Removal Techniques for Dye-containing Wastewaters, Springer Nature Singapore, Gateway, 2021.

[9] K. Takehira, Recent development of layered double hydroxide-derived catalysts – Rehydration, reconstitution, and supporting, aiming at commercial application –, *Appl. Clay Sci.* 136 (2017) 112–141. <https://doi.org/10.1016/j.clay.2016.11.012>.

[10] R. Gabriel, S.H.V. d. Carvalho, J.L. da S. Duarte, L.M.T.M. Oliveira, D.A. Giannakoudakis, K.S. Triantafyllidis, J.I. Soletti, L. Meili, Mixed metal oxides derived from layered double hydroxide as catalysts for biodiesel production, *Appl. Catal. A Gen.* 630 (2022) 118470. <https://doi.org/10.1016/j.apcata.2021.118470>.

[11] V. Vinitha, M. Preeyanghaa, V. Vinesh, R. Dhanalakshmi, B. Neppolian, V. Sivamurugan, Two is better than one: catalytic, sensing and optical applications of doped zinc oxide nanostructures, *Emergent Mater.* 4 (2021) 1093–1124. <https://doi.org/10.1007/s42247-021-00262-x>.

[12] S.S. Narender, V.V.S. Varma, C.S. Srikar, J. Ruchitha, P.A. Varma, B.V.S. Praveen, Nickel Oxide Nanoparticles: A Brief Review of Their Synthesis, Characterization, and Applications, *Chem. Eng. Technol.* 45 (2022) 397–409. <https://doi.org/10.1002/ceat.202100442>.

[13] Y. Deng, R. Zhao, Advanced Oxidation Processes (AOPs) in Wastewater

Treatment, *Curr. Pollut. Reports* 1 (2015) 167–176.  
<https://doi.org/10.1007/s40726-015-0015-z>.

[14] N. Scotti, D. Monticelli, F. Zaccheria, Dispersed copper oxide: A multifaceted tool in catalysis, *Inorganica Chim. Acta* 380 (2012) 194–200.  
<https://doi.org/10.1016/j.ica.2011.10.001>.

[15] Y. Sun, L. Chen, Y. Bao, Y. Zhang, J. Wang, M. Fu, J. Wu, D. Ye, The applications of morphology controlled ZnO in catalysis, *Catalysts* 6 (2016) 188. <https://doi.org/10.3390/catal6120188>.

[16] R.P. Ye, L. Lin, Q. Li, Z. Zhou, T. Wang, C.K. Russell, H. Adidharma, Z. Xu, Y.G. Yao, M. Fan, Recent progress in improving the stability of copper-based catalysts for hydrogenation of carbon-oxygen bonds, *Catal. Sci. Technol.* 8 (2018) 3428–3449. <https://doi.org/10.1039/c8cy00608c>.

[17] Y. Ma, C. Ma, Y. Wang, K. Wang, Advanced Nickel-Based Catalysts for Urea Oxidation Reaction: Challenges and Developments, *Catalysts* 12 (2022).  
<https://doi.org/10.3390/catal12030337>.

[18] M. Muruganandham, J.J. Wu, Synthesis, characterization and catalytic activity of easily recyclable zinc oxide nanobundles, *Appl. Catal. B Environ.* 80 (2008) 32–41. <https://doi.org/10.1016/j.apcatb.2007.11.006>.

[19] Z.P. Xu, J. Zhang, M.O. Adebajo, H. Zhang, C. Zhou, Catalytic applications of layered double hydroxides and derivatives, *Appl. Clay Sci.* 53 (2011) 139–150. <https://doi.org/10.1016/j.clay.2011.02.007>.

[20] T.A. Belay, C.Y. Lin, H.M. Hsiao, M.F. Chang, J.C. Liu, Effect of precursor type on the reduction of concentrated nitrate using zero-valent copper and sodium borohydride, *Water Sci. Technol.* 77 (2018) 114–122.  
<https://doi.org/10.2166/wst.2017.525>.

[21] M.A. Bhosale, B.M. Bhanage, Rapid synthesis of nickel oxide nanorods and its applications in catalysis, *Adv. Powder Technol.* 26 (2015) 422–427.  
<https://doi.org/10.1016/j.apt.2014.11.015>.

[22] S.R. Leandro, I.J. Marques, R.S. Torres, T.A. Fernandes, P.D. Vaz, C.D. Nunes, Nitroarene and dye reduction with 2:1 Co/Al layered double hydroxide catalysts – Is gold still necessary?, *Inorganica Chim. Acta* 521 (2021) 120336. <https://doi.org/10.1016/j.ica.2021.120336>.

[23] H.J. Nam, E.B. Park, D.Y. Jung, Bioinspired polydopamine-layered double hydroxide nanocomposites: Controlled synthesis and multifunctional performance, *RSC Adv.* 6 (2016) 24952–24958.  
<https://doi.org/10.1039/c5ra28103b>.

[24] Z. Wei, Y. Li, L. Dou, M. Ahmad, H. Zhang, Cu<sub>3</sub>-xNi<sub>x</sub>Al-Layered Double Hydroxide-Reduced Graphene Oxide Nanosheet Array for the Reduction of 4-Nitrophenol, *ACS Appl. Nano Mater.* 2 (2019) 2383–2396.  
<https://doi.org/10.1021/acsanm.9b00273>.

[25] J. Pathak, P. Singh, Synthesis and Characterization of Ternary Layered Double Hydroxide containing Zinc/Copper/Nickel and its PANI Composite, *Polym. Compos.* 43 (2022) 7836.  
<https://doi.org/https://doi.org/10.1002/pc.26895>.

[26] J. Pathak, P. Singh, Zinc-Copper-Nickel Mixed Metal Oxide as Heterogeneous Catalytic Material for the Reductive Degradation of Nitroarene and Azo Dye, *Catal. Letters* 154 (2024) 5280–5293. <https://doi.org/10.1007/s10562-024-0166-1>.

04754-3.

[27] D. Huang, J. Ma, C. Fan, K. Wang, W. Zhao, M. Peng, S. Komarneni, Co-Mn-Fe complex oxide catalysts from layered double hydroxides for decomposition of methylene blue: Role of Mn, *Appl. Clay Sci.* 152 (2018) 230–238. <https://doi.org/10.1016/j.clay.2017.11.018>.

[28] P. Singh, R. Nagarajan, Synthesis and characterization of hydrotalcite type structure containing Zn<sup>2+</sup> and La<sup>3+</sup>-ions, *Mater. Lett.* 159 (2015) 58–60. <https://doi.org/10.1016/j.matlet.2015.06.071>.

[29] Z. Mohamed Riyas, R. Gayathri, M.R. Prabhu, K. Velsankar, S. Sudhahar, Green synthesis and biomedical behavior of Mg-doped ZnO nanoparticle using leaf extract of *Ficus religiosa*, *Ceram. Int.* 48 (2022) 24619–24628. <https://doi.org/10.1016/j.ceramint.2022.05.107>.

[30] S. Suresh, S. Thambidurai, J. Arumugam, M. Kandasamy, N. Pugazhenthiran, D. Balaji, B.A. Al-Asbahi, N.R. Reddy, A. Arunkumar, T. Muneeswaran, Antibacterial activity and photocatalytic oxidative performance of zinc oxide nanorods biosynthesized using *Aerva lanata* leaf extract, *Inorg. Chem. Commun.* 139 (2022). <https://doi.org/10.1016/j.inoche.2022.109398>.

[31] A. Annapoorani, A. Koodalingam, M. Beulaja, G. Saiprasad, P. Chitra, A. Stephen, S. Palanisamy, N.M. Prabhu, S.G. You, S. Janarthanan, R. Manikandan, Eco-friendly synthesis of zinc oxide nanoparticles using *Rivina humilis* leaf extract and their biomedical applications, *Process Biochem.* 112 (2022) 192–202. <https://doi.org/10.1016/j.procbio.2021.11.022>.

[32] Z. Li, Q. Zhang, X. Liu, M. Chen, L. Wu, Z. Ai, Mechanochemical synthesis of novel heterostructured Bi<sub>2</sub>S<sub>3</sub>/Zn-Al layered double hydroxide nanoparticles as efficient visible light reactive Z-scheme photocatalysts, *Appl. Surf. Sci.* 452 (2018) 123–133. <https://doi.org/10.1016/j.apsusc.2018.04.237>.

[33] H.A.M. Ahmed, R.M.A. Maaboud, F.F.A. Latif, A.M.K. El-Dean, K.M. El-Shaieb, E. Vilanova, C. Estevan, Different Analytical Methods of Para-Phenylenediamine Based Hair Dye, *J. Cosmet. Dermatological Sci. Appl.* 03 (2013) 17–25. <https://doi.org/10.4236/jcdsa.2013.33a1003>.

[34] Jaidev, S. Ramaprabhu, Poly(p-phenylenediamine)/graphene nanocomposites for supercapacitor applications, *J. Mater. Chem.* 22 (2012) 18775–18783. <https://doi.org/10.1039/c2jm33627h>.

[35] J. Zhang, X. Zhang, Y. Zheng, Synthesis of poly(p-phenylenediamine) encapsulated graphene and its application in steel protection, *Prog. Org. Coatings* 158 (2021) 106330. <https://doi.org/10.1016/j.porgcoat.2021.106330>.

[36] S.G. Jiji, K.G. Gopchandran, Shape dependent catalytic activity of unsupported gold nanostructures for the fast reduction of 4-nitroaniline, *Colloids Interface Sci. Commun.* 29 (2019) 9–16. <https://doi.org/10.1016/j.colcom.2018.12.003>.

[37] N. Garg, S. Bera, L. Rastogi, A. Ballal, M. V. Balaramakrishna, Synthesis and characterization of L-asparagine stabilised gold nanoparticles: Catalyst for degradation of organic dyes, *Spectrochim. Acta - Part A Mol. Biomol. Spectrosc.* 232 (2020) 118126. <https://doi.org/10.1016/j.saa.2020.118126>.

[38] Q. An, M. Tang, S. Deng, Y. Jiao, C. Liu, M. Yang, Z. Ye, B. Zhao, Methyl Orange Degradation with Peroxydisulfate Activated with the Synergistic Effect of the Acid-Modified Red Mud and Biochar Catalyst, *Arab. J. Sci. Eng.*

48 (2023) 8819–8834. <https://doi.org/10.1007/s13369-022-07398-w>.

[39] D. Ariyanti, M. Maillot, W. Gao, Photo-assisted degradation of dyes in a binary system using TiO<sub>2</sub> under simulated solar radiation, *J. Environ. Chem. Eng.* 6 (2018) 539–548. <https://doi.org/10.1016/j.jece.2017.12.031>.

[40] B. Wang, M. Xu, C. Chi, C. Wang, D. Meng, Degradation of methyl orange using dielectric barrier discharge water falling film reactor, *J. Adv. Oxid. Technol.* 20 (2017) 20170021. <http://repositorio.unan.edu.ni/2986/1/5624.pdf> <http://fiskal.kemenkeu.go.id/ejournal> <http://dx.doi.org/10.1016/j.cirp.2016.06.001> <http://dx.doi.org/10.1016/j.powtec.2016.12.055> <https://doi.org/10.1016/j.ijfatigue.2019.02.006> <https://doi.org/10.1>.

[41] F. Guo, Y. Ni, Y. Ma, N. Xiang, C. Liu, Flowerlike Bi<sub>2</sub>S<sub>3</sub> microspheres: Facile synthesis and application in the catalytic reduction of 4-nitroaniline, *New J. Chem.* 38 (2014) 5324–5330. <https://doi.org/10.1039/c4nj00900b>.

[42] M. Chirea, A. Freitas, B.S. Vasile, C. Ghitulica, C.M. Pereira, F. Silva, Gold nanowire networks: Synthesis, characterization, and catalytic activity, *Langmuir* 27 (2011) 3906–3913. <https://doi.org/10.1021/la104092b>.

[43] P. Das, S. Ghosh, M. Baskey, Heterogeneous catalytic reduction of 4-nitroaniline by RGO-Ni nanocomposite for water resource management, *J. Mater. Sci. Mater. Electron.* 30 (2019) 19731–19737. <https://doi.org/10.1007/s10854-019-02323-8>.

[44] J. Pathak, P. Singh, Ultrafast catalytic reduction of organic pollutants using ternary zinc–copper–nickel layered double hydroxide, *Appl. Organomet. Chem.* 38 (2024) e7507. <https://doi.org/10.1002/aoc.7507>.

[45] G.M. El-Subrouti, A.S. Eltaweil, S.A. Sallam, Synthesis of Active MFe<sub>2</sub>O<sub>4</sub>/γ-Fe<sub>2</sub>O<sub>3</sub> Nanocomposites (Metal = Ni or Co) for Reduction of Nitro-Containing Pollutants and Methyl Orange Degradation, *Nano* (2019). <https://doi.org/10.1142/S179329201950125X>.

[46] E.M. Bakhsh, M. Ismail, U. Sharafat, K. Akhtar, T.M. Fagieh, E.Y. Danish, S.B. Khan, M.I. Khan, M.A. Khan, A.M. Asiri, Highly efficient and recoverable Ag–Cu bimetallic catalyst supported on taro-rhizome powder applied for nitroarenes and dyes reduction, *J. Mater. Res. Technol.* 18 (2022) 769–787. <https://doi.org/10.1016/j.jmrt.2022.02.062>.

[47] X. Yu, J. Zhang, J. Zhang, J. Niu, J. Zhao, Y. Wei, B. Yao, Photocatalytic degradation of ciprofloxacin using Zn-doped Cu<sub>2</sub>O particles: Analysis of degradation pathways and intermediates, *Chem. Eng. J.* 374 (2019) 316–327. <https://doi.org/10.1016/j.cej.2019.05.177>.

[48] C. Li, Z. Sun, W. Zhang, C. Yu, S. Zheng, Highly efficient g-C<sub>3</sub>N<sub>4</sub>/TiO<sub>2</sub>/kaolinite composite with novel three-dimensional structure and enhanced visible light responding ability towards ciprofloxacin and *S. aureus*, *Appl. Catal. B Environ.* 220 (2018) 272–282. <https://doi.org/10.1016/j.apcatb.2017.08.044>.

[49] Y. Liu, Q. Wu, Y. Zhao, Biomimetic synthesis of Ag<sub>3</sub>PO<sub>4</sub>-NPs/Cu-NWs with visible-light-enhanced photocatalytic activity for degradation of the antibiotic ciprofloxacin, *Dalt. Trans.* 46 (2017) 6425–6432. <https://doi.org/10.1039/c6dt04656h>.

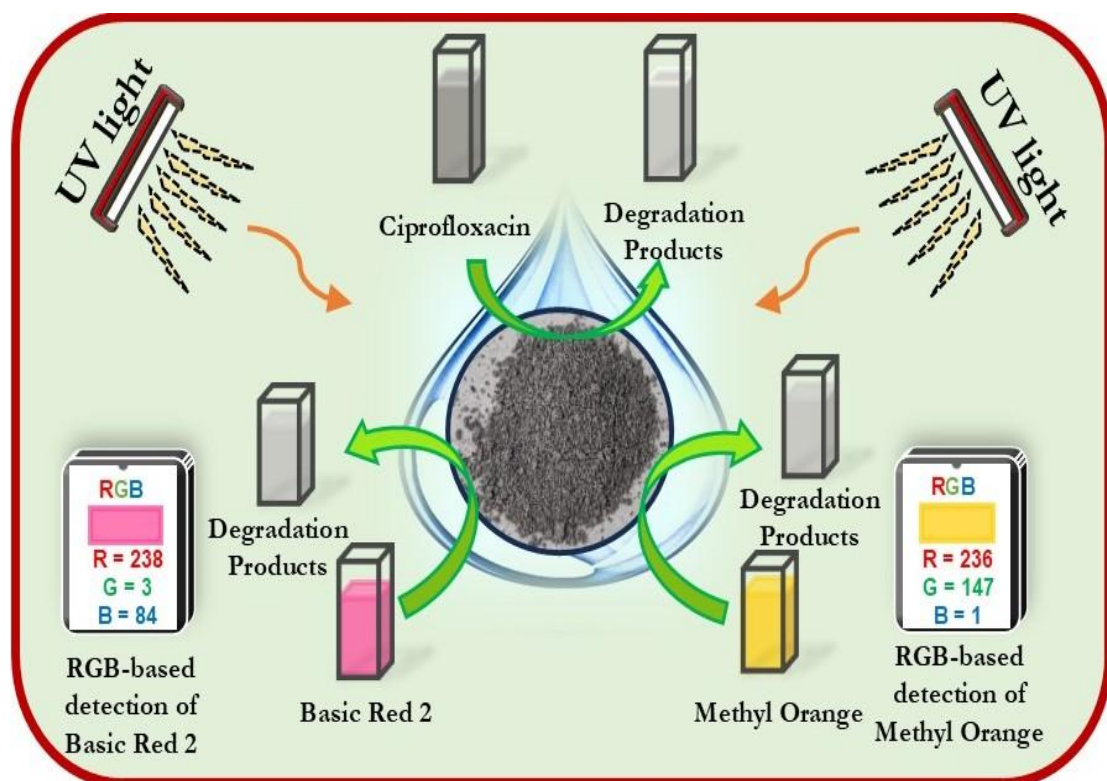
**CHAPTER - 4**

**SYNTHESIS AND CHARACTERIZATION OF**

***ZnCuCe-LAYERED DOUBLE HYDROXIDE***

***AND LAYERED DOUBLE OXIDE FOR***

***PHOTOCATALYTIC APPLICATIONS***



# **CHAPTER - 4**

## **SYNTHESIS AND CHARACTERIZATION OF ZnCuCe-LAYERED DOUBLE HYDROXIDE AND LAYERED DOUBLE OXIDE FOR PHOTOCATALYTIC APPLICATIONS**

---

### **4.1 Introduction**

Porous nanomaterials offer a rising platform for a variety of catalytic applications by virtue of their unique physicochemical properties. Specifically, LDHs are highly favourable nanostructured porous materials that exhibit excellent surface adsorption abilities and have sparked substantial interest in the development of new-age inorganic materials for catalytic applications[1]. In this purview, zinc and copper-based LDHs have emerged as a popular choice for use as catalysts due to their cost-effectiveness, high activity, eco-friendly nature and semiconducting properties[2–4]. Combining the advantageous features of zinc, copper and LDHs in a single lattice has the potential to produce an extremely efficient and low-cost binary catalyst for a multitude of applications. A few reports in literature describe the synthesis and applications of zinc and copper-based LDHs. But often these materials suffer from reduction in catalytic performance due to issues such as leaching of metals, resulting in loss of active centres, formation of carbonaceous deposits, and agglomeration tendencies.

In order to overcome these drawbacks and maximise the catalytic potential of LDHs, many established methodologies have been adopted. One of the most effective methodologies to accomplish this goal is the incorporation of a rare earth cation (RECs) to form a ternary LDH lattice[5]. But this objective presents a daunting challenge due to the difference in atomic radii, pH sensitivity, and high charge density. Due to their unique electronic configuration, RECs exhibit exceptional electronic, optical, magnetic, and luminescent properties. Furthermore, their physicochemical features and multiple oxidation states aid the accommodation of large-sized anions in the interlayer region and stabilisation of redox-active sites in the lattice[6,7]. Additionally, due to their low electronegativity, the incorporation of RECs can

contribute to the enhancement of material basicity[8]. REC ions may also result in reduction of crystallinity, expansion of basal spacing and improvement of hydrophobicity and mechanical properties[9]. However, the discrepancy in ionic radii, charge density and coordination preference make their incorporation in LDHs a difficult task. For this reason, although a few reports describing the synthesis of transition metal-based ternary LDHs do exist in literature, but the realm of rare earth metal incorporation for ternary LDH formation remains relatively unexplored[10–12]. It is also important to highlight that rare earth metals can prove to be an immensely beneficial addition to LDH nanostructures since they possess profound catalytic abilities along with high heat and electrical conductivities. But inspite of this, the incorporation of rare earth metals such as lanthanum (La), indium (In), cerium (Ce), etc remains scarcely reported. Among these metals, cerium has proved to be an extraordinary candidate for enhancement of catalytic performance of LDHs. Ce is an integral part of several industrially significant catalysts due to its redox behaviour, variable oxidation states, oxygen vacancy creation tendency as well as its tendency to improve material stability, and its catalytic performance is comparable to several commercially available single-metal catalysts[13,14]. Therefore, due to their unique structural, geometric and electronic the combination of zinc, copper, and cerium cations in one catalyst can prove to be extremely beneficial for use in

The topotactic transformation of rare earth-containing LDHs into corresponding oxides by means of calcination at temperatures between 350 °C - 550 °C is an effective approach to obtain nanostructured LDOs with distinct properties and high thermal stability. Due to the pre-arrangement of metal cations in the LDH precursor, LDOs contain a uniform distribution of binary and ternary cations at the atomic level without segregation of cations, leading to high homogeneity in the lattice[15]. Furthermore, the incorporation of specific photo-active components such as rare earth cations yield LDOs that possess features such as rapid electron movement, high specific surface area, and good surface basicity and adsorption properties, thereby enabling their profitable use as photocatalysts in wastewater remediation[12]. In the recent years, the photocatalytic degradation process has received immense attention for elimination of organic pollutants using oxide-based photocatalysts. While TiO<sub>2</sub> and ZnO remain the most popular semiconductors for this approach, factors such as large band gap and low

efficiency limit their wide-scale applicability[16,17]. Recently, the use of new-generation heterostructured catalysts, particularly LDOs, as photocatalysts has yielded some interesting results due to their favourable attributes. These materials have been successfully employed for the degradation of several classes of pollutants such as azo dyes, drugs, surfactants and pharmaceutical products[18–20]. But the lack of universality of these materials for the degradation of several different toxins poses a challenging task and required immediate attention towards fabrication of effective and universal photoactive materials.

In addition to this, the development of cost-effective, dependable, portable, and easy-to-use analysis devices with hassle-free applicability in field operations is also the need of the hour since lab-based analysis techniques are often complex and require sophisticated instrumentation as well as trained personnel for correct usage. Recently, the use of colourimetry for water quality analysis based on smartphone imaging has become increasingly popular due to their convenience and portability[21]. In smartphones, the quantification of concentration-dependent colour intensity data can be achieved with relative ease by translation of the colour spectrum of images that typically lies between 400 nm and 700 nm into different colour spaces such as RGB, HSV, HSL, HSI,  $L^*a^*b^*$ , etc. Information about the colour values can be gathered using easily available colour detector softwares and applications[22–24]. Therefore, owing to their multiple advantages, smartphone-based spectrophotometers can prove to be simple, portable, and accessible alternatives to traditionally used lab-based spectrophotometers for on-site analysis of effluents. Owing to these factors, there has been a steep rise in the usage of smartphones for analytical applications in the last few years, and they have been successfully applied in several scientific domains[25,26]. Therefore, the focus of the current study lies on the synthesis and usage of the synthesized heterostructured photocatalyst for the degradation of pollutants. Herein, ZnCuCe-LDO was synthesised from a layered double hydroxide ZnCuCe-LDH precursor by the thermal treatment method. To the best of our knowledge, this lattice has not been previously reported in literature. ZnCuCe-LDO exhibited exceptional photocatalytic abilities of more than 92% for the degradation of both anionic and cationic dyes under UV light irradiation within 120 minutes, suggesting a promising future in the photocatalytic degradation field. Further, the residual dye concentration

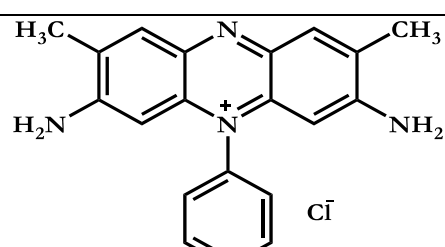
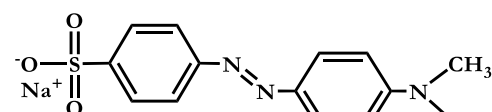
in solution was also measured using a low-cost colourimetric method using a smartphone. The results obtained from UV-Vis spectrophotometer and smartphone-based method were compared to determine its accuracy and assess its utility in field-scale applications.

## 4.2 Experimental Section

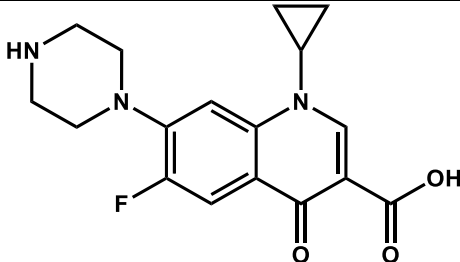
### 4.2.1 Materials

Zinc acetate dihydrate  $\text{Zn}(\text{CH}_3\text{COO})_2 \cdot 2\text{H}_2\text{O}$  (Merck, 98.0% purity), copper acetate monohydrate  $\text{Cu}(\text{CH}_3\text{COO})_2 \cdot \text{H}_2\text{O}$  (Merck, 98.0% purity), hydrogen peroxide  $\text{H}_2\text{O}_2$  (Merck, 30%), cerium acetate hydrate  $\text{Ce}(\text{CH}_3\text{COO})_2 \cdot x\text{H}_2\text{O}$  (Sigma Aldrich, 99.9% purity), Basic Red 2 (CDH Chemicals), Methyl Orange (Merck), and Ciprofloxacin (CDH Chemicals) were of analytical grade unless otherwise stated, and were utilized as received without purification. Table 4.1 gives information about the structure, formulas, and  $\lambda_{max}$  of model pollutant molecules employed in this study.

**Table 4.1** Structure and formula of model pollutants employed in the study.

Pollutant	Structure	$\lambda_{max}$ (nm)	Molecular Formula
Basic Red 2		522	$\text{C}_{20}\text{H}_{19}\text{ClN}_4$
Methyl Orange		464	$\text{C}_{14}\text{H}_{14}\text{N}_3\text{NaO}_3\text{S}$

---

Ciprofloxacin		276	C <sub>17</sub> H <sub>18</sub> FN <sub>3</sub> O <sub>3</sub>
---------------	---	-----	--

---

#### 4.2.2 Synthesis of ZnCuCe-LDH

ZnCuCe-LDH was synthesized as per the acid hydrolysis methodology previously reported by Pathak et al[27]. In a typical synthesis procedure, calculated amounts of zinc acetate dihydrate (0.9877 g), copper acetate monohydrate (0.0499 g), and cerium acetate hydrate (0.0793 g) were dissolved in 10 ml distilled water separately. On complete dissolution, solutions of copper acetate monohydrate and cerium acetate hydrate were added to zinc acetate dihydrate solution and the resultant solution was stirred for 15 minutes till homogeneity was achieved. Then hydrolysis process was initiated by the addition of 30% H<sub>2</sub>O<sub>2</sub> solution (5 mL) and distilled water (20 mL) with constant stirring, following which an instantaneous change in color of solution from pale green to brown was noted. Afterwards, the reaction mixture was sonicated for 30 minutes to ensure size uniformity of LDH particles, and it was then stirred for further 24 hours at room temperature. Finally, the reaction mixture was dried at 60°C in oven till complete removal of solvent to obtain powdery greenish product.

#### 4.2.3 Synthesis of ZnCuCe-LDO

The ZnCuCe-LDO photocatalyst was obtained by calcination of the obtained ZnCuCe-LDH precursor at 350 °C for 6 hours in muffle furnace[28]. The schematic representation of synthesis of ZnCuCe-LDH and ZnCuCe-LDO are presented in Figure 4.1.

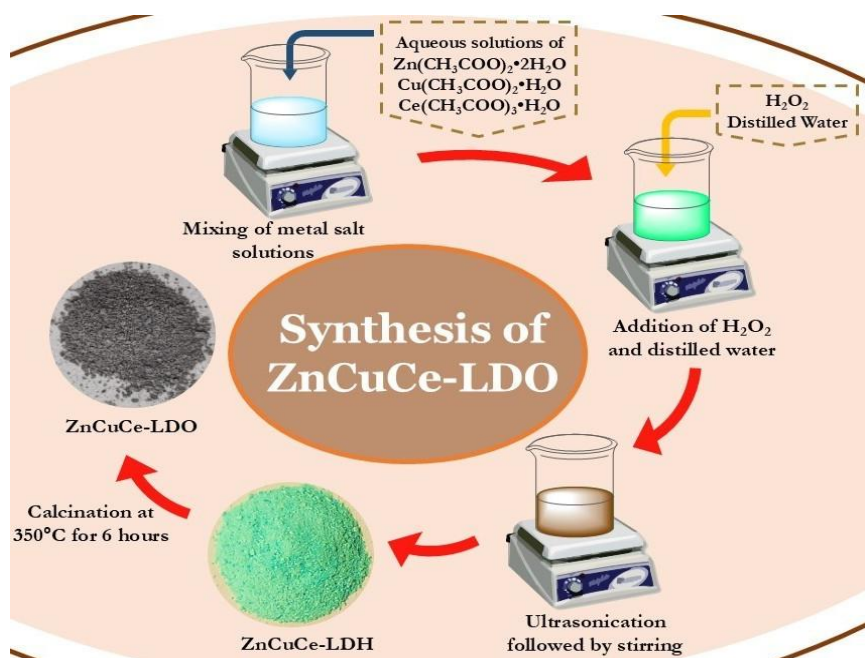


**Figure 4.1** Synthesis of ternary ZnCuCe-LDH and ZnCuCe-LDO.

#### 4.2.4 Characterization

Crystallographic properties of the sample were studied by the use of Powder X-ray diffraction (PXRD) diffractograms collected using a high-resolution Bruker diffractometer (D8 Discover) using Cu K $\alpha$  radiation. Data was recorded at 298 K over the range of  $2\theta = 5\text{--}70^\circ$ . Functional group identification was done using Fourier-transform infrared (FTIR) spectrum collected with the help of Perkin Elmer 2000 FTIR spectrometer by the KBr disk technique. SEM imaging and EDX analysis of the synthesized samples was done using a Zeiss Gemini SEM microscope. The specific surface area ( $S_{BET}$ ) and average pore size distribution were obtained by BET-BJH (Barrett-Joyner-Halenda)  $N_2$  adsorption-desorption technique on a Quanta chrome Nova-1000 instrument at liquid nitrogen temperature 77k. The optical properties of sample were studied using Jasco V-770 UV-DRS spectrophotometer. In order to ascertain surface charge of sample, zeta potential was measured using Malvern Zetasizer Nano-ZSP.

#### 4.2.5 Evaluation of Photocatalytic Activity

Light-stimulated catalytic activity of the as-synthesized photocatalyst was investigated by degrading two dyes - cationic Basic Red 2 (BR2) and anionic Methyl Orange (MO) dye, as well as ciprofloxacin (CIF) drug under UV light illumination at room temperature using a custom-made photocatalytic reactor. The reactor set-up consisted

of a dual-walled quartz tube that encased a high-pressure mercury vapour lamp (OSRAM India, 125 W) used for providing UV light. The tube was immersed in a double-walled pyrex glass vessel and water circulation was maintained around the tube and vessel to avoid thermal effects. The entire set-up was housed in a dark wooden box to avoid any interaction with external light sources. To evaluate the photocatalytic activity, 0.05 g ZnCuCe-LDO was suspended in 100 mL of 20 ppm aqueous solution of dye/drug in the photoreactor. The suspension of the photocatalyst and pollutant solution was initially stirred for 30 minutes in the absence of light in order to attain adsorption-desorption equilibrium. After removal of 3 mL aliquot from the suspension kept in dark, the set-up was irradiated with UV light and then aliquots were removed at pre-fixed interval of 30 minutes. The retrieved solutions were centrifuged to remove solid component and then the concentrations of solutions were determined by measuring absorbance at  $\lambda_{max}$  = 522 nm for BR2, 464 nm for MO and 276 nm for CIF using Shimadzu UV-Vis spectrophotometer. The percentage degradation of chosen toxic moieties was calculated using Equation 4.1:

$$\text{Percentage dye degradation} = \frac{(C_0 - C_t)}{C_0} \times 100 \quad (4.1)$$

where  $C_0$  and  $C_t$  denote the initial and final concentrations of the pollutants.

#### 4.2.6 Smartphone-based Colourimetric Analysis for Estimation of Photocatalytic Degradation of Azo Dyes

The quantification of the unknown concentration of dye obtained after the photocatalytic degradation of dye solution by ZnCuCe-LDO was also attempted using a smartphone-based colourimetric approach. This method is based on the principle of variation in absorbance value and colour of the analyte solution. The colour can be explained in terms of its Red-Green-Blue value, that can be detected using specific detection softwares and applications. Therefore, it can prove to be an effective way for coloured effluent concentration examination. For this approach, a low-cost and portable custom set-up was utilised wherein a cuvette containing dye solution was placed at an appropriate distance from a white light source in a dark box, and a smartphone (model: Samsung S22 having 50 MP + 12 MP + 10 MP triple camera) was used for capturing images of the dye solution. The smartphone was equipped with “RGB Colour Detector” application that was used to obtain R, G, and B values from

the captured images. The custom set-up constructed for the smartphone-based colourimetric analysis of dye solutions is presented in Figure 4.2.

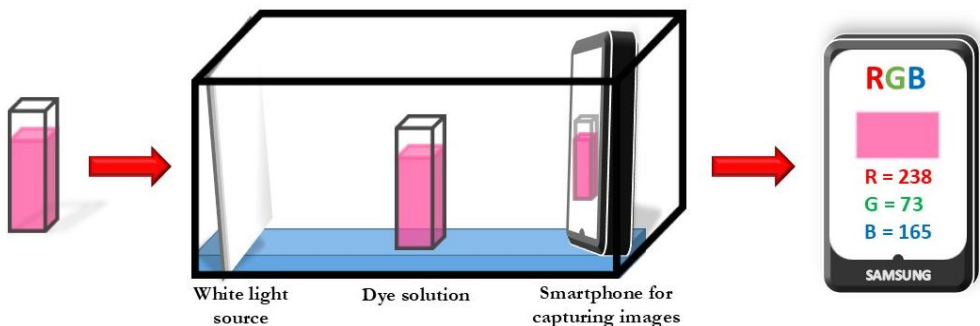


**Figure 4.2** Custom setup designed for smartphone-based colourimetric determination of dye concentration.

The RGB values of few selected known concentrations of dye solutions as well as solution of unknown concentration obtained at the end of the photocatalytic action of ZnCuCe-LDO were determined using Equation 4.2:

$$RGB_{reference/sample} = \frac{(R+G+B)}{3} \quad (4.2)$$

The correlation between RGB values and the solution concentration was obtained using a logarithmic scale, as shown in Equation 4.3, and it was further used for the construction of a calibration curve.

$$RGB_{parameter} = \log \left( \frac{RGB_{reference}}{RGB_{sample}} \right) \quad (4.3)$$

The  $RGB_{parameter}$  is considered to be analogous to the absorbance of light by the solution.

A calibration curve was also drawn using absorbance values of dye solutions of known concentrations that were obtained using UV-Visible spectrophotometer.

### 4.3 Results and Discussion

#### 4.3.1 Microstructural, Morphological, and Optical Characterisation Results

In order to determine the effect of incorporation of rare earth Ce cation by replacing Ni in ZnCuNi-LDH, PXRD pattern was recorded (Figure 4.3). It was observed that the PXRD diffractogram of ZnCuCe-LDH very closely resembled that of previously synthesized ZnCuNi-LDH[27]. Therefore, it was inferred that pure phase ZnCuCe-LDH could be synthesized by replacing Ni with Ce. The peaks were indexed to (002), (003), and (004) crystal planes, and they corresponded to the hexagonal symmetry

while the values of  $d$ -spacing corresponding to  $(002)$  plane and gallery height were calculated to be  $7.45\text{ \AA}$  and  $2.65\text{ \AA}$  respectively.

The effect of topotactical transformation due to calcination of ZnCuCe-LDH on the crystalline phases generated in ZnCuCe-LDO, can provide interesting information about its photocatalytic applications. The PXRD pattern of ZnCuCe-LDO, presented in Figure 4.3, consists of reflections that majorly corresponded to the hexagonally symmetric wurtzite phase of ZnO, and were indexed to the  $(100)$ ,  $(002)$ ,  $(101)$ ,  $(110)$ ,  $(103)$ ,  $(200)$ ,  $(112)$  and  $(201)$   $hkl$  planes[29]. Additionally, the appearance of a low-intensity reflection around  $28.5^\circ$  was attributed to the  $(111)$  plane of cubic CeO<sub>2</sub>[30,31]. Therefore, the PXRD results provided clear evidence for almost complete decomposition of the layered arrangement along with the elimination of interlayer acetate anions and water molecules as a consequence of the calcination of ZnCuCe-LDH precursor at  $350^\circ\text{C}$  for 6 hours. They also suggest the formation of a highly crystalline and pure phase mixed metal oxide product consisting of Zn, Cu and Ce cations.

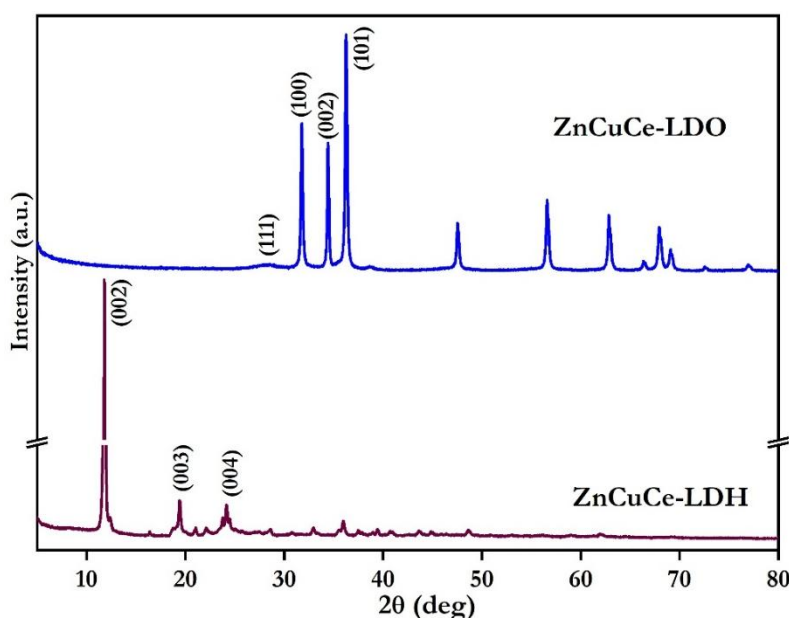


**Figure 4.3** PXRD diffractogram of ternary ZnCuCe-LDH and ZnCuCe-LDO.

The functional groups present in the synthesized samples were identified using FTIR technique. The FTIR spectrum of ZnCuCe-LDH, presented in Figure 4.4, exhibited a broad band at  $3079\text{ cm}^{-1}$ , that was signature of hydrogen-bonded -OH group as well as surface adsorbed and intercalated H<sub>2</sub>O molecules. The characteristic bands of

antisymmetric and symmetric vibration modes of  $\text{COO}^-$  group appeared at  $1553\text{ cm}^{-1}$  and  $1439\text{ cm}^{-1}$ , while bands at  $1017\text{ cm}^{-1}$  and  $954\text{ cm}^{-1}$  represented the fingerprint absorption bands of acetate anions i.e. C-C stretching and bending modes of  $-\text{CO}_2$  moiety respectively[32]. The absorption bands appearing at wavenumbers below  $700\text{ cm}^{-1}$  were related to the characteristic vibration bands between the metal ion and oxygen (M-O), as well as lattice vibrations. Therefore, the obtained FTIR spectrum further confirmed the successful synthesis of ZnCuCe-LDH, having typical structural characteristics of LDHs with intercalated acetate anions.

To study the impact of calcination on the chemical environment of ZnCuCe-LDH, the FTIR spectrum of ZnCuCe-LDO was recorded. The FTIR spectrum of ZnCuCe-LDO, presented in Figure 4.4, was found to be similar to previous reports, with bands appearing at  $2981\text{ cm}^{-1}$  that were ascribed to the O-H stretching of water molecules adsorbed on surface of LDO[33]. In addition, the appearance of a band centered at  $654\text{ cm}^{-1}$  was attributed to the presence of metal-oxygen bending deformation vibrations in ZnCuCe-LDO, while the band at  $526\text{ cm}^{-1}$  could be attributed to the Ce-O bond.

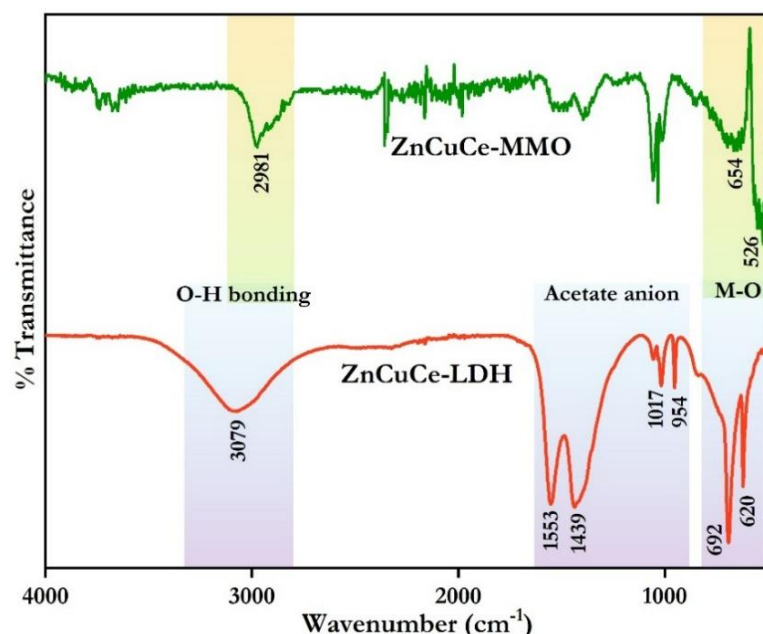
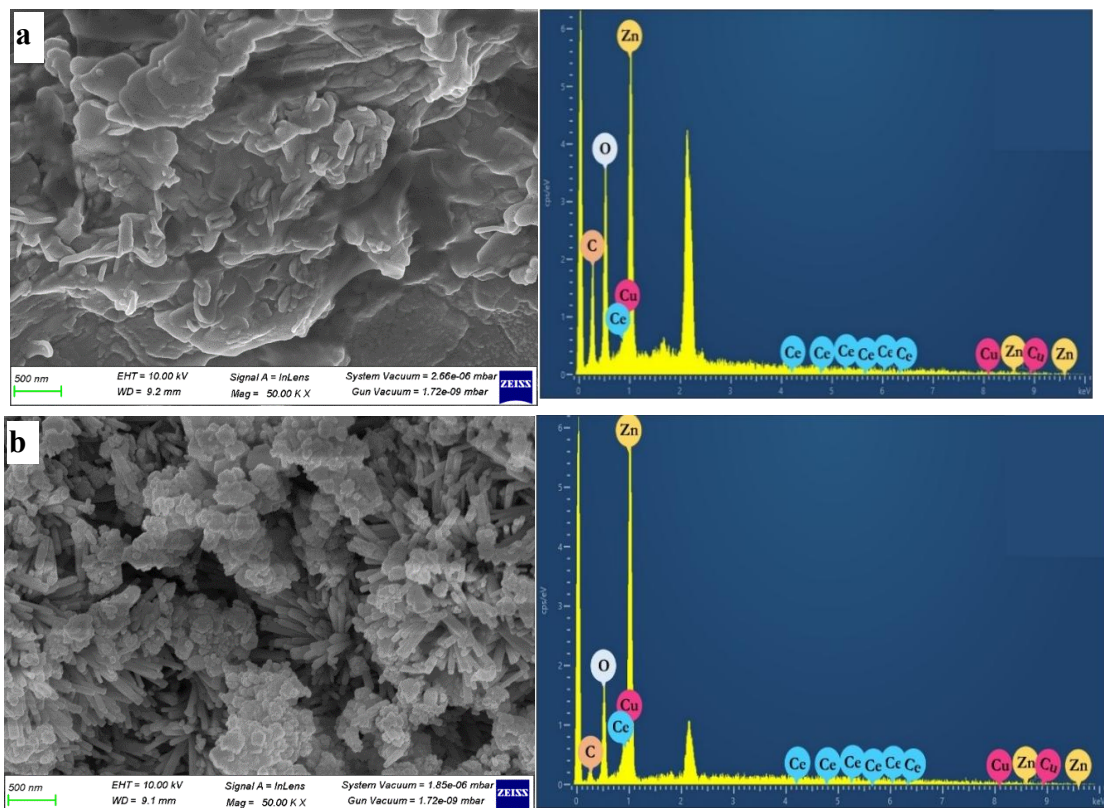


Figure 4.4 FTIR spectrum of ternary ZnCuCe-LDH and ZnCuCe-LDO.

The morphological features of synthesized ZnCuCe-LDH precursor and LDO were assessed using SEM-EDX imaging. The SEM micrograph (Figure 4.5a) clearly shows the characteristic layered arrangement in ZnCuCe-LDH, and the adjoining EDX spectrum presents the uniform distribution of constituent Zn, Cu, Ce, C, and O atoms

throughout the lattice. While the SEM micrograph of ZnCuCe-LDO, presented in Figure 4.5b, shows the existence of spherical and rod-shaped particles that are characteristic of mixed oxides containing zinc[14,34]. The adjoining EDX spectrum indicated that the compositional elements Zn, Cu, and Ce were distributed throughout the calcined product in a homogenous manner.



**Figure 4.5** SEM micrograph and EDX spectrum of ternary (a) ZnCuCe-LDH and (b) ZnCuCe-LDO.

The textural properties and porosity of ZnCuCe-LDO were determined by the use of  $N_2$  adsorption-desorption method at low temperature. The  $N_2$  adsorption-desorption isotherm, presented in Figure 4.6a-b, were identified as a typical Type-IV isotherm (as per IUPAC classification) that are characteristic of mesoporous materials[33]. The presence of H3-type hysteresis loop suggested the presence of irregular slit-like pores in non-rigid aggregated particles of mesoporous solids[35]. Further, the absence of a plateau at high  $P/P_0$  values corresponded to the physisorption of  $N_2$  between the aggregated, stacked plate-like particles that is typical to lamellar materials. The specific surface area ( $S_{BET}$ ), pore volume and average pore diameter (calculated from  $N_2$  desorption data using BJH method) were found to be  $19.784\text{ m}^2\text{g}^{-1}$ ,  $0.104\text{ cc g}^{-1}$ ,

and 15.114 nm respectively. The mesoporosity of the synthesized ZnCuCe-LDO was attributed to the formation of channels and pores as a consequence of the elimination of  $\text{H}_2\text{O}$  and  $\text{CO}_2$  during the thermal treatment of the LDH precursor. Thus, the mesoporosity and high  $S_{BET}$  warranted the use of ZnCuCe-LDO as an effective catalytic material.

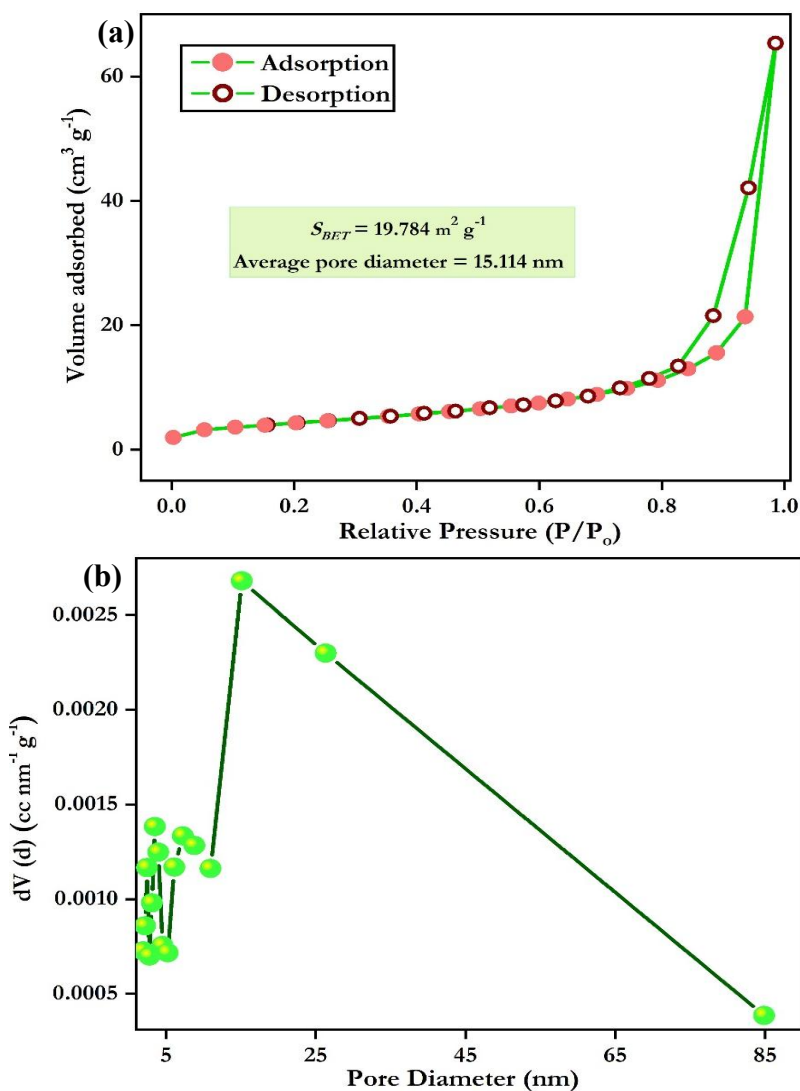


**Figure 4.6** (a)  $\text{N}_2$  adsorption-desorption isotherm and (b) corresponding pore size distribution plots with inset of enlarged view of pore size distribution between 0-20 nm of ternary ZnCuCe-LDO.

The optical properties of semiconductor strongly influence their photocatalytic abilities. For instance, the widely used semiconductor ZnO typically shows absorption band below 380 nm in the UV region, based on which it is used in UV-light stimulated reactions. Therefore, in order to ascertain the optical behaviour of ZnCuCe-LDO, the

optical properties were examined using UV-Vis Diffuse Reflectance spectrum (DRS), and the plot is presented in Figure 4.7a. The spectrum showed a strong absorption band in the 200-400 nm region that is characteristic of ZnO-containing materials[36]. The slight shift in absorption band of synthesized LDO to lower wavelength may be the consequence of the presence of cerium and copper in ZnCuCe-LDO alongside zinc. The band gap energy, estimated from the Tauc equation, was calculated to be 3.07 eV (Figure 4.7b) and it was found to be lower than bulk and nano ZnO that exhibited band gap energy of approximately 3.2 eV[37]. The reduced band gap energy may be attributed to the oxidation state of Zn and the chemical environment in the LDH structure that potentially impacted the valence band of Zn. The reduction of band gap energy is suggestive of faster movement of electrons from the valence band to the conducting band under lower energy irradiation that results in the production of more electron/positive hole pairs and directly contributes towards enhanced photocatalytic activity of ZnCuCe-LDO.

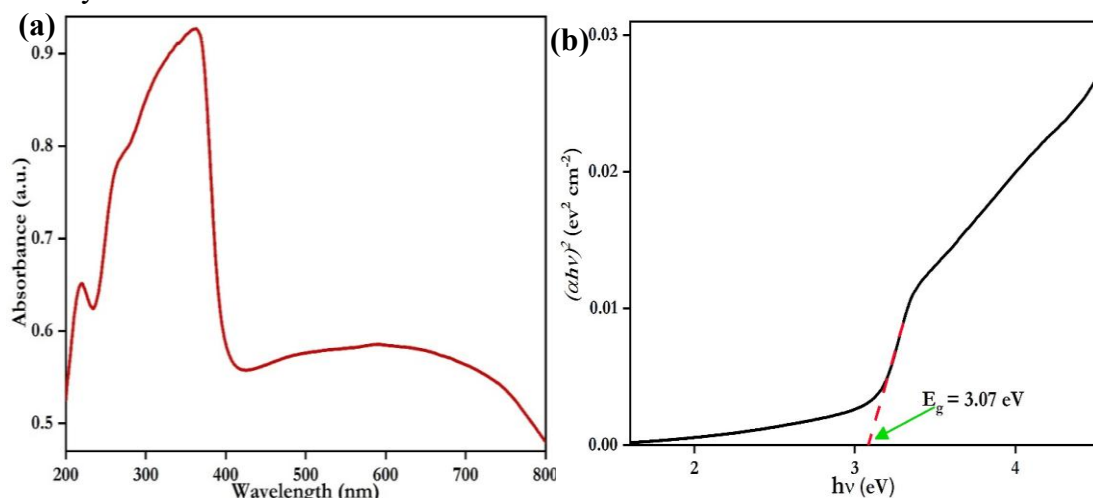


**Figure 4.7** (a) UV-DRS spectrum and (b) Tauc plot of ternary ZnCuCe-LDO.

Zeta potential study was conducted to assess the stability and dispersibility of LDO. The zeta potential of LDO was found to be -9.44 mV, suggesting moderate stability and higher affinity to positively charged moieties due to electrostatic forces of attraction.

### 4.3.2 Photocatalytic Activity

In order to highlight the advantages of semiconductor-based photocatalytic degradation, the photocatalytic activity of ZnCuCe-LDO was studied. Cationic BR2 (20 ppm), anionic MO (20 ppm) dyes and ciprofloxacin drug were selected as the target

contaminants to investigate the photocatalytic activity of as-synthesized LDO (0.05 g). Before illumination, the suspension was stirred for 30 min in the dark to attain the adsorption-desorption equilibrium. A negligible fraction of model molecules BR2, MO, and CIF (<10%) was potentially adsorbed on the surface of the photocatalyst during the first 30 minutes when the suspension was stirred in the absence of UV illumination. Subsequently, on light irradiation, the percentage degradation increased gradually with increase in irradiation time from 30 minutes to 120 minutes for both dyes.

Further, in order to gain a deeper understanding about the degradation activity of model molecules, the kinetics of the photocatalytic reaction were studied. Photodegradation kinetics of organic contaminants in aqueous medium is usually described using the Langmuir-Hinshelwood mechanism since it provides a correlation between the concentration of pollutant and the reaction rate of degradation[38]. The model is described using the Equation 4.4:

$$r = \frac{-dC}{dt} = \frac{k_r K_{ad} C}{1 + K_{ad} C} \quad (4.4)$$

Where  $k_r$  describes the rate constant of degradation reaction,  $C$  depicts the concentration of the contaminant and  $K_{ad}$  is the adsorption equilibrium constant. Since only a negligible amount of pollutant was adsorbed on the catalyst, and the concentration of pollutant was very low, therefore Eqn 4.4 could be reformulated to resemble equation of pseudo first order kinetics that is generally followed by ZnO-containing systems:

$$\ln \left( \frac{C_t}{C_0} \right) = -kt \quad (4.5)$$

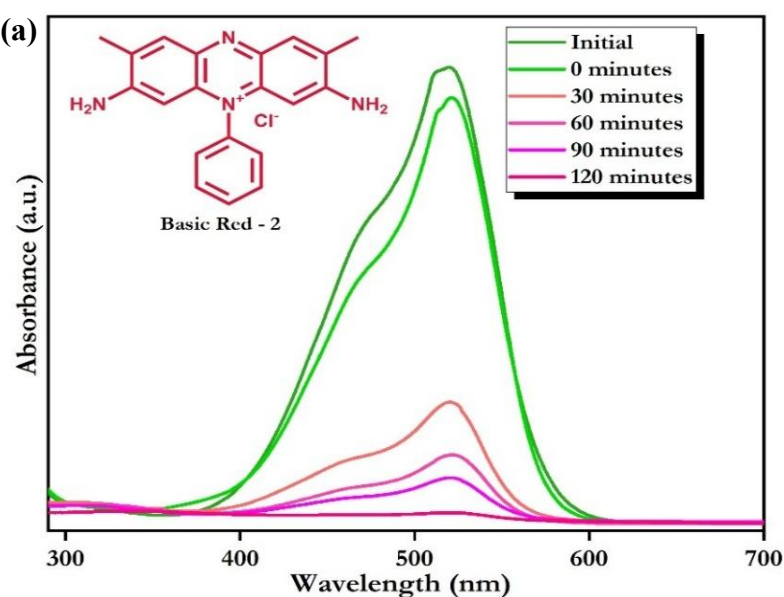
where  $C_0$  is initial pollutant concentration,  $C_t$  represents the final concentration of pollutant after irradiation, while  $k$  is the reaction rate constant and  $t$  signifies the irradiation time.

#### 4.3.2.1 Photodegradation of BR2

The photocatalytic activity of ZnCuCe-LDO towards BR2 degradation was investigated under UV light at room temperature and ambient pressure, and the experimental results are presented below. Figure 4.8a presents the time-dependent UV-Vis extinction spectra of BR2 at various time intervals within a period of 120 minutes. In case of BR2, absorbance maxima appeared around  $\lambda_{max} = 522$  nm. From the

absorption spectra, it was deduced that virtually no amount of BR2 was adsorbed by ZnCuCe-LDO. Subsequently, on UV illumination, with the progress of photocatalytic reaction, the main peak of absorbance maxima for BR2 appearing around  $\lambda_{max} = 522$  nm began decreasing rapidly. It was observed that after UV-irradiation for 60 minutes, ZnCuCe-LDO was able to achieve rapid degradation of approximately 83% of BR2 molecules. On further illumination above 60 minutes, rate of dye degradation reduced slightly as compared to degradation rate before 60 minutes. The complete decolourisation of dye solution after 120 minutes signified the end of the photocatalytic process, and percentage degradation at end of photocatalytic process was found to be 97.6% for BR2. The rapid decrease in intensity of absorbance maxima appearing at  $\lambda_{max} = 522$  nm with increasing time under UV light irradiation may be attributed to the oxidation and bond cleavage of the conjugated system and the chromophore, resulting in degradation of BR2[39].

The kinetics of photocatalytic degradation of BR2 using ZnCuCe-LDO were evaluated by fitting the obtained experimental data to Eqn 4.5 representing the pseudo-first order model, and rate constant  $k$  was determined from the linear regression plotted between  $\ln(C_t/C_0)$  and  $t$  (Figure 4.8b). The  $\ln(C_t/C_0)$  versus time plots for BR2 presented  $R^2$  values of 0.95, signifying that the experimental data was in good agreement with the pseudo-first-order model. Furthermore, values of rate constant  $k$  were calculated to be  $0.0276 \text{ min}^{-1}$  for BR2.



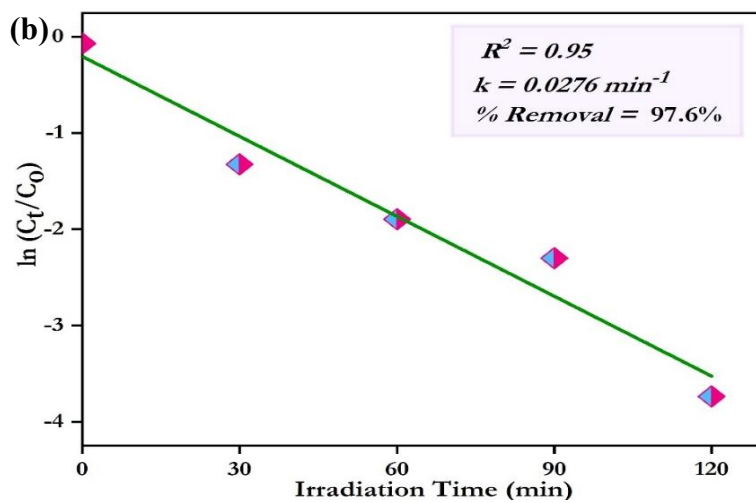


**Figure 4.8** (a) Time-dependent UV-Vis absorbance spectrum and (b) kinetics plot for photocatalytic degradation of BR2 by ZnCuCe-LDO.

#### 4.3.2.2 Photodegradation of MO

The photocatalytic activity of ZnCuCe-LDO towards MO degradation was investigated under UV light at room temperature and ambient pressure, and the experimental results are presented below. The plot depicting change in absorption intensity as a function of UV light irradiation of MO in aqueous solutions in the presence of ZnCuCe-LDO photocatalyst is presented in Figure 4.9a. In case of MO, absorbance maxima appeared around  $\lambda_{max} = 464$  nm. From the absorption spectra, it was deduced that negligible amount of MO was adsorbed by ZnCuCe-LDO. Subsequently, on UV illumination, with the progress of photocatalytic reaction, the main peak of absorbance maxima for MO appearing around  $\lambda_{max} = 464$  nm began decreasing rapidly. It was observed that after irradiation of UV light for 60 minutes, ZnCuCe-LDO was able to achieve rapid degradation of approximately 60% of MO molecules. The complete decolourisation of MO solution after 120 minutes signified the end of the photocatalytic process, and percentage degradation was found to be 92.2% for MO. It may be hypothesized that in case of MO, the intensity of absorption maxima appearing at  $\lambda_{max} = 464$  nm decreased gradually with increasing time, signifying decolourisation of MO solution due to degradation of chromophoric groups present in the dye molecules[40].

The kinetics of photocatalytic degradation of MO using ZnCuCe-LDO were evaluated by fitting the obtained experimental data to Eqn 4.5 representing the pseudo-first order

model, and rate constant  $k$  was determined from the linear regression plotted between  $\ln(C_t/C_0)$  and  $t$  (Figure 4.9b). The  $\ln(C_t/C_0)$  versus time plots for MO presented  $R^2$  values of 0.97, signifying that the experimental data was in good agreement with the pseudo first order model. Furthermore, values of rate constant  $k$  were calculated to be  $0.0206 \text{ min}^{-1}$  for MO.

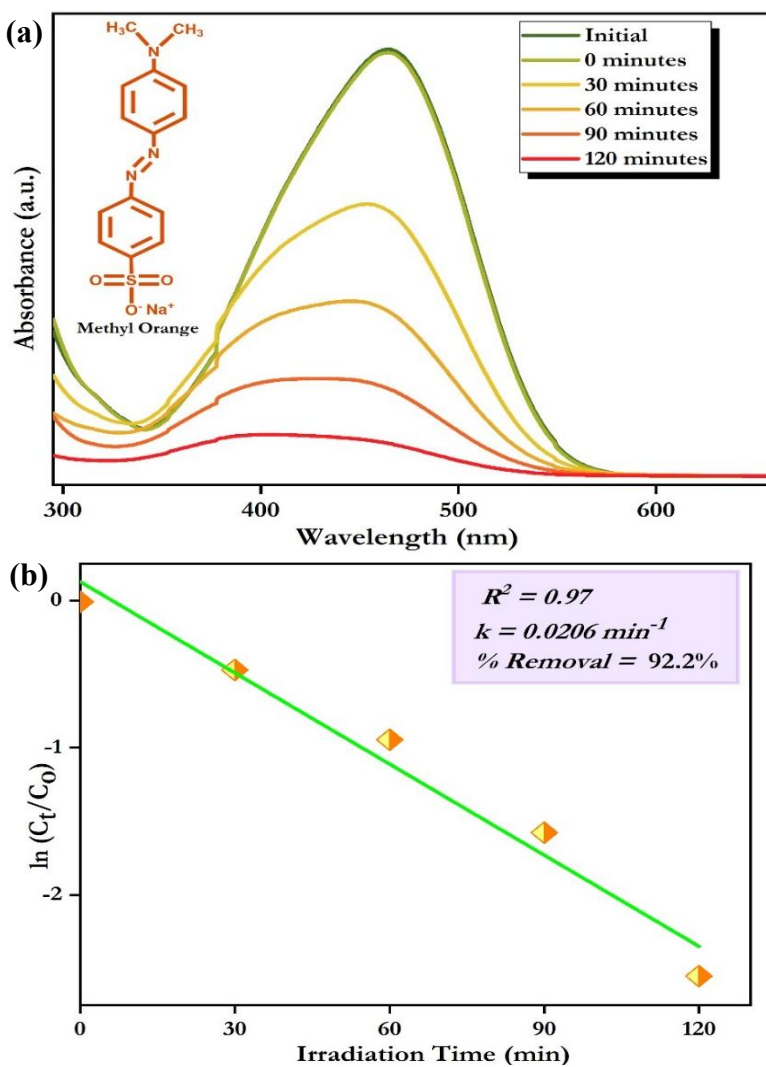


**Figure 4.9** (a) Time-dependent UV-Vis absorbance spectrum and (b) kinetics plot for photocatalytic degradation of MO by ZnCuCe-LDO.

It may be worth noting that the slightly higher degradation efficiency of the synthesized catalyst towards cationic BR2 over anionic MO dye may be attributed to the negative zeta potential of ZnCuCe-LDO surface, that likely exhibits a higher degree of adsorption of the positively charged BR2 molecules than the negatively charged MO molecules. Higher degree of adsorption directly contributes towards

faster and more efficient degradation of BR2 since adsorption is an integral step in the photocatalytic process.

#### 4.3.2.3 Photocatalytic Degradation of Ciprofloxacin

The photocatalytic activity of ZnCuCe-LDO towards CIF drug degradation was investigated under UV light at room temperature and ambient pressure, and the experimental results are presented below. Figure 4.10a represents the time-dependent UV-Vis extinction spectra of CIF at various time intervals within a period of 120 minutes. In case of CIF, a principal extinction peak appears around  $\lambda_{max} = 276$  nm. From the absorption spectra, it may be deduced that virtually no amount of drug was adsorbed by ZnCuCe-LDO. Subsequently, on UV illumination, with the progress of photocatalytic reaction, the main peak of absorbance maxima for CIF appearing around  $\lambda_{max} = 276$  nm began decreasing rapidly. The decrease in absorbance maxima may be attributed to the oxidative decomposition of CIF under the influence of UV light and ZnCuCe-LDO[13]. It may be noted that with the progress of the photocatalytic reaction, the peaks demonstrated a slight blue shift that signifies that CIF decomposition is a mineralization process. Based on the experimental data, it was determined that ZnCuCe-LDO demonstrated percentage degradation of 87.01% within 90 minutes towards CIF molecules.

From the graph plotted between  $C_t/C_0$  and time  $t$  (Figure 4.10a inset), it was deduced that under dark conditions, there was no significant change in drug concentration with time, while on UV illumination, the concentration of CIF decreased with an increase in reaction time. The plot between CIF concentration and time  $t$  presented in Figure 4.10b depicts that there is a good linear relationship between  $\ln(C_t/C_0)$  and  $t$ . Based on the value of  $R^2$  (0.95) obtained from the plot, it was concluded that the kinetics of the reaction could be successfully described using the pseudo first-order model as presented in Eqn 4.5. The value of rate constant  $k$ , calculated from the slope of graph plotted between  $\ln(C_t/C_0)$  and time  $t$ , was found to be  $0.0219 \text{ min}^{-1}$ . Thus, it may be inferred that while adsorptive uptake of CIF by the synthesized catalyst was found to be negligible, ZnCuCe-LDO acted as a highly efficacious photocatalyst for the degradation of CIF under UV light efficiently within 90 minutes.

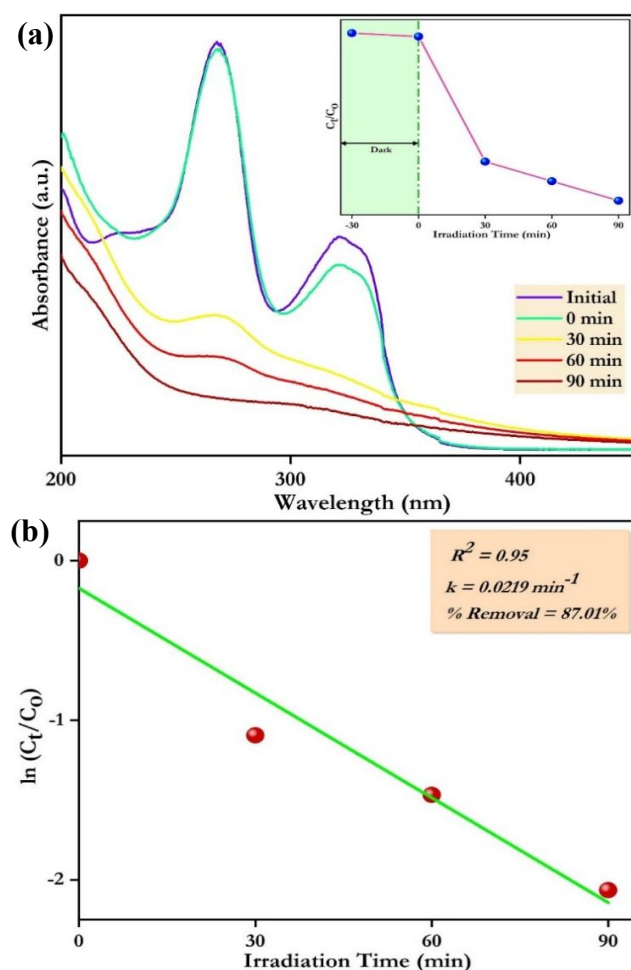


**Figure 4.10** (a) Time-dependent UV-Vis absorbance spectrum with inset plot of  $C_t/C_0$  and time  $t$ , and (b) kinetics plot for photocatalytic degradation of CIF by ZnCuCe-LDO.

#### 4.3.3 Smartphone-based analysis of photocatalytic degradation of azo dyes

The solutions obtained after photocatalytic degradation of BR2 and MO using ZnCuCe-LDO were also evaluated using a smartphone, and the results are shown in Figure 4.11a-d. The values of R, G, B as well as the calculated  $\text{RGB}_{\text{parameter}}$  of known BR2 and MO concentrations are listed in Table 4.2. It may be deduced from the results presented in the table that the higher dye concentration was reflected by highly intense colour and it resulted in elevated  $\text{RGB}_{\text{parameter}}$  values. The calibration curve plotted between  $\text{RGB}_{\text{parameter}}$  and dye concentration was used to determine the unknown concentration of dye solution, and accuracy of the values was checked using calibration curve obtained using UV-Vis spectrum data.

It was found that the spectrophotometric and smartphone-based values were in good agreement for both BR2 and MO dyes, and the  $R^2$  values for the plots were found to be around 0.99. Therefore, it was inferred that smartphone-based colourimetric method could serve as a reliable, sensitive and accurate method for the rapid determination of concentrations of coloured effluents in resource-limited settings.

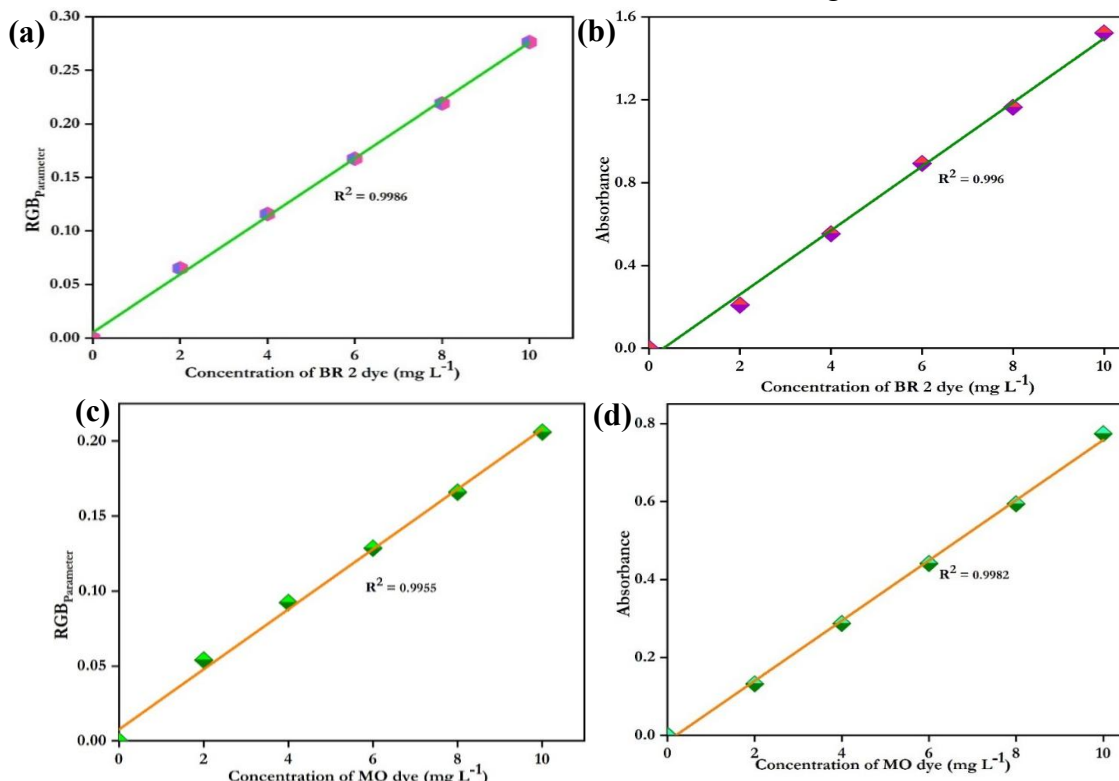


**Figure 4.11** Calibration plots for (a,b) BR2 and (c,d) MO dye concentrations based on  $RGB_{parameter}$  and UV-Vis spectrophotometry respectively.

**Table 4.2** Colour parameters of BR2 and MO dye solutions with different concentrations.

Dye Concentration	R	G	B	$RGB_{parameter}$
<b>BR2</b>				
0	255	255	255	0.0
2	229	187	207	0.08
4	238	140	189	0.13
6	238	100	174	0.17
8	238	73	165	0.20
10	238	49	149	0.24

MO					
0		255	255	255	0.0
2		219	207	185	0.09
4		224	202	155	0.11
6		236	202	115	0.14
8		236	200	86	0.16
10		236	193	65	0.19

#### 4.4 Conclusion

In brief, the current study reports the synthesis of a novel ZnCuCe-LDO through calcination of ZnCuCe-LDH precursor that was utilised for the photo-assisted degradation of azo dyes. The topotactic transformation of LDH into LDO was confirmed by PXRD, FTIR and SEM techniques while the optical studies determined ZnCuCe-LDO to be a UV-active material. The photocatalytic experiments for degradation of anionic and cationic azo dyes in aqueous medium gave evidence for the UV-light stimulated catalytic properties of ZnCuCe-LDO, with it exhibiting approximately 97% dye degradation of cationic BR2 dye and around 92% dye degradation of anionic MO dye respectively within 120 minutes. Furthermore, the smartphone-based approach was found to be conducive for real-time determination of coloured effluent concentration due to its ability to deliver comparable results to UV-Vis spectrophotometer using a low-cost, portable, sensitive and rapid response set-up. With the prevalence of smartphone technology, this colourimetric platform can provide smart solutions for on-site detection and analysis of coloured effluents. Additionally, the photocatalytic degradative ability of ZnCuCe-LDO was also examined towards CIF drug, and the photocatalyst exhibited more than 87% degradation efficiency. It is important to note that while both ZnCuNi-LDH (reported in Chapter 3) and ZnCuCe-LDO possess photocatalytic behaviour, but the efficiency of Ce-based lattice was found to be considerably higher. The variable oxidation state, redox properties as well as the unique geometrical and electronic attributes of cerium provide a platform for high catalytic activity of cerium-containing materials. Therefore, incorporation of rare

earth cations in LDH offers several advantages over conventional materials for catalytic applications.

#### 4.5 References

- [1] G. Fan, F. Li, D.G. Evans, X. Duan, Catalytic applications of layered double hydroxides: Recent advances and perspectives, *Chem. Soc. Rev.* 43 (2014) 7040–7066. <https://doi.org/10.1039/c4cs00160e>.
- [2] S. Megala, S. Prabhu, S. Harish, M. Navaneethan, S. Sohila, R. Ramesh, Enhanced photocatalytic dye degradation activity of carbonate intercalated layered Zn, ZnNi and ZnCu hydroxides, *Appl. Surf. Sci.* 481 (2019) 385–393. <https://doi.org/10.1016/j.apsusc.2019.03.091>.
- [3] L. Mohapatra, K. Parida, M. Satpathy, Molybdate/tungstate intercalated oxo-bridged Zn/Y LDH for solar light induced photodegradation of organic pollutants, *J. Phys. Chem. C* 116 (2012) 13063–13070. <https://doi.org/10.1021/jp300066g>.
- [4] M. Lobo-Sánchez, G. Nájera-Meléndez, G. Luna, V. Segura-Pérez, J.A. Rivera, G. Fetter, ZnAl layered double hydroxides impregnated with eucalyptus oil as efficient hybrid materials against multi-resistant bacteria, *Appl. Clay Sci.* 153 (2018) 61–69. <https://doi.org/10.1016/j.clay.2017.11.017>.
- [5] M.B. Gawande, R.K. Pandey, R. V. Jayaram, Role of mixed metal oxides in catalysis science - Versatile applications in organic synthesis, *Catal. Sci. Technol.* 2 (2012) 1113–1125. <https://doi.org/10.1039/c2cy00490a>.
- [6] L. Tang, X. Xie, C. Li, Y. Xu, W. Zhu, L. Wang, Regulation of Structure and Anion-Exchange Performance of Layered Double Hydroxide: Function of the Metal Cation Composition of a Brucite-like Layer, 2022. <https://doi.org/10.3390/ma15227983>.
- [7] X. Wang, Y. Tang, J.-M. Lee, G. Fu, Recent advances in rare-earth-based materials for electrocatalysis, *Chem Catal.* 2 (2022) 967–1008. <https://doi.org/https://doi.org/10.1016/j.chechat.2022.02.007>.
- [8] R. Zăvoianu, R. Bîrjega, E. Angelescu, O.D. Pavel, Effect of hydration temperature on the structure reconstruction of MgAlY layered materials, *Comptes Rendus Chim.* 21 (2018) 318–326. <https://doi.org/https://doi.org/10.1016/j.crci.2017.07.002>.
- [9] L. Wang, B. Li, X. Zhao, C. Chen, J. Cao, Effect of rare earth ions on the properties of composites composed of ethylene vinyl acetate copolymer and layered double hydroxides, *PLoS One* 7 (2012) e33781. <https://doi.org/10.1371/journal.pone.0033781>.
- [10] P. Singh, R. Nagarajan, Synthesis, Structure, Optical and Magnetic Properties of Layered Hydroxide Acetates Containing Zinc and Lanthanides, *Adv. Porous Mater.* 2 (2015) 149–156. <https://doi.org/10.1166/apm.2014.1063>.
- [11] Z. Song, Q. Yin, Z. Zhao, X. Li, Z. Li, J. Yu, Q. Yuan, D. Zhao, Y. zhi Li, Y.

Sui, J. Qi, J. Han, Fluoride-Ion-Mediated Fabrication of Cerium-Incorporated Ternary Layered Double Hydroxide Microflowers for Enhanced Chlorine Storage, *Adv. Funct. Mater.* (2025). <https://doi.org/10.1002/adfm.202500494>.

[12] X. Feng, J. Zeng, J. Zhu, K. Song, X. Zhou, X. Guo, C. Xie, J.W. Shi, Gd-modified Mn-Co oxides derived from layered double hydroxides for improved catalytic activity and H<sub>2</sub>O/SO<sub>2</sub> tolerance in NH<sub>3</sub>-SCR of NO<sub>x</sub> reaction, *J. Colloid Interface Sci.* 659 (2024) 1063–1071. <https://doi.org/10.1016/j.jcis.2024.01.043>.

[13] L. Wolski, K. Grzelak, M. Muńko, M. Frankowski, T. Grzyb, G. Nowaczyk, Insight into photocatalytic degradation of ciprofloxacin over CeO<sub>2</sub>/ZnO nanocomposites: Unravelling the synergy between the metal oxides and analysis of reaction pathways, *Appl. Surf. Sci.* 563 (2021). <https://doi.org/10.1016/j.apsusc.2021.150338>.

[14] M. Faisal, A.A. Ismail, A.A. Ibrahim, H. Bouzid, S.A. Al-Sayari, Highly efficient photocatalyst based on Ce doped ZnO nanorods: Controllable synthesis and enhanced photocatalytic activity, *Chem. Eng. J.* 229 (2013) 225–233. <https://doi.org/10.1016/j.cej.2013.06.004>.

[15] P. Gholami, A. Khataee, M. Ritala, Template-free hierarchical trimetallic oxide photocatalyst derived from organically modified ZnCuCo layered double hydroxide, *J. Clean. Prod.* 366 (2022) 132761. <https://doi.org/10.1016/j.jclepro.2022.132761>.

[16] Y. He, A.U. Rehman, M. Xu, C.A. Not, A.M.C. Ng, A.B. Djurišić, Photocatalytic degradation of different types of microplastics by TiO<sub>x</sub>/ZnO tetrapod photocatalysts, *Heliyon* 9 (2023) e22562. <https://doi.org/10.1016/j.heliyon.2023.e22562>.

[17] M. Muruganandham, J.J. Wu, Synthesis, characterization and catalytic activity of easily recyclable zinc oxide nanobundles, *Appl. Catal. B Environ.* 80 (2008) 32–41. <https://doi.org/10.1016/j.apcatb.2007.11.006>.

[18] J. Liang, Y. Wei, Y. Yao, X. Zheng, J. Shen, G. He, H. Chen, Constructing high-efficiency photocatalyst for degrading ciprofloxacin: Three-dimensional visible light driven graphene based NiAlFe LDH, *J. Colloid Interface Sci.* 540 (2019) 237–246. <https://doi.org/10.1016/j.jcis.2019.01.011>.

[19] L. Ju, P. Wu, X. Lai, S. Yang, B. Gong, M. Chen, N. Zhu, Synthesis and characterization of Fullerene modified ZnAlTi-LDO in photo-degradation of Bisphenol A under simulated visible light irradiation, *Environ. Pollut.* 228 (2017) 234–244. <https://doi.org/10.1016/j.envpol.2017.05.038>.

[20] X. Wang, P. Wu, Y. Lu, Z. Huang, N. Zhu, C. Lin, Z. Dang, NiZnAl layered double hydroxides as photocatalyst under solar radiation for photocatalytic degradation of orange G, *Sep. Purif. Technol.* 132 (2014) 195–205. <https://doi.org/10.1016/j.seppur.2014.05.026>.

[21] V.P. Singh, A. Susaniya, S.C. Jain, R. Vaish, Demonstrating a Rice-Husk-

Based Adsorption Process Using Smartphone Colorimetry to Teach Students about Kinetic Models and Their Applications, *J. Chem. Educ.* 98 (2021) 3288–3296. <https://doi.org/10.1021/acs.jchemed.1c00065>.

[22] B. Pandey, P. Singh, R. Kumar, Ultrasonic-Assisted Adsorptive Uptake of Malachite Green Dye Onto Zn/Cu-Layered Double Oxide: Spectrophotometric and Smartphone-Based Detection, *Appl. Organomet. Chem.* 39 (2025) e7981. <https://doi.org/https://doi.org/10.1002/aoc.7981>.

[23] H. Bahrami, M. Mejmarian, H. Jafari, F. Rasekh, Synthesis of new Fe/Cr LDH for removal of  $Hg^{2+}$  ion from aqueous solutions and adsorption study using smartphone-based colorimetry, *Environ. Nanotechnology, Monit. Manag.* 18 (2022) 100702. <https://doi.org/10.1016/j.enmm.2022.100702>.

[24] J. Huang, D.D. Koroteev, M. Zhang, Smartphone-based study of cement-activated charcoal coatings for removal of organic pollutants from water, *Constr. Build. Mater.* 300 (2021) 124034. <https://doi.org/10.1016/j.conbuildmat.2021.124034>.

[25] P. Kumbhakar, R.S. Ambekar, P.L. Mahapatra, C. Sekhar Tiwary, Quantifying instant water cleaning efficiency using zinc oxide decorated complex 3D printed porous architectures, *J. Hazard. Mater.* 418 (2021) 126383. <https://doi.org/10.1016/j.jhazmat.2021.126383>.

[26] H. Laddha, P. Yadav, M. Agarwal, R. Gupta, Quick and hassle-free smartphone's RGB-based color to photocatalytic degradation rate assessment of malachite green dye in water by fluorescent Zr–N–S co-doped carbon dots, *Environ. Sci. Pollut. Res.* 29 (2022) 56684–56695. <https://doi.org/10.1007/s11356-022-19808-5>.

[27] J. Pathak, P. Singh, Synthesis and Characterization of Ternary Layered Double Hydroxide containing Zinc/Copper/Nickel and its PANI Composite, *Polym. Compos.* 43 (2022) 7836. <https://doi.org/https://doi.org/10.1002/pc.26895>.

[28] J. Pathak, P. Singh, Zinc-Copper-Nickel Mixed Metal Oxide as Heterogeneous Catalytic Material for the Reductive Degradation of Nitroarene and Azo Dye, *Catal. Letters* 154 (2024) 5280–5293. <https://doi.org/10.1007/s10562-024-04754-3>.

[29] M. Thejaswini, V. Lakshmi Ranganatha, H.B. Vasanth Patil, S. Pramila, G. Nagaraju, C. Mallikarjunaswamy, Phyto-mediated facile synthesis of ZnO nanoparticles: enhanced photocatalysis, biological, and electrochemical properties, *Ionics (Kiel)*. (2024). <https://doi.org/10.1007/s11581-024-05710-2>.

[30] A. Arumugam, C. Karthikeyan, A.S. Haja Hameed, K. Gopinath, S. Gowri, V. Karthika, Synthesis of cerium oxide nanoparticles using Gloriosa superba L. leaf extract and their structural, optical and antibacterial properties, *Mater. Sci. Eng. C* 49 (2015) 408–415. <https://doi.org/10.1016/j.msec.2015.01.042>.

[31] C. Ge, C. Xie, S. Cai, Preparation and gas-sensing properties of Ce-doped

ZnO thin-film sensors by dip-coating, *Mater. Sci. Eng. B* 137 (2007) 53–58. <https://doi.org/10.1016/j.mseb.2006.10.006>.

[32] J. Pathak, P. Singh, Ultrafast catalytic reduction of organic pollutants using ternary zinc–copper–nickel layered double hydroxide, *Appl. Organomet. Chem.* 38 (2024) e7507. <https://doi.org/10.1002/aoc.7507>.

[33] O. Bechambi, A. Touati, S. Sayadi, W. Najjar, Effect of cerium doping on the textural, structural and optical properties of zinc oxide: Role of cerium and hydrogen peroxide to enhance the photocatalytic degradation of endocrine disrupting compounds, *Mater. Sci. Semicond. Process.* 39 (2015) 807–816. <https://doi.org/10.1016/j.mssp.2015.05.052>.

[34] M. Irfan, H. Munir, H. Ismail, Characterization and fabrication of zinc oxide nanoparticles by gum Acacia modesta through green chemistry and impregnation on surgical sutures to boost up the wound healing process, *Int. J. Biol. Macromol.* 204 (2022) 466–475. <https://doi.org/10.1016/j.ijbiomac.2022.02.043>.

[35] K.S.W. Sing, R.T. Williams, Physisorption hysteresis loops and the characterization of nanoporous materials, *Adsorpt. Sci. Technol.* 22 (2004) 773–782. <https://doi.org/10.1260/0263617053499032>.

[36] S. Moghe, A.D. Acharya, S.B. Shrivastava, Study of metal oxide doped polymeric thin films, in: *AIP Conf. Proc.*, 2020. <https://doi.org/10.1063/5.0006263>.

[37] S. Suresh, S. Thambidurai, J. Arumugam, M. Kandasamy, N. Pugazhenthiran, D. Balaji, B.A. Al-Asbahi, N.R. Reddy, A. Arunkumar, T. Muneeswaran, Antibacterial activity and photocatalytic oxidative performance of zinc oxide nanorods biosynthesized using Aerva lanata leaf extract, *Inorg. Chem. Commun.* 139 (2022). <https://doi.org/10.1016/j.inoche.2022.109398>.

[38] Z. Kalaycıoğlu, B. Özüğür Uysal, Ö. Pekcan, F.B. Erim, Efficient Photocatalytic Degradation of Methylene Blue Dye from Aqueous Solution with Cerium Oxide Nanoparticles and Graphene Oxide-Doped Polyacrylamide, *ACS Omega* (2023). <https://doi.org/10.1021/acsomega.3c00198>.

[39] M.R. Abukhadra, M. Shaban, F. Sayed, I. Saad, Efficient photocatalytic removal of safarnin-O dye pollutants from water under sunlight using synthetic bentonite/polyaniline@Ni<sub>2</sub>O<sub>3</sub> photocatalyst of enhanced properties, *Environ. Sci. Pollut. Res.* 25 (2018) 33264–33276. <https://doi.org/10.1007/s11356-018-3270-x>.

[40] C. Baiocchi, M.C. Brussino, E. Pramauro, A.B. Prevot, L. Palmisano, G. Marcí, Characterization of methyl orange and its photocatalytic degradation products by HPLC/UV-VIS diode array and atmospheric pressure ionization quadrupole ion trap mass spectrometry, *Int. J. Mass Spectrom.* 214 (2002) 247–256. [https://doi.org/10.1016/S1387-3806\(01\)00590-5](https://doi.org/10.1016/S1387-3806(01)00590-5).

**CHAPTER - 5**

***INSIGHTS INTO THE LOW SOLVENT  
SYNTHESIS, STRUCTURAL MEMORY  
EFFECT PROPERTY AND ANION  
EXCHANGE ABILITY OF ZnCuNi-LAYERED  
DOUBLE HYDROXIDE***

---

# **CHAPTER - 5**

## **INSIGHTS INTO THE LOW SOLVENT SYNTHESIS, STRUCTURAL MEMORY EFFECT PROPERTY AND ANION EXCHANGE ABILITY OF ZnCuNi-LAYERED DOUBLE HYDROXIDE**

---

### **5.1 Introduction**

The recent boom in nanotechnology has shifted the focus on two-dimensional materials having layered structures that act as host-guest materials with exchangeable ions. These materials are characterized by traits such as strong intralayer bonding and weak interlayer interactions. Specifically, anionic clays having positively charged layers have garnered immense attention due to their extraordinary structural features and physiochemical properties[1]. Among the various types of anionic clays currently being researched, layered double hydroxides (LDHs) have caught the eye of several research groups due to their structural and compositional flexibility[2,3]. Due to these attributes, LDHs exhibit properties such as surface basicity, anion exchangeability and intercalation behaviour. Further, the endless possibilities for variation in their structure by using various cations and anions opens up avenues for their use in applications such as catalysis, adsorption, sensing, energy storage, and biomedicine[3–5]. But inspite of all these advantages, the synthesis of LDHs to introduce new features and/or moieties while maintaining particle integrity is a topic of great interest. Conventionally, the synthesis of LDHs is generally achieved through methods such as coprecipitation, sol-gel route, urea hydrolysis, hydrothermal method, salt-oxide method, etc[6,7]. But these methods often call for the use of toxic precursors, large amounts of solvents, and harsh reaction conditions. Therefore, the focus of LDH-based research is now moving towards devising new synthesis methods that overcome these drawbacks. One significant way to improve existing synthesis methods is the use of lesser amounts of solvents than typically required. The use of lesser amount of solvent aids the formation

of more homogenous and small-sized particles due to high concentration of reactants that leads to uniform nucleation in the reaction medium[8]. It also minimises uncontrolled growth and aggregation, thereby forming LDHs with higher stability and dispersibility. Therefore, these low-solvent synthesis methods are green approaches that involve the minimization or elimination of solvent use for the synthesis of desired products. These methods hold several advantages over conventional synthesis methods such as enhanced safety, cost-effectiveness, simpler product processing, reduced waste production, and lower environmental footprint.

Another method that is widely used for the synthesis of LDHs is the regeneration process, that utilises the well-known structural “memory effect” property of LDHs and utilises the process of calcination and subsequent regaining of structure[9]. It is well-reported in literature that LDHs calcined at temperatures above 500 °C result in the formation of spinel-type layered double oxides due to the removal of physisorbed, chemisorbed and interlayer water molecules, intercalated anions and the collapse of the layered arrangement. But it has been observed that LDOs prepared by the calcination of LDHs at moderate temperatures (300 °C – 500 °C) can regain their original layered structure on being treated with desired intercalant anions in aqueous medium[10]. This unique and attractive feature displayed by LDHs is termed as the “structural memory effect” property and is one of the major reasons for the increasing progress of research into LDH-based materials in recent years. This property is the basis of the reconstruction method of LDH synthesis since it is generally believed that regaining the layered structure is essentially a rehydration process from mixed oxides to multi-metallic hydroxide. Therefore, it can be exploited to achieve several goals such as the sequestration of pollutants, preparation of new LDH species, intercalation of various inorganic/organic anions in the interlayer region, composite formation and insights into the structure of LDHs etc. Benhiti et al. utilised the memory effect property of MgAl-LDH to evaluate the uptake of chromium from aqueous solution, and compared it with chromium removal by traditional adsorption methods[11]. In another study, Gao et al. investigated the effect of humic acid on the memory effect property of LDHs, and found that type of humic acid and nature of metal cations both determine the memory effect based-regeneration ability of LDHs[12]. Although this

unique property has garnered significant attention, but in-depth reports discussing the mechanism of action and the cause behind this property are lacking. Therefore, Jin et al. attempted to gain a better understanding into the mechanism of memory effect property and to devise a new LDH synthesis method by utilising *ex situ* and *in situ* solid-state NMR techniques to determine the atomic level changes in local structure during the structure regaining process of Mg/Al-LDH[13]. They inferred that structure recovery is a retro-topotactic phenomenon and occurs via a dissolution-recrystallization mechanism with water quantity playing a critical role in the process.

The layered framework of LDHs grants a variety of unique physicochemical properties to these nanostructures, that opens up several avenues for their utilisation. The scope of their applications can be expanded further by the intercalation of various guest molecules in the interlayer region. The process of intercalation potentially stabilises the lattice and may also result in the expansion of interlayer distance due to incorporation of large-sized guest molecules[14]. Intercalation may also result in partial/incomplete incorporation of guest molecules into the host material. In order to achieve complete replacement on the interlayer moieties, the anion exchange abilities of LDHs are often favoured since they can be used to bring about drastic changes in the physicochemical, optical, electronic and magnetic features of the lattice[15]. The anion exchange method involves the complete substitution of one anion by another anion in the host lattice as part of the intercalation process. This method is favourable for fabricating LDH-based composite materials with new and enhanced properties. A variety of inorganic, organic and polymeric species have been incorporated into the host LDH lattices using this method[16]. Everaert et al. prepared a Mg-Al LDH intercalated with nitrate ( $\text{NO}_3^-$ ) anions, and exchanged them with phosphate anions[17]. The resulting phosphate exchanged-LDH was applied as a slow-release phosphate fertiliser. In another study, Xu et al. intercalated polyoxometalates anions  $[\text{P}_2\text{W}^{17}]^{10-}$  and  $[\text{CoW}_{12}]^{5-}$  were intercalated into ZnAlFe-LDH lattice by means of the anion exchange method[18]. The new lattice was utilised for the adsorptive removal and photocatalytic degradation of methylene blue (MB) dye. In order to tailor LDHs for specific applications such as environmental remediation, energy storage, and sensing, the incorporation of conjugated polymeric species such as polyaniline (PANI),

polypyrrole (PPy), has been widely investigated via anion exchange[19,20]. Among these species, PANI shows immense promise due to its facile synthesis, excellent environmental stability and thermal resistance as well as high electrical conductivity and specific capacitance. The easy conversion of PANI to its conducting emeraldine base form by doping and oxidation using protonic acids is especially useful for the formation of composite materials[21] (Figure 5.1).

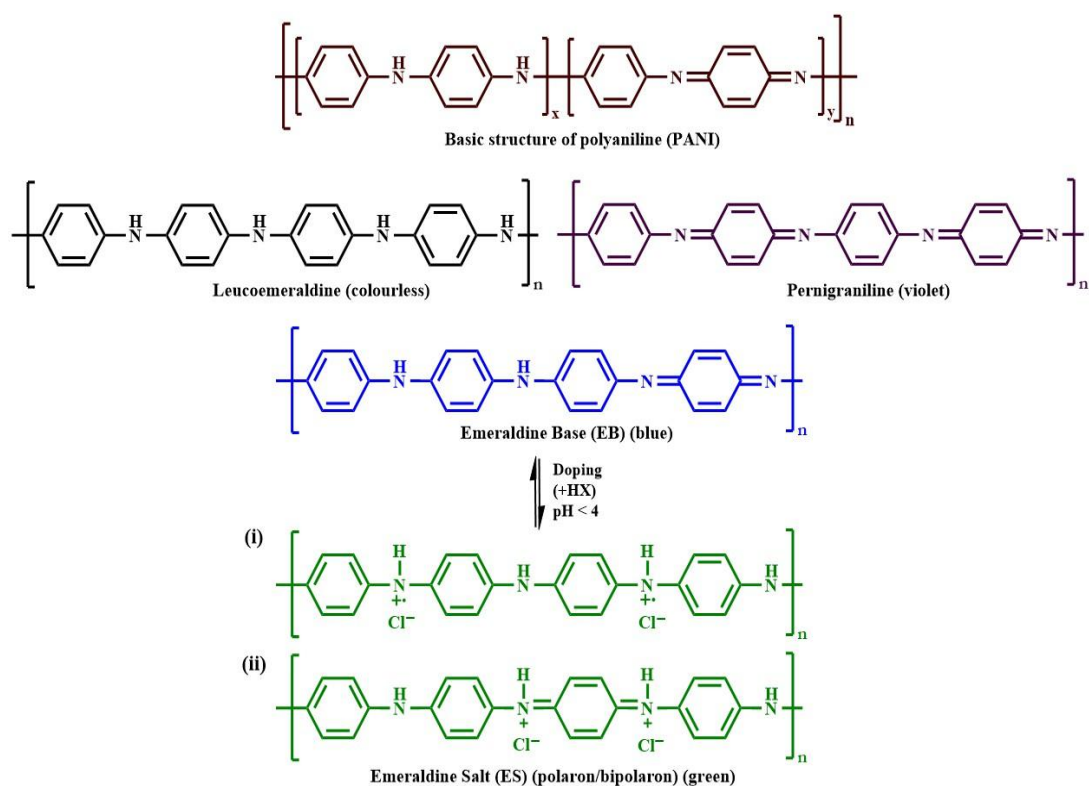


**Figure 5.1** Structures of different forms of polyaniline.

But even though PANI exhibits excellent conducting behaviour, it possesses poor solubility and mechanical limitations, low biocompatibility, high aggregation tendency and complexity in synthesis. Meanwhile, combining PANI with LDHs is an effective way to overcome the drawbacks of both PANI and LDH, while enhancing their physicochemical properties and maintaining biocompatibility is an effective way to exploit their complementary properties[22]. As a result, PANI/LDH composites possess good structural stability and versatility, enhanced conductivity, as well as great adsorptive and catalytic efficacies, that can unlock their potential for use in advanced environmental, energy storage, and catalytic applications[23,24]. For instance, PANI-

Mg/Al LDH nanocomposites were fabricated using a melt compounding technique, and the nanocomposites exhibited good electrical conductivity[25]. In another report, NiCo-LDH nanoscroll@PANI nanocomposite, synthesized using a combination of electrodeposition and hydrothermal treatment, was utilized for the fabrication of a battery-type supercapacitor[26]. A study by Qin et al. described the synthesis of PANI/ZnTi-LDH nanocomposite using oxidative polymerization, and it was subsequently used for the sensing of NH<sub>3</sub>[27].

But the facile and economic synthesis of PANI/LDH composites still poses a daunting challenging to researchers. Keeping this in view, the anion exchange method can be the perfect technique for the synthesis of these composites since it allows the incorporation of large-sized molecules into the LDH galleries, while maintaining structural integrity and fabricating materials of strategic importance. Therefore, the objectives of the current study are three-fold – first is the synthesis of ZnCuNi-LDH using an alternate methodology utilising low amount of solvent; secondly, the evaluation of the memory effect property for regeneration of ZnCuNi-LDH lattice, and finally, the intercalation of PANI into ZnCuNi-LDH galleries by exchanging with interlayer acetate anions via the anion exchange method.

## 5.2 Experimental Section

### 5.2.1 Low Solvent Synthesis

The synthesis of ZnCuNi-LDH was carried out using low amount of solvent as per previously reported acid hydrolysis methodology[28]. For the synthesis, zinc acetate dihydrate (0.4664 g), copper acetate monohydrate (0.0374 g), and nickel acetate tetrahydrate (0.0466 g) were mixed and ground up into a fine powder using a pestle-mortar. For synthesis, 30 mL distilled water and 5 mL H<sub>2</sub>O<sub>2</sub> were utilised. The prepared sample was labelled as ZnCuNi-LDH(LS).

### 5.2.2 Calcination and Regeneration of ZnCuNi-LDH

ZnCuNi-LDO, obtained on calcination of ZnCuNi-LDH at 350°C, was dispersed in CH<sub>3</sub>COOH (50 mL) and the mixture was boiled with continuous stirring till the volume of solution reduced to 10 mL. Then 2 mL of 30% H<sub>2</sub>O<sub>2</sub> and 30 mL milliQ

water were added to the reaction mixture and stirred for 24 hours, following which the beaker was placed in oven at 60°C till sample was completely dried. The schematic representation of the calcination-regeneration process is shown in Figure 5.2.

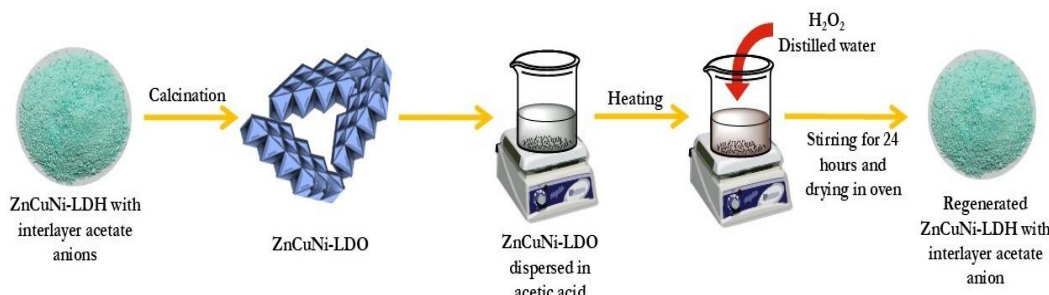


**Figure 5.2** Schematic representation of the calcination-regeneration process for demonstrating memory effect property of LDHs.

### 5.2.3 Fabrication of PANI/ZnCuNi-LDH composite

In order to exploit the composite forming ability of LDHs, an in-situ oxidative polymerisation method was employed to achieve the intercalation of PANI into the interlayer region of ZnCuNi-LDH. Briefly, 0.25 g of ZnCuNi-LDH, previously synthesized using acid hydrolysis method, 25 mL aniline monomer and 2.5 mL of 30% H<sub>2</sub>O<sub>2</sub> were added to a round bottom flask. Subsequently, the reaction mixture was refluxed at 60°C for 9 hours in an oil bath with constant stirring at 400 rpm. The greenish-brown precipitate obtained was filtered, washed with acetone, ethanol, and DMSO, and then dried overnight in oven at 60°C till complete removal of solvent. The schematic representation of the synthesis of PANI/ZnCuNi-LDH composite using anion exchange property is shown in Figure 5.3.

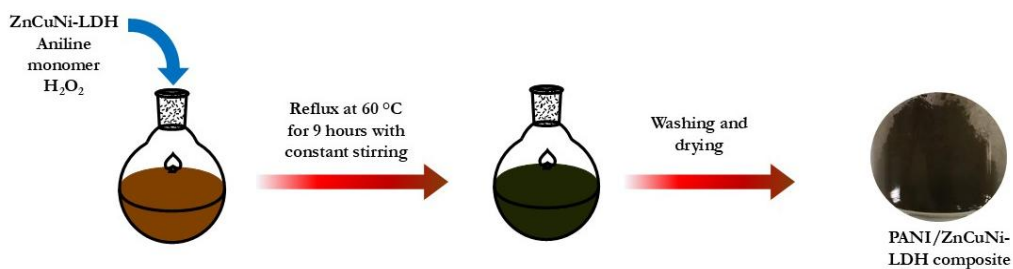


**Figure 5.3** Schematic representation of the synthesis of PANI/ZnCuNi-LDH composite using anion exchange property.

### 5.2.4 Instrumentation

The PXRD patterns of the synthesized samples were recorded using an advanced Bruker D8 diffractometer over the range of  $2\theta = 5-70^\circ$ , employing Copper  $K\alpha$  radiation with  $1.5418 \text{ \AA}$  wavelength acquired via a gobel mirror with 1.0 second/step scan rate and  $0.02^\circ$  step size at 298 K. FTIR spectrum was recorded using a PerkinElmer FTIR (version 10.5.3). Thermogravimetric analysis was conducted using the PerkinElmer TGA in the 50-900°C range under flowing nitrogen and at a uniform heating rate of  $10^\circ\text{C min}^{-1}$ . SEM with EDX analysis of PANI/ZnCuNi-LDH was accomplished using a Zeiss Gemini SEM instrument.

## 5.3 Results and Discussion

### 5.3.1 Low-Solvent Synthesis

The PXRD pattern of ZnCuNi-LDH(LS) presented in Figure 5.4 exhibited all the characteristic peaks of hydrotalcite-type materials and closely resembled the PXRD pattern of previously synthesized ZnCuNi-LDH. The appearance of sharp reflection at lower  $2\theta$  angles and symmetric, low-intensity reflections at higher  $2\theta$  angles corroborated the formation of pure-phase ZnCuNi-LDH. Therefore, it was inferred that low-solvent synthesis could prove to be a beneficial methodology for the large-scale synthesis of ZnCuNi-LDH since it requires the use of minimized amount of solvent.

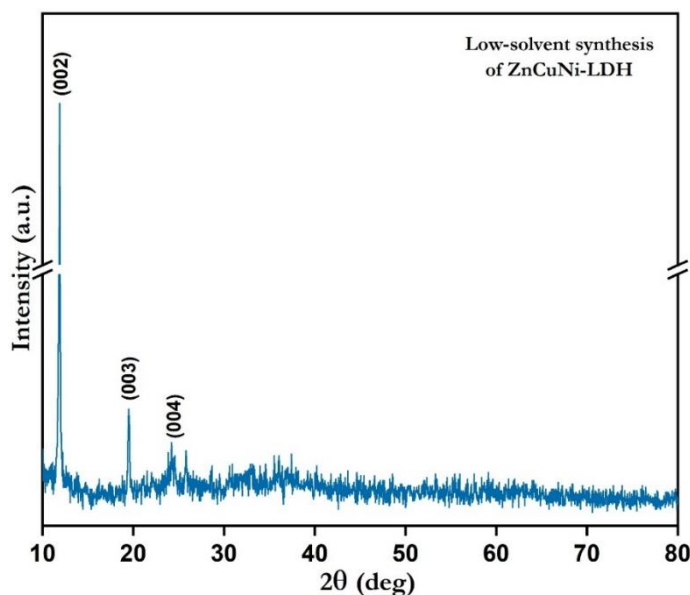


**Figure 5.4** PXRD pattern of ZnCuNi-LDH synthesized using low-solvent synthesis approach.

### 5.3.2 Demonstration of Memory Effect Property

The unique memory effect property of LDHs lends a structure-regaining ability to them. For an in-depth investigation of this phenomenon, previously synthesized ZnCuNi-LDH was first calcined and then rehydrated in presence of acetate anions, and PXRD patterns were recorded for the calcined and rehydrated samples. The PXRD diffractogram of the parent sample presents the characteristic peaks that are typical to LDHs, with high intensity and low intensity reflections appearing at lower  $2\theta$  and higher  $2\theta$  angles respectively. On the other hand, the PXRD pattern of the calcined product, presented in Figure 5.5, demonstrated the disappearance of the characteristic LDH peaks along with the appearance of several new peaks at  $2\theta = 31.7^\circ, 34.4^\circ, 36.2^\circ, 47.5^\circ, 56.5^\circ, 62.8^\circ$ , and  $68.0^\circ$ , thereby suggesting the collapse of layered structure. Furthermore, the newly appeared peaks were ascribed to the  $hkl$  planes  $(100), (002), (101), (102), (110), (103)$ , and  $(112)$  corresponding to the formation of ZnCuNi-LDO possessing a hexagonal wurtzite structure[29].

On treatment with acetate anions in aqueous medium, the calcined product regained its original structure to reform parent LDH lattice, that was corroborated from the PXRD pattern of the regenerated lattice displayed in Figure 5.5. The appearance of the characteristic peaks in PXRD diffractogram of regenerated LDH, along with similar  $d$ -spacing values with slight decrease in intensities indicated the successful regaining of the layered structure. The weakening of peak intensities may be attributed to the loss of some crystallinity due to the calcination-rehydration process[10].

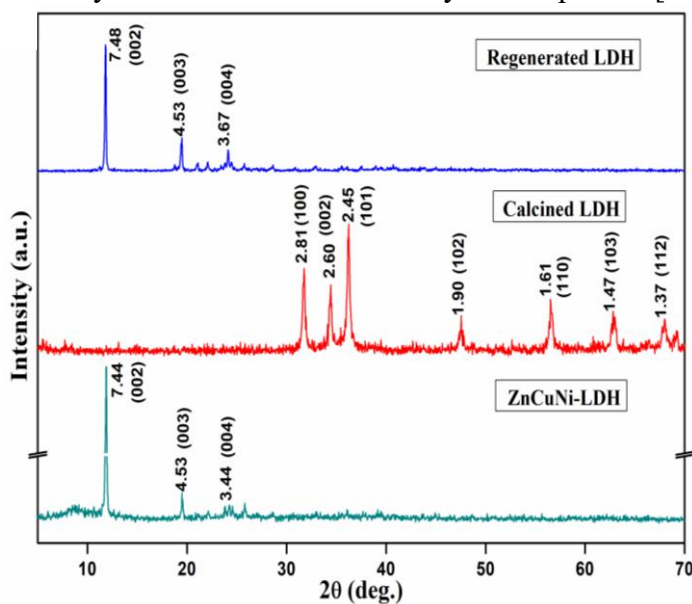


**Figure 5.5** Comparative plots of PXRD patterns of pristine, calcined, and regenerated ZnCuNi-LDH.

The comparative FTIR spectra of parent ZnCuNi-LDH, calcined product and regenerated ZnCuNi-LDH is presented in Figure 5.6. In the FTIR spectrum of the calcined product, the disappearance of the -OH stretching band that typically appears around  $3400\text{ cm}^{-1}$  as well as the absence of bands around  $1579\text{ cm}^{-1}$ ,  $1410\text{ cm}^{-1}$ ,  $1024\text{ cm}^{-1}$ , and  $683\text{ cm}^{-1}$  corresponding to the acetate anion may be attributed to the removal of hydroxyl groups and the loss of interlayer acetate anion that was the consequence of the thermal treatment of ZnCuNi-LDH[28]. This corroborated the hypothesis that calcination resulted in the loss of layered structure of LDH and culminated in the formation of mixed oxide. Meanwhile, the similarities in the FTIR spectra of parent ZnCuNi-LDH and regenerated ZnCuNi-LDH signified that layered structure of LDH had been regained on treatment of calcined product with acetate anions in aqueous medium. Therefore, the results of FTIR analysis supported the conclusion that ZnCuNi-LDH successfully demonstrated the memory effect property since it regained its structure after calcination and subsequent rehydration with acetate anions.

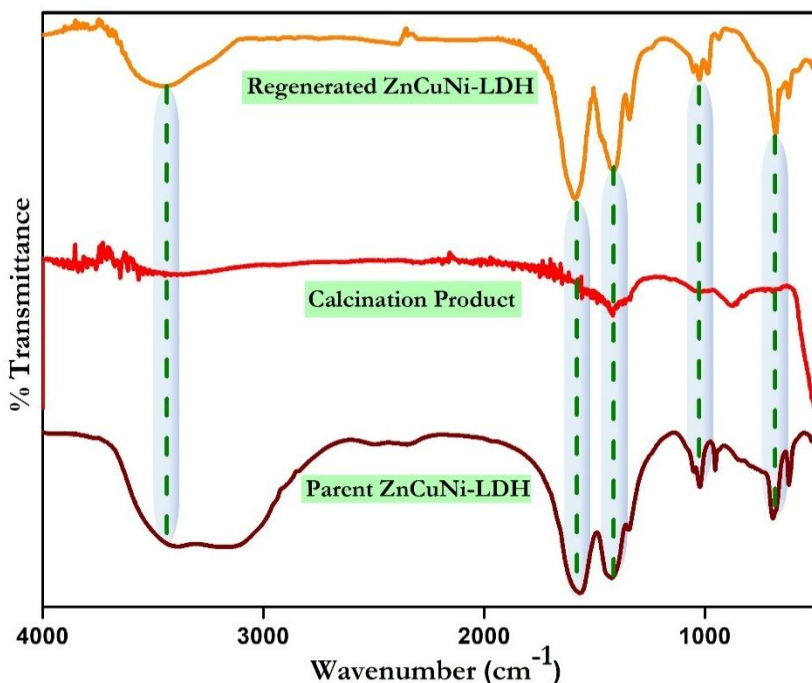


**Figure 5.6** Comparative FTIR spectra comparison of parent ZnCuNi-LDH, its calcined product and regenerated ZnCuNi-LDH

### 5.3.3 Characterization of PANI intercalated ZnCuNi-LDH

The ability of LDHs to act as anion-exchangeable host-guest materials and incorporate various types of organic and inorganic moieties in their interlayer region can be utilized to tailor their properties for various applications. Therefore, an attempt was made to incorporate PANI in the parent ZnCuNi-LDH lattice to determine the flexibility of interlayer region. The synthesized composite is hypothesized to possess enhanced physiochemical properties. The PXRD pattern of PANI intercalated ZnCuNi-LDH presented in Figure 5.7 was found to differ from that of pristine ZnCuNi-LDH in various aspects. These differences included the shift of characteristic peaks of LDH to lower  $2\theta$  angles from  $11.88^\circ$  to  $5.59^\circ$  along with a decrease in their peak intensities. Furthermore, the emergence of new peaks at  $20.2^\circ$  and  $23.4^\circ$  may be indicative of the formation of the emeraldine base form of polyaniline in the composite material[30]. The increase in  $d$ -spacing value of the characteristic  $(002)$  crystal plane of LDHs from  $7.44\text{ \AA}$  to  $15.64\text{ \AA}$  indicated the expansion of LDH interlayer spacing on incorporation of guest PANI molecules. The slight broadening of the peaks indicated that while the structural integrity of the parent lattice was still maintained in the PANI/ZnCuNi-LDH composite, but the organic PANI macromolecule imparted a slight amorphous character to the composite material upon intercalation in LDH galleries.

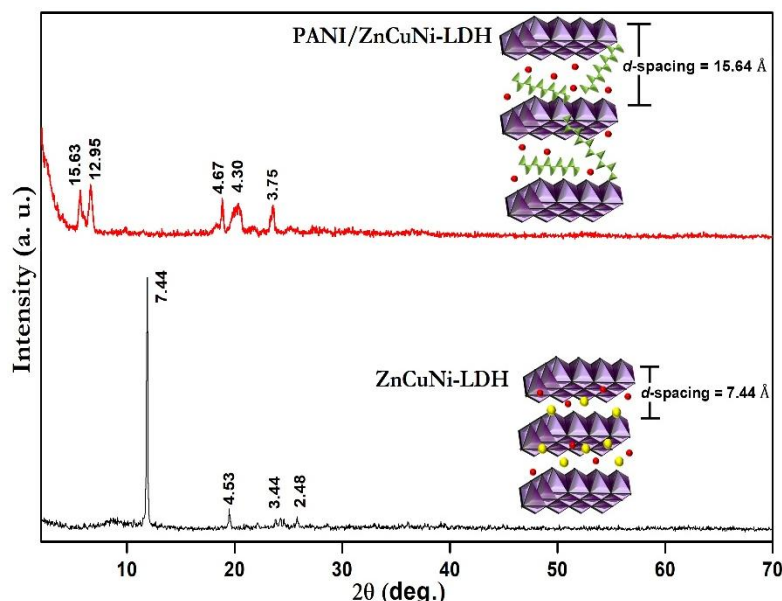


**Figure 5.7** Comparative plots of PXRD patterns of ZnCuNi-LDH and PANI/ZnCuNi-LDH composite.

Functional group analysis in parent ZnCuNi-LDH and PANI/ZnCuNi-LDH was conducted using the FTIR technique, and the results are presented in Figure 5.8 (Table 5.1). The FTIR spectrum of ZnCuNi-LDH presented the characteristic broad band of O-H stretching at  $3408\text{ cm}^{-1}$ , while the fingerprint bands of acetate group (anti-symmetric and symmetric stretch. of  $\text{COO}^-$  group, C-H rocking, C-C stretching, O-C-O bending and  $\text{CO}_2^-$  rocking) appeared at  $1567\text{ cm}^{-1}$ ,  $1417\text{ cm}^{-1}$ ,  $1017\text{ cm}^{-1}$ ,  $953\text{ cm}^{-1}$ ,  $690\text{ cm}^{-1}$ , and  $614\text{ cm}^{-1}$  respectively. The band corresponding to metal-oxygen linkage appeared at  $517\text{ cm}^{-1}$ , thereby corroborating the formation of ZnCuNi-LDH with acetate anions present in the interlayer region. Meanwhile, in the FTIR spectrum of PANI fabricated ZnCuNi-LDH, bands corresponding to both PANI and ZnCuNi-LDH were observed. The appearance of bands at  $3448\text{ cm}^{-1}$  and  $3265\text{ cm}^{-1}$  was ascribed to the stretching vibrations of free and binding O-H and N-H bonds respectively that are hydrogen bonded to the ZnCuNi-LDH surface. The singular weak band at  $3058\text{ cm}^{-1}$  corresponded to the vibrational mode of  $\text{NH}^{2+}$  of the  $^\circ\text{C}_6\text{H}_4\text{NH}^{2+}\text{C}_6\text{H}_4^-$  moiety while the characteristic bands of PANI i.e. C=N and C=C stretching vibrations of the quinoid imine and benzenoid units were observed at  $1573\text{ cm}^{-1}$  and  $1509\text{ cm}^{-1}$ [31,32]. A small band appearing around  $1630\text{ cm}^{-1}$  may be ascribed to the H-O-H bending vibrations of water molecules present in the interlayer region. The C=N stretching and C-N stretching of secondary aromatic amines, typical of polyaniline base, appeared at  $1339\text{ cm}^{-1}$  and  $1293\text{ cm}^{-1}$ , while the vibrational mode of  $\text{NH}_2^+=(\text{N}=\text{Q}=\text{N})$  arising during the protonation reaction of benzenoid and quinoid form appeared at  $1170\text{ cm}^{-1}$ , along with the band at  $844\text{ cm}^{-1}$  that signified out-of-plane stretching vibrations of C-H from the para-disubstituted benzene ring. These prominent bands signified the successful polymerization of aniline to polyaniline. The bands below  $750\text{ cm}^{-1}$  can be ascribed to M-O, O-M-O, and M-O-M skeletal vibrations (M=Zn, Cu, Ni) of the LDH network[33]. Therefore, FTIR analysis corroborated the successful incorporation of PANI in ZnCuNi-LDH.

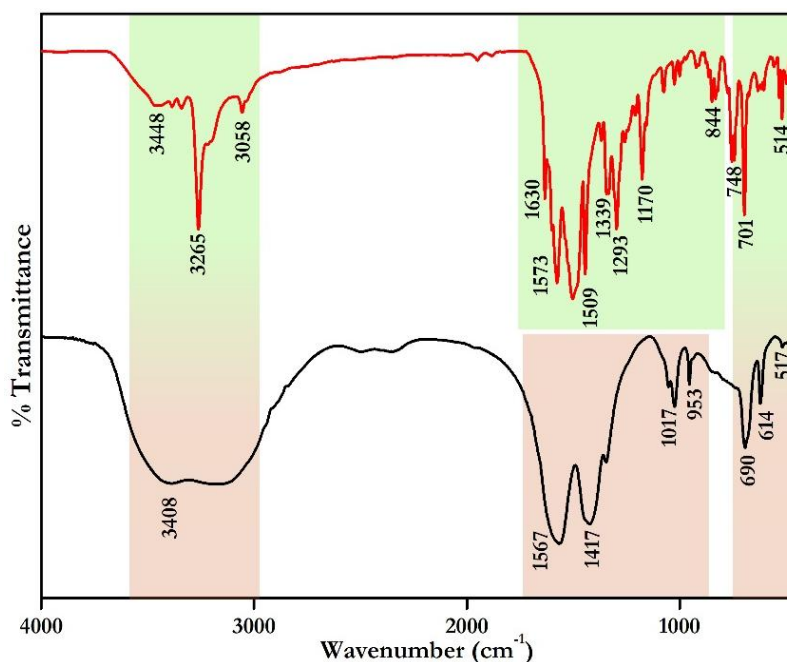


**Figure 5.8** Comparative plots of FTIR spectra of ZnCuNi-LDH and PANI/ZnCuNi-LDH composite.

**Table 5.1** Functional group analysis of PANI-intercalated LDH.

Wavenumber (cm <sup>-1</sup> )	Functional group	Inference
<b>ZnCuNi-LDH</b>		
3408	O-H stretching	Stretching vibration of hydroxyl groups, and broadness indicates the H-bonding between -OH groups and interlayer H <sub>2</sub> O molecules
1567 & 1417	Anti-symmetric and symmetric stretch. of COO <sup>-</sup> group	Confirm the presence of acetate anions
1017	C-H rocking	
953	C-C stretch.	
690	O-C-O bending	
614	CO <sub>2</sub> <sup>-</sup> rocking	
517	M-O stretching	Presence of metal-oxygen linkage

<b>PANI/ZnCuNi-LDH</b>		
3448	N-H & O-H stretching	Presence of free hydroxyl and amine groups
3265		Binding N-H & O-H
3058	NH <sup>2+</sup> vibration	$\text{C}_6\text{H}_4\text{NH}^{2+}\text{C}_6\text{H}_4^-$ moiety
1630	H-O-H bending vibration	Interlayer water molecules
1573	C=N stretching	Confirm the presence of
1509	C=C stretching	quinoid imine and benzenoid units of polyaniline
1339	C=N stretching	Presence of secondary aromatic amines
1293	C-N stretching	
1170	NH <sub>2</sub> <sup>+</sup> = vibration	Protonation of benzenoid and quinoid form
844	C-H bending	C-H bending localized on quinoid ring
748	M-O, M-O-M, O-M-O	Metal-oxygen linkages
701		
514		

The effect of PANI incorporation on the thermal stability of ZnCuNi-LDH was assessed using TGA, and the thermograms are presented in Figure 5.9. The thermal degradation of ZnCuNi-LDH is a three-tier weight loss process wherein the first tier from room temperature to 210°C can be accredited to the elimination of water molecules that are physically adsorbed on and present in between the layers of the lamellar lattice[34]. The second tier, from 210°C to 370°C, arises from the loss of decarboxylation, dehydroxylation, and interlayer acetate anions, while the final tier above 370°C reflects further decarboxylation and the dismantling of the layered structure (Figure 5.9a). In case of PANI intercalated ZnCuNi-LDH, the weight loss below 240°C may be attributed to the removal of physically adsorbed and interlayer water molecules, while the weight loss above 240°C is a consequence of the elimination of interlayer anion and dehydroxylation, accompanied by the destruction of the PANI backbone (Figure 5.9b)[33] The steep downward curve and lower amount of char residue in the thermogram of PANI intercalated ZnCuNi-LDH is indicative of

the higher degree of weight loss in case of PANI intercalated ZnCuNi-LDH as compared to ZnCuNi-LDH.

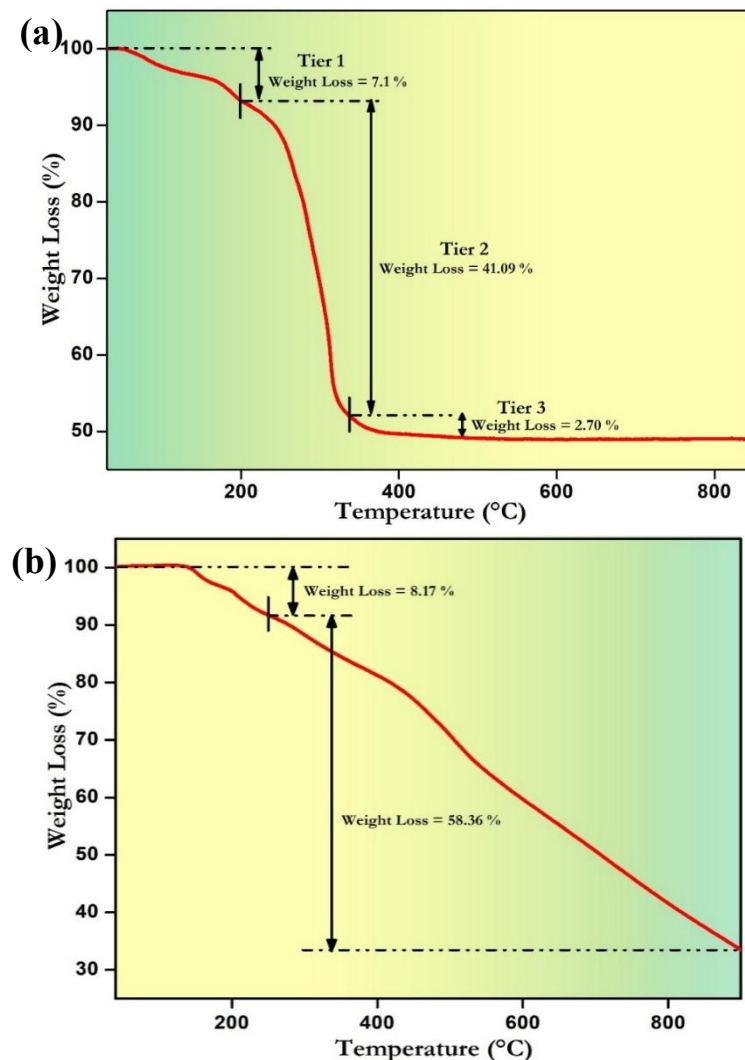


**Figure 5.9** Thermogravimetric traces of (a) ZnCuNi-LDH with interlayer acetate anion and (b) PANI intercalated ZnCuNi-LDH.

The morphological attributes of ZnCuNi-LDH and PANI intercalated ZnCuNi-LDH were examined using SEM-EDX. The SEM micrograph of ZnCuNi-LDH, presented in inset of Figure 5.10a, gave clear evidence for the lamellar structure of LDH lattice, while the EDX spectrum showed the uniform distribution of C, O, Zn, Cu, and Ni elements in the lattice[34]. While in case of PANI intercalated ZnCuNi-LDH, the appearance of nanotubes of PANI alongside the homogeneously distributed platelet-like LDH particles corroborates the formation of PANI intercalated ZnCuNi-LDH composite[35]. The EDX analysis and elemental mapping (Figure 5.10b) indicated the

presence of Zn, Cu, Ni, C and N elements in the composite, thereby confirming the successful intercalation of PANI in ZnCuNi-LDH. Additionally, the elemental mapping results also corroborated the homogeneous distribution of the constituent elements in PANI/ZnCuNi-LDH composite (Figure 5.10c).

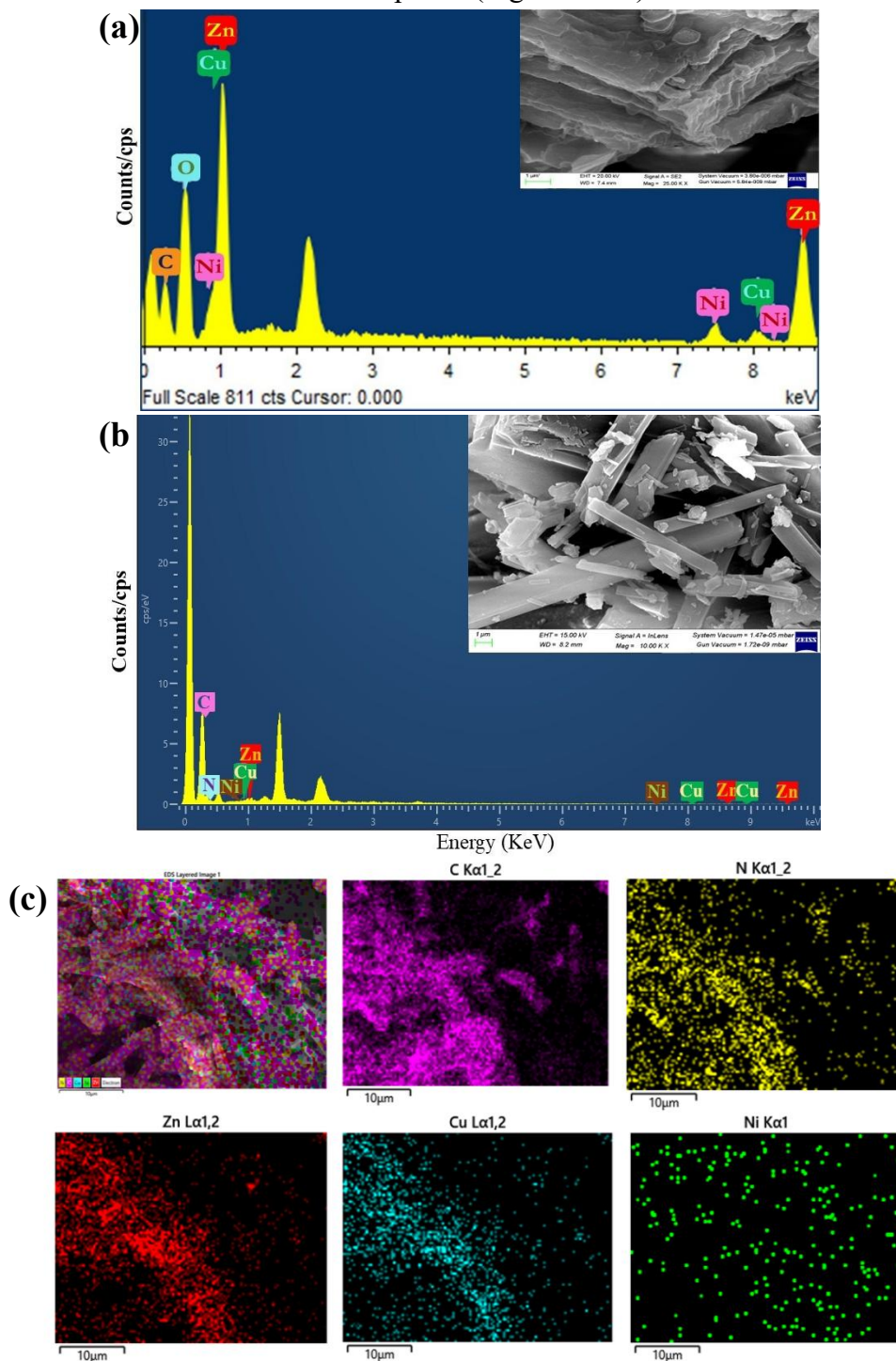


**Figure 5.10** (a) SEM-EDX image of ZnCuNi-LDH, and (b,c) SEM-EDX image and elemental mapping in PANI intercalated ZnCuNi-LDH.

## 5.4 Conclusions

This chapter demonstrates the synthesis of ZnCuNi-LDH via the acid hydrolysis method using minute amount of solvent that was confirmed from the PXRD results. Furthermore, the regeneration experiment corroborated the structure-regaining ability of ZnCuNi-LDH by virtue of its memory effect property. Therefore, this method could be utilized for tailoring LDHs with desired properties, and it holds the potential to deliver great practical benefits in environmental and catalytic applications that demand recyclability, sustained performance, and adaptability. Additionally, the in-situ oxidative polymerisation method was used for the intercalation of PANI in the ZnCuNi-LDH by exchanging the interlayer acetate anions. The intercalation of macromolecular PANI chains in the interlayer region contributed to swelling of the lattice, that was accompanied by an increase in the d-spacing from 7.42 Å to 15.63 Å. But despite the swelling of lattice, the fundamental integrity of LDH layered framework remained intact, indicating that anion exchange of acetate anion had happened successfully. PXRD, FTIR, SEM-EDX and elemental mapping results further corroborated the intercalation of PANI. The thermal degradation studies, conducted using TGA, suggested that incorporation of PANI in the lattice resulted in increased thermal stability of the PANI/ZnCuNi-LDH composite due to the confinement of PANI backbone within the layers. Therefore, the current work opens up pathways and avenues for the synthesis of new LDH lattices having enhanced physicochemical properties that can be tailored according to desirability for utilisation in various applications.

## 5.5 References

- [1] S.D. Xie, Y. Liu, Z.Y. Wu, G.L. Shen, R.Q. Yu, Application of Inorganic Layered Materials in Electrochemical Sensors, *Chinese J. Anal. Chem.* 43 (2015) 1648–1655. [https://doi.org/10.1016/S1872-2040\(15\)60879-9](https://doi.org/10.1016/S1872-2040(15)60879-9).
- [2] S. Daniel, S. Thomas, Layered Double Hydroxides: Fundamentals To Applications, in: Layer. Double Hydroxide Polym. Nanocomposites, 1st ed., 2020: pp. 1–76. <http://dx.doi.org/10.1016/B978-0-08-102261-0.00001-5>.
- [3] B. Saifullah, M.Z.B. Hussein, Inorganic nanolayers: Structure, preparation, and biomedical applications, *Int. J. Nanomedicine* 10 (2015) 5609–5633. <https://doi.org/10.2147/IJN.S72330>.
- [4] C. Madhusha, I. Munaweera, V. Karunaratne, N. Kotegoda, Synthesis and

characterisation of LDH-type anionic nanomaterials for the effective removal of doxycycline from aqueous media, *J. Agric. Food Chem.* 68 (2020) 8962–8975. <https://doi.org/10.1111/wej.12526>.

[5] S.S. Ray, D. Mosangi, S. Pillai, Layered Double Hydroxide-Based Functional Nanohybrids as Controlled Release Carriers of Pharmaceutically Active Ingredients, *Chem. Rec.* 18 (2018) 913–927. <https://doi.org/10.1002/tcr.201700080>.

[6] K. Yan, G. Wu, W. Jin, Recent Advances in the Synthesis of Layered, Double-Hydroxide-Based Materials and Their Applications in Hydrogen and Oxygen Evolution, *Energy Technol.* 4 (2016) 354–368. <https://doi.org/10.1002/ente.201500343>.

[7] J. He, M. Wei, B. Li, Y. Kang, D.G. Evans, X. Duan, Preparation of layered double hydroxides, *Struct. Bond.* 119 (2005) 89–119. [https://doi.org/10.1007/430\\_006](https://doi.org/10.1007/430_006).

[8] K.C. Majhi, Water as the Green Solvent in Organic Synthesis, in: *Ind. Appl. Green Solvents – Vol. II Mater. Res. Found.* 54, 2019: pp. 182–201. <https://doi.org/10.21741/9781644900314-8>.

[9] J. Das, D. Das, K.M. Parida, Preparation and characterization of Mg-Al hydrotalcite-like compounds containing cerium, *J. Colloid Interface Sci.* 301 (2006) 569–574. <https://doi.org/10.1016/j.jcis.2006.05.014>.

[10] K. Klemkaite, I. Prosycevas, R. Taraskevicius, A. Khinsky, A. Kareiva, Synthesis and characterization of layered double hydroxides with different cations (Mg, Co, Ni, Al), decomposition and reformation of mixed metal oxides to layered structures, *Cent. Eur. J. Chem.* 9 (2011) 275–282. <https://doi.org/10.2478/s11532-011-0007-9>.

[11] R. Benhiti, A. Ait Ichou, A. Aboussabek, G. Carja, M. Zerbet, F. Sinan, M. Chibani, Efficient removal of Cr (VI) from aqueous solution using memory effect property of layered double hydroxide material, *Chemosphere* 341 (2023) 140127. <https://doi.org/https://doi.org/10.1016/j.chemosphere.2023.140127>.

[12] Z. Gao, K. Sasaki, X. Qiu, Structural Memory Effect of Mg-Al and Zn-Al layered Double Hydroxides in the Presence of Different Natural Humic Acids: Process and Mechanism, *Langmuir* 34 (2018) 5386–5395. <https://doi.org/10.1021/acs.langmuir.8b00059>.

[13] L. Jin, X. Zhou, F. Wang, X. Ning, Y. Wen, B. Song, C. Yang, D. Wu, X. Ke, L. Peng, Insights into memory effect mechanisms of layered double hydroxides with solid-state NMR spectroscopy, *Nat. Commun.* 13 (2022) 6093. <https://doi.org/10.1038/s41467-022-33912-7>.

[14] M. Bini, F. Monteforte, Layered Double Hydroxides (LDHs): Versatile and Powerful Hosts for Different Applications, *J. Anal. Pharm. Res.* 7 (2018) 1–3. <https://doi.org/10.15406/japlr.2018.07.00206>.

[15] S. Mallakpour, E. Khadem, Opportunities and challenges in the use of layered double hydroxide to produce hybrid polymer composites, Elsevier Ltd, 2017. <https://doi.org/10.1016/B978-0-08-100791-4.00009-4>.

[16] N. Chubar, R. Gilmour, V. Gerda, M. Mičušík, M. Omastova, K. Heister, P. Man, J. Fraissard, V. Zaitsev, Layered double hydroxides as the next generation inorganic anion exchangers: Synthetic methods versus applicability, *Adv. Colloid Interface Sci.* 245 (2017) 62–80. <https://doi.org/10.1016/j.cis.2017.04.013>.

[17] M. Everaert, R. Warrinnier, S. Baken, J.P. Gustafsson, D. De Vos, E. Smolders, Phosphate-Exchanged Mg-Al Layered Double Hydroxides: A New Slow Release Phosphate Fertilizer, *ACS Sustain. Chem. Eng.* 4 (2016) 4280–4287. <https://doi.org/10.1021/acssuschemeng.6b00778>.

[18] M. Xu, B. Bi, B. Xu, Z. Sun, L. Xu, Polyoxometalate-intercalated ZnAlFe-layered double hydroxides for adsorbing removal and photocatalytic degradation of cationic dye, *Appl. Clay Sci.* 157 (2018) 86–91. <https://doi.org/10.1016/j.clay.2018.02.023>.

[19] N. Kalaivasan, S. Syed Shafi, Synthesis of various polyaniline / clay nanocomposites derived from aniline and substituted aniline derivatives by mechanochemical intercalation method, *E-Journal Chem.* 7 (2010) 1477–1483. <https://doi.org/10.1155/2010/364680>.

[20] M. Shao, Z. Li, R. Zhang, F. Ning, M. Wei, D.G. Evans, X. Duan, Hierarchical Conducting Polymer@Clay Core-Shell Arrays for Flexible All-Solid-State Supercapacitor Devices, *Small* 11 (2015) 3530–3538. <https://doi.org/10.1002/smll.201403421>.

[21] S. Bhadra, D. Khastgir, N.K. Singha, J.H. Lee, Progress in preparation, processing and applications of polyaniline, *Prog. Polym. Sci.* 34 (2009) 783–810. <https://doi.org/10.1016/j.progpolymsci.2009.04.003>.

[22] C. Taviot-Guého, F. Leroux, In situ polymerization and intercalation of polymers in layered double hydroxides, *Struct. Bond.* 119 (2005) 121–159. [https://doi.org/10.1007/430\\_001](https://doi.org/10.1007/430_001).

[23] H. Xu, S. Zhu, M. Xia, F. Wang, Rapid and efficient removal of diclofenac sodium from aqueous solution via ternary core-shell CS@PANI@LDH composite: Experimental and adsorption mechanism study, *J. Hazard. Mater.* 402 (2021) 123815. <https://doi.org/10.1016/j.jhazmat.2020.123815>.

[24] H. Wang, Z. Gao, H. Shi, X. Cui, J. Jia, H. Xu, Reinforcing the assembly of NiV-LDH and MoS<sub>2</sub> with PANI as a coupling agent to form a ternary composite of NiV-LDH/PANI/MoS<sub>2</sub> for enhanced supercapacitor performance, *J. Electroanal. Chem.* 951 (2023) 117933. <https://doi.org/10.1016/j.jelechem.2023.117933>.

[25] B. Kutlu, A. Leuteritz, R. Boldt, D. Jehnichen, U. Wagenknecht, G. Heinrich, PANI-LDH prepared by polymerization-adsorption method and processing to

conductive compounds, *Appl. Clay Sci.* 72 (2013) 91–95. <https://doi.org/10.1016/j.clay.2013.01.002>.

[26] W. Hu, L. Chen, M. Du, Y. Song, Z. Wu, Q. Zheng, Hierarchical NiCo-layered double hydroxide nanoscroll@PANI nanocomposite for high performance battery-type supercapacitor, *Electrochim. Acta* 338 (2020) 1–9. <https://doi.org/10.1016/j.electacta.2020.135869>.

[27] Y. Qin, L. Wang, X. Wang, A high performance sensor based on PANI/ZnTi-LDHs nanocomposite for trace NH<sub>3</sub> detection, *Org. Electron.* 66 (2019) 102–109. <https://doi.org/10.1016/j.orgel.2018.12.018>.

[28] J. Pathak, P. Singh, Synthesis and Characterization of Ternary Layered Double Hydroxide containing Zinc/Copper/Nickel and its PANI Composite, *Polym. Compos.* 43 (2022) 7836. <https://doi.org/https://doi.org/10.1002/pc.26895>.

[29] D. Bresser, F. Mueller, M. Fiedler, S. Krueger, R. Kloepsch, D. Baither, M. Winter, E. Paillard, S. Passerini, Transition-metal-doped zinc oxide nanoparticles as a new lithium-ion anode material, *Chem. Mater.* 25 (2013) 4977–4985. <https://doi.org/10.1021/cm403443t>.

[30] S.M. Budi , Yusmaniar , F. Rahmadi , Maryanti, The high capacitance and surface area of a polyaniline/polypyrrole composite, *J. Chem. Technol. Metall.* 55 (2020) 28–33.

[31] F.L. Long, C.G. Niu, N. Tang, H. Guo, Z.W. Li, Y.Y. Yang, L.S. Lin, Highly efficient removal of hexavalent chromium from aqueous solution by Calcined Mg/Al-layered double hydroxides/polyaniline composites, *Chem. Eng. J.* 404 (2020) 127084. <https://doi.org/10.1016/j.cej.2020.127084>.

[32] X. Hu, L. Liu, H.Y. Zeng, S. Xu, X. Cao, X.J. Cao, An Advanced NiCoFeO/Polyaniline Composite for High-Performance Supercapacitors, *Chem. - An Asian J.* 14 (2019) 977–985. <https://doi.org/10.1002/asia.201801905>.

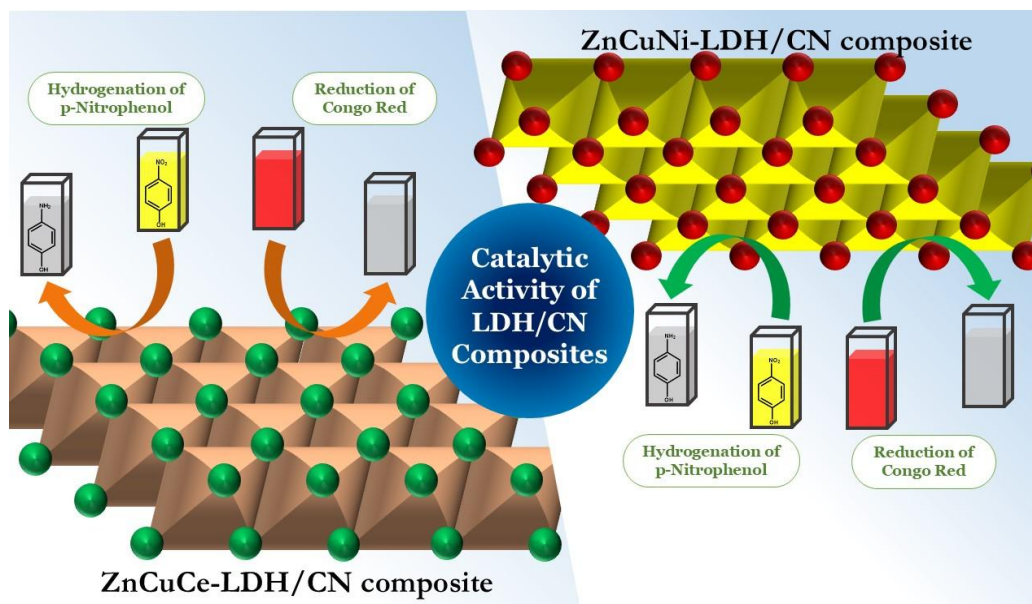
[33] K. Zhu, Y. Gao, X. Tan, C. Chen, Polyaniline-Modified Mg/Al Layered Double Hydroxide Composites and Their Application in Efficient Removal of Cr(VI), *ACS Sustain. Chem. Eng.* 4 (2016) 4361–4369. <https://doi.org/10.1021/acssuschemeng.6b00922>.

[34] B. Pandey, P. Singh, V. Kumar, Facile synthesis of Zn/Cu and PANI modified layered double hydroxides with insights into structural memory effect property, *Bull. Mater. Sci.* 45 (2022) 169. <https://doi.org/10.1007/s12034-022-02754-w>.

[35] A.A. Wani, A.M. Khan, Y.K. Manea, M.A.S. Salem, M. Shahadat, Selective adsorption and ultrafast fluorescent detection of Cr(VI) in wastewater using neodymium doped polyaniline supported layered double hydroxide nanocomposite, *J. Hazard. Mater.* 416 (2021) 125754. <https://doi.org/10.1016/j.jhazmat.2021.125754>.

**CHAPTER - 6**

***SYNTHESIS, CHARACTERIZATION AND CATALYTIC APPLICATIONS OF CARBON NITRIDE/LDH-BASED COMPOSITE MATERIALS***



## **CHAPTER - 6**

# **SYNTHESIS, CHARACTERIZATION AND CATALYTIC APPLICATIONS OF CARBON NITRIDE/LDH-BASED COMPOSITE MATERIALS**

---

### **6.1 Introduction**

A recent and quite exciting breakthrough in the field of materials science is the fabrication of composites that result from the synergistic combination of two or more materials. The combination of two or more distinct constituents results in the formation of new materials that possess enhanced and tailorable chemical, mechanical, thermal, and optical properties[1]. These synergistically combined composites help in overcoming several techno-economic and environmental disadvantages associated with conventional materials that hinder their profitable use in a variety of applications[2]. This breakthrough has resulted in improved functional properties in composites such as high surface area, stability and durability, re-usability, enhanced mechanical strength, enhanced separability, and usually better catalytic efficiency relative to traditionally employed catalytic materials. In literature, composites of a variety of materials such as inorganic/organic polymers, carbonaceous materials, metal and metal oxide nanoparticles, clays, etc have been reported[3–5]. In particular, carbon and carbon-based composites have become the focal point of research due to their tailorability and versatility[6,7].

In this purview, carbon nitride ( $C_3N_4$ ), a carbonaceous polymer, can be considered a nexus material owing to its unique properties. It consists of a two-dimensional conjugated polymer composed of C and N atoms, and possesses several exemplary features such as large surface area, high stability, low toxicity and excellent biocompatibility[8]. The exceptional physicochemical properties of  $C_3N_4$  render it as an effective material for a wide range of applications such as energy storage, water remediation,  $CO_2$  and  $H_2$  production and biomedics[9–12]. Specifically, the unique

chemical makeup and attributes including rapid transfer of electrons, inherent structural attributes like  $\pi$ - $\pi$  conjugation and excellent catalytic activity associated with  $\text{C}_3\text{N}_4$  enable its use in a variety of catalytic applications[13,14]. Therefore,  $\text{C}_3\text{N}_4$  has caught the fascination of researchers for its potential applications in wastewater purification. In order to further advance its practical utility, coupling of  $\text{C}_3\text{N}_4$  with other nanostructures to form interfaces could prove to be an effective methodology due to the exfoliation ability of the layered structure and availability of tunable surface moieties[15–19].

For this purpose, the combination of  $\text{C}_3\text{N}_4$  with clay materials has proven to be an exciting avenue. Among the variety of clays available, the use of LDHs is highly favoured due to its versatile structure and modifiable properties. These anionic clay materials are becoming increasingly interesting as compared to conventional materials since the hybrid materials of LDHs offer a combination of the properties of LDHs and other materials[20–22]. These composites often exhibit higher specific surface areas, excellent anion exchange capabilities, higher number of binding sites, enhanced stability and reduced agglomeration tendencies in solution. Several research groups have paired up LDHs with  $\text{C}_3\text{N}_4$ , since the combination of LDHs with  $\text{C}_3\text{N}_4$  helps in increasing their performance, and have reported their use in several practical applications. For instance, Nayak et al. reported the synthesis of a composite material by coupling of  $\text{g-C}_3\text{N}_4$  with NiFe-LDH and studied its water splitting behaviour towards both  $\text{H}_2$  and  $\text{O}_2$  evolution[23]. Khan et al. fabricated  $\text{g-C}_3\text{N}_4/\text{LiAl-LDH}$  composite and applied it for the adsorptive removal of methyl orange (MO) dye[24]. In literature most studies have reported the use of LDH/ $\text{C}_3\text{N}_4$  composites for adsorption, photocatalytic, water splitting, and energy storage applications, but their utility in the field of catalytic transformations remains severely underexplored. To date, the combination of LDH with  $\text{C}_3\text{N}_4$  has not been utilised for the  $\text{NaBH}_4$ -assisted catalytic degradation of pollutant molecules for water remediation that is an urgent issue that needs the attention of the masses.

The major contributors to rising water pollution levels include azo dyes and NACs, since they possess carcinogenic, mutagenic, and teratogenic characteristics, but they are highly stable molecules, thereby making their elimination extremely

challenging[25,26]. Specifically, *p*-Nitrophenol (*p*-NP) is a commercially widespread but toxic molecule that has been known to cause dermal, optical, and respiratory damage. In addition, Congo Red (CR) is an anionic diazo dye that is used widely in printing and textile industry, and is commonly used as an indicator and histological stain. But the dye is known to possess carcinogenic potential, and can be metabolized by aquatic organisms into benzidine, a carcinogen that can harm humans. Furthermore, due to its complex aromatic structure, CR is resistant to photodegradation and bacterial breakdown.

An innovative approach to overcome the issue of contaminant degradation and water pollution is the utilisation of catalytic materials in presence of a reductant, that can serve the two-fold purpose of water purification by targeting a variety of pollutants without generating perilous secondary pollutants. The use of NaBH<sub>4</sub> aids toxin degradation and is also used for the conversion of *p*-NP to *p*-Aminophenol (*p*-AP), that is utilised in various industries while the catalyst helps in progress of reaction. Furthermore, the breakdown products obtained after catalytic breakdown of the pollutants can be identified simply with methods like absorption spectroscopy[27]. Traditional materials used as catalysts possess certain disadvantages such as agglomeration tendency, complex and expensive synthesis methods, and low catalytic efficiency, due to which the use of these materials is not favoured (Figure 6.1). For instance, Ahmad et al. synthesized a composite consisting of iron oxide functionalised with Cu nanoparticles and applied it for NaBH<sub>4</sub>-assisted reduction of several organic pollutants[28].



**Figure 6.1** Various types of nanocatalysts used for wastewater remediation.

Lately, the use of LDH-based composites with  $\text{NaBH}_4$  as a reductant has become a popular choice for the catalytic degradation of pollutant molecules since it combines the advantageous features of LDH-based composite materials with the facile nature and easy applicability of this method. Specifically, hybrid materials comprising of LDHs and  $\text{C}_3\text{N}_4$  are potentially promising catalysts for the removal of organic pollutants from wastewater on account of the excellent physiochemical properties, benign nature, and synergistic effects in these composites that can result in higher catalytic activities[23,29]. The flexibility of design that can be achieved in these composites by varying factors such as interlayer spacing, number of layers, surface groups, and functionalization provides a high degree of control over the fine-tuning and, inadvertently, the profitable applicability of these novel composites. Furthermore, the robust two-dimensional architecture and interfacial bonding render these structures highly mechanically, thermally and chemical stable, with the added advantage of higher surface area and larger number of available active sites for catalytic reactions to take place. These multifunctional materials can overcome the drawbacks of both LDH and  $\text{C}_3\text{N}_4$ , and can surpass the properties of both in terms of catalytic, environmental, and electrochemical performances[30,31].

Therefore, the objectives of this research work include: (i) synthesis of carbon nitride ( $\text{C}_3\text{N}_4$ ), (ii) synthesis of two composites coupling  $\text{C}_3\text{N}_4$  with  $\text{ZnCuNi-LDH}$  and  $\text{ZnCuCe-LDH}$  using electrostatic self-assembly method, (iii) investigation of the structural and morphological properties of synthesized hybrids, and (iv) exploration of the catalytic prowess of the composites towards the elimination of *p*-NP and Congo red dye from aqueous media.

## 6.2 Materials and Methods

### 6.2.1 Materials

Zinc acetate dihydrate  $\text{Zn}(\text{CH}_3\text{COO})_2 \cdot 2\text{H}_2\text{O}$  (Merck, 98.0% purity), copper acetate monohydrate  $\text{Cu}(\text{CH}_3\text{COO})_2 \cdot \text{H}_2\text{O}$  (Merck, 98.0% purity), hydrogen peroxide  $\text{H}_2\text{O}_2$  (Merck, 30%), nickel acetate tetrahydrate  $\text{Ni}(\text{CH}_3\text{COO})_2 \cdot 4\text{H}_2\text{O}$  (CDH, 98.00% purity), cerium acetate hydrate  $\text{Ce}(\text{CH}_3\text{COO})_2 \cdot x\text{H}_2\text{O}$  (Sigma Aldrich, 99.9% purity), Melamine Pure (CDH),  $\text{NaBH}_4$  (Sigma Aldrich,  $\geq 98.00\%$ ), *p*-Nitrophenol (GLR

chemicals, 98.00%), Congo Red (Merck) were of analytical grade unless otherwise stated, and were utilised as received without purification. Table 6.1 gives information about the structure, formulas, and  $\lambda_{max}$  of model pollutant molecules employed in this study.

**Table 6.1** Structure and formula of model pollutants employed in the study.

Pollutant	Structure	$\lambda_{max}$ (nm)	Molecular Formula
<i>p</i> -Nitrophenol		320	C <sub>6</sub> H <sub>5</sub> NO <sub>3</sub>
Congo Red		497	C <sub>32</sub> H <sub>22</sub> N <sub>6</sub> Na <sub>2</sub> O <sub>6</sub> S <sub>2</sub>

## 6.2.2 Synthesis of Carbon Nitride (CN)

CN powder was prepared by the thermal polycondensation of pure melamine powder. Briefly, 5.0 g of melamine powder was calcined at 550 °C for 4 hours to obtain yellowish-white product. The product was stored in a glass vial in the oven at 60 °C for further use.

## 6.2.3 Synthesis of ZnCuNi-LDH and ZnCuCe-LDH

ZnCuNi-LDH was prepared in accordance with the previously described acid hydrolysis methodology[32]. In brief, this method first entailed the preparation of aqueous solutions of zinc acetate dihydrate, copper acetate monohydrate, and nickel acetate tetrahydrate in 10 mL distilled water separately. Following this, solutions of copper acetate monohydrate and nickel acetate tetrahydrate were combined with zinc acetate dihydrate solution with constant stirring until complete homogeneity was achieved. The acid hydrolysis process was initiated by adding 5 mL of 30% H<sub>2</sub>O<sub>2</sub> solution along with 30 mL distilled water to the reaction solution. A shift in the solution color from greenish-blue to brown indicated the formation of ZnCuNi-LDH.

Subsequently, the reaction mixture was subjected to ultrasonication for 30 minutes to prevent aggregate formation and to attain uniformly-sized LDH particles. The reaction mixture was then stirred continuously for 24 hours at room temperature and finally, the solution was placed in oven at 60 °C for complete drying to obtain the blue-green ZnCuNi-LDH precursor.

ZnCuCe-LDH was synthesized in a similar manner using 0.9877 g zinc acetate dihydrate, 0.0499 g copper acetate monohydrate and 0.0793 g cerium acetate hydrate. On completion of synthesis process, the greenish-white product was stored in oven for further use.

#### 6.2.4 Synthesis of ZnCuNi-LDH/CN and ZnCuCe-LDH/CN composites

ZnCuNi-LDH/CN and ZnCuCe-LDH/CN composites were synthesized using a facile electrostatic self-assembly method with 10% CN loading (relative to LDH) using methanol as a dispersion medium. For composite preparation, appropriate amounts of CN and LDH were added to 20 mL methanol in separate beakers, and then they were covered and ultrasonicated till complete homogeneity was attained. Subsequently, the CN dispersed in methanol was added dropwise to the LDH dispersion, and the reaction mixture was stirred for another 1 hour. Afterwards, the final dispersion was uncovered and stirred continuously till the methanol was completely volatilized. The remaining pale greenish-blue product was dried at 100 °C in hot air oven. The synthesis scheme for CN and LDH/CN composites is presented in Figure 6.2.

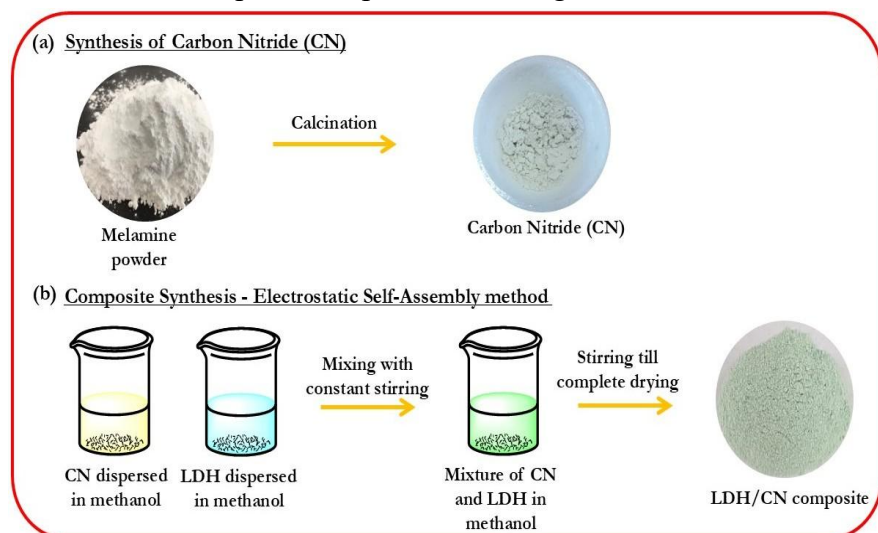


**Figure 6.2** Preparation of (a) carbon nitride (CN) and (b) LDH/CN composites.

### 6.2.5 Instrumentation

Crystallographic properties of the sample were studied by the use of Powder X-ray diffraction (PXRD) diffractograms collected using a high-resolution Bruker diffractometer (D8 Discover) using Cu K $\alpha$  radiation. Data was recorded at 298 K over the range of  $2\theta = 5\text{--}85^\circ$  at scan rate of 1.0 s/step and step size 0.02. SEM imaging, EDX analysis, and elemental mapping of the synthesized samples were done using a Zeiss Gemini SEM microscope.

### 6.2.6 Evaluation of Catalytic Activity

A typical experiment was carried out to evaluate the catalytic abilities of ZnCuNi-LDH/CN and ZnCuCe-LDH/CN composites, and for this purpose, fresh solutions of NaBH<sub>4</sub> (100 mM), *p*-NP (10 mM) and CR (100 mg L<sup>-1</sup>) were prepared using distilled water. Further solutions were prepared by diluting the stock solutions as required. The reaction progress was monitored by means of visual examination and by using a UV-Vis spectrophotometer, and the disappearance and appearance of absorption bands in the time-dependent UV spectrum signified the degradation of model molecules and formation of by-products by the catalytic action of synthesized composite materials.

NaBH<sub>4</sub>-assisted hydrogenation of *p*-Nitrophenol (*p*-NP) using synthesized composites was accomplished by adding freshly prepared NaBH<sub>4</sub> solution (100 mM, 1 mL) and distilled water (1 mL) to aqueous solution of *p*-NP (1 mM, 1 mL) in a cuvette, and it was mixed well to ensure homogeneity. This was followed by the addition of composite catalyst (0.001 g) to the reaction mixture at room temperature, and the absorbance spectrum was recorded on a Shimadzu UV-Vis spectrophotometer at fixed time intervals. The reaction kinetics were evaluated by analysing the variation in intensity of absorbance maxima appearing at  $\lambda_{max} = 400$  nm at a time interval of one minute till the complete decolourization of solution and disappearance of the  $\lambda_{max}$  band.

Reduction of Congo Red in presence of NaBH<sub>4</sub> using the synthesized composites was attempted by mixing CR solution (100 mg L<sup>-1</sup>, 1 mL) with freshly prepared NaBH<sub>4</sub> solution (100 mM, 1 mL) and distilled water (1 mL). Following this, the composite catalyst (0.001 g) was added to the above solution to initiate catalytic reaction, and reaction progress was determined by recording the absorbance maxima at  $\lambda_{max} = 497$

nm for CR at one-minute intervals till the solution was completely decolourised and the band of absorbance maxima disappeared completely.

The percentage degradation efficiency of model molecules was calculated using Equation 6.1:

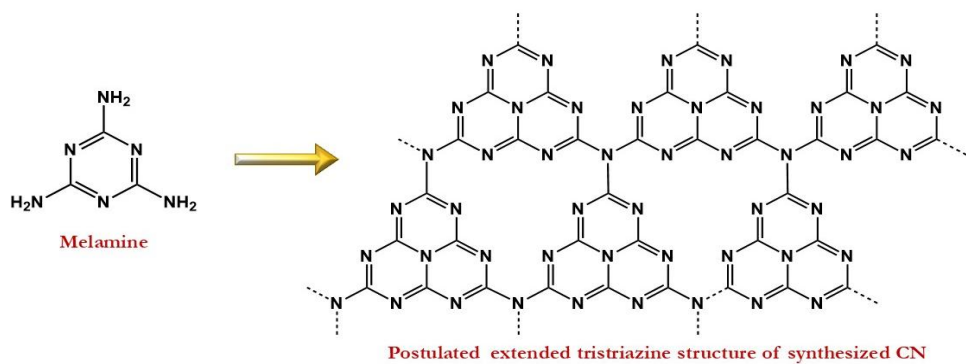
$$\text{Percentage degradation} = \frac{(C_0 - C_t)}{C_0} \times 100 \quad (6.1)$$

where  $C_0$  and  $C_t$  denote the initial and terminal concentrations of NAC and azo dye.

### 6.3 Results and Discussion

#### 6.3.1 Structural and Morphological Properties

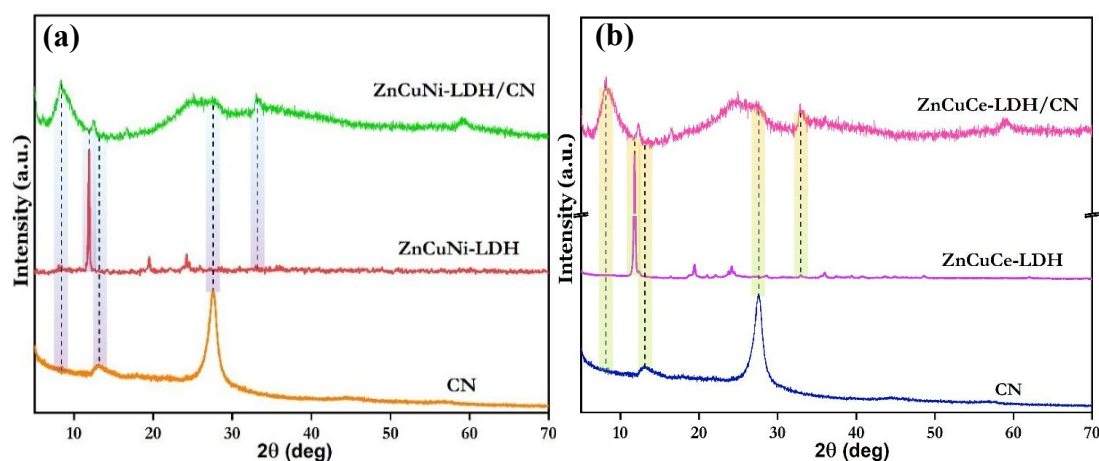
PXRD technique was used to confirm the formation of pure CN, pristine ZnCuNi-LDH and ZnCuCe-LDH, and LDH/CN composites. The diffractograms of pure CN as well as ZnCuNi-LDH and ZnCuNi-LDH/CN, ZnCuCe-LDH and ZnCuCe-LDH/CN are presented below. The PXRD diffractogram of CN exhibited its characteristic pattern, with the appearance of a weak reflection around  $13.2^\circ$  that was indexed to the  $(100)$   $hkl$  plane corresponding to the in-plane structural packing of tristriazine units (Figure 6.3). The second reflection around  $28.5^\circ$  was indexed to  $(002)$  crystal plane and its appearance was attributed to the presence of interplane stacked conjugated aromatic rings in the layered CN structure[33]. The absence of any extra peaks in the PXRD data indicated the successful synthesis of pure-phase g-C<sub>3</sub>N<sub>4</sub>.



**Figure 6.3** Structures of melamine and postulated tristriazine structure of CN.

Meanwhile, the diffractograms of ZnCuNiLDH and ZnCuCe-LDH (Figure 6.4a) bore a close resemblance to PXRD patterns of hydrotalcite-type materials previously reported in literature, since they illustrate a singular high intensity reflection at lower  $2\theta$  angle and low intensity, symmetrical reflections appearing at higher  $2\theta$  angles[34]. The characteristic reflections were indexed to (002), (003), and (004)  $hkl$  planes, and they corresponded to a turbostratic lattice possessing hexagonal symmetry, that is typical of anionic layered materials. Additionally, the absence of any peaks corresponding to hydroxy acetate compounds corroborated the formation of pure phase, crystalline ZnCuNi-LDH and ZnCuCe-LDH.

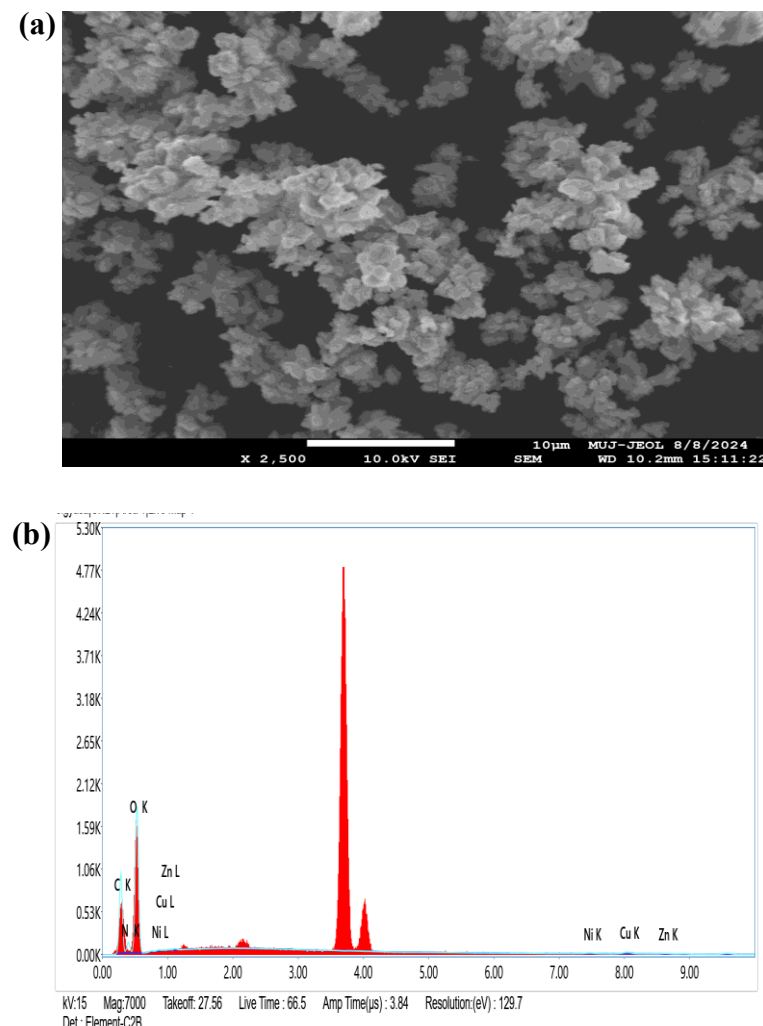
In case of ZnCuNi-LDH/CN and ZnCuCe-LDH/CN composites, the diffractograms exhibited the presence of a predominant halo-type reflection below  $10^\circ$  that is characteristic of layered materials and was attributed to the LDH component of the lattice (Figure 6.4b). The appearance of a low-intensity reflection around  $13^\circ$  as well as a broad reflection around  $28^\circ$  may be attributed to the incorporation of CN in the composite that acted as a carbon backbone and supported the exfoliated LDH layers on its surface[24]. The outcomes obtained from the PXRD technique substantiated the hypothesis that both LDH and CN were successfully incorporated into the LDH/CN composite heterostructures.



**Figure 6.4** Comparative PXRD patterns of (a) CN, ZnCuNi-LDH, ZnCuNi-LDH/CN, and (b) CN, ZnCuCe-LDH, ZnCuCe-LDH/CN.

In order to determine the morphological attributes of the composite, the microscale morphology and elemental composition of ZnCuNi-LDH/CN composite were studied

using SEM-EDX and elemental mapping techniques and the results are presented in Figure 6.5. The SEM micrograph in Figure 6.5a shows the random distribution of clusters with aggregates having irregular shapes and sizes that may have formed due to the synergistic interactions between LDH and  $C_3N_4$ . This agglomeration is a direct consequence of the interactions between the positively charged LDH and negatively charged  $C_3N_4$ , and is extremely essential for the stability of the composite[35]. The absence of visible layers may be attributed to the exfoliation process, that results in the delamination of the LDH and  $C_3N_4$  layers. The corresponding EDX spectrum clearly indicated the well-defined spatial distribution of all the constitutional elements Zn, Cu, Ni, C, N and O (Figure 6.5b). Additionally, the elemental mapping results displayed the uniform distribution of the constituent elements throughout the lattice, thereby successfully validating the formation of ZnCuNi-LDH/CN composite (Figure 6.5c).



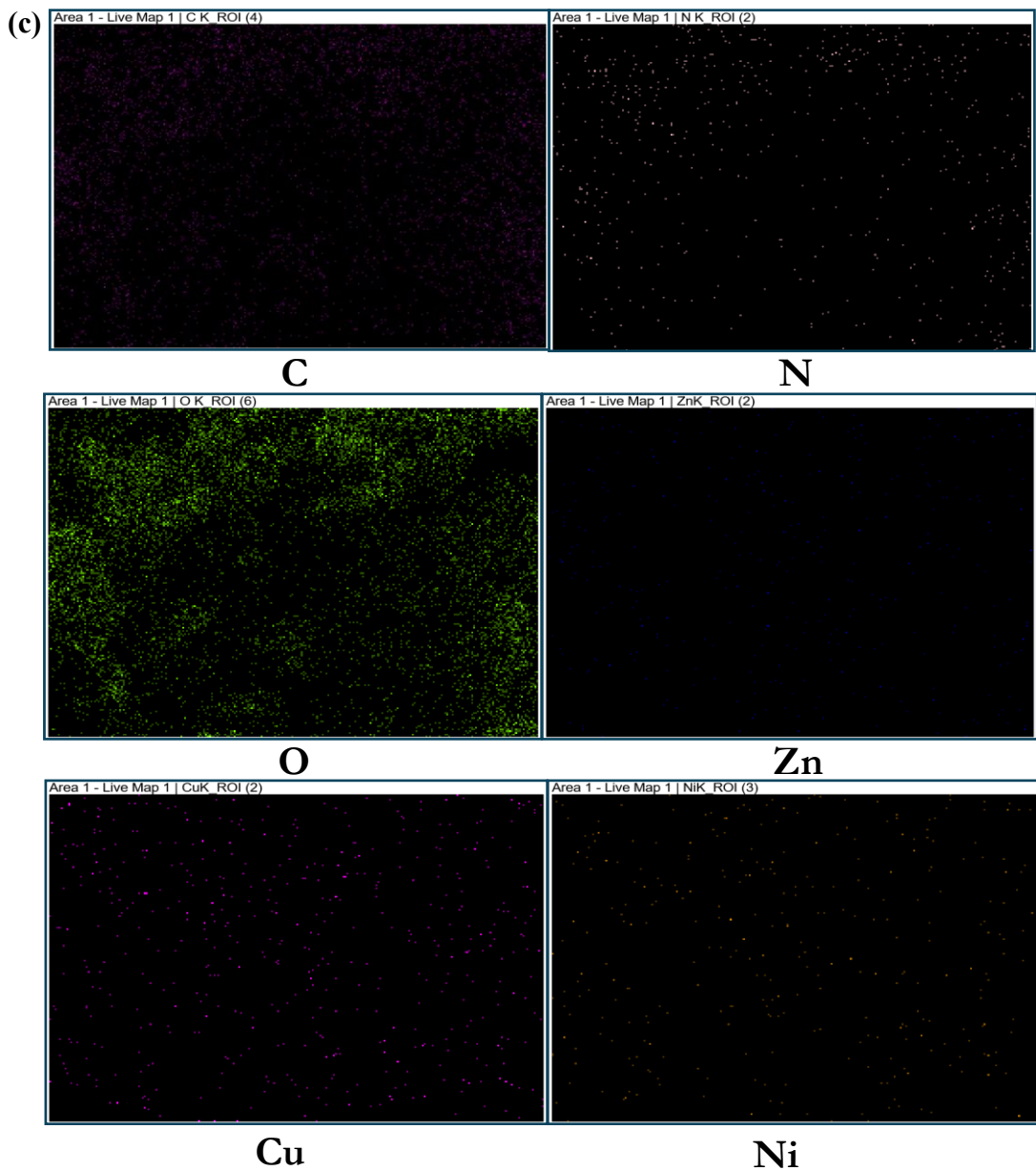


**Figure 6.5** (a) SEM micrograph, (b) EDX spectrum and (c) elemental mapping of ZnCuNi-LDH/CN composite.

### 6.3.2 Catalytic Activity

Catalytic degradation using  $\text{NaBH}_4$  with the assistance of a co-catalyst is a highly effective way to reduce toxin molecules without resulting in the production of secondary pollutants. Therefore, in the current study, the catalytic degradation of *p*-NP and CR was studied as model reaction.

The NaBH<sub>4</sub>-assisted catalytic efficiencies of synthesized ZnCuNi-LDH/CN and ZnCuCe-LDH/CN composites for *p*-NP and CR reduction were examined using UV-Visible spectrophotometer. The progress of catalytic reaction was determined by observing the variation in absorbance of pollutant molecules solutions. Further, since NaBH<sub>4</sub> (100 mM) solution was highly concentrated as compared to *p*-NP (1 mM) and CR (100 mg L<sup>-1</sup>), the reaction rate was considered to be free of the influence of BH<sub>4</sub><sup>-</sup> concentration. Hence, the hydrogenation of NAC and reduction of azo dyes was considered to follow pseudo-first order kinetics, and is shown in Equation 6.2:

$$\ln\left(\frac{C_t}{C_0}\right) = K \quad (6.2)$$

Where K denotes rate constant, and C<sub>0</sub> and C<sub>t</sub> are the initial and final concentrations of NAC and azo dyes.

Since the model molecules possessed distinct colours and yielded peaks in the visible region, reaction rate was calculated in terms of comparative absorptive intensity. Therefore, using Beer-Lambert's law (Equation 6.3)

$$A = \varepsilon Cl \quad (6.3)$$

Kinetics of reaction are expressed in terms of absorption by Equation 6.4:

$$\ln\left(\frac{C_t}{C_0}\right) = \ln\left(\frac{A_t}{A_0}\right) = kt \quad (6.4)$$

Where A<sub>0</sub> and A<sub>t</sub> are the initial and final absorbance of NAC and azo dyes.

### 6.3.2.1 Catalytic activity of ZnCuNi-LDH/CN composite

The catalytic activity of ZnCuNi-LDH/CN was ascertained against *p*-NP and CR using NaBH<sub>4</sub> as a reductant. In case of *p*-NP, when NaBH<sub>4</sub> and *p*-NP were mixed, the appearance of an absorbance peak at  $\lambda_{max} = 400$  nm was observed that may be attributed to the formation of nitrophenolate ion, as seen in Figure 6.6a. On addition of the synthesized composite catalyst, the peak at  $\lambda_{max} = 400$  nm started decreasing instantaneously, thereby confirming the decrease in *p*-NP concentration as a result of the successful hydrogenation of the nitro group of *p*-NP molecules. Meanwhile, a new peak appeared at 302 nm that was indicative of the formation of *p*-AP as the

hydrogenation product of *p*-NP. The complete disappearance of the peak after 6 minutes suggested the rapid hydrogenation of *p*-NP. The percentage hydrogenation of *p*-NP, evaluated using Eqn 6.1, was found to be 93.95%. The rate of reaction (*k*) was evaluated from the linear plot between  $\ln(C_t/C_0)$  and reaction time *t* (min), and it was calculated to be  $0.432 \text{ min}^{-1}$  ( $R^2 = 0.86$ ) in accordance to pseudo-first order model (Figure 6.6b).

The UV-Vis absorbance vs wavelength plot for the catalytic reduction of CR is presented in Figure 6.6c. CR molecules contain chromophoric azo (-N=N-) groups that impart its characteristic red colour, due to which they present absorption bands at 497 nm ( $\pi \rightarrow \pi^*$ ) and 350 nm ( $n \rightarrow \pi^*$ ) in the UV-Vis absorbance spectrum. For the purpose of this experiment, the change in absorbance was noted at absorbance maxima  $\lambda_{max} = 497 \text{ nm}$ . On addition of  $\text{NaBH}_4$  to the CR solution, no changes in the peak intensity and position were observed. Furthermore, there was no significant change in color of the solution. While on addition of  $\text{ZnCuNi-LDH/CN}$  catalyst, a considerable change was observed in the color of the reaction mixture along with the reduction in the intensity of peak present at  $\lambda_{max} = 497 \text{ nm}$ , that may be credited to the reduction of the azo bond. With the progress of reaction, the peak intensity decreased rapidly until its eventual disappearance after 4 minutes, accompanied by the complete decolourisation of the reaction mixture that signified complete dye breakdown. The percentage of dye degraded at the end of catalytic reaction, calculated using Eqn 6.1, was found to be 99.30%. The rate constant *k*, obtained by linearly regressing experimental data to the pseudo first order model in the plot between  $\ln(C_t/C_0)$  and reaction time *t* (min), was evaluated to be  $0.956 \text{ min}^{-1}$  ( $R^2 = 0.7$ ) (Figure 6.6d). Therefore, the dissipation of peak at  $\lambda_{max} = 497 \text{ nm}$  and emergence of new peaks in the recorded absorbance spectra gave evidence for the rapid degradation of CR in presence of  $\text{ZnCuNi-LDH/CN}$  composite and  $\text{NaBH}_4$ . Furthermore, the new peaks arising in the UV-Vis absorbance spectrum were attributed to the formation of colourless aromatic amines as by-products due to cleavage of the azo groups to form hydrazo (-NH-NH-) or amine (-NH-) moieties in the catalysis reaction.

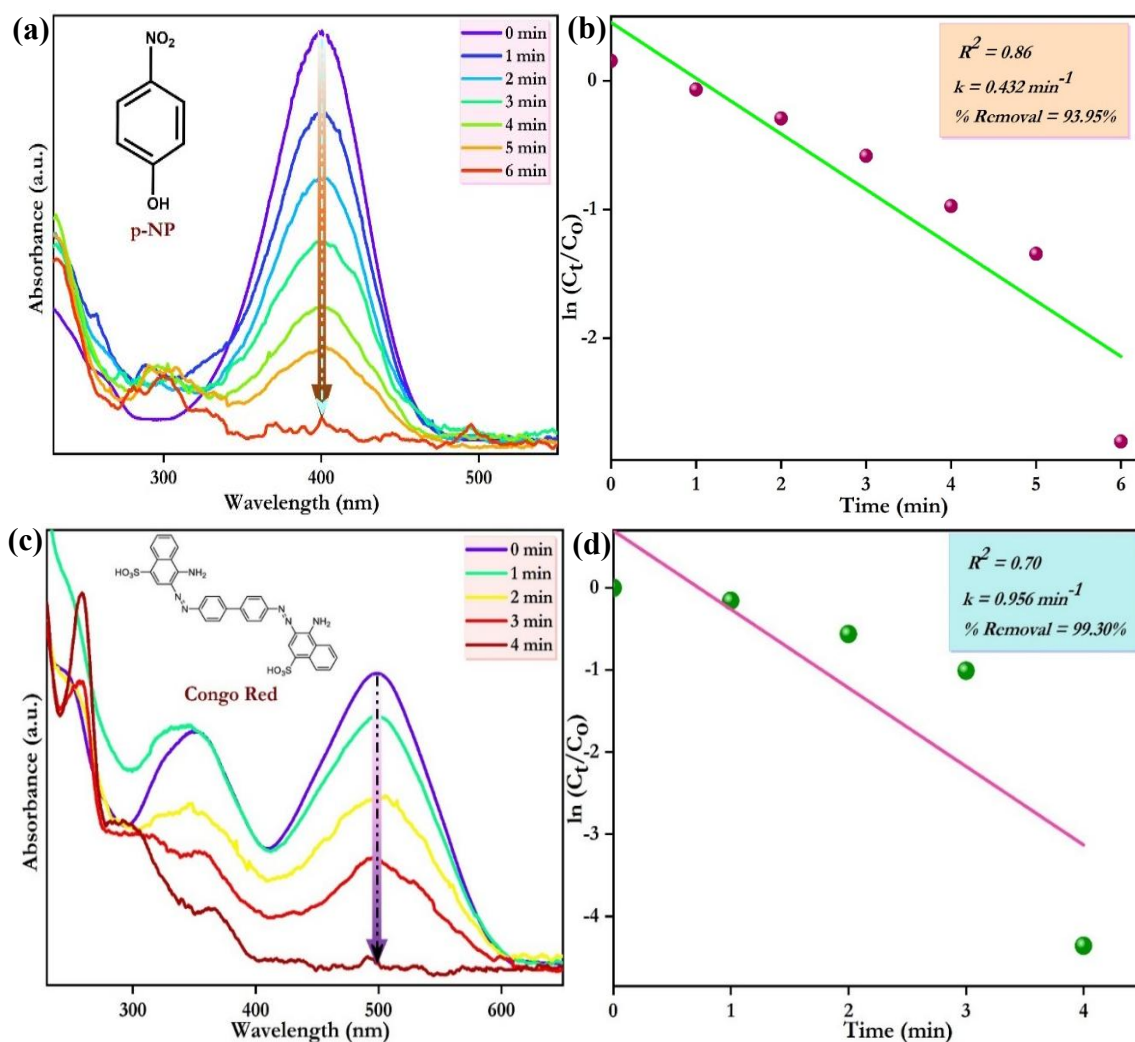


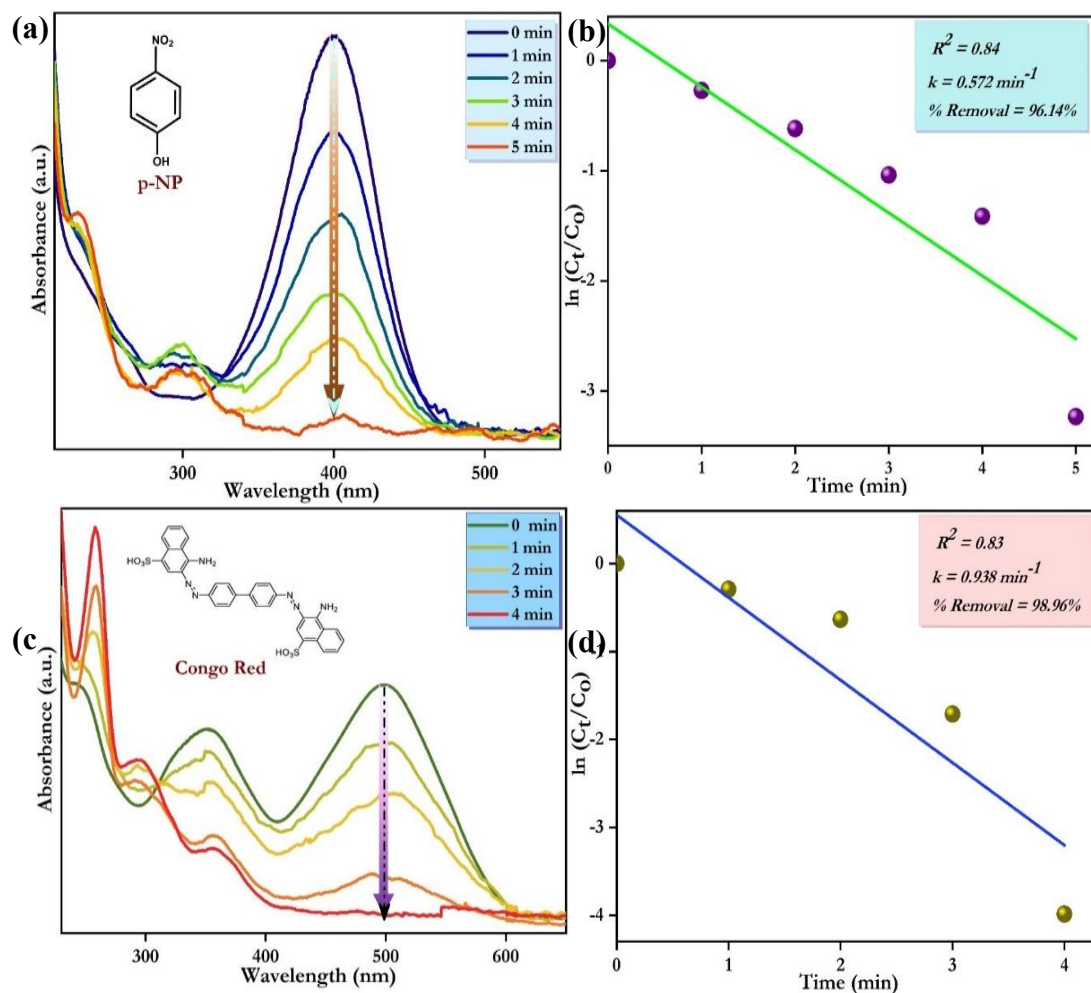
**Figure 6.6** UV-Vis absorption spectrum and linear fitting of pseudo-first kinetics model respectively for the  $\text{NaBH}_4$ -assisted catalytic reduction of (a,b) *p*-NP and (c,d) CR dye using  $\text{ZnCuNi-LDH/CN}$  composite.

### 6.3.2.2 Catalytic activity of $\text{ZnCuCe-LDH/CN}$

The ability of  $\text{ZnCuCe-LDH/CN}$  to act as a catalyst for the hydrogenation of *p*-NP and reduction of CR was also evaluated using  $\text{NaBH}_4$  as a reductant. The time-dependent absorption spectra of composite-catalysed *p*-NP hydrogenation is presented in Figure 6.7a. On addition of  $\text{NaBH}_4$  to *p*-NP solution, a singular absorbance peak was observed at  $\lambda_{max} = 400 \text{ nm}$  and intense colouration of solution to a bright yellow colour was observed. Then upon addition of  $\text{ZnCuCe-LDH/CN}$  composite catalyst to the solution, the intensity of peak appearing at  $\lambda_{max} = 400 \text{ nm}$  decreased rapidly and completely dissipated after 5 minutes. Visual investigation of the reaction mixture showed the

disappearance of the bright yellow colour, and may be attributed to the conversion of the nitro group to amine group (-NH<sub>2</sub>) on addition of H<sub>2</sub> to the nitro group during hydrogenation of *p*-NP molecules. Further, appearance of a new peak at 302 nm corroborated the formation of hydrogenation product *p*-AP. The percentage degradation efficacy described in Eqn 6.1 was calculated to be 96.14% for *p*-NP hydrogenation. The rate of reaction was evaluated by monitoring the decrease in absorbance of *p*-NP at  $\lambda_{max} = 400$  nm, and rate constant of reduction (*k*) was determined by linearly plotting  $\ln(C_t/C_0)$  versus reaction time *t* (min). Therefore, *k* was calculated from the kinetics data using Eqn 6.4 by employing the pseudo first order model and was found to be 0.572 min<sup>-1</sup> ( $R^2 = 0.84$ ) (Figure 6.7b).

The UV-Vis absorbance vs wavelength plot for the catalytic reduction of CR is presented in Figure 6.7c. Absorbance change was noted at absorbance maxima  $\lambda_{max} = 497$  nm for CR. No change in the peak intensity and position was observed on addition of NaBH<sub>4</sub> alone. But when ZnCuCe-LDH/CN composite was added to the solution, a visible change in the intensity of color of the reaction mixture was observed and the intensity of absorbance maxima present at  $\lambda_{max} = 497$  nm decreased rapidly. With the progress of the catalytic reaction, the peak kept decreasing steadily until its eventual disappearance and the complete decolourisation of reaction mixture within 4 minutes, that signified the complete reduction of CR molecules. Percentage degradation of dye was calculated using Eqn 6.1, and was found to be 98.96%. The rate constant *k*, obtained from the plot between  $\ln(C_t/C_0)$  versus reaction time *t* (min) by linearly regressing experimental data to the pseudo-first-order model, was evaluated to be 0.938 min<sup>-1</sup> ( $R^2 = 0.83$ ) (Figure 6.7d). In the time dependent UV-Vis spectrum for CR reduction using ZnCuCe-LDH/CN, the emergence of new absorption peaks was ascribed to the generation of colourless aromatic amines that were formed by the reductive cleavage of the azo (-N=N-) linkages to form hydrazo (-NH-NH-) or amine (-NH-) intermediates during the catalytic transformation.



CR	99.30	0.956
<b>ZnCuCe-LDH/CN</b>		
<i>p</i> -NP	96.14	0.572
CR	98.96	0.938

### 6.3.2.3 Postulated Mechanism

On the basis of the aforementioned catalytic investigation results, a plausible mechanism for the catalytic reduction using  $\text{NaBH}_4$  in the presence of LDH/CN catalysts has been proposed.  $\text{NaBH}_4$  hydrolyses in aqueous medium to form  $\text{BH}_4^-$  and  $\text{Na}^+$  ions. Subsequently, the  $\text{NaBH}_4$ -assisted catalytic reaction proceeds through the Langmuir-Hinshelwood mechanism that consists of three steps: (1) breakdown of  $\text{BH}_4^-$  into  $\text{BO}_2^-$  and  $\text{H}_2$ , and transfer of hydride to catalyst surface forming M-H linkages, (2) adsorption of pollutant molecules onto the catalyst surface, and (3) reduction of adsorbed pollutant molecules due to transfer of electrons and H from catalyst. Subsequently, the byproducts formed are desorbed from the catalyst surface, resulting in reactivation of the catalyst for further catalytic reactions. Herein, step 2 i.e. adsorption of pollutants is the slowest in nature, therefore it is the rate determining step for this process. In the present study, the reduction of *p*-NP and CR using  $\text{NaBH}_4$  in the presence of LDH/CN composites occurs via the same pathway.

In case of *p*-NP, the catalytic reaction is initiated by diffusion and adsorption of *p*-NP onto the active sites on the catalyst surface due to  $\pi$ - $\pi$  stacking interactions. The nitro groups of *p*-NP strongly withdraw electrons from the aromatic ring, that further exacerbates the  $\pi$ - $\pi$  interactions between *p*-NP and the composite catalyst. Subsequently, the adsorbed nucleophilic  $\text{BH}_4^-$  moiety donates hydrogen atoms on its hydrolysis to the catalyst, that is then followed by the formation of a metal-hydride (M-H) complex. Due to the high concentration of *p*-NP on catalyst surface, and the difference in electronegativities of hydride radical and catalyst cations, the hydride radical from the M-H complex attacks the nitro group of *p*-NP to form the nitroso and hydroxylamine intermediates, followed by the generation of final hydrogenation product *p*-AP[36]. On completion of this step, *p*-AP molecules are desorbed from the

catalyst surface, thereby freeing the active sites and reactivating the catalyst for further reduction.

The reduction of CR dye molecules proceeds through the transfer of electrons from the hydrolysed  $\text{BH}_4^-$  ions to the CR molecules via the composite catalyst that acts as a redox catalyst. Electrophilic CR molecules adsorbed on the catalyst surface receive electrons from the nucleophilic  $\text{BO}_2^-$  through the catalyst acting as an electron mediator, resulting in their reduction. The toxic CR molecules are successfully converted into environmentally benign products by the use of this environment-friendly green catalyst. Finally, the reduction by-products are desorbed from the catalyst surface into the reaction medium.

In the catalytic reaction, the  $\text{ZnCuNi-LDH/CN}$  and  $\text{ZnCuCe-LDH/CN}$  composites play a multivariate role. First, the catalyst augments the rate of reduction reaction by lowering the activation energy barrier, thereby making the reaction kinetically feasible. Secondly, the porous structure provides large surface area and easy access to the active sites of catalyst for the rapid transport and diffusion of hydride and electrons, thereby enabling the reaction to occur readily. Third, the synergistic interactions between the Cu and Ni cations in  $\text{ZnCuNi-LDH/CN}$ , and Cu and Ce cations in  $\text{ZnCuCe-LDH/CN}$  composites enhance the electron relay ability of the catalysts, while the CN component participates in the  $\pi-\pi$  stacking interactions with the pollutant molecules, thereby increasing their rate of adsorption onto the catalyst surface. Additionally, the anchoring of LDH nanosheets on CN creates a robust architecture that resists aggregation and leaching, thereby preserving the catalyst's active surface area and active sites throughout the catalyst process. The interactions between the 2D surfaces of the LDH and CN create a chemically inert structure with exposure to an abundant number of active sites, thereby resulting in excellent catalytic activity of the composites for the degradation of pollutant molecules. The synergy between the composite components leads to significant improvements in both the stability and efficiency of catalytic reactions, making LDH/CN composites highly suitable for use as sustainable and robust catalytic materials.

### 6.3.2.4 Comparison with Reported Catalysts

The superior catalytic activity of ZnCuNi-LDH/CN and ZnCuCe-LDH/CN composites for the catalytic degradation of *p*-NP and CR is highlighted on being compared with those previously reported catalysts (Table 6.3). This study reports the synthesis and characterisation of novel ZnCuNi-LDH/CN and ZnCuCe-LDH/CN composites using a facile electrostatic self-assembly method. On comparison with previously reported catalysts, it was inferred that both ZnCuNi-LDH/CN and ZnCuCe-LDH/CN composites showed enhanced activity within shorter reaction times. The excellent catalytic activity of the composites may be attributed to the synergistic interactions between the transition metal Cu and Ni atoms. Furthermore, the formation of catalyst by supporting exfoliated LDH layers on the carbon support C<sub>3</sub>N<sub>4</sub> also contributes to the enhancement of catalytic activity by providing increased surface area and exposure to active sites. Although the composites were able to effectively reduce *p*-NP, it is important to note that the synthesized composites were also able to effectively reduce anionic CR dye. CR molecules contain two azo bonds that are often difficult to reduce due to their lower reduction potential and higher resonance stabilization of its azo bonds, thus reducing the efficacy of the procedure. But both the synthesized composites were able to demonstrate effective reduction of CR dye, that was previously not achieved when only ZnCuNi-LDH was used. Thus, it may be inferred that the synthesized ZnCuNi-LDH/CN and ZnCuCe-LDH/CN composites are one-of-a-kind novel materials that possess superior catalytic activities towards both NACs and anionic azo dyes.

**Table 6.3** Comparison of catalytic performance of ZnCuNi-LDH/CN and ZnCuCe-LDH/CN composites with previously reported catalysts.

<b>Pollutant</b>	<b>Catalyst</b>	<b>Time (min)</b>	<b>Removal</b>	<b>Reference</b>
			<b>Efficiency (%)</b>	
<i>p</i> -NP	Guar Gum-stabilised Pt NPs	7	93.7	[37]
	Nanoscale zero valent iron	20	98	[38]

	Bi <sub>2</sub> O <sub>2</sub> CO <sub>3</sub> /ZnFe <sub>2</sub> O <sub>4</sub> 30%	30	Complete Reduction	[39]
	ZnCuNi-LDH	3	95.3	[32]
	ZnCuNi-LDH/CN	6	93.95	This work
	ZnCuCe-LDH/CN	5	96.14	This work
CR	Cobalt NPs	7	100	[40]
	HKUST-1/PAA hydrogel composite	25	100	[41]
	N-doped fluorescent carbon nanodots	10	100	[42]
	ZnCuNi-LDH	4	96.4	[32]
	ZnCuNi-LDH/CN	4	99.30	This work
	ZnCuCe-LDH/CN	4	98.96	This work

#### 6.4 Conclusion

The current work describes the synthesis of carbon nitride (C<sub>3</sub>N<sub>4</sub>) via thermal treatment of pure melamine powder and further summarizes the fabrication of heterostructured ZnCuNi-LDH/CN and ZnCuCe-LDH/CN composites using the facile electrostatic self-assembly method in the presence of methanol as a dispersion medium. The structural and morphological properties of synthesized composites were studied using PXRD, SEM-EDX, and elemental mapping techniques. Further, the potential applications of synthesized ZnCuNi-LDH/CN and ZnCuCe-LDH/CN composites as catalytic materials for wastewater remediation were explored. The composites were utilized as catalysts for the NaBH<sub>4</sub>-assisted degradation of *p*-NP and CR. The findings of the catalytic experiments suggested that the combination of ZnCuNi-LDH and ZnCuCe-LDH with CN yields a highly efficient catalyst that was capable of reducing CR dye, that was previously unattainable with pristine LDH samples. Furthermore, ZnCuNi-LDH/CN and ZnCuCe-LDH/CN were able to effectively achieve the hydrogenation of *p*-NP within a short time span of 6 and 5 minutes respectively, while both the composites reduced CR dye molecules within just 4 minutes. The synthesized composites exhibited more than 93% removal efficiencies for *p*-NP and CR. Therefore,

this study proposes that composites of CN and LDHs possess noticeable catalytic activity and could be effectively applied as green catalysts in practical wastewater remediation applications.

## 6.5 References

- [1] D. Hull, T.W. Clyne, *An Introduction to Composite Materials*, 1993. [https://doi.org/10.1016/0306-4522\(93\)90120-5](https://doi.org/10.1016/0306-4522(93)90120-5).
- [2] D. Hull, T.W. Clyne, Fibres and matrices, in: *An Introd. to Compos. Mater.*, 2012: pp. 9–38. <https://doi.org/10.1017/cbo9781139170130.004>.
- [3] R.G. Adli, A. Kianvash, M.G. Hosseini, A. Hajalilou, E. Abouzari-Lotf, Mechanochemically synthesized NiCo<sub>2</sub>O<sub>4</sub>/Vulcan/PANI nanocomposite and investigation of its electrochemical behavior as a supercapacitor, *Ceram. Int.* 44 (2018) 20049–20057. <https://doi.org/10.1016/j.ceramint.2018.07.279>.
- [4] Z.A.A. Latif, A.M. Mohammed, N.M. Abbass, Synthesis and characterization of polymer nanocomposites from methyl acrylate and metal chloride and their application, *Polym. Bull.* 77 (2020) 5879–5898. <https://doi.org/10.1007/s00289-019-03047-9>.
- [5] N. Miyamoto, S. Yamamoto, *Functional Layered Compounds for Nanoarchitectonics*, Elsevier Inc., 2017. <https://doi.org/10.1016/B978-0-323-37829-1.00007-9>.
- [6] R. Yadav, A.K. Sharma, S. Sharma, Advance Development in Natural Graphite Material and Its Applications: A Review, *Mining, Metall. Explor.* 42 (2025) 361–385. <https://doi.org/10.1007/s42461-024-01167-z>.
- [7] S. Bose, T. Kuila, A.K. Mishra, R. Rajasekar, N.H. Kim, J.H. Lee, Carbon-based nanostructured materials and their composites as supercapacitor electrodes, *J. Mater. Chem.* 22 (2012) 767–784. <https://doi.org/10.1039/c1jm14468e>.
- [8] Y. Yao, Y. Wang, T. Lu, J. Zhang, K. Hu, H. Zhang, T. Pukala, Y. Liu, X. Duan, S. Wang, In-plane implanting carbon rings into carbon nitride to intrigue nonradical photodegradation, *Appl. Catal. B Environ.* 342 (2024) 123363. <https://doi.org/10.1016/j.apcatb.2023.123363>.
- [9] A.M. Sadanandan, J.-H. Yang, V. Devtade, G. Singh, N. Panangattu Dharmarajan, M. Fawaz, J. Mee Lee, E. Tavakkoli, C.-H. Jeon, P. Kumar, A. Vinu, Carbon nitride based nanoarchitectonics for nature-inspired photocatalytic CO<sub>2</sub> reduction, *Prog. Mater. Sci.* 142 (2024) 101242. <https://doi.org/https://doi.org/10.1016/j.pmatsci.2024.101242>.
- [10] P. Chaluvachar, Y.N. Sudhakar, G.T. Mahesha, V.G. Nair, N. Desai, D.K. Pai, Emerging role of graphitic carbon nitride in advanced supercapacitors: A comprehensive review, *J. Energy Chem.* 103 (2025) 498–524.

<https://doi.org/https://doi.org/10.1016/j.jechem.2024.11.075>.

[11] C. Wang, Y. Lu, Z. Wang, H. Liao, W. Zhou, Y. He, S.M. Osman, M. An, Y. Asakura, Y. Yamauchi, L. Wang, Z. Yuan, Salt-assisted construction of hydrophilic carbon nitride photocatalysts with abundant water molecular adsorption sites for efficient hydrogen production, *Appl. Catal. B Environ. Energy* 350 (2024) 123902.  
<https://doi.org/https://doi.org/10.1016/j.apcatb.2024.123902>.

[12] Z. Chen, G. Ding, Z. Wang, Y. Xiao, X. Liu, L. Chen, C. Li, H. Huang, G. Liao, Precision Molecular Engineering of Carbon Nitride for Efficient and Selective Photoreduction of CO<sub>2</sub> to C<sub>2</sub>H<sub>6</sub> in Pure Water, *Adv. Funct. Mater.* 35 (2025) 2423213. <https://doi.org/https://doi.org/10.1002/adfm.202423213>.

[13] S. Yuan, L. Dai, M. Xie, J. Liu, H. Peng, Modification optimization and application of graphitic carbon nitride in photocatalysis: Current progress and future prospects, *Chem. Eng. Sci.* 296 (2024) 120245.  
<https://doi.org/https://doi.org/10.1016/j.ces.2024.120245>.

[14] M.A. Ahmed, S.A. Mahmoud, A.A. Mohamed, Unveiling the photocatalytic potential of graphitic carbon nitride (g-C<sub>3</sub>N<sub>4</sub>): a state-of-the-art review, *RSC Adv.* 14 (2024) 25629–25662. <https://doi.org/10.1039/d4ra04234d>.

[15] S. Suganthi, K. Ahmad, T.H. Oh, Progress in Graphitic Carbon Nitride-Based Composite Materials for Electrochemical Sensing and Energy Storage Applications, *ChemistrySelect* 10 (2025) e202404670.  
<https://doi.org/https://doi.org/10.1002/slct.202404670>.

[16] F. Basumatary, A. Sarkar, N. Mushahary, B. Das, P. Saikia, M. Selvaraj, S. Basumatary, Graphitic carbon nitride composites as advanced versatile materials for adsorption and photocatalytic degradation of emerging pollutants from wastewater, *Process Saf. Environ. Prot.* 191 (2024) 2416–2468.  
<https://doi.org/https://doi.org/10.1016/j.psep.2024.09.077>.

[17] N. Manjubaashini, A. Sowndarya, T.D. Thangadurai, Metal oxide-graphitic carbon nitride composites: An inimitable nanoarchitectures for energy storage using supercapacitor devices, *J. Alloys Compd.* 1036 (2025) 181950.  
<https://doi.org/https://doi.org/10.1016/j.jallcom.2025.181950>.

[18] M.A. Zaed, J. Cherusseri, R. Saidur, K.H. Tan, A.K. Pandey, Synthesis and characterization of hierarchical Ti<sub>3</sub>C<sub>2</sub>T<sub>x</sub> MXene/graphitic-carbon nitride/activated carbon@luffa sponge composite for enhanced water desalination, *Open Ceram.* 19 (2024) 100645.  
<https://doi.org/https://doi.org/10.1016/j.oceram.2024.100645>.

[19] M. Zheng, M. Guo, F. Ma, W. Li, Y. Shao, Recent advances in graphitic carbon nitride-based composites for enhanced photocatalytic degradation of rhodamine B: mechanism, properties and environmental applications, *Nanoscale Adv.* (2025) 4780–4802. <https://doi.org/10.1039/d5na00439j>.

[20] T. Sun, G.P. Benedictto, M.R. Gonzalez, M.S. Legnoverde, E. Raymundo-

Piñero, E.I. Basaldella, C. Ania, Photocatalytic activity of NiZnAl hydrotalcite-like compound/carbon nitride composites for the degradation of methylparaben, *Catal. Today* 459 (2025) 115432.  
<https://doi.org/https://doi.org/10.1016/j.cattod.2025.115432>.

[21] R. Kulkarni, S.R. Patil, L.P. Lingamdinne, N. Chodankar, Y.-Y. Chang, J. Bae, J.R. Koduru, Graphitic Carbon Nitride-Supported Layered Double Hydroxides (GCN@FeMg-LDH) for Efficient Water Splitting and Energy Harvesting, *ACS Appl. Mater. Interfaces* 17 (2025) 9253–9265.  
<https://doi.org/10.1021/acsami.4c17996>.

[22] S.H.A. Shah, A. Shah, I. Shah, Sustainable energy generation from water splitting using trimetallic layered-double hydroxide and graphitic carbon nitride nanocomposite, *Discov. Sustain.* 6 (2025) 456.  
<https://doi.org/10.1007/s43621-025-01333-3>.

[23] S. Nayak, L. Mohapatra, K. Parida, Visible light-driven novel g-C<sub>3</sub>N<sub>4</sub>/NiFe-LDH composite photocatalyst with enhanced photocatalytic activity towards water oxidation and reduction reaction, *J. Mater. Chem. A* 3 (2015) 18622–18635. <https://doi.org/10.1039/c5ta05002b>.

[24] R. Khan, U. Jadoon, N. Ali, A.A. Tahir, M. Siddique, M. Bilal, M. Sillanpaa, T.M. Almutairi, A.A.A. Mohammed, S. Yousaf, S. Kanwal, Layered double hydroxide and graphitic carbon nitride hybrid as nanoadsorbent for selected azo-dye removal from aqueous solution, *Int. J. Environ. Sci. Technol.* (2022).  
<https://doi.org/10.1007/s13762-022-04649-z>.

[25] S.H. Hashemi, M. Kaykhaii, Chapter 15 - Azo dyes: Sources, occurrence, toxicity, sampling, analysis, and their removal methods, in: T. Dalu, N.T.B.T.-E.F.P. Tavengwa (Eds.), Elsevier, 2022: pp. 267–287.  
<https://doi.org/https://doi.org/10.1016/B978-0-12-822850-0.00013-2>.

[26] J.O. Tijani, O.O. Fatoba, L.F. Petrik, A Review of Pharmaceuticals and Endocrine-Disrupting Compounds: Sources, Effects, Removal, and Detections, *Water, Air, Soil Pollut.* 224 (2013) 1770.  
<https://doi.org/10.1007/s11270-013-1770-3>.

[27] A.A. Kassem, H.N. Abdelhamid, D.M. Fouad, S.A. Ibrahim, Hydrogenation reduction of dyes using metal-organic framework-derived CuO@C, *Microporous Mesoporous Mater.* 305 (2020) 110340.  
<https://doi.org/10.1016/j.micromeso.2020.110340>.

[28] I. Ahmad, K. Manzoor, G. Aalam, M. Amir, S.W. Ali, S. Ikram, Facile Synthesis of L-Tryptophan Functionalized Magnetic Nanophotocatalyst Supported by Copper Nanoparticles for Selective Reduction of Organic Pollutants and Degradation of Azo Dyes, *Catal. Letters* 153 (2023) 2604–2623. <https://doi.org/10.1007/s10562-022-04182-1>.

[29] G. Salehi, R. Abazari, A.R. Mahjoub, Visible-Light-Induced Graphitic-C<sub>3</sub>N<sub>4</sub>@Nickel-Aluminum Layered Double Hydroxide Nanocomposites with Enhanced Photocatalytic Activity for Removal of Dyes in Water, *Inorg.*

Chem. 57 (2018) 8681–8691. <https://doi.org/10.1021/acs.inorgchem.8b01636>.

[30] C. Madhusha, I. Munaweera, V. Karunaratne, N. Kottegoda, Synergistic adsorption-photocatalytic degradation of different antibiotics in seawater by a porous g-C<sub>3</sub>N<sub>4</sub> / calcined-LDH and its application in synthetic mariculture wastewater, J. Agric. Food Chem. 68 (2020) 8962–8975. <https://doi.org/10.1016/j.jhazmat.2021.126183>.

[31] S. Nayak, K. Parida, Comparison of NiFe-LDH based heterostructure material towards photocatalytic rhodamine B and phenol degradation with water splitting reactions, Mater. Today Proc. 35 (2021) 243–246. <https://doi.org/10.1016/j.matpr.2020.05.332>.

[32] J. Pathak, P. Singh, Ultrafast catalytic reduction of organic pollutants using ternary zinc–copper–nickel layered double hydroxide, Appl. Organomet. Chem. (2024) 1–17. <https://doi.org/10.1002/aoc.7507>.

[33] C. Feng, J. Luo, C. Chen, S. Zuo, Y. Ren, Z.P. Wu, M. Hu, S. Ould-Chikh, J. Ruiz-Martínez, Y. Han, H. Zhang, Cooperative tungsten centers in polymeric carbon nitride for efficient overall photosynthesis of hydrogen peroxide, Energy Environ. Sci. 17 (2024) 1520–1530. <https://doi.org/10.1039/d3ee03032f>.

[34] J. Pathak, P. Singh, Synthesis and Characterization of Ternary Layered Double Hydroxide containing Zinc/Copper/Nickel and its PANI Composite, Polym. Compos. 43 (2022) 7836. <https://doi.org/https://doi.org/10.1002/pc.26895>.

[35] Y. Zou, P. Wang, W. Yao, X. Wang, Y. Liu, D. Yang, L. Wang, J. Hou, A. Alsaedi, T. Hayat, X. Wang, Synergistic immobilization of UO<sub>2</sub><sup>2+</sup> by novel graphitic carbon nitride @ layered double hydroxide nanocomposites from wastewater, Chem. Eng. J. 330 (2017) 573–584. <https://doi.org/10.1016/j.cej.2017.07.135>.

[36] L. Qin, H. Yi, G. Zeng, C. Lai, D. Huang, P. Xu, Y. Fu, J. He, B. Li, C. Zhang, M. Cheng, H. Wang, X. Liu, Hierarchical porous carbon material restricted Au catalyst for highly catalytic reduction of nitroaromatics, J. Hazard. Mater. 380 (2019) 120864. <https://doi.org/10.1016/j.jhazmat.2019.120864>.

[37] S. Pandey, S.B. Mishra, Catalytic reduction of p-nitrophenol by using platinum nanoparticles stabilised by guar gum, Carbohydr. Polym. 113 (2014) 525–531. <https://doi.org/10.1016/j.carbpol.2014.07.047>.

[38] S. Bae, S. Gim, H. Kim, K. Hanna, Effect of NaBH<sub>4</sub> on properties of nanoscale zero-valent iron and its catalytic activity for reduction of p-nitrophenol, Appl. Catal. B Environ. 182 (2016) 541–549. <https://doi.org/10.1016/j.apcatb.2015.10.006>.

[39] P. Zarringhadam, S. Farhadi, Novel sheet-like bismuth subcarbonate-zinc ferrite (Bi<sub>2</sub>O<sub>2</sub>CO<sub>3</sub>/ZnFe<sub>2</sub>O<sub>4</sub>) magnetically recyclable nanocomposites:

Synthesis, characterization and enhanced catalytic performance for the reduction of nitrophenols and nitroanilines, *Appl. Organomet. Chem.* 32 (2018) e4518. <https://doi.org/10.1002/aoc.4518>.

- [40] M.N. Khan, O. Bashir, T.A. Khan, S.A. Al-Thabaiti, Z. Khan, Catalytic Activity of Cobalt Nanoparticles for Dye and 4-Nitro Phenol Degradation: A Kinetic and Mechanistic Study, *Int. J. Chem. Kinet.* 49 (2017) 438–454. <https://doi.org/10.1002/kin.21089>.
- [41] A. Nachaichot, O. Kenvised, S. Choram, S. Nijpanich, S. Budsombat, Catalytic reduction of nitrophenols and dyes by HKUST-1/hydrogel composite, *RSC Adv.* 15 (2025) 6974–6983. <https://doi.org/10.1039/d5ra00081e>.
- [42] V. Arul, P. Chandrasekaran, M.G. Sethuraman, Reduction of Congo red using nitrogen doped fluorescent carbon nanodots obtained from sprout extract of *Borassus flabellifer*, *Chem. Phys. Lett.* 754 (2020) 137646. <https://doi.org/10.1016/j.cplett.2020.137646>.

# CHAPTER - 7

## SYNTHESIS, CHARACTERIZATION AND CATALYTIC APPLICATIONS OF MAGNETICALLY SEPARABLE $Fe_3O_4/SiO_2/ZnCuNi$ -LDH BASED COMPOSITE MATERIALS



---

# **CHAPTER - 7**

## **SYNTHESIS, CHARACTERIZATION AND CATALYTIC APPLICATIONS OF MAGNETICALLY SEPARABLE $\text{Fe}_3\text{O}_4/\text{SiO}_2/\text{ZnCuNi-LDH}$ BASED COMPOSITE MATERIALS**

---

### **7.1 Introduction**

In recent years, remarkable progress has been achieved in the field of composite materials due to advancements in the development of inorganic-organic hybrid materials. Composites are engineered by the strategic combination of multiple components (matrix and reinforcement) with distinct but complementary features, and the resulting product is an advanced material with enhanced characteristics[1]. The particular interest in composites arises due to their significant advantages over conventional single-component materials, including easy tailorability, excellent mechanical, electrical and thermal properties, high chemical resistance as well as their versatility. These composites exhibit improved functionality in various aspects of material performance, outperforming even that of constituent materials used individually[2]. The scope of the practical utility, functionality and applicability of composites can be further widened by (i) having one of the phases in one, two, or three dimensions of less than 100 nm, or (ii) having the repeat distances between the different phases of the material in nanoscale. These materials, termed as nanocomposites possess significantly enhanced properties due to the high surface area-to-volume ratios of the reinforcing phase and excellent dispersibility, that contribute to high specific surface areas, and result in superior thermal, magnetic, electrical, mechanical, and flame-retardant properties[3]. Therefore, these nanostructures can be highly tuned for a multitude of applications, including water remediation, catalysis, sensing, biomedics, etc[4–7]. Among the wide spectrum of nanocomposites that are currently being developed and used, magnetic nanocomposites have emerged as a promising candidate for performing performance and overcoming drawbacks faced by

traditional nanocomposites[8–10]. Their intrinsic magnetic abilities can be advantageously used to achieve maximum output of performance with minimum input needed for their separation from various media since it can be easily achieved by the use of external magnetic field. To formulate these materials, the use of iron oxide nanoparticles (IONPs) is highly favoured since they occur in several phases (magnetite, hematite, etc), and each phase possesses distinct magnetic properties that can be tailored at per the required application. Furthermore, their synthesis has been widely reported in literature using both chemical and green methods. Keijok et al. synthesized superparamagnetic iron oxide nanoparticles using the coprecipitation method, and employed them for the adsorption of bovine serum albumin (BSA) molecules[11]. Recently, Naik et al. reported the biosynthesis of iron oxide nanoparticles using *Bacillus subtilis*, and investigated their potential to mitigate salinity stress in rice[12]. Therefore, based on the fact that they are economical, biocompatible and chemically stable, IONPs have quickly become one the most researched materials in recent times. However, the fact that these materials possess agglomeration tendencies, are unstable and cannot be stored for long, combined with their limited adsorptive and catalytic abilities hinders their commercial usage. In order to overcome these drawbacks, iron oxide nanoparticles (IONPs) are often combined with various classes of active materials such as inorganic and organic polymers, carbonaceous materials, surfactants, metals and metallic oxides, etc. to form magnetic nanocomposites. For instance, Abd-Elrahman reported the synthesis of iron oxide (IO)-polyaniline nanocomposite and utilised it for the electrochemical elimination of lead and cadmium ions from polluted water[13]. Raheem et al. developed a graphene oxide (GO) -iron oxide nanocomposite using *Myrtus communis* extract via a pulse laser ablation (PLA) and a hydrothermal method. The nanocomposite was utilised for the sensing of  $\text{NO}_2$  and  $\text{NH}_3$  gases[14]. A biphasic lithium iron oxide nanocomposite was developed by Ghosh et al., who used the system for EMI shielding due to its magnetic properties[15]. In this regard, a recently emerging class of active materials possessing multifunctionality that can be advantageously combined with IONPs are the hydrotalcite-type layered double hydroxides (LDHs).

LDHs are exemplary anionic layered materials that possess a host of unique physicochemical features such as high specific surface area, anion exchange abilities, stability in colloidal solutions, exfoliation ability, etc, due to which they have been successfully utilised as multifunctional materials in a multitude of applications such as water treatment, biomedics, energy storage, sensing, etc. The presence of positively charged layers composed of conjoined  $M(OH)_6$  octahedra ( $M$  = divalent and trivalent metal cation, OH = hydroxyl group) in the lamellar framework renders them as excellent active materials for usage in various avenues. Since LDHs can be synthesized with relative ease, and they exhibit high chemical and thermal stability and pH buffering abilities, the use of LDHs in various fields been previously reported. For example, Tao et al. synthesized a hybrid CoNi-LDH having both crystalline and amorphous character, and utilised it for the fabrication of a supercapacitor[16]. The asymmetric supercapacitor exhibited excellent high areal energy density and areal capacitance. In another study, Li et al. prepared  $Ni_{0.67}V_{0.33}$ -LDH and integrated it with aminoxy radical to form an electrocatalyst for the electrochemical oxidation of primary alcohols to aldehydes[17]. Furthermore, the use of transition metals in LDHs takes their catalytic prowess one step further due to the variable oxidation states, redox behaviour, and unique geometrical and electrochemical attributes of transition metals. But in spite of all these advantages, the main issues encountered during the usage of LDHs are their high aggregation tendencies that lead to reduced catalytic activity, and the difficulty in separation from the dispersion medium that inadvertently contributes to low material performance. An innovative and revolutionary solution to overcome these drawbacks is to combine LDHs with magnetic nanoparticles to form magnetic nanocomposites.

As a consequence of nanocomposite formation, synergistic interactions come into effect between the iron cation and the cations of LDH lattice, which in turn leads to enhanced catalytic abilities. Additionally, nanocomposite formation prevents aggregation or restacking of exfoliated LDH layers, while also facilitating faster ion diffusion and improving robustness of the catalyst. The combination of LDH with IONPs also provides some degree of control over the size and shape of the IONPs. Therefore, LDH-functionalised IONPS are the perfect choice for use in catalytic

applications since they combine the several advantageous features of LDHs (facile synthesis, high surface area, abundance of active sites, adsorption ability, good dispersibility and exfoliation ability, excellent catalytic ability, benign nature, biocompatibility) with that of IONPs (economical synthesis, magnetic nature, easy separability, resistance to oxidation, low toxicity, ease of functionalisation, good biodegradability). Consequentially, these LDH-IONP nanocomposites are ideal for the construction of a multifunctional platform that can be used to achieve maximum output of performance with minimum input required for their separation from various media since it can be easily achieved by the use of external magnetic field[18,19].

Furthermore, during the process of nanocomposite formation, pristine, uncoated IONPs often tend to oxidize readily in air, thereby losing their magnetic properties and subsequently facing problems in functionalisation with LDHs. Their handling is also often deemed to be quite cumbersome due to high agglomeration tendency of IONPs by virtue of their magnetic interactions. Therefore, in order to reduce structural degradation and maximise IONP stability, surface modifiability while also reducing particle agglomeration, protection of IONP surface with silica ( $\text{SiO}_2$ ) is generally preferred due to its benign nature. The silica coating enhances their colloidal stability, and also safeguards their external surface against several degradative chemical phenomena such as oxidation, leaching, and corrosion under harsh environments. The silanol ( $\text{Si-OH}$ ) groups of  $\text{SiO}_2$  also act as functionalisation sites, thereby enabling the adherence of LDH layers onto their surface to attain stable, biocompatible, and tunable nanostructures. Based on this premise, these composites can prove to be beneficial for use in catalysis, since the availability of abundant active sites and their magnetic separability render them as the ideal catalyst that may be profitably used in the field of wastewater remediation[20].

This knowledge can prove to be important for combating increasing levels of water pollution that are a consequence of the explosive growth in agriculture and industrialisation in recent years. Contamination of freshwater sources by the uninhibited release of toxin-laden effluents, especially dyes and nitroarene compounds (NACs), into water bodies aggravates the already existing global water crisis[21]. Specifically, dyes such as rhodamine B and NACs including *p*-NP that are widely used

in the textile, food, paper, and leather industries need immediate absolution due to their carcinogenic and mutagenic characteristics and resistance to bacterial action. In particular, Rhodamine B, a cationic dye belonging to the xanthene family, is renowned for its strong absorption and fluorescence within the visible region of the electromagnetic spectrum. The uniquely high photostability, intense emission, and fluorescent behaviour of this dye make it highly valuable in applications such as bioimaging, fluorescence microscopy, and laser technologies[22]. Additionally, features such as vivid coloration and excellent dyeability have led to its extensive use in the textile and cosmetic industries. However, the high chemical resilience of Rhodamine B contributes to its widespread use, that inadvertently culminates in contribution to water pollution levels. Fortunately, researchers have tried to keep pace with ever-increasing water pollution levels by developing efficient solutions and methodologies to combat this issue and evade its impact on the environment[23].

The treatment of pollutants with  $\text{NaBH}_4$  and catalyst to achieve their degradation is a promising technique that is focused on chemically reducing toxin molecules to their simple, benign and non-toxic derivatives or breaking them down to form  $\text{H}_2\text{O}$  and  $\text{CO}_2$  without resulting in the formation of secondary pollutants. But from the perspective of profitable usability, the inevitable problem of catalyst separation needs to be addressed. LDH-IONP nanocomposites hold the potential to provide solutions to all problems that are faced with existing catalytic materials since they fulfil all the criteria for ideal catalysts while also providing the added bonus of easy and cost-effective synthesis, and easy recoverability using an external magnetic field.

In literature, several reports have documented the use of LDHs and their various composites as catalysts, and others have described their use for wastewater remediation[24–27]. However, based on extensive literature survey, it was deduced that the synthesis of LDH/IONP nanocomposites and their use for azo dye and NAC degradation remains severely underexplored. Therefore, the present study describes the facile and eco-friendly synthesis of a magnetically separable hybrid catalyst composed of  $\text{ZnCuNi-LDH}$  and IONPs. In order to maximise the advantages of this catalyst,  $\text{SiO}_2$  was utilised to achieve maximum adherence of LDH layers onto the IONPs. Further, the synthesized nanocomposite was applied as a co-catalyst alongside

NaBH<sub>4</sub> for the hydrogenation of *p*-NP and the reduction of cationic rhodamine B (RhB) dye. The nanocomposite exhibited good catalytic ability for the reduction of dye as well as NAC, and was also easily separated from the reaction medium with the help of an external magnet.

## 7.2 Materials and Methods

### 7.2.1 Materials

Zinc acetate dihydrate Zn(CH<sub>3</sub>COO)<sub>2</sub>·2H<sub>2</sub>O (Merck, 98.0% purity), copper acetate monohydrate Cu(CH<sub>3</sub>COO)<sub>2</sub>·H<sub>2</sub>O (Merck, 98.0% purity), hydrogen peroxide H<sub>2</sub>O<sub>2</sub> (Merck, 30%), nickel acetate tetrahydrate Ni(CH<sub>3</sub>COO)<sub>2</sub>·4H<sub>2</sub>O (CDH, 98.00% purity), ferric chloride FeCl<sub>3</sub> (Merck), tetraethyl orthosilicate Si(OC<sub>2</sub>H<sub>5</sub>)<sub>4</sub> (Sigma-Aldrich, ≥99.0% (GC)), NaBH<sub>4</sub> (Sigma Aldrich, ≥98.00%), *p*-Nitrophenol (GLR chemicals, 98.00%), Rhodamine B (Merck) were of analytical grade unless otherwise stated, and were used as received without purification. *Cleome viscosa* seeds were obtained from local market in Haldwani, Uttarakhand. Table 7.1 gives information about the structure, formulas, and  $\lambda_{max}$  of model pollutant molecules employed in this study.

**Table 7.1** Structure and formula of model pollutants employed in the study.

Model Pollutant	Structure	$\lambda_{max}$ (nm)	Molecular Formula
<i>p</i> -Nitrophenol		320	C <sub>6</sub> H <sub>5</sub> NO <sub>3</sub>
Rhodamine B		552	C <sub>28</sub> H <sub>31</sub> ClN <sub>2</sub> O <sub>3</sub>

### 7.2.2 Preparation of *Cleome viscosa* seed extract

5.0 g *Cleome viscosa* seeds were washed properly to remove any impurities, following which they were added to 100 mL distilled water in a beaker and heated for 5 hours.

Then the solution was filtered and the aqueous extract thus obtained was further used for nanoparticle synthesis. The schematic representation of the synthesis of *Cleome viscosa* seed extract is presented in Figure 7.1.

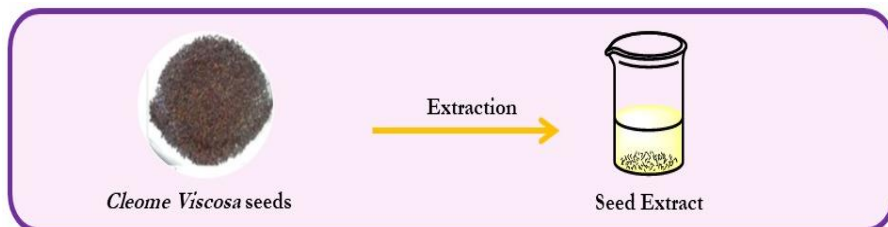


**Figure 7.1** Schematic representation of synthesis of seed extract and  $\text{Fe}_3\text{O}_4$  NPs.

### 7.2.3 Synthesis of Iron Oxide nanoparticles

The synthesis of magnetic iron oxide nanoparticles was achieved through the phytonanofabrication method[28]. Herein, 0.01 M aqueous solution of  $\text{FeCl}_3$  was prepared by stirring appropriate amount of  $\text{FeCl}_3$  in 10 mL distilled water for 15 minutes. On complete dissolution, the solution was allowed to boil for 15 minutes, following which 5 mL of *Cleome viscosa* seed extract was added to it. Colour of the reaction mixture instantly turned to dark brown, and it was followed by the appearance of brown precipitate, indicating the formation of IONPs. Subsequently, the solution was filtered, and the obtained precipitates were washed with distilled water and acetone, followed by complete drying in oven at 60°C. The schematic representation of the synthesis of IONPs using *Cleome viscosa* seed extract is presented in Figure 7.2.

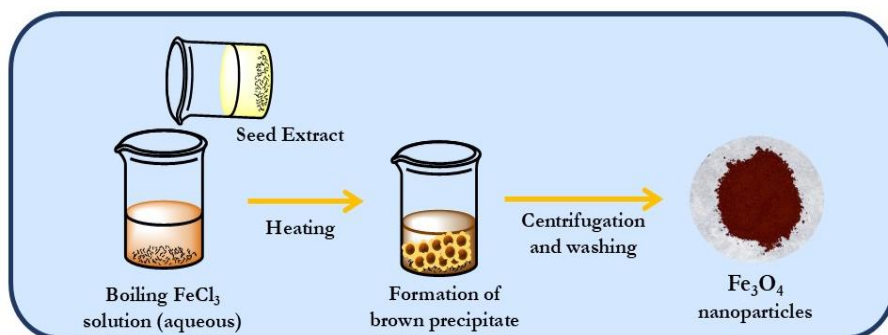


**Figure 7.2** Schematic representation of synthesis of  $\text{Fe}_3\text{O}_4$  NPs using seed extract.

### 7.2.4 Synthesis of $\text{SiO}_2$ coated IONPS

The facile Stober's method was used for coating IONPs with  $\text{SiO}_2$ . In this method, green synthesized IONPs were dispersed in ethanol-distilled water mixture by ultrasonication for 1 hour. After 1 hour, 1 mL TEOS was added to the dispersion and it was further sonicated for 30 minutes. Then, 0.5 mL ammonia solution was added to

the reaction mixture, and it was heated with constant stirring to obtain  $\text{SiO}_2$  coated IONPs. Finally, the product was filtered, washed with distilled water and acetone, and completely dried in the oven. The schematic representation of the synthesis of  $\text{SiO}_2$ -coated IONPS is presented in Figure 7.3.



**Figure 7.3** Schematic representation of synthesis of seed extract and  $\text{Fe}_3\text{O}_4$  NPs.

#### 7.2.5 Synthesis of magnetically separable $\text{Fe}_3\text{O}_4/\text{SiO}_2/\text{ZnCuNi-LDH}$ composite

$\text{ZnCuNi-LDH}$  was prepared using previously reported acid hydrolysis route. The facile electrostatic self-assembly method was employed for the fabrication of magnetically separable  $\text{Fe}_3\text{O}_4/\text{SiO}_2/\text{ZnCuNi-LDH}$  composite. To obtain this product, initially,  $\text{ZnCuNi-LDH}$  was dispersed in methanol, and  $\text{SiO}_2$  coated  $\text{Fe}_3\text{O}_4$  NPs were dispersed in a methanol-water mixture by means of ultrasonication. After one hour of agitation, the LDH dispersion was added to the dispersion of  $\text{SiO}_2$ -coated  $\text{Fe}_3\text{O}_4$  NPs while stirring the reaction mixture continuously. The resulting mixture was stirred at room temperature until the methanol and water vapourised completely, and a brown-colored dried product was obtained. The product was further dried in the oven at  $60\text{ }^\circ\text{C}$ . The schematic representation of the synthesis of  $\text{Fe}_3\text{O}_4/\text{SiO}_2/\text{ZnCuNi-LDH}$  composite is presented in Figure 7.4.

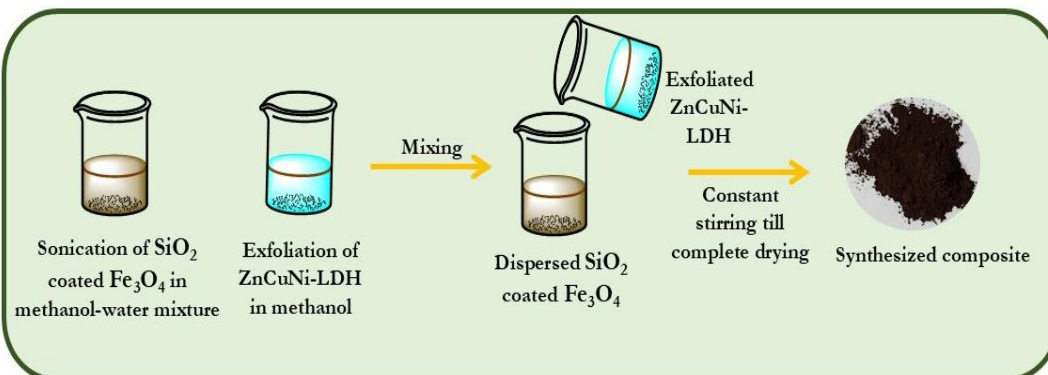


**Figure 7.4** Schematic representation of synthesis of  $\text{Fe}_3\text{O}_4/\text{SiO}_2/\text{ZnCuNi-LDH}$  composite.

### 7.2.6 Instrumentation

Crystallographic properties of the sample were studied by the use of Powder X-ray diffraction (PXRD) diffractograms collected using a high-resolution Bruker diffractometer (D8 Discover) using Cu K $\alpha$  radiation. Data was recorded at 298 K over the range of  $2\theta = 5-85^\circ$  at scan rate of 1.0 s/step and step size 0.02. The various functional group present in synthesized material were analyzed using Fourier transform infrared (FTIR) spectrum collected with the help of a Perkin Elmer 2000 Fourier-transform infrared spectrometer by the KBr disk technique. The morphological features and element compositions of the synthesized samples were studied using SEM imaging, EDX analysis and elemental mapping recorded on a Zeiss Gemini SEM microscope.

### 7.2.7 Evaluation of Catalytic Activity

The hydrogenation of *p*-NP to *p*-AP and degradation of RhB by NaBH<sub>4</sub> is thermodynamically achievable but it is kinetically sluggish due to electrostatic repulsion between the intermediate anions and BH<sub>4</sub><sup>-</sup>. Hence, an efficient catalyst is required to increase the speed of the conversion reaction. Therefore, in order to investigate the efficacy of Fe<sub>3</sub>O<sub>4</sub>/SiO<sub>2</sub>/ZnCuNi-LDH as a catalytic agent, catalytic degradation of *p*-NP and Rhodamine B dye was carried out. For this purpose, solutions of NaBH<sub>4</sub> (100 mM), *p*-NP (10 mM) and RhB (100 mg L<sup>-1</sup>) were prepared using distilled water, and further solutions were prepared by diluting the stock solutions as required. The reaction progress was monitored by means of visual examination and by using a UV-Vis spectrophotometer, and the appearance and disappearance of absorption bands in the time-dependent UV-Vis spectrum signified the degradation of model molecules by the catalytic action of synthesized catalyst.

To accomplish the hydrogenation of *p*-NP, initially, 1 mL of 100 mM NaBH<sub>4</sub> solution and 1 mL aqueous solution of *p*-NP (1 mM) were mixed well to ensure homogeneity. The absorption maxima of intermediary *p*-nitrophenolate ions appearing at  $\lambda_{max} = 400$  nm was recorded. Consequently, 0.001 g catalyst was added to the above mixture and time-dependent UV-Vis spectra was recorded in the range of 200-600 nm at fixed time intervals using a Shimadzu UV-Vis spectrophotometer. The reaction kinetics were determined by analysing the change in intensity of absorption band at  $\lambda_{max} = 400$  nm at

a time interval of one minute till the complete decolourization of solution and disappearance of the band at 400 nm.

The reduction of RhB by the synthesized composite using NaBH<sub>4</sub> as a reductant was studied by mixing RhB solution (100 mg L<sup>-1</sup>, 1 mL) with freshly prepared NaBH<sub>4</sub> solution (100 mM, 1 mL) and distilled water (1 mL). Following this, the composite catalyst (0.001 g) was added to the reaction mixture, and the progress of reaction was assessed by measurement of the absorbance at  $\lambda_{max} = 552$  nm at one-minute intervals till the solution was completely decolourised and absorbance maxima disappeared completely.

The percentage degradation efficiency of model molecules was calculated using Equation 7.1:

$$\text{Percentage degradation} = \frac{(C_o - C_t)}{C_o} \times 100 \quad (7.1)$$

where C<sub>o</sub> and C<sub>t</sub> denote the initial and terminal concentrations of NAC and azo dyes.

### 7.2.8 Reusability and Recyclability

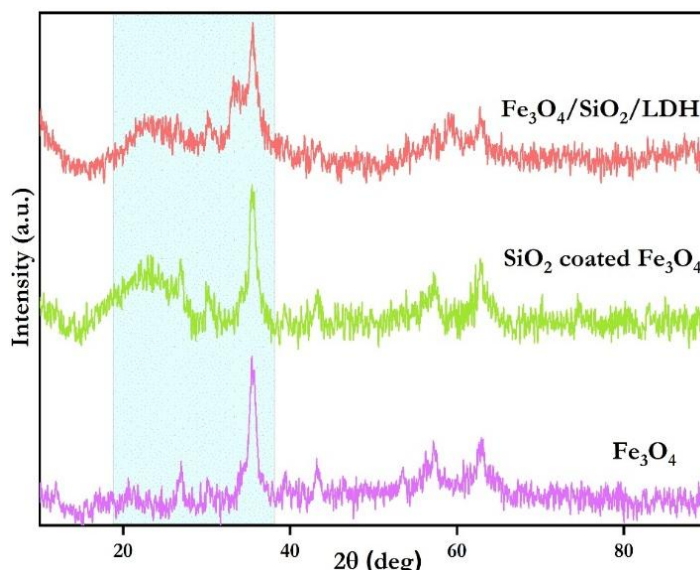
The reusability and recoverability of Fe<sub>3</sub>O<sub>4</sub>/SiO<sub>2</sub>/ZnCuNi-LDH for reduction of *p*-NP and RhB was investigated for five cycles. After each reduction reaction, catalyst was recovered and washed twice with distilled water, dried at 60°C, and then used for subsequent catalytic cycles.

## 7.3 Results and Discussion

### 7.3.1 Structural and Morphological Analysis

The crystal structures of synthesized samples were investigated using PXRD, and the diffractograms are displayed in Figure 7.5. The PXRD spectrum of IONPs exhibited the characteristic peaks of iron oxide nanoparticles that were well-directed to face-centered cubic Fe<sub>3</sub>O<sub>4</sub> (JCPDS No. 19-0629)[29]. The appearance of the typical Fe<sub>3</sub>O<sub>4</sub> pattern and the absence of any extra peaks indicated the formation of nanoparticles having good purity and crystallinity using the phytonanofabrication method[30]. Meanwhile, the PXRD pattern of ZnCuNi-LDH presented a series of diffraction peaks that can be indexed to the characteristic basal (002), (003), (004) and non-basal planes

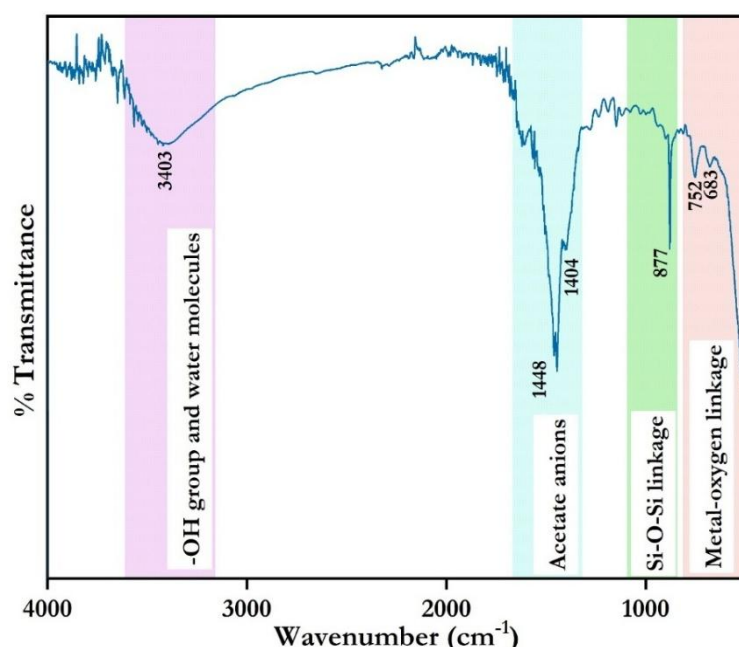
(101), (006), and (103) of layered materials possessing a turbostratic arrangement[31]. This typical pattern having sharp and highly intense reflection at lower  $2\theta$  angle and symmetric, low intensity reflections at higher  $2\theta$  angle corroborated the successful formation of ZnCuNi-LDH with acetate anion present in the interlayer region. In case of SiO<sub>2</sub>-coated Fe<sub>3</sub>O<sub>4</sub>, the appearance of the characteristic peaks of Fe<sub>3</sub>O<sub>4</sub>, along with an additional broad reflection centered around 23° that was ascribed to amorphous silica, corroborated the functionalisation of SiO<sub>2</sub> onto the surface of Fe<sub>3</sub>O<sub>4</sub> NPs[32]. In the PXRD pattern of Fe<sub>3</sub>O<sub>4</sub>/SiO<sub>2</sub>/ZnCuNi-LDH composite, the characteristic peaks of Fe<sub>3</sub>O<sub>4</sub> and SiO<sub>2</sub> were evident, but the characteristic peaks of LDH were not visible, owing to the exfoliation and subsequent anchoring of LDH on SiO<sub>2</sub> coated Fe<sub>3</sub>O<sub>4</sub>. The splitting in the peak appearing around 34° was attributed to the introduction of exfoliated LDH layers into the SiO<sub>2</sub> coated Fe<sub>3</sub>O<sub>4</sub> nanostructure. Furthermore, the slight reduction in peak intensity on composite formation may be attributed to structural disorder in the lattice. Therefore, these observations suggest the successful formation of Fe<sub>3</sub>O<sub>4</sub>/SiO<sub>2</sub>/ZnCuNi-LDH composite.



**Figure 7.5** Comparative plot of PXRD patterns of ZnCuNi-LDH, Fe<sub>3</sub>O<sub>4</sub>, SiO<sub>2</sub> coated Fe<sub>3</sub>O<sub>4</sub>, and Fe<sub>3</sub>O<sub>4</sub>/SiO<sub>2</sub>/ZnCuNi-LDH.

The FTIR spectral analysis of magnetic Fe<sub>3</sub>O<sub>4</sub>/SiO<sub>2</sub>/ZnCuNi-LDH composite is illustrated in Figure 7.6. The intense and broad absorption band centered around 3403 cm<sup>-1</sup> was attributed to the O-H stretching vibration of the hydroxyl groups present on

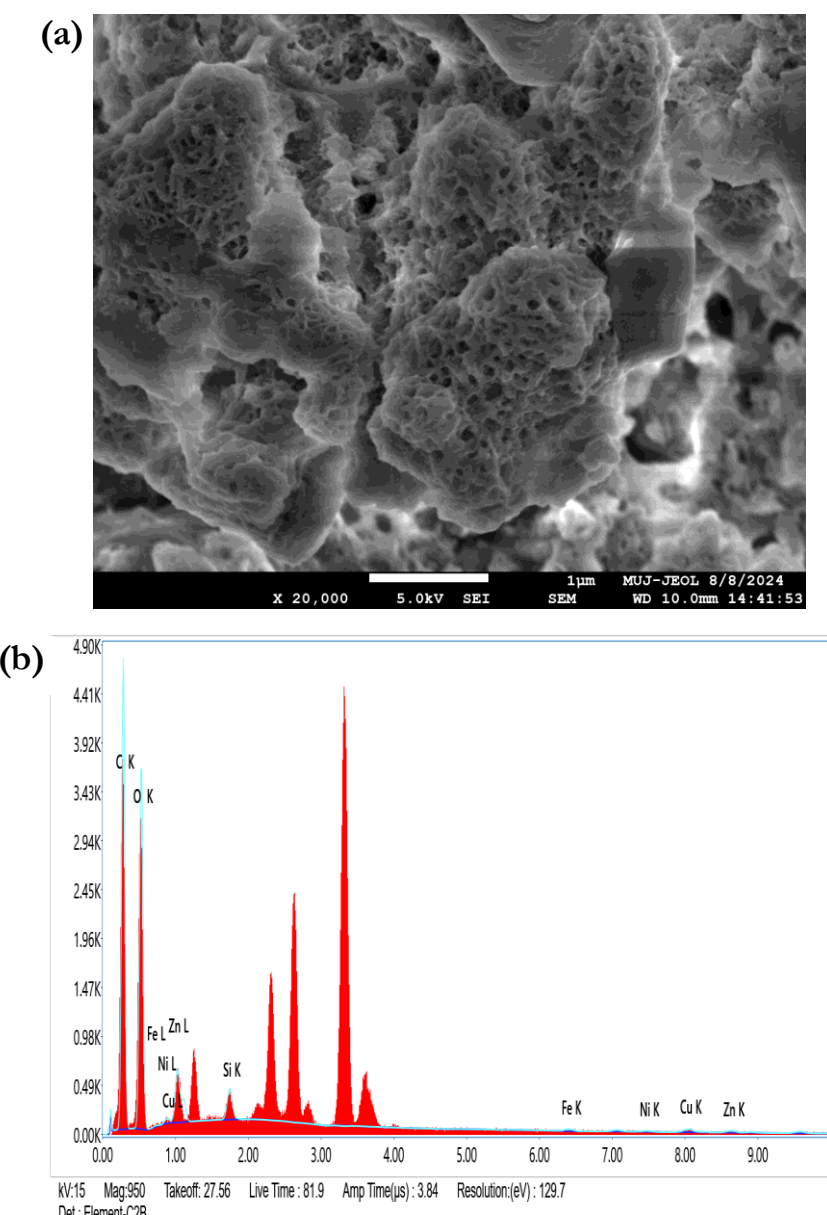
the LDH layer surface. The fingerprint bands of acetate anions present along with ZnCuNi-LDH appeared at  $1448\text{ cm}^{-1}$  and  $1404\text{ cm}^{-1}$  and were ascribed to the asymmetric and symmetric vibration modes of the  $\text{CO}_2$ -moiety[33]. The spectrum also showed a sharp band at  $877\text{ cm}^{-1}$  that corresponded to the vibration modes of the Si-O-Si bonds present in  $\text{SiO}_2$ [34]. The characteristic band at  $752\text{ cm}^{-1}$  arises due to the metal-oxygen linkages in ZnCuNi-LDH and the band at  $683\text{ cm}^{-1}$  corresponded to the stretch vibration of Fe–O bonds of the  $\text{Fe}_3\text{O}_4$  NPs. These results provide clear evidence for the successful formation of  $\text{Fe}_3\text{O}_4/\text{SiO}_2/\text{ZnCuNi-LDH}$ .



**Figure 7.6** FTIR spectrum of  $\text{Fe}_3\text{O}_4/\text{SiO}_2/\text{ZnCuNi-LDH}$ .

The structural and morphological attributes of the  $\text{Fe}_3\text{O}_4/\text{SiO}_2/\text{ZnCuNi-LDH}$  composite were studied using SEM-EDX and elemental mapping techniques. The SEM micrograph presented in Figure 7.7a illustrates irregular, aggregated particles composed of cubic  $\text{Fe}_3\text{O}_4$  NPs coated with rough and porous silica layer[20]. The SEM image indicated that the components of the composite do not exist independently in the lattice, and confirms the functionalisation of  $\text{Fe}_3\text{O}_4$  with  $\text{SiO}_2$ . Additionally, the lack of visibility of sheet-like morphology of ZnCuNi-LDH may be attributed to the exfoliation of the LDH layers. Therefore, in order to ascertain the presence of ZnCuNi-LDH in the lattice along with  $\text{Fe}_3\text{O}_4$  and  $\text{SiO}_2$ , EDX spectrum was recorded. The spectrum (Figure 7.7b) showed the presence of Fe, Si, Zn, Cu, Ni, C, and O elements

in the lattice, thereby confirming the successful formation the composite. Additionally, the element composition was confirmed using elemental mapping technique, and it illustrated the homogenous distribution of Fe, Si, Zn, Cu, and Ni elements throughout the lattice, thereby corroborating composite formation (Figure 7.7c). These results prove the successful synthesis of  $\text{Fe}_3\text{O}_4/\text{SiO}_2/\text{ZnCuNi-LDH}$  composite.



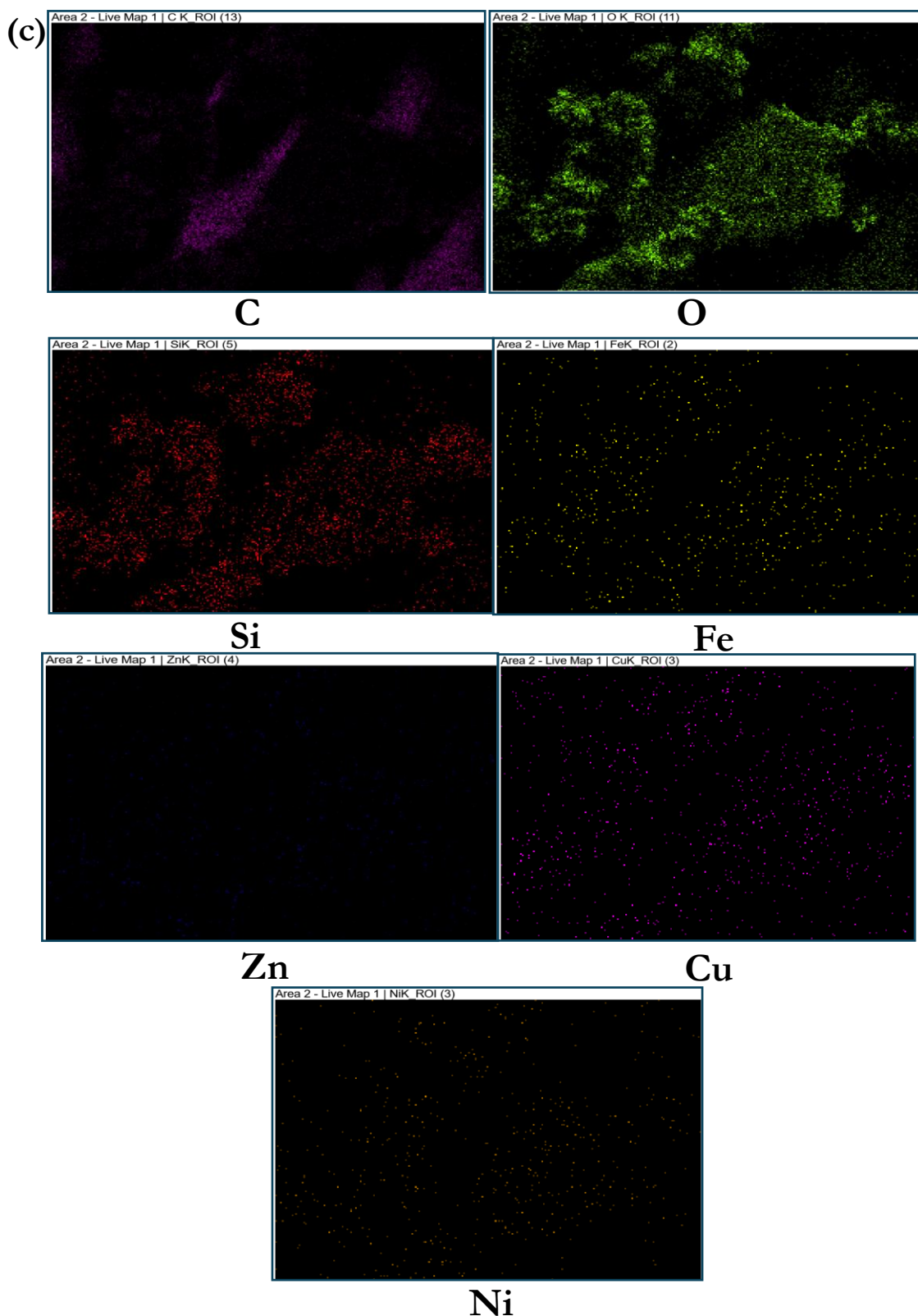


**Figure 7.7** (a) SEM micrograph, (b) EDX spectrum and (c) elemental mapping of  $\text{Fe}_3\text{O}_4/\text{SiO}_2/\text{ZnCuNi-LDH}$ .

### 7.3.2 Catalytic Activity

Catalytic degradation using  $\text{NaBH}_4$  with the assistance of a co-catalyst is a highly effective way to reduce contaminants without resulting in the production of secondary pollutants. Therefore, in the current study, the catalytic degradation of *p*-NP and RhB was studied as model reaction. The  $\text{NaBH}_4$ -assisted catalytic efficiencies of synthesized  $\text{Fe}_3\text{O}_4/\text{SiO}_2/\text{ZnCuNi-LDH}$  composite for *p*-NP and RhB reduction were examined using UV-Visible spectrophotometer. The progress of catalytic reaction was determined by observing the variation in absorbance of pollutant molecules solutions. Further, since  $\text{NaBH}_4$  (100 mM) solution was highly concentrated as compared to *p*-NP (1 mM) and RhB (100 mg L<sup>-1</sup>), the reaction rate was considered to be free of the influence of  $\text{BH}_4^-$  concentration. Hence, the hydrogenation of *p*-NP and reduction of RhB dye was considered to follow pseudo-first order kinetics, and is shown in Equation 7.2:

$$\ln\left(\frac{C_t}{C_0}\right) = K \quad (7.2)$$

Where K denotes rate constant, and  $C_0$  and  $C_t$  are the initial and final concentrations of chosen pollutants.

Since the evaluated molecules possessed distinct colours and yielded peaks in the visible region, reaction rate was calculated in terms of comparative absorptive intensity. Therefore, using Beer-Lambert's law (Equation 7.3)

$$A = \varepsilon Cl \quad (7.3)$$

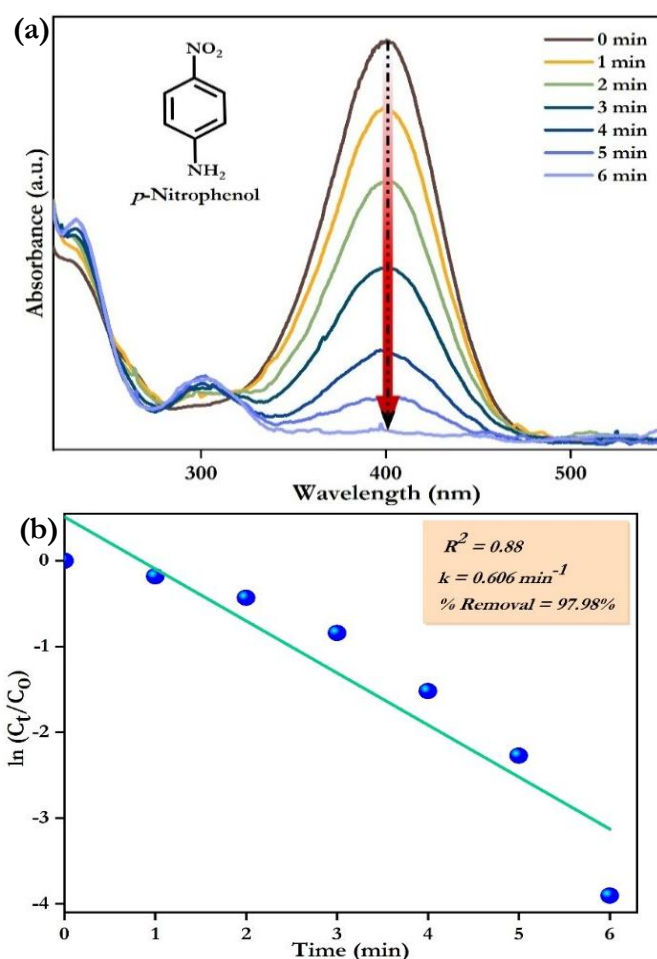
Kinetics of reaction are expressed in terms of absorption by Equation 7.4:

$$\ln\left(\frac{C_t}{C_0}\right) = \ln\left(\frac{A_t}{A_0}\right) = kt \quad (7.4)$$

Where  $A_0$  and  $A_t$  are the initial and final absorbance of NAC and dye.

In case of *p*-NP, when  $\text{NaBH}_4$  and *p*-NP are mixed, the appearance of an absorbance peak at  $\lambda_{max} = 400$  nm was observed that may be attributed to the formation of nitrophenolate ion, as seen in Figure 7.8a. On addition of synthesized composite catalyst, the peak at  $\lambda_{max} = 400$  nm started decreasing instantaneously, thereby

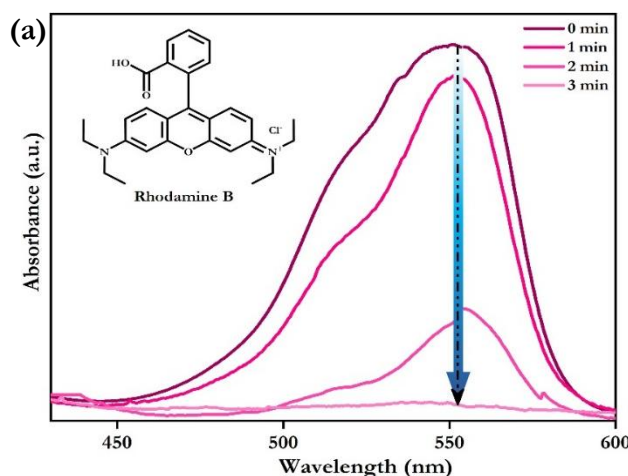
confirming the decrease in *p*-NP concentration as a result of the successful hydrogenation of the nitro group of *p*-NP. Meanwhile, a new peak appeared at 302 nm that may be indicative of the formation of *p*-AP as a hydrogenation product of *p*-NP. The complete disappearance of the peak at  $\lambda_{max} = 400$  nm suggested the rapid hydrogenation of *p*-NP. Furthermore, the appearance of isosbestic points at 224, 250, 280, and 316 nm gave evidence for the hypothesis that *p*-AP was the singular by-product formed on the hydrogenation of *p*-NP. The percentage hydrogenation of *p*-NP was evaluated using Eqn 7.1 and was found to be 97.98%. The rate of reaction (*k*) was evaluated to be  $0.606 \text{ min}^{-1}$  ( $R^2 = 0.88$ ) in accordance to pseudo-first order model (Figure 7.8b).



**Figure 7.8** (a) UV-Vis absorption spectrum and (b) linear fitting of pseudo-first kinetics model for the  $\text{NaBH}_4$  - assisted catalytic reduction of *p*-NP using  $\text{Fe}_3\text{O}_4/\text{SiO}_2/\text{ZnCuNi-LDH}$  composite.

In aqueous medium, Rhodamine B (RhB) exists in the ionic form ( $\text{RhB}^+$ ), and the oxidized form of RhB exhibits absorption maxima at  $\lambda_{max} = 552$  nm in UV-Vis absorption spectrum. By taking advantage of this feature, composite surface-catalyzed reduction of RhB was studied by recording the time-dependent UV-Vis absorbance spectra of the reaction mixture at stipulated time intervals. The UV-Vis absorbance vs wavelength plot for the catalytic reduction of cationic RhB is presented in Figure 7.9a. On addition of  $\text{NaBH}_4$  to the RhB solution, no changes in the peak intensity and position were observed. Furthermore, there was no change in color of the solution. However, on addition of catalyst, an instantaneous change was observed in the color of the reaction mixture along with the reduction in the intensity of peak present at  $\lambda_{max} = 552$  nm. The peak intensity decreased rapidly until its eventual disappearance after 3 mins, and the complete decolourisation of the pink-coloured reaction mixture signified the transformation of pink RhB to colorless leuco-rhodamine B. Percentage degradation of dye was evaluated using Eqn 7.1, and was calculated to be 97.69%. The rate constant  $k$ , obtained by linearly regressing experimental data to the pseudo first order model, was evaluated to be  $1.261 \text{ min}^{-1}$  ( $R^2 = 0.85$ ) (Figure 7.9b).

The dissipation of absorbance maxima appearing at  $\lambda_{max} = 552$  nm in the recorded absorbance spectra gave evidence for the rapid degradation of RhB. The cohesive action of  $\text{NaBH}_4$  and  $\text{Fe}_3\text{O}_4/\text{SiO}_2/\text{ZnCuNi-LDH}$  composite reduced the xanthene core of RhB, thereby disturbing the extended  $\pi$  - conjugation of the dye that is responsible for its characteristic pink colour, leading to decolourisation of reaction mixture due to saturation of conjugated system and resulting in the conversion of RhB to its non-fluorescent, and colourless leuco form.



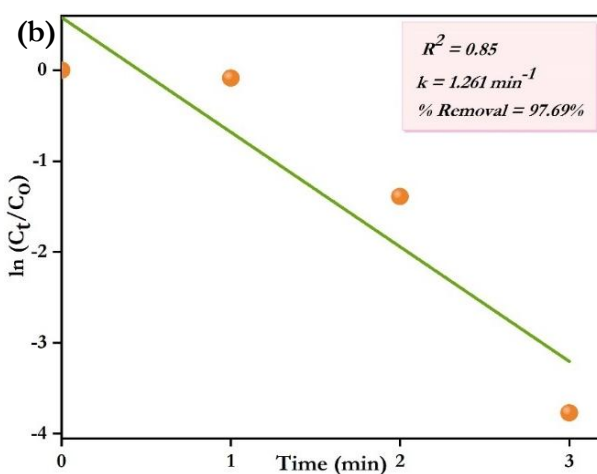


**Figure 7.9** (a) UV-Vis absorption spectrum and (b) linear fitting of pseudo-first kinetics model for the  $\text{NaBH}_4$  - assisted catalytic reduction of *p*-NP using  $\text{Fe}_3\text{O}_4/\text{SiO}_2/\text{ZnCuNi-LDH}$  composite.

### 7.3.3 Recyclability and Catalyst Recovery

In addition to high catalytic efficacy, reusability and recoverability are two major parameters that govern commercial utility and therefore must be considered when evaluating the applications of catalysts, since they can bring about a drastic reduction in material and method costs. The majority of conventionally employed catalysts possess low reusability and get deactivated after one or two reaction cycles. Therefore, designing robust catalysts with good recyclability and recoverability should be prioritised in order to obtain the maximum benefits from synthesized materials while minimising wastage of resources. Therefore, the recyclability of  $\text{Fe}_3\text{O}_4/\text{SiO}_2/\text{ZnCuNi-LDH}$  composite for reduction of *p*-NP and RhB was assessed in this study. The study was carried out for five consecutive cycles wherein near complete reduction of the model molecules was achieved. The results presented in Figure 7.10a indicate that the composite catalyst demonstrated almost similar catalytic activity in first two cycles, but a small decrease from third cycle was observed, that may be the consequence of catalyst due to repeated use and adsorption of reactants. The slight decrease in removal efficacy may also be the consequence of the loss and agglomeration of catalytic material during the recovery and reuse stages. Inspite of this, the catalyst sustained approximately 90% degradation efficacy for the reduction of both *p*-NP and RhB even after 5 cycles.

Furthermore, the magnetic separability of  $\text{Fe}_3\text{O}_4/\text{SiO}_2/\text{ZnCuNi-LDH}$  composite was also evaluated by placing a magnet near the cuvette at the end of the catalytic reduction reaction. The photographic evidence of the magnetic separation process of  $\text{Fe}_3\text{O}_4/\text{SiO}_2/\text{ZnCuNi-LDH}$  composite under the influence of an external magnetic field is presented in Fig 7.10b. On placing the magnet near the cuvette, the prompt and rapid separation of the catalyst from the reaction medium was observed, following which the reaction mixture became clear, thereby demonstrating the high magnetic sensitivity of  $\text{Fe}_3\text{O}_4/\text{SiO}_2/\text{ZnCuNi-LDH}$  composite. Based on these results, it was inferred that  $\text{Fe}_3\text{O}_4/\text{SiO}_2/\text{ZnCuNi-LDH}$  composite is a robust catalyst that can be easily recovered and utilized for consecutive catalytic cycles without any significant decrease in catalytic performance.

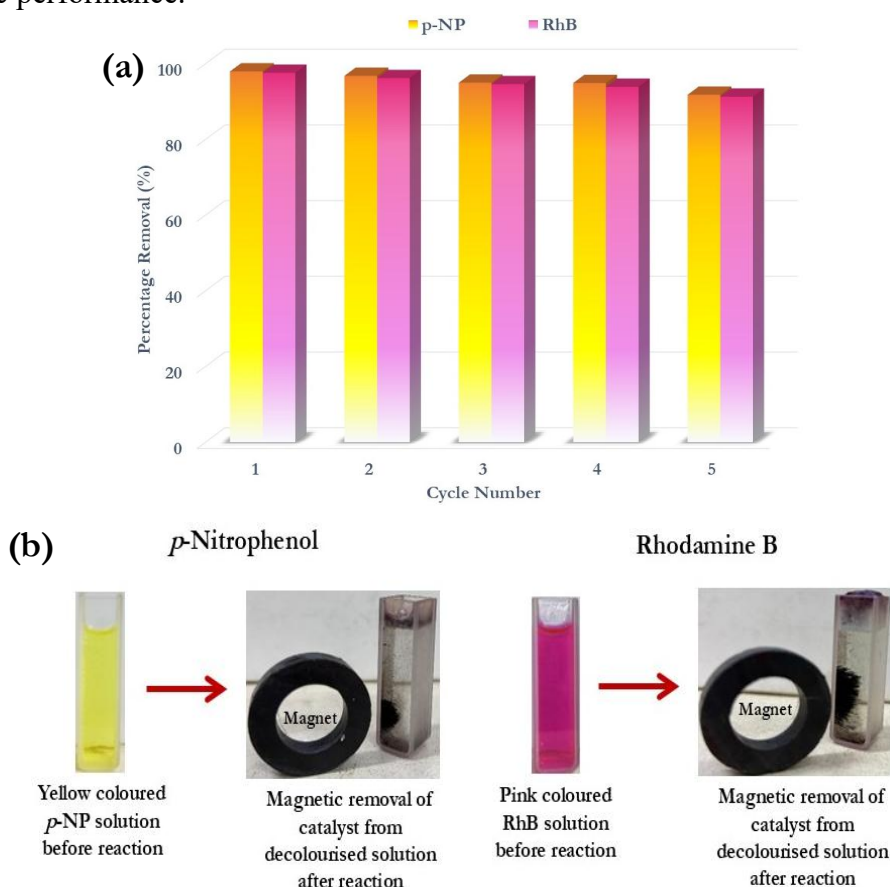


**Figure 7.10** (a) Recyclability studies of  $\text{Fe}_3\text{O}_4/\text{SiO}_2/\text{ZnCuNi-LDH}$  composite for catalytic reduction of *p*-NP and RhB (b) Magnetic separation of  $\text{Fe}_3\text{O}_4/\text{SiO}_2/\text{ZnCuNi-LDH}$  composite after reduction of *p*-NP and RhB.

### 7.3.4 Comparison with Reported Catalysts

The superior catalytic activity of  $\text{Fe}_3\text{O}_4/\text{SiO}_2/\text{ZnCuNi-LDH}$  for the catalytic degradation of *p*-NP and RhB is highlighted on being compared with those previously reported catalysts (Table 7.2). Although several reports describing reduction of *p*-NP and RhB are available in literature, majority of them contain complex synthesis methods, use of toxic precursors and/or long time periods for near-complete reduction of pollutants. Meanwhile,  $\text{Fe}_3\text{O}_4/\text{SiO}_2/\text{ZnCuNi-LDH}$  reported in this work has been synthesized using low-cost, facile and environment-friendly methodology that aligns with the principles of green chemistry. It also exhibits equal or better catalytic activities than the majority of reported catalysts within shorter reaction times, with the bonus of easy separability. It is also critical to highlight the fact that while ZnCuNi-LDH precursor was able to reduce only anionic dyes,  $\text{Fe}_3\text{O}_4/\text{SiO}_2/\text{ZnCuNi-LDH}$  composite reduced cationic RhB dye efficaciously within a short period of time. Thus, it may be inferred that the synthesized  $\text{Fe}_3\text{O}_4/\text{SiO}_2/\text{ZnCuNi-LDH}$  composite is a one-of-its-kind novel material having superior catalytic properties along with easy separability.

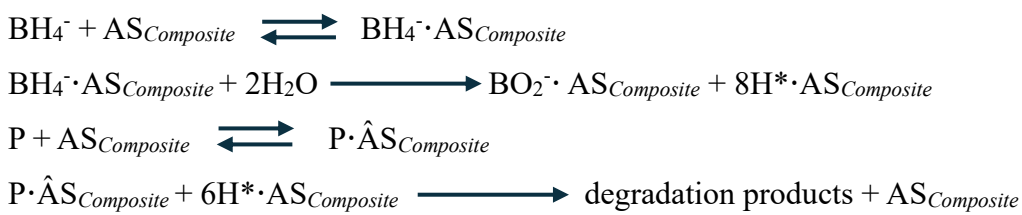
**Table 7.2** Comparison of catalytic activity of  $\text{Fe}_3\text{O}_4/\text{SiO}_2/\text{ZnCuNi-LDH}$  composite for reduction of *p*-NP and RhB with previously reported catalysts.

Pollutant	Catalyst	Rate constant ( <i>k</i> ) (min <sup>-1</sup> )	Reaction Time	Reference
<i>p</i> -NP	Pd/NiFe-LDH	0.37	9	[35]
	Ag NPs	0.35	10	[36]
	platinum-rhodium alloyed nano- multipods	0.209	20	[37]
	ZnCuNi-LDH	1.058	4	[38]
	$\text{Fe}_3\text{O}_4/\text{SiO}_2/\text{ZnCuNi-}$ LDH	0.606	6	This work
RhB	CoFe <sub>2</sub> O <sub>4</sub> -P4VP@Ag NPs	0.260	20	[39]

platinum-rhodium alloyed nano- multipods	0.354	14	[37]
Fe <sub>3</sub> O <sub>4</sub> @PS@Ag	0.809	4	[40]
Fe <sub>3</sub> O <sub>4</sub> /SiO <sub>2</sub> /ZnCuNi- LDH	1.261	3	This work

### 7.3.5 Postulated Mechanism

The catalytic hydrogenation of *p*-NP and reduction of RhB is presumed to follow the Langmuir-Hinshelwood mechanism that has been widely discussed in literature (Figure 7.11)[41]. In accordance with the Langmuir-Hinshelwood model, initially, the NaBH<sub>4</sub> species breaks down into Na<sup>+</sup> and borohydride (BH<sub>4</sub><sup>-</sup>) ions. These BH<sub>4</sub><sup>-</sup> anions are adsorbed on the surface of Fe<sub>3</sub>O<sub>4</sub>/SiO<sub>2</sub>/ZnCuNi-LDH composite and break down further into BO<sub>2</sub><sup>-</sup> and H<sub>2</sub>. The subsequent formation of metal-hydride complex that is the active hydrogen species enables the transfer of H<sub>2</sub> and electrons to the -NO<sub>2</sub> group. Therefore, *p*-nitrophenolate molecules, adsorbed on the surface of composite were hydrogenated by the active hydrogen species to produce a stable intermediate *p*-hydroxylaminophenol and *p*-aminophenol as the final product. Consequentially, desorption of the products occurs from the surface of composite. The catalytic process can be outlined in the form of reactions as follows:



where AS<sub>Composite</sub> represents the active sites (AS) present on composite surface, BH<sub>4</sub><sup>-</sup>·AS<sub>Composite</sub> represents the borohydride anions adsorbed on composite surface, H<sup>·</sup>·AS<sub>Composite</sub> denotes the active hydrogen species adsorbed on the surface, P represents the pollutant molecules, and P·AS<sub>Composite</sub> denotes pollutant molecules adsorbed on composite surface[42].

For the reduction of RhB dye, the catalytic reaction can be explained on basis of an electrochemical process. The redox activity of the ZnCuNi-LDH supported on the SiO<sub>2</sub>

coated  $\text{Fe}_3\text{O}_4$  helps in the relay of electrons from the electron donating  $\text{BH}_4^-$  to the electron accepting RhB molecules. First,  $\text{BH}_4^-$  and RhB molecules diffuse from aqueous solution onto the composite surface and hydride moiety is produced from  $\text{BH}_4^-$ . The transfer of electrons from hydride to the xanthene core of RhB molecules, facilitated by ZnCuNi-LDH supported on  $\text{SiO}_2$  functionalised  $\text{Fe}_3\text{O}_4$ , disrupts the extended  $\pi$ -conjugation in the xanthene core, leading to saturation and reduction of RhB, that is observed as the decolourisation of dye solution.

It is important to note that the homogenously dispersed constituent metals of ZnCuNi-LDH act as active sites for catalytic reaction and play the critical role of storing electrons after hydride formation and transfer of electrons from  $\text{H}_2$  to ZnCuNi-LDH. The combination of LDH with  $\text{Fe}_3\text{O}_4$  contributes to enhanced surface area and active site density, and the synergistic electronic interactions between  $\text{Fe}_3\text{O}_4$  and ZnCuNi-LDH facilitates rapid electron transfer and charge separation for enhanced catalytic activities. Additionally,  $\text{SiO}_2$  coated  $\text{Fe}_3\text{O}_4$  acts as a magnetic support for the active catalytic sites, and holds the LDH molecules for catalytic reaction while also aiding the easy recovery of the catalyst from the reaction medium on completion of reaction. Therefore, synergy between the constituents of the composite results in a highly efficient, stable and easily retrievable catalyst that can be applied successfully in catalysis and environmental remediation applications.



**Figure 7.11** Postulated mechanism for the  $\text{NaBH}_4$  - assisted catalytic degradation of *p*-NP and RhB using  $\text{Fe}_3\text{O}_4/\text{SiO}_2/\text{ZnCuNi-LDH}$  composite.

The observations of this study, *vis-a-vis* the catalytic performance, stability, reusability and recovery from reaction medium of  $\text{Fe}_3\text{O}_4/\text{SiO}_2/\text{ZnCuNi-LDH}$  composite clearly

outline that this composite can play a pivotal role in the field of advanced heterogenous catalysis, especially for wastewater remediation amongst other environmental concerns. The coupling of ZnCuNi-LDH with  $\text{Fe}_3\text{O}_4$  brings about synergistic effects in the composite, and endow the composite with high catalytic efficiency. Consequentially, the facile green synthesis, economic cost, exemplary catalytic activity, and good stability and recoverability of  $\text{Fe}_3\text{O}_4/\text{SiO}_2/\text{ZnCuNi-LDH}$  composite favours its use over conventional catalysts that are currently used in large-scale settings.

#### 7.4 Conclusion

At present, the majority of materials being used for catalytic degradation of pollutants are in powder form. But even though these materials exhibit incredible performances as catalysts, their separation from reaction media as well as their recyclability are complex issues that need to be addressed in order to achieve their profitable usage in commercial applications. Therefore, the development of novel catalysts that can be recovered using facile and efficient recovery processes is garnering immense attention. In this regard, our study described the facile synthesis of a magnetically separable catalyst based on ZnCuNi-LDH using the electrostatic self-assembly method. The IONPs were synthesized via the green phytonanofabrication method using *Cleome viscosa* seed extract, and they were functionalised with  $\text{SiO}_2$  to anchor the exfoliated ZnCuNi-LDH layers using methanol as dispersion medium. The successful synthesis of  $\text{Fe}_3\text{O}_4$  NPs, their functionalisation with  $\text{SiO}_2$  and the fabrication of  $\text{Fe}_3\text{O}_4/\text{SiO}_2/\text{ZnCuNiLDH}$  composite was supported by the PXRD and FTIR results, while the homogenous distribution of constituent elements in the composite was confirmed from the SEM-EDX and elemental mapping results. This composite exhibited excellent catalytic activity for  $\text{NaBH}_4$  – assisted reduction of *p*-NP as well as cationic RhB dye that is previously unreported in our study, and displayed 97.98% degradation efficiency for *p*-NP and 97.69% for Rhodamine B dye. The synthesized composite exhibited more than 90% reduction efficiency even after 5 regeneration cycles and it was conveniently separated from the reaction mixture with the help of an external magnet.  $\text{NaBH}_4$ - assisted degradation process was found to be monitored by the Langmuir-Hinshelwood-type mechanism. Thus, this work presents  $\text{Fe}_3\text{O}_4/\text{SiO}_2/\text{ZnCuNi-LDH}$  composite as an ideal candidate for the remediation of

wastewater by the catalytic elimination of various anthropogenic pollutants that hold possible health and ecological concerns for plant, animal and public health.

## 7.5 References

- [1] D. Hull, T.W. Clyne, Fibres and matrices, in: An Introd. to Compos. Mater., 2012: pp. 9–38. <https://doi.org/10.1017/cbo9781139170130.004>.
- [2] T.W. Clyne, D. Hull, An Introduction to Composite Materials, Cambridge University Press, 2019. <https://books.google.co.in/books?id=4oKWDwAAQBAJ>.
- [3] M. Sen, Nanotechnology and the Environment, IntechOpen, 2020. <https://books.google.co.in/books?id=tGwtEAAAQBAJ>.
- [4] J. Joy, A. Krishnamoorthy, A. Tanna, V. Kamathe, R. Nagar, S. Srinivasan, Recent Developments on the Synthesis of Nanocomposite Materials via Ball Milling Approach for Energy Storage Applications, *Appl. Sci.* 12 (2022). <https://doi.org/10.3390/app12189312>.
- [5] N.C. Joshi, P. Gururani, Advances of graphene oxide based nanocomposite materials in the treatment of wastewater containing heavy metal ions and dyes, *Curr. Res. Green Sustain. Chem.* 5 (2022) 100306. <https://doi.org/https://doi.org/10.1016/j.crgsc.2022.100306>.
- [6] S. Karki, M.B. Gohain, D. Yadav, P.G. Ingole, Nanocomposite and bio-nanocomposite polymeric materials/membranes development in energy and medical sector: A review, *Int. J. Biol. Macromol.* 193 (2021) 2121–2139. <https://doi.org/https://doi.org/10.1016/j.ijbiomac.2021.11.044>.
- [7] I. Barbaros, Y. Yang, B. Safaei, Z. Yang, Z. Qin, M. Asmael, State-of-the-art review of fabrication, application, and mechanical properties of functionally graded porous nanocomposite materials, *Nanotechnol. Rev.* 11 (2022) 321–371. <https://doi.org/10.1515/ntrev-2022-0017>.
- [8] S. Abolghasemi, A. Nasiri, M. Hashemi, S. Rajabi, F. Rahimi, Magnetic nanocomposites: innovative adsorbents for antibiotics removal from aqueous environments—a narrative review, *Appl. Water Sci.* 15 (2025) 30. <https://doi.org/10.1007/s13201-025-02360-1>.
- [9] S. Moudrikoudis, A. Kostopoulou, A.P. LaGrow, Magnetic Nanoparticle Composites: Synergistic Effects and Applications, *Adv. Sci.* 8 (2021) 2004951. <https://doi.org/https://doi.org/10.1002/advs.202004951>.
- [10] J. Nikić, M. Watson, A. Tubić, M. Šolić, J. Agbaba, Recent trends in the application of magnetic nanocomposites for heavy metals removal from water: A review, *Sep. Sci. Technol.* 59 (2024) 293–331. <https://doi.org/10.1080/01496395.2024.2315626>.
- [11] W. Juvencio Keijok, L.A. Contreras Alvarez, A.M. de S. Gomes, F. Vasconcelos Campos, J.P. de Oliveira, M.C.C. Guimarães, Optimized

Synthesis and Stabilization of Superparamagnetic Iron Oxide Nanoparticles for Enhanced Biomolecule Adsorption, *ACS Omega* 10 (2025) 1976–1987. <https://doi.org/10.1021/acsomega.4c07371>.

[12] H. Naik, S. Manoharadas, N. Bommayasamy, J. Thomas, M. Gobi, S.R. Dewala, N. Amaresan, Green synthesis of iron oxide nanoparticles using *Bacillus subtilis* to mitigate salinity stress in rice (*Oryza sativa L.*) plants and enhance physiological activities, *Environ. Sci. Nano* 12 (2025) 2421–2435. <https://doi.org/10.1039/D4EN01184H>.

[13] R. Abd-Elrahman, H.M.A. El-Lateef, N.A. El-Maali, A.M. Abdel-Mawgoud, M. Elrouby, Highly efficient magnetic iron oxides-polyaniline nanocomposite for electrochemical removal of lead and cadmium ions from contaminated water, *J. Taiwan Inst. Chem. Eng.* 173 (2025) 106187. <https://doi.org/10.1016/j.jtice.2025.106187>.

[14] A.H.A. Raheem, N. Qasim, D.A. Kadhim, M.A. Abid, Development of graphene oxide/iron oxide nanocomposite preparation from *Myrtus communis* extract by two methods for the gas sensor application, *Diam. Relat. Mater.* 153 (2025) 112101. <https://doi.org/10.1016/j.diamond.2025.112101>.

[15] S. Ghosh, P. Rangaiah, M. Aboulsaad, S. Slimani, J. Cedervall, B. Aslubeiki, R. Augustine, T. Edvinsson, G. Barucca, D. Peddis, T. Sarkar, Biphasic lithium iron oxide nanocomposites for enhancement in electromagnetic interference shielding properties, *J. Alloys Compd.* 1010 (2025) 177017. <https://doi.org/10.1016/j.jallcom.2024.177017>.

[16] W. Tao, H. Quan, Z. Tu, Z. Zhang, D. Chen, Crystalline-amorphous hybrid CoNi layered double hydroxides for high areal energy density supercapacitor, *J. Colloid Interface Sci.* 683 (2025) 1–13. <https://doi.org/10.1016/j.jcis.2024.12.061>.

[17] S. Li, S. Wang, Y. Wang, J. He, K. Li, J.B. Gerken, S.S. Stahl, X. Zhong, J. Wang, Synergistic enhancement of electrochemical alcohol oxidation by combining NiV-layered double hydroxide with an aminoxy radical, *Nat. Commun.* 16 (2025). <https://doi.org/10.1038/s41467-024-55616-w>.

[18] G.H. Gwak, M.K. Kim, J.M. Oh, Nanocomposites of Magnetite and Layered Double Hydroxide for Recyclable Chromate Removal, *J. Nanomater.* 2016 (2016). <https://doi.org/10.1155/2016/8032615>.

[19] V. Yousefi, V. Tarhriz, S. Eyyazi, A. Dilmaghani, Synthesis and application of magnetic@layered double hydroxide as an anti-inflammatory drugs nanocarrier, *J. Nanobiotechnology* 18 (2020) 1–11. <https://doi.org/10.1186/s12951-020-00718-y>.

[20] S. Mortazavi-Derazkola, M. Salavati-Niasari, O. Amiri, A. Abbasi, Fabrication and characterization of Fe<sub>3</sub>O<sub>4</sub>@SiO<sub>2</sub>@TiO<sub>2</sub>@Ho nanostructures as a novel and highly efficient photocatalyst for degradation of organic pollution, *J. Energy Chem.* 26 (2017) 17–23. <https://doi.org/https://doi.org/10.1016/j.jecchem.2016.10.015>.

[21] E. MacAfee, Pharmaceuticals and Personal Care Products in the Marine Environment: An Emerging Issue, 2017.

[22] S.H. Hashemi, M. Kaykhaii, Chapter 15 - Azo dyes: Sources, occurrence, toxicity, sampling, analysis, and their removal methods, in: T. Dalu, N.T.B.T.-E.F.P. Tavengwa (Eds.), Elsevier, 2022: pp. 267–287. <https://doi.org/10.1016/B978-0-12-822850-0.00013-2>.

[23] B. Zümreoglu-Karan, A.N. Ay, Layered double hydroxides - Multifunctional nanomaterials, *Chem. Pap.* 66 (2012) 1–10. <https://doi.org/10.2478/s11696-011-0100-8>.

[24] R. Devesa-Rey, J. Del Val, J. Feijoo, J. González-Coma, G. Castiñeira, L. González-Gil, Preparation of synthetic clays to remove phosphates and ibuprofen in water, *Water (Switzerland)* 13 (2021). <https://doi.org/10.3390/w13172394>.

[25] Y. Dou, J. Zhou, F. Yang, M.J. Zhao, Z. Nie, J.R. Li, Hierarchically structured layered-double-hydroxide@zeolitic-imidazolate-framework derivatives for high-performance electrochemical energy storage, *J. Mater. Chem. A* 4 (2016) 12526–12534. <https://doi.org/10.1039/c6ta04765c>.

[26] A. Li, Y. Zhang, W. Ge, Y. Zhang, L. Liu, G. Qiu, Removal of heavy metals from wastewaters with biochar pyrolyzed from MgAl-layered double hydroxide-coated rice husk: Mechanism and application, *Bioresour. Technol.* (2021) 126425. <https://doi.org/10.1016/j.biortech.2021.126425>.

[27] H. Sun, Y.-J. Heo, J.-H. Park, K.Y. Rhee, S.-J. Park, Advances in layered double hydroxide - based ternary nanocomposites for photocatalysis of contaminants in water, *Nanotechnol. Rev.* 9 (2020) 1381–1396.

[28] I. Ashraf, N.B. Singh, A. Agarwal, Green synthesis of iron oxide nanoparticles using Amla seed for methylene blue dye removal from water, *Mater. Today Proc.* 72 (2023) 311–316. <https://doi.org/10.1016/j.matpr.2022.07.404>.

[29] V. Arumugam, K.G. Moodley, A. Dass, R.M. Gengan, D. Ali, S. Alarifi, M. Chandrasekaran, Y. Gao, Ionic liquid covered iron-oxide magnetic nanoparticles decorated zeolite nanocomposite for excellent catalytic reduction and degradation of environmental toxic organic pollutants and dyes, *J. Mol. Liq.* 342 (2021) 117492. <https://doi.org/10.1016/j.molliq.2021.117492>.

[30] H.S. Devi, M.A. Boda, M.A. Shah, S. Parveen, A.H. Wani, Green synthesis of iron oxide nanoparticles using *Platanus orientalis* leaf extract for antifungal activity, *Green Process. Synth.* 8 (2019) 38–45. <https://doi.org/10.1515/gps-2017-0145>.

[31] J. Pathak, P. Singh, Synthesis and characterization of ternary layered double hydroxide containing zinc/copper/nickel and its PANI composite, *Polym. Compos.* 43 (2022) 7836–7844. <https://doi.org/10.1002/pc.26895>.

[32] A. Romero-Morán, J.L. Sánchez-Salas, J. Molina-Reyes, Influence of selected reactive oxygen species on the photocatalytic activity of TiO<sub>2</sub>/SiO<sub>2</sub> composite

coatings processed at low temperature, *Appl. Catal. B Environ.* 291 (2021). <https://doi.org/10.1016/j.apcatb.2020.119685>.

[33] P. Meenakshi, U. Sitharaman, N. Rajamani, Facile synthesis and characterization of acetate intercalated Co-La layered double hydroxide, *J. Rare Earths* 35 (2017) 474–479. [https://doi.org/10.1016/S1002-0721\(17\)60936-0](https://doi.org/10.1016/S1002-0721(17)60936-0).

[34] M. Yasaei, M. Khakbiz, A. Zamanian, E. Ghasemi, Synthesis and characterization of Zn/Al-LDH@SiO<sub>2</sub> nanohybrid: Intercalation and release behavior of vitamin C, *Mater. Sci. Eng. C* 103 (2019). <https://doi.org/10.1016/j.msec.2019.109816>.

[35] X. Zhou, J. Shi, X. Bai, Ultrasonic assisted preparation of ultrafine Pd supported on NiFe-layered double hydroxides for p-nitrophenol degradation, *Environ. Sci. Pollut. Res.* 29 (2022) 56178–56199. <https://doi.org/10.1007/s11356-022-19641-w>.

[36] T.T.T. Le Hoang, N. Insin, N. Sukpirom, Catalytic activity of silver nanoparticles anchored on layered double hydroxides and hydroxyapatite, *Inorg. Chem. Commun.* 121 (2020) 108199. <https://doi.org/10.1016/j.inoche.2020.108199>.

[37] Q. Yan, X.Y. Wang, J.J. Feng, L.P. Mei, A.J. Wang, Simple fabrication of bimetallic platinum-rhodium alloyed nano-multipods: A highly effective and recyclable catalyst for reduction of 4-nitrophenol and rhodamine B, *J. Colloid Interface Sci.* 582 (2021) 701–710. <https://doi.org/10.1016/j.jcis.2020.08.062>.

[38] J. Pathak, P. Singh, Ultrafast catalytic reduction of organic pollutants using ternary zinc–copper–nickel layered double hydroxide, *Appl. Organomet. Chem.* 38 (2024) e7507. <https://doi.org/10.1002/aoc.7507>.

[39] Y. Li, Y. Wang, H. Lu, X. Li, Preparation of CoFe<sub>2</sub>O<sub>4</sub>–P4VP@Ag NPs as effective and recyclable catalysts for the degradation of organic pollutants with NaBH<sub>4</sub> in water, *Int. J. Hydrogen Energy* 45 (2020) 16080–16093. <https://doi.org/10.1016/j.ijhydene.2020.04.002>.

[40] Y. Wang, P. Gao, Y. Wei, Y. Jin, S. Sun, Z. Wang, Y. Jiang, Silver nanoparticles decorated magnetic polymer composites (Fe<sub>3</sub>O<sub>4</sub>@PS@Ag) as highly efficient reusable catalyst for the degradation of 4-nitrophenol and organic dyes, *J. Environ. Manage.* 278 (2021) 111473. <https://doi.org/10.1016/j.jenvman.2020.111473>.

[41] S. Kansal, P. Singh, S. Biswas, A. Chowdhury, D. Mandal, S. Priya, T. Singh, A. Chandra, Superior-catalytic performance of Ni–Co layered double hydroxide nanosheets for the reduction of p-nitrophenol, *Int. J. Hydrogen Energy* 48 (2023) 21372–21382. <https://doi.org/10.1016/j.ijhydene.2022.04.213>.

[42] M. Kohantorabi, M.R. Gholami, Kinetic Analysis of the Reduction of 4-Nitrophenol Catalyzed by CeO<sub>2</sub> Nanorods-Supported CuNi Nanoparticles, *Ind. Eng. Chem. Res.* 56 (2017) 1159–1167. <https://doi.org/10.1021/acs.iecr.6b04208>.

***CHAPTER - 8***

***CONCLUSIONS, FUTURE PROSPECTS AND  
SOCIAL IMPACT***

---

## **CHAPTER - 8**

### **CONCLUSIONS, FUTURE PROSPECTS AND SOCIAL IMPACT**

---

#### **8.1 Conclusion**

In the past, the lack of availability of catalytically active ternary LDHs has posed a critical research gap due to difficulty in governing oxidation states of cations and impure phase formation. Therefore, the current work reported the synthesis of novel ternary ZnCuNi-LDH using a facile acid hydrolysis methodology that fulfilled a critical research gap which was faced due to difficulties in incorporation of third cation in LDH lattice. The successful formation of layered structure, investigation of functional groups, thermal stability, surface morphology, elemental composition, and surface area were carried out using suitable techniques. Based on the characterisation results, the use of these materials as catalysts for the degradation of various azo dyes and NACs was explored. It was found that ZnCuNi-LDH acted as an efficient catalyst and was able to effectively reduce azo dyes and NACs in presence of NaBH<sub>4</sub>. Based on the results obtained from the synthesis and catalytic behaviour of ZnCuNi-LDH, efforts were made to synthesize ZnCuNi-LDO, that exhibited good catalytic activity towards reduction of azo dyes and NACs. The LDO also exhibited photocatalytic behaviour and efficiently degraded ciprofloxacin drug under UV light illumination, that was previously found to be lacking in ZnCuNi-LDH.

After the successful formation of layered structure using transition metal cations, the interest of the research work shifted towards the incorporation of rare earth metal

cation in LDHs. It has been reported that Ni and Ce possess significantly different ionic radii of  $0.69\text{\AA}$  and  $1.0\text{\AA}$  respectively. Additionally, while Ni cations can only exhibit coordination upto 6, Ce cations may hold values upto 12. Therefore, in order to explore the amount of Ce cations that can be incorporated in LDH and the extent to which LDH layers can be expanded without collapse of the layers, a fixed percentage of Ce cations was utilised. Using the selected ratio, successful synthesis of layered ZnCuCe-LDH was achieved without impurities or structure deformation. Since cerium possesses better optical and catalytic activities as compared to nickel, therefore the synthesized ZnCuCe-LDO expectedly exhibited enhanced photocatalytic behaviour towards degradation of azo dyes and drug.

The structure-property relationships and behaviour of synthesized ZnCuNi-LDH were evaluated by studying the structure-regaining ability by virtue of memory effect property and intercalation behaviour via anion exchange reactions. The lattice was successfully able to regain its parent structure on calcination and subsequent rehydration. Furthermore, the intercalation of PANI in the lattice was achieved using in-situ oxidative polymerization, and it was observed that the incorporation of PANI resulted in the expansion of the interlayer region of the LDH lattice. The synthesized PANI incorporated ZnCuNi-LDH could be potentially utilized for energy storage, environmental and catalytic applications in the future. These results could also open new avenues for the incorporation of other macromolecules into the LDH lattice.

Although LDHs possess a host of desirable structural features and properties, these properties can be further enhanced by their combination with other materials via composite formation. Therefore, for this purpose, carbon nitride and iron oxide

nanoparticles were selected as the appropriate materials for composite fabrication. The use of CN provides unique electronic properties and brings about synergistic interactions in the lattice, thereby reducing the agglomeration tendency in composites while also enhancing their stability. The synthesized LDH/CN composites exhibited excellent catalytic reduction efficiencies for diazo dyes, that was not observed in the pristine LDH lattices. Meanwhile, the selection of IONPs was contingent on their magnetic properties. Therefore, the synthesized  $\text{Fe}_3\text{O}_4/\text{SiO}_2/\text{ZnCuNi-LDH}$  acted as an efficient catalyst that could be recovered magnetically, which was not possible in the previously synthesized lattices.

Therefore, this thesis deals with the synthesis and characterization of a series of ternary layered double hydroxides (LDHs) as well as LDH-based layered double oxides (LDOs) and their composites that can prove to be ideal candidates for the development of multipurpose nanoplatforms.

## 8.2 Future Scope

This thesis has highlighted the issue of water contamination, investigated the synthesis of LDHs, LDOs, and their composites, and explored the possibilities of utilising the as-synthesised materials in practical wastewater remediation applications. The majority of work on LDHs and their composites has been based on a framework of synthesis and laboratory-based applications, followed by comparisons with previous literature studies. Future studies could focus on direct evaluations, as well as quantitative and qualitative determination of their composition, properties, and applications. Based on the findings from this PhD work, some future pathways that can be explored to advance the field of layered double hydroxides include:

- Fabrication of LDH lattices consisting of other transition and rare earth metal cations.
- Expansion of catalytic and photocatalytic degradation behaviour for emerging pollutants (eg. endocrine disruptors, PCPs, microplastics, agricultural waste, etc.).
- Tuning of LDH structures for visible light and sunlight-driven photocatalysis.
- Development of PANI/LDH composite and LDH-based materials for sensing and energy storage applications.
- Exploration of Density functional theory (DFT) studies to predict LDH stability, electronic structure, and reaction pathways.

### 8.3 Social Impact

The exponentially increasing burden of environmental pollution poses a significant threat to ecosystem and human health. This research aims to address the issue of wastewater remediation with a special focus on pollutant degradation through the development of technologically important advanced LDH-based materials. The materials synthesized during this research offer low-cost, sustainable, and efficient solutions for removing dyes, toxic metals, and emerging contaminants from water bodies. Their high anion exchange capacity, tunable redox properties, and reusability make them promising candidates for use in rural and urban water treatment systems, potentially improving access to clean water and reducing waterborne diseases.

Furthermore, the adoption of green synthesis techniques and recyclable materials aligns with the goals of sustainable development and circular economy. By contributing to cleaner technologies and waste management strategies, this research

supports policy frameworks targeting environmental protection and public health. The outcomes of this work have the potential to benefit various industrial sectors (e.g., textile, pharmaceutical, and chemical industries) by offering effective solutions for effluent treatment, thus minimizing ecological footprints. Overall, the thesis not only advances scientific knowledge but also aims to translate into real-world technologies with positive societal and environmental impacts. Ultimately, the outcomes are aligned with the United Nations Sustainable Development Goals (especially SDGs 6, 12, and 13), promoting environmental health and social well-being.

## ***LIST OF PUBLICATIONS***

---

## LIST OF PUBLICATIONS

### Journal Articles

1. **Jigyasa Pathak**, Sarla Yadav, Bhamini Pandey, Poonam Singh. Comprehensive Insights into Anionic Layered Materials: Assembly, Synthesis, Reactivity, and Application Paradigms, *Advances in Colloid and Interface Science*, Elsevier. <https://doi.org/10.1016/j.cis.2025.103696> (I.F. = 19.3) (SCIE)
2. Sarla Yadav, **Jigyasa Pathak**, Purusottam Majhi, Sandeep Kaushik, A.K. Shukla, Raminder Kaur, Ravinder Kumar, Poonam Singh. Lac-based-biosynthesis of zinc–copper mixed metal oxide nanoparticles and evaluation of their antifungal activity against *A. alternata* and *F. oxysporum*. *Materials Chemistry and Physics* 2025;330:130152. <https://doi.org/10.1016/j.matchemphys.2024.130152> (I.F. = 4.7) (SCIE)
3. **Jigyasa Pathak** and Poonam Singh. Zinc-Copper-Nickel Mixed Metal Oxide as Heterogeneous Catalytic Material for the Reductive Degradation of Nitroarene and Azo Dye. *Catalysis Letters* 2024;154:5280-5293. <https://doi.org/10.1007/s10562-024-04754-3> (I.F. = 2.4) (SCIE)
4. **Jigyasa Pathak** and Poonam Singh. Ultrafast catalytic reduction of organic pollutants using ternary zinc–copper–nickel layered double hydroxide. *Applied Organometallic Chemistry* 2024;38:e7507. <https://doi.org/10.1002/aoc.7507> (I.F. = 3.5) (SCIE)

5. **Jigyasa Pathak** and Poonam Singh. Layered double hydroxides–polymer matrix composites: nexus materials for energy storage applications. *Chemical Papers* 2024;78:7375-7393. <https://doi.org/10.1007/s11696-024-03624-x> (I.F. = 2.5) (**SCIE**)
6. **Jigyasa Pathak**, Bhamini Pandey, Poonam Singh, Ravinder Kumar, Sandeep Kaushik, Ishwar Prasad Sahu, Tarun Kumar Thakur. Exploring the Paradigm of Phyto-Nanofabricated Metal Oxide Nanoparticles: Recent Advancements, Applications, and Challenges. *Molecular Biotechnology* 2023. <https://doi.org/10.1007/s12033-023-00799-8> (I.F. = 2.86) (**SCIE**)
7. Bhamini Pandey, **Jigyasa Pathak**, Poonam Singh, Ravinder Kumar, Amit Kumar, Sandeep Kaushik and Tarun Kumar Thakur. Microplastics in the Ecosystem : An Overview on Detection, Removal, Toxicity Assessment, and Control Release 2023;15:51. <https://doi.org/https://doi.org/10.3390/w15010051> (I.F. = 3.0) (**SCIE**)
8. **Jigyasa Pathak** and Poonam Singh. Synthesis and characterization of ternary layered double hydroxide containing zinc/copper/nickel and its PANI composite. *Polymer Composites* 2022;43:7836-7844. <https://doi.org/10.1002/pc.26895> (I.F. = 4.7) (**SCI/SCIE**)
9. **Jigyasa Pathak** and Poonam Singh. Adsorptive Removal of Congo Red Using Organically Modified Zinc–Copper–Nickel Ternary Metal Hydroxide: Kinetics, Isotherms and Adsorption Studies. *Journal of Polymers and the Environment* 2022;31:327-344. <https://doi.org/10.1007/s10924-022-02612-0> (I.F. = 5.0) (**SCIE**)
10. **Jigyasa Pathak** and Poonam Singh. Evaluating the photocatalytic activity of ZnCuCe-MMO for the degradation of Basic Red 2 and Methyl Orange dyes:

Spectrophotometric and Smartphone-based detection. Journal of Molecular Structure (1st Revision received)

11. **Jigyasa Pathak**, Bhamini Pandey, Poonam Singh et al. Structure–Activity Correlation in ZnCu-Layered Materials: Influence of Ni Doping and Thermal Conversion. (Communicated)

12. Sarla Yadav, **Jigyasa Pathak**, Poonam Singh et al. Microplastics as Emerging Contaminants: An Overview of their Properties, Distribution, Analysis, Remediation and Challenges. (Communicated)

13. **Jigyasa Pathak** and Poonam Singh. Catalytic decoloration of water-soluble nitro compound and azo dye using LDH/CN composites. (Under preparation)

14. **Jigyasa Pathak** and Poonam Singh. Synergistic Catalytic Activity of  $\text{Fe}_3\text{O}_4/\text{SiO}_2/\text{ZnCuNi-LDH}$ -based Magnetic Composite for NAC and Azo Dye Detoxification in Aqueous Medium. (Under preparation)

### **Book Chapters**

1. **Jigyasa Pathak**, Ravinder Kumar, Poonam Singh, Municipal Solid Waste and Climate Change BT - Integrated Waste Management: A Sustainable Approach from Waste to Wealth, in: A. Gupta, R. Kumar, V. Kumar (Eds.), Springer Nature Singapore, Singapore, 2024;207–221. [https://doi.org/10.1007/978-981-97-0823-9\\_10](https://doi.org/10.1007/978-981-97-0823-9_10).

## Comprehensive insights into anionic layered materials: Assembly, synthesis, reactivity, and application paradigms

Jigyasa Pathak <sup>a</sup>, Sarla Yadav <sup>a</sup>, Bhamini Pandey <sup>b</sup>, Poonam Singh <sup>a,\*</sup>

<sup>a</sup> Department of Applied Chemistry, Delhi Technological University, Delhi 110042, India

<sup>b</sup> GLA University, Mathura, Uttar Pradesh 281406, India

### ARTICLE INFO

**Keywords:**  
Sustainable  
Layered double hydroxides  
Hydroxy double salts  
Topotactic  
Intercalation  
Assembly chemistry

### ABSTRACT

During recent times, the study of two-dimensional anionic layered materials (ALMs) has become an area of significant research. ALMs exhibit a wide spectrum of structural characteristics involving simple exchange of anions within the interlayer region, i.e., anion-exchange as well as the intercalation of various complex guest species, enabling control over chemical composition and surface functionalities. The present review comprehensively summarizes the synthesis of layered double hydroxides and their derivatives via conventional and novel synthetic methodologies for enhancing the physical, chemical, optical, and catalytic properties of layered materials. Further, a detailed overview of the structural chemistry, compositional flexibility, anion exchange behaviour, surface modification, topotactic transformation, and colloidal stability that act as key attributes for governing their functional performance and adaptability in diverse applications has also been discussed. The review further highlights the integral role of advanced spectroscopic and microscopic techniques—including powder X-ray diffraction (PXRD), Fourier-transform infrared spectroscopy (FTIR), and electron microscopy—in elucidating the layered framework and verifying intercalation phenomena. The applications of ALMs across diverse fields, including water remediation, ceramics, biomedicine, antimicrobial agents, biosensing, and display technologies have also been critically examined. We believe that this review holds immense potential to deepen the understanding of structural chemistry, properties, and applications of ALMs, underscoring their promising role in sustainable technology development and advanced functional materials.

### 1. Introduction

During past few years, rapid advancements in modern technology and growing interest in sustainable living have invoked immense interest in the development of multifunctional nanomaterials. Among the various categories of advanced nanomaterials that are currently being developed, layered materials have emerged out as notable crystalline solids that have gained substantial attention specifically in the field of materials science. Basically, Layered solids belongs to the class of two-dimensional (2-D) solids consisting of stacked layers owing to the bonds among the intraplanar atoms that are much stronger than the interaction among the adjacent planes [1]. The intraplanar atoms are held together by covalent bonds while VanderWaal attraction forces hold the adjacent layers in place, thereby contributing to the formation of the layered structure. The compositional layers may vary in thickness i.e. the layers may be one layer thick, or may be made of several atoms in thickness. Layered solids are classified based on the thickness of the

individual layers as well as on the presence of fixed charges in the planar macromolecule [2]. Based on the parameter of layer thickness, layered materials can be categorized into Class I, Class II and Class III type. *Class I* layered solids are formed from atomic monolayers; typical examples for this class are graphite, that is homopolar and boron nitride, a binary layered material [3]. Layered dichalcogenides and FeOCl belongs to *Class II* layered solids that are formed from layers which are a few atoms thick. While *class III* consists of the constituent layers which are many atoms thick, for example, silicate clays and metal (IV) phosphates. Furthermore, depending on the presence of fixed charges in the planar macromolecule, these materials may be (i) cationic - that have negatively charged layers (e.g. Metal phosphates and phosphonates, phyllosilicate-group containing clays), (ii) neutral that have no charge on layers (e.g. Graphite, magnesium hydroxide) or (iii) anionic that have positive charge on layers (e.g. Layered double hydroxides (LDHs), layered hydroxy salts (LHSs)) that is offset by the presence of interlayer anions to restore charge neutrality [4]. The creation of charges on the

\* Corresponding author.  
E-mail address: [poonam@dtu.ac.in](mailto:poonam@dtu.ac.in) (P. Singh).

<https://doi.org/10.1016/j.cis.2025.103696>

Received in revised form 25 September 2025;

Available online 26 October 2025

0001-8686/© 2025 Elsevier B.V. All rights are reserved, including those for text and data mining, AI training, and similar technologies.

## Lac-based-biosynthesis of zinc-copper mixed metal oxide nanoparticles and evaluation of their antifungal activity against *A.alternata* and *F. oxysporum*

Sarla Yadav <sup>a</sup>, Jigyasa Pathak <sup>a</sup>, Purusottam Majhi <sup>c</sup>, Sandeep Kaushik <sup>b</sup>, A.K. Shukla <sup>c</sup>,  
Raminder Kaur <sup>a</sup>, Ravinder Kumar <sup>a,\*</sup>, Poonam Singh <sup>a,\*</sup>

<sup>8</sup> Department of Applied Chemistry, Delhi Technological University, Delhi, 110042, India

<sup>b</sup> Department of Pharmaceutical Sciences, Indian Council of Medical Research-National Institute of Mental Health and Neurosciences, Madikeri, Kodagu, 571401, India

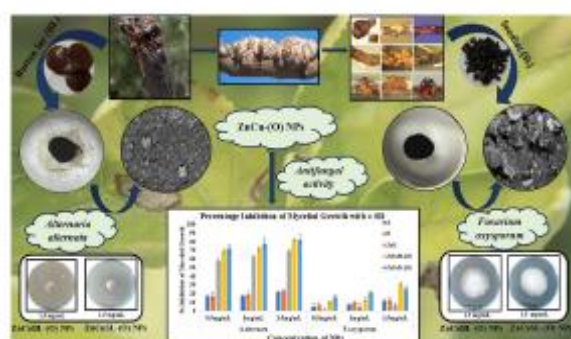
<sup>7</sup>Microbiology Laboratories, Department of Botany, Indian Gandhi National Tribal University, Amarkantak, Madhya Pradesh, 494007, India

<sup>4</sup> Department of Chemistry, Gurukul Kangri (Deemed to be University), Haridwar, U.P. 249404, India

## HIGHLIGHTS

- Phytomanufactured Zinc-copper mixed metal oxide nanoparticles (ZnCu-(O) NPs) were successfully prepared using Button-lac (BL) and Seed-lac (SL) obtained from *Keria lacca*.
- Button-lac and seed-lac act as reducing, capping and stabilizing agents.
- The synthesized ZnCuSL-(O) NPs exhibit maximum antifungal activity against both fungal strains than that of ZnCuBL-(O) NPs and chemically synthesized ZnCu-(O) NPs.
- In comparison to ZnCu-(O) NPs and ZnCuSL-(O) NPs, ZnCuSL-(O) NPs show a maximum zone of inhibition of 71.66 and 15.76 against both fungi, that is, *Alternaria alternata* and *Penicillium oxyphorum* at 0.5 mg/ml concentration of fungal strains.
- This study highlights the potential of green nanotechnology in synthesizing sustainable and efficient antifungal agents against pathogenic fungi.

#### GRAPHICAL ABSTRACT



ARTICLE INFO

**Keywords:**  
Nanoparticles  
Mixed metal oxide  
Eco-friendly  
Green synthesis

#### ABSTRACT

The use of animal-based sources for biosynthesis resonates with the growing market for sustainable and eco-friendly materials, but remains severely unexplored in comparison to plant-based and microbial sources. In this purview, shellac, a bioresin obtained from the *Kerria lacca* insect, is emerging as an ideal candidate for nanomaterial fabrication due to its abundant availability and anti-microbial properties. It is commonly available in the form of shellac lac, as a green agent for the synthesis of zinc-copper mixed metal oxide nanomaterials, and the potential of shellac as a green agent for the synthesis of zinc-copper mixed metal oxide nanomaterials, and the

\* Corresponding author.

\*\* Corresponding author.

E-mail address: [avinder.kumar@sky.ac.in](mailto:avinder.kumar@sky.ac.in) (R. Kumar), [poonam@dtu.ac.in](mailto:poonam@dtu.ac.in) (P. Singh).

<https://doi.org/10.1016/j.matchmedu.2024.130152>

Received 12 October 2024; Received in revised form 11 November 2024; Accepted 15 November 2024

Received 12 August 2024; Received in revised form 15 November 2024

Available online 16 November 2024  
© 2024, Elsevier B.V. All rights reserved. No part of this journal may be reproduced, stored in a retrieval system, or transmitted, in whole or in part, in any form or by any means, electronic, mechanical, photocopying, or otherwise, without the prior permission of the publisher.



## Zinc-Copper-Nickel Mixed Metal Oxide as Heterogeneous Catalytic Material for the Reductive Degradation of Nitroarene and Azo Dye

Jigyasa Pathak<sup>1</sup> · Poonam Singh<sup>1</sup>

Received: 1 April 2024 / Accepted: 12 June 2024  
© The Author(s), under exclusive licence to Springer Science+Business Media, LLC, part of Springer Nature 2024

### Abstract

Transition metal-based mixed metal oxides (MMOs) are nexus nanomaterials that garner significant interest from scientists because of their unique magnetic, electronic, optical and catalytic properties that can easily be tailored by varying their composition and structure. Although MMOs hold significant potential in multifunctional applications, but they are plagued by certain challenges such as identifying the appropriate method for synthesis, complications in controlling the surface area and the oxidation states of the constituent transition metals, while also ensuring the homogenous distribution of the constituent metal ions. Therefore, the present work aims to study the formation of homogenous and porous zinc-copper-nickel mixed metal oxide (ZnCuNi-MMO) by performing calcination of ZnCuNi-LDH at 350 °C. The obtained ZnCuNi-MMO was characterized using PXRD, SEM-EDX and BET techniques. Thereafter, ZnCuNi-MMO was applied as a heterogeneous catalyst for the hydrogenation of *p*-nitroaniline (*p*-NA) and catalytic reduction of methyl orange (MO) dye. The pollutant degradation characteristics were assessed using time-dependent UV-Visible absorption spectroscopy showing advanced efficient behavior of ZnCuNi-MMO towards the hydrogenation of *p*-NA (96.98%) and reduction of MO (95.58%). The catalyst exhibited fast reaction rates (0.402 min<sup>-1</sup> for hydrogenation of *p*-NA and 0.471 min<sup>-1</sup> for catalytic reduction of MO) and kinetics analysis of the experimental data was found to be coherent with the pseudo-first order model, thereby implying that the catalysis proceeded through the Langmuir–Hinshelwood mechanism. Thus the obtained experimental results highlight the utility and viability of synthesized MMO as an efficacious and sustainable catalytic material.

---

✉ Poonam Singh  
poonam@dtu.ac.in

<sup>1</sup> Department of Applied Chemistry, Delhi Technological University, Delhi 110042, India

Published online: 27 June 2024

Springer

Content courtesy of Springer Nature, terms of use apply. Rights reserved.

## Ultrafast catalytic reduction of organic pollutants using ternary zinc–copper–nickel layered double hydroxide

Jigyasa Pathak | Poonam Singh

Department of Applied Chemistry, Delhi Technological University, Delhi, India

**Correspondence**

Poonam Singh, Department of Applied Chemistry, Delhi Technological University, Delhi 110042 India.  
Email: [poonam@dtu.ac.in](mailto:poonam@dtu.ac.in)

**Funding information**

The authors are grateful to UGC BSR Startup Grant No. F.30-416/2018 (BSR) for the funds to carry out this research. Author JP would like to thank Delhi Technological University for providing a fellowship.

Water is the utmost essential commodity for the support of life process in animals. In recent decades, rapid industrialization and uncontrolled agricultural practices have led to increased level of toxic pollutants in groundwater, including organic pollutants (dyes, nitroarene compounds, antibiotics, etc.), inorganic pollutants (heavy metals, nanoparticles, etc.), and pesticides, posing a serious threat to human health and the environment. Although various technologies such as adsorption, photocatalysis, reverse osmosis, filtration, sedimentation, flocculation, and precipitation are available for the elimination of toxic pollutants from wastewater, issues such as their cost and efficacy limit their usage. Recently, catalysis has been found to be the most effective approach since it exhibits significant capability to eliminate almost all the pollutants and offers the benefit of simple design and low initial cost. In the present study, ternary zinc–copper–nickel layered double hydroxide (ZnCuNi-LDH) synthesized using facile acid hydrolysis method was employed as an efficacious heterogeneous catalyst for the reduction of NACs (para-nitrophenol and para-nitroaniline) and degradation of organic azo dyes (methyl orange, amaranth, and brilliant black). ZnCuNi-LDH exhibited superior catalytic activity for the reduction of all five model pollutants with reduction efficiency of more than 95% within a short time span of 5 min. Therefore, keeping in view the layered structure, high specific surface area, and remarkable catalytic performance, ZnCuNi-LDH holds immense potential for the large-scale catalytic degradation of refractory pollutants.

**KEY WORDS**

azo dyes, catalytic reduction, layered double hydroxide, nitroarene compounds, wastewater purification

### 1 | INTRODUCTION

The expulsion of refractory pollutants from water sources holds prime significance for the sustenance of ecosystems and bio-diversities, since the availability of potable water has become a burgeoning predicament because of increasing industrialization and urbanization. The contamination of water by a variety of toxic pollutants

including dyes, phenolic compounds, volatile organic compounds (VOCs), drugs, and surfactants is a matter of grave concern as these pollutants exhibit toxic, carcinogenic, and mutagenic effects, thereby threatening human health and the ecosystem.<sup>1</sup> Nitroarene compounds (NACs) and azo dyes are among the most vicious organic pollutants that are responsible for deteriorating water quality. Their ubiquitous presence in water resources is a



## Layered double hydroxides–polymer matrix composites: nexus materials for energy storage applications

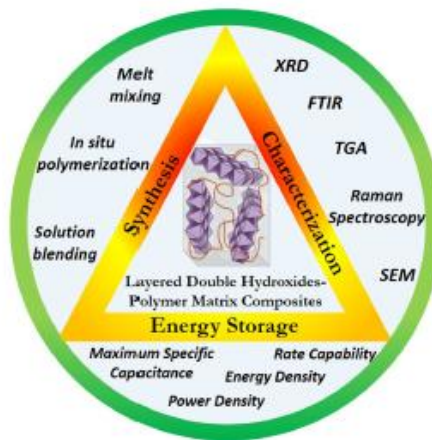
Jigyasa Pathak<sup>1</sup> · Poonam Singh<sup>1</sup>

Received: 14 February 2024 / Accepted: 22 July 2024  
© The Author(s), under exclusive licence to the Institute of Chemistry, Slovak Academy of Sciences 2024

### Abstract

In order to overcome burgeoning energy demands along with the ecological crisis caused by dwindling amounts of fossil fuel and increasing levels of carbonaceous emission, there is an immediate need to develop economical, eco-friendly systems for energy applications. To overcome this issue, use of non-carbon materials has been suggested, but their commercial usage is limited due to intermittency and high operational costs. Currently, layered double hydroxides (LDHs) are prospective contenders for energy applications by virtue of unique physicochemical properties and excellent theoretical specific capacitance. Additionally, LDH–polymer matrix composites (PMCs) have also emerged as nexus materials in energy storage sector since they surpass disadvantages of both LDHs and polymers and broaden the horizons for their practical applications. The current review highlights applications of LDH–PMCs as supercapacitors in terms of maximum specific capacitance, energy density, power density, and rate capability along with insights into mechanism of capacitance, thereby outlining their utility in energy storage.

### Graphical abstract



**Keywords** Layered double hydroxides · Energy storage · Pseudocapacitors · Conducting polymers · Layered double hydroxides–polymer matrix composites

Extended author information available on the last page of the article

Published online: 02 August 2024

Springer



## Exploring the Paradigm of Phyto-Nanofabricated Metal Oxide Nanoparticles: Recent Advancements, Applications, and Challenges

Jigyasa Pathak<sup>1</sup> · Bhamini Pandey<sup>1</sup> · Poonam Singh<sup>1</sup> · Ravinder Kumar<sup>2</sup> · Sandeep Kaushik<sup>3</sup> · Ishwar Prasad Sahu<sup>4</sup> · Tarun Kumar Thakur<sup>3</sup> · Amit Kumar<sup>5</sup> 

Received: 8 April 2023 / Accepted: 13 June 2023  
© The Author(s), under exclusive licence to Springer Science+Business Media, LLC, part of Springer Nature 2023

### Abstract

The development of nanotechnology, in particular metal oxide nanoparticles, has captured immense scientific attention in the global arena due to their unique properties leading to their unique diverse applications. But the use of toxic precursors and high operational cost make existing methodologies inefficient for synthesising metal oxide nanoparticles (MONPs). Biogenic synthesis of MONPs has been hailed as a more sustainable approach for the synthesis of NPs due to its alignment with the principles of green chemistry. Microorganisms (bacteria, yeast, algae), animal sources (silk, fur, etc.), and plants are effective, low-cost, and eco-friendly means of synthesizing MONPs since they possess a high bio-reduction abilities to produce NPs of various shapes and sizes. The current review encompasses recent advancements in the field of plant-mediated MONP synthesis and characterisation. The detailed evaluation of various synthesis processes and parameters, key influencing factors affecting the synthesis efficiency and product morphology, practical applications with insight into the associated limitations and challenges presents a valuable database that will be helpful in developing alternative prospects and potential engineering applications.

**Keywords** Green chemistry · Nanoparticles · Metal oxide · Phytonanofabrication · Environmental

### Introduction

In the recent years, the development and advancements in industries have heavily impacted the environment; releasing toxic waste into the ecosystems and causing irreplaceable

damage on a regular basis. It is therefore essential in every aspect of science and engineering to move towards a more sustainable approach. Nanoscience holds the potential to bring about a new revolution, as it is one of the fastest growing fields of applied science today [1]. This discipline of science majorly deals with miniaturization of various materials used in different fields to nanoscale devices. Therefore, developing new nanomaterials for their application in the real-world has become a major focus of nanoscale synthesis. A nanomaterial can be defined as a material with one or more external dimensions in the range of 1–100 nm and possess unique electronic, optical, magnetic, and thermal properties as compared to their large analogues. The nanomaterials based on the dimensions can be categorized as zero-dimensional (0-D), one-dimensional (1-D), two-dimensional (2-D), and three-dimensional (3-D) (as shown in Fig. 1) [2]. The 0-D class of nanomaterials have their dimensions below 100 nm and consist of spherical and cube-shaped materials, as well as nanorods, polygons, hollow spheres, metals, quantum dots (QDs) as well as core–shell nanomaterials. A 0-D nanomaterial based on magnetic graphene quantum dots (Fe-GQDs) was synthesized by Pathan

✉ Poonam Singh  
poonam@dtu.ac.in

✉ Amit Kumar  
amitkdah@nuist.edu.cn

<sup>1</sup> Department of Applied Chemistry, Delhi Technological University, New Delhi 110042, India

<sup>2</sup> Department of Chemistry, Gurukul Kangri Vishwavidyalaya, Haridwar, Uttarakhand 249404, India

<sup>3</sup> Department of Environmental Science, Indira Gandhi National Tribal University, Amarkantak, Madhya Pradesh 484887, India

<sup>4</sup> Department of Physics, Indira Gandhi National Tribal University, Amarkantak, Madhya Pradesh 484887, India

<sup>5</sup> School of Hydrology and Water Resources, Nanjing University of Information Science and Technology, Nanjing 210044, China

Review

## Microplastics in the Ecosystem: An Overview on Detection, Removal, Toxicity Assessment, and Control Release

Bhamini Pandey <sup>1</sup>, Jigyasa Pathak <sup>1</sup>, Poonam Singh <sup>1,\*</sup>, Ravinder Kumar <sup>2</sup>, Amit Kumar <sup>3,\*</sup>, Sandeep Kaushik <sup>4</sup> and Tarun Kumar Thakur <sup>4</sup>

<sup>1</sup> Department of Applied Chemistry, Delhi Technological University, Delhi 110042, India

<sup>2</sup> Department of Chemistry, Gurukula Kangri (Deemed to be University), Haridwar 249404, Uttarakhand, India

<sup>3</sup> School of Hydrology and Water Resources, Nanjing University of Information Science and Technology, Nanjing 210044, China

<sup>4</sup> Department of Environmental Science, Indira Gandhi National Tribal University Amarkantak, Madhya Pradesh 484887, India

\* Correspondence: poonam@dtu.ac.in (P.S.); amitkdah@nuist.edu.cn (A.K.)

**Abstract:** In recent decades, the accumulation and fragmentation of plastics on the surface of the planet have caused several long-term climatic and health risks. Plastic materials, specifically microplastics (MPs; sizes < 5 mm), have gained significant interest in the global scientific fraternity due to their bioaccumulation, non-biodegradability, and ecotoxicological effects on living organisms. This study explains how microplastics are generated, transported, and disposed of in the environment based on their sources and physicochemical properties. Additionally, the study also examines the impact of COVID-19 on global plastic waste production. The physical and chemical techniques such as SEM-EDX, PLM, FTIR, Raman, TG-DSC, and GC-MS that are employed for the quantification and identification of MPs are discussed. This paper provides insight into conventional and advanced methods applied for microplastic removal from aquatic systems. The finding of this review helps to gain a deeper understanding of research on the toxicity of microplastics on humans, aquatic organisms, and soil ecosystems. Further, the efforts and measures that have been enforced globally to combat MP waste have been highlighted and need to be explored to reduce its potential risk in the future.

**Citation:** Pandey, B.; Pathak, J.; Singh, P.; Kumar, R.; Kumar, A.; Kaushik, S.; Thakur, T.K. Microplastics in the Ecosystem: An Overview on Detection, Removal, Toxicity Assessment, and Control Release. *Water* **2023**, *15*, 51. <https://doi.org/10.3390/w15010051>

Academic Editor: Grzegorz Naleć-Jawicki

Received: 30 November 2022

Revised: 19 December 2022

Accepted: 20 December 2022

Published: 23 December 2022



Copyright: © 2022 by the authors. Licensee MDPI, Basel, Switzerland. This article is an open access article distributed under the terms and conditions of the Creative Commons Attribution (CC BY) license (<https://creativecommons.org/licenses/by/4.0/>).

### 1. Introduction

Today's world relies heavily on plastic on a global scale, infiltrating almost every aspect of human lives. Plastics are organic polymers that exhibit exceptional properties such as durability, flexibility, lightness, and mechanical and thermal stability which contribute to their widespread applications in construction, food and packaging industries, pharmaceuticals, and many more sectors [1]. Despite annual expansion in the plastic industry, the demand for plastic does not seem to be decreasing. The amount of plastic generation is estimated to reach approximately 33 billion tons by the year 2050 [2]. The environmental impact of plastic has been a considerable concern for government entities, the scientific community, and the general public, regardless of its long-term industrial benefit [3]. The production and distribution of plastics possessing high degradation resistance are increasing at a rapid pace, which has serious environmental and ecological consequences. Geyer et al. [4] reported the contamination of the marine environment by 4–12 million metric tons of land-generated plastic waste by 2010.

Environmental pollution caused by plastic debris has become increasingly apparent

## Synthesis and characterization of ternary layered double hydroxide containing zinc/copper/nickel and its PANI composite

Jigyasa Pathak | Poonam Singh 

Department of Applied Chemistry, Delhi Technological University, Delhi, India

**Correspondence**

Poonam Singh, Department of Applied Chemistry, Delhi Technological University, Delhi 110042, India.  
Email: [poonam@dtu.ac.in](mailto:poonam@dtu.ac.in)

**Funding information**

UGC BSR Start up Grant, Grant/Award Number: 30-416/2018; Delhi Technological University

**Abstract**

In this study, ternary layered double hydroxide (LDH) containing Zn, Cu, and Ni was synthesized successfully using hydrolysis route. Upon calcination at a lower temperature of 350 °C, the synthesized lattice transformed into ZnO containing Cu and Ni that can be reformed back to the layered structure simply by a phenomenon known as 'memory effect'. Furthermore, the synthesized lattice was used for the formation of polyaniline (PANI)-based composite material. The structural and morphological details of the as-prepared samples were studied using various spectroscopic techniques, that is, powder X-ray diffraction (PXRD), Fourier transform infrared (FTIR), thermo gravimetric analysis (TGA), and scanning electron microscopy-energy dispersive X-ray analysis (SEM-EDX), indicating the formation of single-phase ternary LDH as well as the successful incorporation of PANI in the interlayer region. Owing to the combined advantages of LDH and conducting polymer (PANI), zinc copper nickel layered double hydroxide (ZnCuNi-LDH)/PANI composite may be exploited as a potential candidate for a variety of applications in the future.

**KEY WORDS**

hydrolysis, layered double hydroxide, memory effect, multilayer structure, polymeric composites, powder technology

### 1 | INTRODUCTION

Layered double hydroxides (LDHs) have gathered significant interest in recent times due to their unique structure, ion-exchange properties, biocompatibility, and low toxicity.<sup>[1]</sup> Basically, LDHs represent a class of synthetic 2D network solids with hierarchical structure, also known as anionic or hydrotalcite-type clays. The crystallographic structure of LDHs resembles that of brucite, consisting of positively charged  $\text{MO}_6$  octahedral sheets held together by weak attractive forces.<sup>[2]</sup> The general structural formula of LDH is  $[(\text{M}^{2+})_{1-y} \text{M}^{3+}_y (\text{OH})_2] (\text{A}^{x-})_{y/x} \cdot m\text{H}_2\text{O}$ , where  $\text{M}^{2+}$  are divalent cations (e.g.,  $\text{Zn}^{2+}$ ,  $\text{Co}^{2+}$ ,  $\text{Mg}^{2+}$ , etc.),  $\text{M}^{3+}$  are trivalent cations (e.g.,  $\text{Fe}^{3+}$ ,  $\text{Cu}^{3+}$ ,  $\text{Ln}^{3+}$ , etc.) and  $\text{A}^{x-}$  is the charge compensating mobile anion trapped in the interlayer

region (e.g.,  $\text{CO}_3^{2-}$ ,  $\text{NO}_3^-$ , etc.) while  $y$  is the ratio of  $(\text{M}^{3+})/(\text{M}^{2+} + \text{M}^{3+})$ .<sup>[3]</sup> Thus LDHs possess tunable chemical compositions in terms of metal cations and interlayer anion, that facilitates variable charge density on the layers.<sup>[4]</sup> In addition, anion exchange route can also be followed for further modifying the inherent properties of LDHs, that is, electrochemical stability, conductivity, and inorganic/organic hybrid formation ability, etc.

The anion exchange ability in LDHs arises from the presence of positively charged layers, facilitating their use as an anion exchanger and anion scavenger. For successful exchange of interlayer anion in LDH, the pre-existing anion should have lower affinity for the interlayer region than the desired anion to be intercalated. The increasing order of anionic affinity for the



## Adsorptive Removal of Congo Red Using Organically Modified Zinc–Copper–Nickel Ternary Metal Hydroxide: Kinetics, Isotherms and Adsorption Studies

Jigyasa Pathak<sup>1</sup> · Poonam Singh<sup>1</sup>

Accepted: 26 September 2022  
© The Author(s), under exclusive licence to Springer Science+Business Media, LLC, part of Springer Nature 2022

### Abstract

In the current study synthesis of composite material consisting of ethylene glycol (EG) functionalized Zinc–Copper–Nickel (Zn–Cu–Ni) ternary metal hydroxide was successfully carried out and was characterized using various techniques. The formation of layered structure was confirmed using Powder X-Ray Diffraction (PXRD), Fourier Transform Infrared spectroscopy (FTIR) and Scanning Electron Microscopy (SEM) while thermal stability was assessed using Thermogravimetric Analysis (TGA). The presence of metal ions and their respective oxidation states was confirmed using Energy Dispersive X-Ray Analysis (EDX), elemental mapping, and X-Ray Photoelectron Spectroscopy (XPS). Pore size of the synthesized material, estimated using Brunauer–Emmett–Teller (BET) analysis technique, was found to be  $15.08 \text{ nm g}^{-1}$ . The synthesized material was subsequently utilized for the sequestration of toxic Congo red (CR) dye from untreated water. Investigation of controlling parameters i.e. concentration, contact time and pH was undertaken to see their influence on the adsorption performance. The maximum dye removal efficacy of the adsorbent was observed at pH 7, suggesting good buffering ability of EG functionalized Zn–Cu–Ni composite material. The experimental data for equilibrium studies was favoured by the Langmuir model, suggesting monolayer adsorption while the kinetic study was best-correlated with the model of pseudo-second order. The capacity of synthesized material for dye uptake was ascertained to be  $127.71 \text{ mg g}^{-1}$  along with the good reutilization capacity even after five consecutive cycles. These results demonstrate that EG functionalized Zn–Cu–Ni ternary metal hydroxide may be effectively used as an adsorbent for the separation of dye effluents from aqueous medium.

✉ Poonam Singh  
poonam@dtu.ac.in

<sup>1</sup> Department of Applied Chemistry, Delhi Technological University, Delhi 110042, India

# Municipal Solid Waste and Climate Change



Jigyasa Pathak, Ravinder Kumar, and Poonam Singh

## 1 Introduction

With the advent of the twentieth century, there has been an exponential rise in industrialization, urbanization, and the global population, which have, in turn, opened up various avenues for growth and production. But with rapidly increasing development opportunities, the production and accumulation of waste in our environment has increased multi-fold, thereby making it an issue of grave concern worldwide [1]. The growth of 'big' cities brings with itself betterment of healthcare facilities, advanced employment opportunities, and varied consumption patterns, which contribute to waste generation. But this also exacerbates waste generation, which poses a huge problem to waste management facilities at the municipal level. Municipal solid waste (MSW) poses health risks to the public and contributes to ecological imbalances. The presence of organic waste in the environment leads to microbial contamination and contributes to the leaching of contaminants into water and soil, thereby adversely affecting the water and soil quality. Previously published studies (Table 1) have touched upon the issue of solid waste management and disposal techniques, but virtually none of them provides a clear overview of its short-term impact on climate change and the immediate need for greenhouse gas (GHG) mitigation [2–5]. Further, the investigation of challenges faced by authorities during the solid waste management has been largely omitted from published works. Bearing this in view, the primary focus of this chapter is to discuss the various aspects associated with municipal solid waste management (MSWM) and its impact on climate change.

---

J. Pathak · P. Singh (✉)  
Department of Applied Chemistry, Delhi Technological University, Delhi 110042, India  
e-mail: [poonam@dtu.ac.in](mailto:poonam@dtu.ac.in)

R. Kumar (✉)  
Department of Chemistry, Gurukula Kangri (Deemed to Be University), Haridwar, UK 249404,  
India  
e-mail: [ravinder.kumar@gkv.ac.in](mailto:ravinder.kumar@gkv.ac.in)

© The Author(s), under exclusive license to Springer Nature Singapore Pte Ltd. 2024 207  
A. Gupta et al. (eds.), *Integrated Waste Management*,  
[https://doi.org/10.1007/978-981-97-0823-9\\_10](https://doi.org/10.1007/978-981-97-0823-9_10)



## **DELHI TECHNOLOGICAL UNIVERSITY**

(Formerly Delhi College of Engineering)

Shahbad Daulatpur, Main Bawana Road, Delhi-42

### **PLAGIARISM VERIFICATION**

Title of the Thesis **“Synthesis of Ternary Layered Double Hydroxides and their Composites for Environmental Applications”**

Total Pages **272**, Name of the Scholar **Jigyasa Pathak**

Supervisor (s)

**(1) Poonam Singh**

Department **Applied Chemistry**

This is to report that the above thesis was scanned for similarity detection. Process and outcome is given below:

Software used: **Turnitin**, Similarity Index: **10%**, Total Word Count: **61,219**.

Date: **08-09-2025**

**Candidate's Signature**

**Signature of Supervisor(s)**

# Jigyasa Pathak PhD Thesis.docx

Delhi Technological University

## Document Details

Submission ID  
trn:oid::27535:111319912

Submission Date  
Sep 8, 2025, 4:30 PM GMT+5:30

Download Date  
Sep 8, 2025, 4:48 PM GMT+5:30

File Name  
Jigyasa Pathak PhD Thesis.docx

File Size  
38.6 MB

272 Pages

61,219 Words

371,521 Characters



Page 2 of 203 - Integrity Overview

Submission ID trn:oid::27535:111319912

## 10% Overall Similarity

The combined total of all matches, including overlapping sources, for each database.

### Filtered from the Report

- » Bibliography
- » Quoted Text
- » Cited Text
- » Small Matches (less than 10 words)

### Exclusions

- » 4 Excluded Sources
- » 18 Excluded Matches

### Match Groups

- 302 Not Cited or Quoted 10%  
Matches with neither in-text citation nor quotation marks
- 0 Missing Quotations 0%  
Matches that are still very similar to source material
- 0 Missing Citation 0%  
Matches that have quotation marks, but no in-text citation
- 0 Cited and Quoted 0%  
Matches with in-text citation present, but no quotation marks

### Top Sources

6%	Internet sources
7%	Publications
5%	Submitted works (Student Papers)

### Integrity Flags

#### 1 Integrity Flag for Review

- Replaced Characters  
31 suspect characters on 53 pages  
Letters are swapped with similar characters from another alphabet.

Our system's algorithms look deeply at a document for any inconsistencies that would set it apart from a normal submission. If we notice something strange, we flag it for you to review.

A Flag is not necessarily an indicator of a problem. However, we'd recommend you focus your attention there for further review.

# CURRICULUM VITAE

---

## Jigyasa Pathak

---

Female | 19<sup>th</sup> May, 1995 | Indian



📍 Delhi | 📞 +919910313070, +919643025753 |

✉️ jigyasapathak1503@gmail.com |

🔗 [www.linkedin.com/in/jigyasa-pathak-bb6781b4](https://www.linkedin.com/in/jigyasa-pathak-bb6781b4) |

👉 <https://scholar.google.com/citations?user=rXPSK1MAAAAJ&hl=en>

### Professional Summary

---

Motivated and research-oriented individual with 6+ of experience in advanced research, scientific writing, and academic presentation. Demonstrates strong expertise in materials chemistry, nanomaterials, and environmental remediation. Committed to fostering research and academic excellence through innovative teaching, interdisciplinary collaboration, and continuous research engagement.

### Research Interests

---

- Inorganic and Materials Chemistry
- Nanostructured Materials
- Environmental Remediation and Sustainable Materials
- Layered Double Hydroxides (LDHs) and Composite Systems
- Surface Chemistry and Photocatalysis

### Research Portfolio

---

SCI/SCIE Indexed Journal Publications	9 Published
Book Chapters	1 Published
H Index/ i10 Index	6/3
Conferences/Workshops Attended	10
Citations	165

---

### Academic Qualifications

---

**Delhi Technological University, Ph. D.** 2019 - 2025

Subject: Chemistry

**Jamia Millia Islamia, M.Sc.** 2016 - 2018

Major: Materials Chemistry | SGPA: 8.2

**University of Delhi, B.Sc.** 2013 - 2016

Major: Chemistry | CGPA: 7.9

## Experience

---

- Delivered laboratory classes for B.Tech (1<sup>st</sup>) Inorganic Chemistry in Department of Applied Chemistry, Delhi Technological University.
- Collaborated with and guided M.Sc. Chemistry students for dissertation project in Delhi Technological University under the supervision of Dr. Poonam Singh

## Skills and Abilities

---

**Analytical Instruments:** UV–Vis, FTIR, XRD, SEM, UV-DRS, Zeta sizer, High-speed Centrifuge, pH meter, Ultrasonicator, and Refractometer

**AI & Digital Tools:** Microsoft Office Suite (Excel, Word, PowerPoint, Teams), ChatGPT, Perplexity, Grammarly, QuillBot, Turnitin, Mendeley, Zotero, ChemDraw, OriginPro, X’Pert HighScore, PowderX

**Core Competencies:** AI-Enhanced Research | Scientific Writing | Data Interpretation | Research Design | Digital Pedagogy | Academic Mentorship | Collaboration with Stakeholders

## Certifications

---

- *The Fundamentals of Peer Review and Responding to Reviewer Comments* - Wiley Researcher Academy
- *How to develop qualities necessary to succeed as a scientific researcher* - Wiley Researcher Academy
- *All you need to know to become an effective peer reviewer* - Wiley Researcher Academy
- *Peer Review Excellence* online course - IOP Publishing

## Key Achievements

---

- Recipient of **Research Excellence Award (2023, 2024 & 2025)**, Delhi Technological University.
- Completed **multiple editorial certifications** from Wiley Researcher Academy and IOP Publishing.

